PART I. EXPERIMENTAL INVESTIGATION OF AN ARC-HEATED SUPERSONIC FREE JET

PART II. ANALYSIS OF ONE-DIMENSIONAL ISENTROPIC FLOW FOR PARTIALLY IONIZED ARGON

Thesis by

Arvel B. Witte

In Partial Fulfillment of the Requirements

For the Degree of

Doctor of Philosophy

California Institute of Technology

Pasadena, California

1967

(Submitted May 25, 1967)

ACKNOWLEDGEMENTS

I am deeply indebted to Professor Toshi Kubota under whose guidance this investigation was conducted and to Professor Lester Lees with whom I have had stimulating discussions on many aspects of this thesis.

I am grateful to Mrs. T. van Harreveld for her careful numerical and graphical work; Miss J. Greene for reducing the raw test data; the Staff of the GALCIT Hypersonic Wind Tunnel, P. Baloga, H. Mazurowski, G. van Halewyn, S. Roman and J. van Dijk for their generous assistance in designing the facility and conducting the tests; the Staff of the Electronics Lab. under M. Jessey for assistance with the design and repair of instrumentation; the Staff of the Aeronautics Shop, especially G. Carlson, H. MacDonald, E. Dahl, and A. Slater for machining the arc heaters and probes; and Mrs. V. Conner for typing the rough draft and Mrs. E. Fox the final draft of this thesis.

I wish to thank my wife Carol, and my children, Gretchen and John, for providing the inspiration necessary to finish this work.

The work discussed in this thesis was carried out under the sponsorship and with the financial support of the U. S. Army Research Office and the Advanced Research Projects Agency, Contract No. DA-31-124-ARO(D)-33. This research is a part of Project DEFENDER sponsored by the Advanced Research Projects Agency.

ABSTRACT

I. Experimental Investigation of an Arc-Heated Supersonic Free Jet

An experimental investigation of the flow field of a highly ionized supersonic free jet has been carried out in a continuous-flow test facility. Measurements of impact pressure, mass flux, total enthalpy and stagnation point heat transfer profile were made in this flow field with two water cooled probes.

Argon gas, at a flowrate of 0.5 gm/sec, was heated in a magneto-plasma-dynamic arc heater without an external magnetic field operating from between 200 amp and 40 volts to 1000 amp and 25 volts. The total pressure ranged from between 20 and 35 mm Hg, at constant flowrate, and the atom-ion number density was approximately 10^{15} cm^{-3} at the exit plane. The average total enthalpy calculated from a heat balance ranged from between about 5,000 to 10,000 BTU/lb_m, while the probe measurements showed that the peak total enthalpy on the jet centerline near the exit plane was about three times the average total enthalpy.

The impact and mass flux measurements showed that the flow was hypersonic, source-like, chemically frozen, and in other details very much like the under-expanded free jet flow of a perfect gas. By combining these measurements with the total enthalpy measurements it was shown that the fraction of the total energy contained in ionization was about 0.6 which is quite close to the equilibrium stagnation value. For equilibrium stagnation conditions, the total temperature ranges from between 12,000° to 20,000°K. The species mass fraction ranges from 0.2 for the atoms and 0.8 for the singly-ionized ions, to 0.8 for the singly-ionized ions and 0.2 for doubly-

ionized ions.

Examination of the electron energy equation showed that within a few diameters from the exit plane the electrons become energetically isolated from the ions and the electron heat conduction term dominates.

A preliminary attempt to correlate the stagnation point heat transfer measurements along the axis shows that the electron temperature ($T_E \neq T_I$ in general) plays an important role.

II. Analysis of One-Dimensional Isentropic Flow for Partially Ionized Argon

One-dimensional isentropic-flow variables of partially ionized argon have been calculated by coupling the isentropic flow equations with the partition-function method of deriving equilibrium thermodynamic properties. Tabulated gas properties and flow variables are presented for stagnation conditions of 0.1, 0.5, 1.0, 2.0, and 3.0 atm pressure and temperatures from 6,000 to 14,000°K in 1,000°K increments. The gas properties computed for this flow process include the sound speed, entropy, enthalpy, electron concentration, ionization fraction, electrical conductivity and static-to-stagnation ratios of temperature, pressure, and density. Flow variables include velocity, mass flux, area ratio, and Reynolds number per centimeter. Compared to results obtainable from perfect gas relationships (neglecting excitation and ionization), the results indicate that electronic excitation, and especially ionization effects, significantly alter the flow variables, particularly at the lower stagnation

pressures and higher temperatures considered. However, with the exception of the effect of one excited state (the first excited state of the ion) on the equilibrium-composition equation, the thermodynamic properties calculated by neglecting excitation yielded results which were within 1% of those predicted by including excitation.

TABLE OF CONTENTS

TABLE OF CONTENTS (Cont'd)

TABLE OF CONTENTS (Cont'd)

LIST OF TABLES PART I

LIST OF TABLES PART II

LIST OF FIGURES PART I

LIST OF FIGURES PART I (Cont'd)

LIST OF FIGURES PART I (Cont'd)

LIST OF FIGURES PART II

NOMENCLATURE PART I

$\underline{B}$	magnetic field
c_i	mass fraction of the i^{th} species
c_{pi}	specific heat at constant pressure of the i^{th} species, $\frac{\gamma}{\gamma-1}\frac{\kappa}{m_i}$
c_{pf}	specific heat at constant pressure of mixture, $c_{pA}(1+\alpha)$
C	Chapman-Rubesin function, $\frac{\rho\mu}{\rho_e\mu_e}$
d	body diameter
D_{ij}	binary diffusion coefficient, Eq. D-6
D_{amb}	ambipolar diffusion coefficient
D	diameter
D_*	anode diameter, 0.75 in.
e	electronic charge
$\underline{E}$	electric field
g_w	ratio of wall to free-stream total enthalpy, h_w/h_{te}
G_{ij}	defined in Eq. D-3
h	static enthalpy
I	ionization potential; current
$\underline{J}$	current density
k	thermal conductivity
Kn	Knudsen number
Le	Lewis number, $\rho D_{amb} c_{pf}/k$
M	Mach number
m_i	mass of the i^{th} particle
$\dot{m}$	mass flowrate
n_i	number density of the i^{th} species, particles per unit volume
p	static pressure

P	electrical power input to arc heater
Pr	Prandtl number, $c_{pf}\mu/k$
q	heat flux
Q	heat loss to the cathode-anode coolant
Q_{ij}	collision cross section
r	body radius; jet radial distance
R	gas constant per unit mass of argon
T	static temperature
t	time
u	jet axial velocity
$\underline{U}$	local gas velocity
$\underline{V}$	diffusion velocity
V	arc voltage drop; volume
x	jet axial distance measured from exit plane
$\bar{x}$	x/D_*
X_i	mole fraction of i^{th} specie
z_{Iw}	non dimensional ion mass fraction, c_{Iw}/c_{Ie}
α	degree of ionization, c_I
β	shock wave angle
δ	boundary layer thickness
ε	$(\gamma-1)/(\gamma+1)$
γ	ratio of specific heats
ξ	r/x
κ	Boltzmann constant
λ	mean free path
μ	viscosity

μ_o	magnetic permeability of free space
ϕ	potential associated with $\underline{E} = -\nabla\phi$
θ	polar angle
ν_i	collision frequency of the i^{th} particle
ρ	density

Subscripts

A	atom species
a	average condition
aw	adiabatic wall condition
b	inviscid jet boundary; body
BL	boundary layer condition
c	arc heater plenum condition; condition at cold end of tube
e	boundary layer edge condition
E	electron species
f	chemically frozen condition
h	condition at hot end of tube
i	impact condition; species i
I	ion species; inviscid condition
II	doubly-ionized species
j	jet condition
m	measured quantity
o	refers to the sum of the ions and atoms
p	refers to probe
s	fully singly ionized; refers to source flow; stagnation point condition

t	local stagnation condition
t2	stagnation condition downstream of shock when Rayleigh supersonic Pitot formula applies
tank	condition in quiescent gas outside of jet
2	static conditions downstream of normal shock wave
∞	free-stream condition

Mathematical Symbols and Abbreviations

$\cong$	approximately equal to
$\sim$	varies directly as
LVM	low voltage mode
HVM	high voltage mode

NOMENCLATURE PART II

A	Helmholtz free energy
A/A^*	area ratio
A	argon atom
A^+	argon ion
a	speed of sound
C_p	specific heat at constant pressure
E	energy level
$\mathcal{E}_0$	zero-point energy level
e^-	electron
g_n	degeneracy of n^{th} energy level
h	Planck's constant
H	enthalpy per mole
$\overline{H}$	enthalpy per unit mass
I	ionization potential, $\mathcal{E}_0(A^+) = I$
K	equilibrium constant
k	Boltzmann's constant
M	Mach number
$\mathcal{M}$	molecular weight
$\overline{\mathcal{M}}$	molecular weight of ionized gas
m	particle mass
N_0	Avogadro's number, 6.023×10^{23} particles/gram-mole
N	number of particles
$\mathcal{N}$	number of moles
p	pressure
Q	partition function

R	gas constant per unit mass of unionized species
$\mathcal{R}$	gas constant per mole
Re/D	Reynolds number per unit length
S	entropy per mole
$\bar{S}$	entropy per unit mass
$\mathcal{S}$	collision cross-section
T	temperature, $T_0 = 273^\circ K$
U	internal energy
u	x-component of velocity
V	volume per mole
X	mole fraction
x	coordinate
Y(y)	general notation meaning Y of y
α	ionization fraction; ion mass fraction
ρ	density
σ	electrical conductivity

Subscripts

c	close encounters
d	distant encounters
e	equilibrium flow quantity
int	internal
i,n	summation indices
n	principal quantum number
pg	perfect gas
T	stagnation

tr	translational
0	frozen flow quantity

Superscripts

0	standard state condition
*	sonic conditions

I. INTRODUCTION PART I

For certain experiments at low densities the flow field produced by an under-expanded free jet has a number of decisive advantages over the flow field produced by the more conventional wind tunnel nozzle operating at the same stagnation-to-vacuum chamber pressure ratio, p_t/p_{tank}. For instance the boundary layer displacement effects present in conventional nozzles are absent in the free jet because all pressure waves reflected from the free shear layer which bounds the jet laterally are members of the same family of characteristics which coalesce to form the barrel shock.

Consisting primarily of a plenum chamber, either a sonic orifice or sonic nozzle, and a vacuum chamber into which the effluxing gas is expanded, the free jet test facility has been used extensively in molecular beam studies [1, 2 and others compiled by French (3)], as well as low density aerodynamic studies ranging from continuum to free molecule flow (4, 5, 6, 7, 8). The inviscid flow solution for the underexpanded free jet was obtained by Owen and Thornhill (9), Love et al. (4), Ashkenas and Sherman (8) and Sherman (10) by the method of characteristics. The survey paper on molecular beams by French (3) includes a bibliography of numerous investigators who have been concerned with the production of molecular beams from continuum sources. Recently Chou and Talbot (11) proposed a model for an ionized argon free jet which included the effect of radiation, elastic and inelastic species collisions, unequal electron and heavy species temperature, and different "radial" and "longitudinal" species temperature. However, they did not include

the effect of electron heat conduction whose importance is measured by one over the Peclet number, Pe, (= RePr), which was of order one for the high degree of ionization cases which they considered.

Of particular interest in the present investigation is the possibility of using an arc heater to provide a high enthalpy, low density, highly ionized, supersonic free jet continuous flow facility. The present state-of-the-art of arc heater technology does not permit the design of such a device to meet certain a priori performance requirements. Rather, the success of such an approach is usually the result of an arc heater development program which involves almost a trial and error iteration of design changes which eventually leads to an acceptable arc heater design. During the past decade most of the effort in arc heater development was directed toward increasing the average total enthalpy of such devices in order to provide reentry simulation for ablation and heat transfer studies. Very little experimental work has been done to relate the measurement of arc heater performance quantities, such as arc current and voltage drop, average total enthalpy, and arc heater plenum pressure, to local flow quantities such as temperature, pressure, mass flux, and total enthalpy. In fact no one has completed a flow field calibration for any substantially ionized steady gas flow test facility. The problem of interpretation of probe measurements and survival of the probe itself in this hostile environment have complicated the use of diagnostics tools, and thus have allowed only rather slow progress even in such a fundamental task as flow field calibration.

The arc heater used in the present investigation is one version of the so-called Magneto-Plasma-Dynamic (MPD) source (Section II. 2) which has been studied by a number of investigators (12, 13, 14, 15) during the past four years. The MPD source was chosen because of its current use in several phases of plasma technology, the spectroscopic purity of the jet it produces (Section III. 1), and the fact that recent studies of the effluxing supersonic jet have been made. With the exception of a few investigators (15, 16), the current interest in this source has been directed towards its potential use as a Hall current accelerator (12, 13, 14) which is obtained when an externally applied field, a "donut" coil or solenoid, is aligned with the jet axis and positioned to circumscribe the arc discharge region.

Central to the concept of a free jet, as envisioned in the present investigation, is that the arc discharge be restricted to a region very near the electrodes, so that the electromagnetic effects on the effluxing jet far from the orifice are at most small perturbations to the flow field of an otherwise source-like free jet. In this regard several investigators (17, 18, 19) have measured the current distribution in such a jet from an MPD source with an applied magnetic field. Of particular interest here is the experimental investigation by Powers (17) who measured the induced magnetic fields with a water-cooled Hall-effect sensor to deduce the current density distribution from Ampere's law (which relates the current density to the magnetic field and its spatial derivatives) in the jet effluxing from an MPD source. His MPD source had a 2 cm long, 45^{o} half-angle nozzle

expansion whose exit diameter was $D_{ex} \cong 5.3$ cm. Surveys taken at 5 cm ($x/D_{ex} \cong 1$) from the exit plane with nitrogen showed that $B_\theta(r)$ was approximately proportional to the applied field and decreased to zero when the applied field was reduced to zero. From Ampere's law, this result implies that the radial and axial components of current are zero. The azimuthal current density could not be determined nearly as accurately, but was much less than the radial and axial components when operating with the applied field. With the maximum applied field of 1500 Gauss, Powers (17) found that substantially less current was contained in the jet when operating with argon as compared with nitrogen. On the basis of his investigation there is good reason to believe that the electromagnetic effects on the jet produced by an MPD source operating without an applied field are confined to the discharge region at the exit plane. The other investigators (18, 19) gave no experimental results without an applied field nor was their investigation nearly as comprehensive as the work by Powers (17).

Kelly, Nerheim and Gardner (15) and Nerheim (20) determined the electron temperature spectroscopically near the exit plane of the MPD source operating at a main gas flowrate of 0.3 gm/sec argon and at 1000 and 1600 amp. in the low voltage mode (operating modes of the MPD source are discussed in Section II. 2 and III. 1). The combined range of electron temperature caused by changes in axial and radial position and arc current level was between $16,300 \pm 1000^{\circ}K$ and $17,800 \pm 500^{\circ}K$ where $\pm 1,000$ and $\pm 500^{\circ}K$ refers to the error band of the measurements. These measurements made in the intense

core of the jet showed that the electron temperature was nearly independent of radius for the two axial positions investigated at 1 and 5 cm (x/D_* of about 1/2 and 3) from the exit plane. From an exit plane static pressure measurement and the measured electron temperature, the Saha equation was used to estimate electron number density. For an argon plasma in which the electrons are in equilibrium at this temperature and pressure some multiply-ionized species exist. Under these conditions the energy of ionization alone for a fully singly-ionized gas was shown to exceed the average total enthalpy calculated from an energy balance of the MPD source. From this result they (15) concluded that the electron number density must be much lower than that required for equilibrium with the measured electron temperature. An alternative explanation of this result is that not all the gas effluxing from the jet is fully singly-ionized; rather, the MPD source produces a very highly-ionized core of gas but a much cooler region of un-ionized, radiating gas outside this core region.

The incompleteness of the flow field studies made by former investigators leaves a number of questions unanswered concerning the usefulness of the MPD source to provide a highly-ionized supersonic free jet in which aerodynamic studies can be conducted. For instance, no measurements have been reported to show the structure of the flow field and its similarity or dissimilarity to the "classical" underexpanded free jet. The objectives of Part I of this investigation were three-fold: (1) to design and develop a low density, high enthalpy test facility; (2) to build and develop suitable diagnostic probes to

withstand steady operation in an extremely hostile plasma environment; and (3) to use these probes to study and define the flow field of an arc-heated, highly-ionized argon free jet.

The experimental equipment and measurement technique is described in Part I, Section II. The results of the impact pressure, mass flux, total enthalpy, and stagnation point heat transfer measurements, which were made primarily in the supersonic part of the jet, are described in Part I, Section III. Probe corrections as well as transport properties of argon are discussed in the Appendixes.

Included also in Part I of the Appendixes is a discussion of transport properties for argon as well as a comparison between two current methods of predicting transport properties.

II. EXPERIMENTAL EQUIPMENT AND MEASUREMENT TECHNIQUE

II.1. Low Density Facility

The vacuum facility shown schematically in Fig. 1 is equipped with an Edwards Model 30 B5 Speedovac vapor booster pump having an unbaffled peak speed of 9,000 to 10,000 liters/sec in air between about 10^{-4} and 6.5×10^{-3} mm Hg, and about 8,300 liters/sec for argon over the same pressure range. The booster pump has an ultimate vacuum of about 10^{-4} mm Hg. This pump is backed with a Beech-Russ Model 325-D rotary piston pump whose displacement is about 8,000 liters/sec and has an ultimate vacuum of about 0.1 mm Hg. The performance characteristic of the facility is shown in Fig. 2. This characteristic may vary somewhat from test to test depending upon out gassing, external air leaks and occasional internal water leaks from the water cooled equipment such as the heat exchanger, arc heater, and probe. The ultimate vacuum of the vacuum facility is about 10 microns Hg. The leak rate is about 30 microns Hg/hr.

The results of a simple calculation given in Section III.2 relates jet flowrate, $\dot{m}_j$, static pressure behind the disk shock, p_2, ($p_2 \cong p_{tank}$) and stagnation temperature to the disk shock position x_s of a highly underexpanded free jet as

$$x_s = (\dot{m}_j/p_2)^{1/2} (\pi)^{-1/2} \left[\frac{\gamma}{2(\gamma-1)}\right]^{1/4} (RT_t)^{1/4}$$

For the conditions of the cold flow tests conducted here, ($\dot{m}_j \cong 0.5$ gm/sec),

$x_s \cong 3$ in.

Under these same conditions, the disk shock and maximum barrel shock diameters are approximately 1.5 in. and 1.8 in. respectively. The heated jet, at the same flowrate, was about twice this size.

II.2. Arc Heater

The arc heater shown in Fig. 3 is a modified design of the so-called MPD (Magneto-Plasma-Dynamic) arc heater used at the Jet Propulsion Laboratory*. The JPL MPD arc heater was modified first by eliminating the copper cathode base and then by changing from tangential to radial gas injection. These modifications were made in order to eliminate arc attachment at the braze joint between the 2% -thoriated tungsten rod and the copper base and to eliminate the destabilizing effect on the arc due to the tangential injection scheme. Probably because of the diffuse arc discharge at these pressures, neither tangential injection nor the tangential $[F_\theta = J_r B_x]$ body force produced on the discharge by an axially aligned solenoid is needed to rotate and hence distribute the discharge attachment uniformly between the cathode and anode surfaces.

The arc starting procedure was as follows: An open-circuit voltage of 320 v. was applied between the anode and cathode at a welder setting near 1,000 amp and at an elevated gas flowrate of

---

* The JPL MPD arc heater had a conical copper cathode mount whose base converged from the aft or cooled end of the cathode at 45° and intersected the 2% -thoriated tungsten (cathode) rod (which ran through the copper base) at a brass braze joint. It also utilized tangential gas injection and did not have the cathode shield shown in Fig. 3.

about 1 gm/sec. Because of the high open circuit voltage, the arc is self-starting. After the discharge was initiated the flowrate was reduced to 0.5 gm/sec to eliminate any back streaming of diffusion pump oil.

Gas flowrate, flowrate and temperature rise of the coolant and electrical power input were measured and recorded for each test and used to calculate average total enthalpy and energy transfer efficiency. A description of the water and gas flowmeters, thermocouples, voltmeter and ammeter are given in Section II.4, and a discussion of the arc heater performance and discharge model are given in Section III.1.

II.3. Diagnostics Probes and Instrumentation

II.3.1. Hemisphere-Cylinder Impact Pressure Probe

In order to maintain the structural integrity of any probe exposed in steady state to the extremely high enthalpies produced by the arc heater described in Section II.2, provision must be made for water cooling in addition to any radiation cooling already present.

The hemispherical-nosed 0.148 in. outside dia., 0.046 in. inside dia., stainless steel water-cooled impact pressure probe shown in Fig.4 employs an annulus and a single tube baffle which form the water-cooling jacket. All joints were silver soldered except the tip which was heli-arc welded. In this regard it should be mentioned that the advantages of using stainless steel tubing, as compared to copper tubing, include ease of machining and welding, wide selectivity of tube sizes, and resistance to corrosion. The

major disadvantage of using stainless steel in this application was its low thermal conductivity which is about 1/20 that of copper.

A Haynes 25 radiation cooled shield was used to provide additional thermal protection for the manifold. Although this shield was bolted to the probe base and as such received some additional cooling by conduction, melting occurred at the point where the probe leading edge shock impinged on the shield while probing in the vicinity of the jet exit.

The probe water flow rate was maintained at about 2.5 gm/sec and was supplied at about 50 psig from the laboratory tap.

In addition two bare-wire copper-constantan thermocouples were installed close to the probe manifold, one inside the inlet and the outlet of the water supply lines in order to measure the probe water temperature rise, and another copper-constantan thermocouple was located in the aft section of the impact tube to measure gas temperature. Instrumented in this way, this impact pressure probe had the capability of being used as a total enthalpy measuring probe using the calorimetric technique developed for subsonic flow by Grey et al. (21) who used a probe of nearly the same design.

Numerous tip burnouts with subsequent leakage of probe water occurred when making impact pressure measurements near the jet exit plane, i.e., for x/D_* between 1 and 2 while operating the arc heater at 1,000 amps. An estimate of the maximum allowable probe heat flux was obtained by calculating the heat flux at the upper limit of nucleate boiling, q_{ul}, from the experiments by Welsh (22) who correlated q_{ul} as a function of average coolant velocity, u_a, and

degree of subcooling, $\Delta T_{sub} = (T_{sat} - T_a)$, for water flowing in electrically-heated stainless steel tubes. T_{sat} is the saturation temperature of water corresponding to the local water pressure and T_a is the local average or bulk temperature of the coolant. Welsh (22) gave the empirical relationship

$$q_{ul} = 0.0476\ (0.132u_a^2 + \Delta T_{sub})\ \text{BTU/(in}^2\ \text{sec)}$$

with u_a and ΔT_{sub} in ft/sec and $^{\circ}F$ respectively. Since $u_a \lesssim 10$ ft/sec and $\Delta T_{sub} \cong (300 - 80)^{\circ}F$, coolant velocity played a secondary role as compared to degree of subcooling or local water pressure, here $q_{ul} \cong 10$ BTU/(in^2 sec) for $p_{water} \cong 50$ psig. Subsequent measurements of stagnation point heat flux indicated that this impact probe may have been subjected to a heat flux nearly twice this value of q_{ul}. Because of this high heat flux, the probe experienced numerous burnouts and was finally replaced by the probe discussed in Section II.3.2.

II.3.2. Combined Impact Pressure, Mass Flux and Total Enthalpy Probe

The possibility of making more than one measurement, consecutively, with the same probe, at a given jet operating condition and probe position led to the design of the combined impact pressure, mass flux and total enthalpy probe shown in Fig. 5.

This probe differs in design from the hemispherical nosed impact pressure probe (Section II.3.1.) in three important ways: (1) removable and hence interchangeable probe tips; (2) an external coolant passage designed to shield the calorimeter which is the

internal coolant passage; and (3) a water cooled probe shield, all shown in Fig. 5. One disadvantage of this probe design is its large after-body size; however, this feature is not too serious as long as measurements are confined to supersonic flow regions.

This probe was fabricated using stainless steel and was instrumented with thermocouples in a manner conceptually the same as the hemispherical nosed probe (Section II.3.1.). The purpose of the external coolant passage was to isolate the calorimeter thermally from the tip support and after-body heating. As a result of this design, the manifold had to be split several times as shown in Fig. 5 and hence "O" ring seals were required on mating surfaces to prevent coolant leakage.

Chamfered tips of various size were machined from molybdenum, tungsten and carbon. For the reasons discussed in Appendix A the tips used for mass flow, ρu, measurements in supersonic flow were required to have sharp leading edges. The leading edge thicknesses of the molybdenum and tungsten tips were between about 0.0005 and 0.001 in. as measured with a Kodak contour projector, whereas tip cracking and chipping difficulties during machining limited tip leading edges of the carbon tips to about 0.0015 in. at best. A Leeds and Northrup Model 8622-C portable optical pyrometer was used to measure tip temperatures as high as 2,800°K for tungsten and somewhat lower for carbon tips for probe measurements at $x/D_* = 1$. Tips made from molybdenum (melting point $\cong$ 2,900°K) melted under similar conditions.

Flow rates of probe water ranged from 7 to 40 gm/sec and

from 1 to 20 gm/sec for the external and internal passages respectively. In order to increase the cooling margin or upper limit of nucleate boiling, a pressurized water system was installed to supply untreated tap water to the probe at 150 psig. This step increased the margin of safety by about 40% or to an upper limit of nucleate boiling, q_{ul}, discussed in Section II.3.1, of about 14 BTU/in^{2}sec. Even with the thermal shielding provided by the probe tips the forward joint of the coolant passages melted and the stainless steel tubing had to be replaced by copper tubing having nearly the same dimensions. No further burnouts were encountered.

All impact pressure measurements reported here with this probe in hot flow were made with the 0.15 dia. tip. An 8 in. piece of 1/4 in. dia. copper tubing joined the aft end of the impact pressure tube to the Statham pressure transducer described in Section II.3.4. Also joined to the aft end of the impact pressure tube was a larger 1 in. inside dia. copper tube to which was clamped a 4 ft. piece of flexible, but non-collapsible, vacuum hose. This hose was joined through a nipple in the top of the tank to valve A (shown in Fig. 6 of the mass flux sampling system. A detailed discussion of the mass sampling technique is given in Appendix A. When the probe was used to measure total enthalpy, a stubby tip was used (see Fig. 5) so that radiative and convective heat transfer from the tip to the aspirated gas sample would be eliminated. The inside diameter of the impact pressure tube was chosen large enough so that a measurable thermocouple signal could be obtained from the calorimeter when operating the probe where the total enthalpy flux was quite small, i.e., for

$x/D_* >> 1$. Knowledge of three measured quantities, the aspirated gas flowrate, the calorimeter water temperature rise, and water flowrate, was enough to calculate the total enthalpy of the gas.

The most serious problem associated with measuring the total enthalpy concerned heat leakage from the calorimeter to the external coolant passage at the tip joint. A theoretical model of the heat transfer to the calorimeter was developed and applied in Appendix B in an attempt to account for the tip heat leakage.

II.3.3. Stagnation Point Heat Transfer Probe

The stagnation point heat transfer probe shown in Fig. 7 has an external coolant passage which cools the "shoulder" of the hemisphere and the cylindrical afterbody and an internal or calorimetric coolant passage which cools the 60° included angle copper sensor portion of the hemispherical probe tip. The internal water passage was isolated from the external water passage by a 0.001 in. "air" gap at the tip and a 0.010 in. gap from somewhat beyond the tip to the manifold to minimize calorimeter heat leaks. With the exception of the copper sensor the probe was fabricated from stainless steel. Joints were silver soldered and the manifolding of the coolant passages was sealed with "O" rings. Although not shown in Fig. 7, 1/4 in. dia. water-cooled copper tubing was silver soldered to the manifold shield to provide additional thermal isolation of the calorimetry manifolding.

Three series-connected bare-wire copper-constantan thermocouples were used in the water inlet and outlet lines to measure the calorimeter water temperature rise. Typical water temperature

rise between the inlet and outlet of the calorimeter ranged from between 7 and 40°F as probe position ranged from between 1 and 12 anode diameters from the exit. The water flowrate was about 7 gm/sec in the external coolant passage and ranged from between about 1.5 and 7 gm/sec in the calorimeter. An iron-constantan thermocouple was silver soldered to the aft end of the sensor to provide the stagnation point wall temperature.

Knowledge of the calorimeter water flowrate and temperature rise permitted the calculation of the average heat transfer rate to the sensor, q_a. In Appendix C a correction is developed for the effect of finite sensor area and angle-of-attack so that q_a may be related to the stagnation point heat transfer rate, q_s.

II.3.4. Instrumentation

The vacuum tank (Fig. 1) pressure and the mass flux collector tank (Fig. 6) pressure were measured in the preliminary cold flow part of the investigation by a Vacustat gauge which is a miniature McLeod gauge. However, due to the poor resolution and lack of repeatability, this gauge was replaced by a three pressure-ranged McLeod gauge manufactured by Todd Scientific Co.

The impact pressure measurements in cold flow were made with a ± 0.05 psi differential pressure transducer (Statham Model No. PM97TC ± 0.05-350, Serial No. 11242). For reasons of transducer safety, the vacuum tank was used as a reference pressure which was measured with the Vacustat. The combined errors in impact pressure due to lack of repeatability of the Vacustat and the small pressure fluctuations inherent in the diffusion ejection pumping

system were estimated to be as much as 5% in cold flow. The impact pressure measurements in hot flow were made with a 0-1 psia Statham pressure transducer (Model No: PA731TC-1-350, Serial No. 12448) which was calibrated using the McLeod gauge. The calibration is shown in Fig. 8. The pressure transducer was encased in a water-cooled "can" and located about 8 in. from the impact pressure probe in order to remove it from the region of direct jet impingement. A shielded cable led from the transducer through a hermetically sealed bulkhead to the zeroing potentiometers (balance circuit) and d.c. power supply. The signal was amplified and either plotted on a Moseley X-Y plotter or read on a digital voltmeter (Kintel 501B or Fairchild's Digital Integrating Voltmeter Model Number 7100). A schematic diagram of the pressure measuring circuit is shown in Fig. 9. A Beckman Fitgo Model RP-B1 d.c. amplifier was used for the hot flow measurements and either a Sanborn Model No. 1500-860S or Astro Model No. 885 d.c. amplifier was used for the cold flow measurements. The accuracy of the combined transducer and recording system was within about 1%.

The arc heater, vacuum tank heat exchanger, and probes were water cooled. Temperature measurements required for calorimetry were made with copper-constantan thermocouples fabricated and installed with Swagelok fittings as shown in Fig.10. Those probe thermocouples which were installed in the inlet and outlet tubes of the probe manifold (not shown here), were stainless steel sheathed magnesium oxide-wrapped thermocouple formed from stock supplied by Thermo Electric or Leeds and Northrup which was modified to

include a Swagelok fitting.

Very often a difference in temperature between the inlet and outlet of a cooling circuit was required rather than the absolute value. In these instances, either the inlet or outlet temperature could be considered as a reference temperature and the thermocouple output was related to the temperature difference, ΔT, through a conversion factor which was a constant 45.5 mv/^{o}F within 1% for thermocouple grade copper-constantan thermocouple wire for small ΔT's above room temperature. This conversion factor, which is just the slope of the temperature vs. milli-volt output curve, as obtained from the Leeds and Northrup Conversion Tables for Thermocouples (23), was also verified for the temperature range of application by using a laboratory grade mercury-filled glass thermometer having an accuracy of about 1/2^{o}F.

Probably due to stray currents made possible by the joint anode-cathode coolant passage of the arc heater, bare-wire thermocouples in the anode-cathode coolant passages did not yield repeatable data for otherwise steady operating conditions. This problem was solved by using the glass insulated thermocouple shown in Fig.10.

All thermocouples except those associated with the total enthalpy and stagnation point heat transfer measurements were read out on a Brown (Minneapolis-Honeywell), 0-5 mv, 24 point strip-chart recorder. The outputs from the total enthalpy probe and stagnation point heat transfer probe thermocouples were amplified by a Leeds and Northrup (Model No. 9835B) stabilized d.c. microvolt amplifier whose output was recorded on a Moseley Audograph

Model 7001 X-Y Recorder. The combined error of amplification and recording of these measurements is less than about 1%.

The water flowrates through the vacuum tank heat exchangers and probe shield were measured by calibrated Venturi meters to within an accuracy of about 2%. The arc heater water flowrate was measured by a Fischer and Porter Precision Bore Flowrator, tube No. FP-1-35-G-10/80, calibrated to 1% of full scale from 0.1 to 0.9 lb_m/sec. The probe water flowrates were measured with Fischer and Porter Tri-Flat Precision Bore Flowmeters having 1/4 in. dia. tubes using glass and tantalum floats which were calibrated to 1% of full scale reading from 25 to 100% of full scale.

The argon flowrate to the arc heater was measured with a Fischer and Porter Model No. 10A0735M Precision Bore Flowrator which was calibrated at 1% of the scale reading from 0.10 to 0.56 gm/sec at 50 psig and 70°F.

The voltage across the arc was measured with a Simpson Model 1700 Multi-Range DC Voltmeter Standard as well as recorded on the Brown strip-chart recorder. The arc current was measured with a Simpson Model 1701 Multi-Range DC Ammeter.

III. RESULTS AND DISCUSSION

III.1.1 Arc Heater Performance

Probably the least understood operating feature of the unshielded cathode arc heater (Fig. 3, but without cathode shield), was its two modes in "electrical" characteristic as shown in Fig. 11. The discharge was initiated as described in Section II.2 at 1000 amp. with an argon flowrate of 0.5 gm/sec and the resultant arc voltage was typically 17 to 19 v. This condition is called the low voltage mode (LVM). Generally, but not always, after 15 minutes to one-half hour, the arc voltage began to rise and fall aperiodically for about five minutes. Then, quite suddenly, typically in a matter of five seconds, a rise in voltage occurred to about 23 to 25 v., or what was called the high voltage mode (HVM), and again the voltage and current levels were steady. (See for instance the transition at 200 amp. shown in Fig. 11.) During the five-minute transition, the chamber pressure also rose and fell with the voltage. The reverse transition from the HVM to the LVM was observed only seldomly at 200 amp. when the voltage would drop from about 40 to 20 v., again at constant current. This reverse transition was never observed at 1000 amp.

By using an anode (see Fig. 12) modified to include a static pressure tap, for one test shown in Fig. 13, the effect of operating the arc heater in the LVM and HVM on arc heater plenum pressure, p_c, and exit pressure, p_{ex}, was investigated. Although p_c is a rather strong function of input power, P, as well as operating mode, p_{ex}, is weakly dependent on P and appears to be independent of operating mode.

Without any heating of the gas the ratio of plenum-to-tank pressure p_c/p_{tank} is large enough that choking occurs at the minimum area or in the annulus. For the LVM it is suspected that the discharge is confined to the aft (upstream) end of the annulus formed by the cathode and anode, whereas for the HVM it is confined to a region near the exit plane. Operation in the LVM is analogous to the case of heat addition to a gas flowing in a pipe for which the exit Mach number was one (choked f low) prior to the heating process. The effect of heat addition causes p_c to rise above its value in cold flow. This increase in p_c is necessary to offset the loss in total pressure caused by heat addition as well as to provide the increased total pressure necessary at the sonic condition to maintain a constant flowrate, i.e., $\left[p_t/(T_t)^{1/2}\right]_{sonic}$ = constant. Since less heating occurs prior to the sonic condition for the HVM, p_c is lower than that observed for the LVM.

Although arc heater performance and limited probe measurements were obtained in the LVM, it became quite difficult, if not impossible, to finish a set of profile measurements in the free jet without being disrupted, by a complete change in operating mode (transition) which had measurable effects on the free jet as well. Therefore a series of modifications of the arc heater led to the installation of a boron nitride cathode shield over much of the jointly exposed electrode surfaces as shown in Fig. 3 . The gas was now injected through the annulus formed by the slot between the cathode and the insulator. The arc again started in the LVM. However after several minutes the voltage began to rise monotonically and

steadily over about a five minute transition into the HVM. The shielded cathode characteristic is also shown in Fig. 11 for a typical test.

Arc heater operation at about 150 amp. and below was unstable in the sense that the arc discharge and jet plume either pulsed noticeably or deflected appreciably from the normal jet centerline. Significant erosion of the copper anode almost always accompanied this abnormal operation. Operation of the arc heater at higher (0.7 gm/s) and lower (0.3 and 0.1 gm/s) flowrates was unsatisfactory for similar reasons.

Although no detailed spectroscopic assessment of impurity presence and level was made in this investigation, such an attempt was made at the Jet Propulsion Laboratory by Nerheim (24) who operated the JPL MPD arc heater (without the cathode shield) at the same gas flowrate and power input as were used here. Numerous spectra, between 2900 Å and Tri-X cutoff, were taken using a 3 meter Jerrell Ash spectrograph, but none of them revealed any of the persistent copper or tungsten lines. Since there is no indication that the copper anode erodes from test to test the absence of copper spectral lines is not surprising. The tungsten cathode does erode; however, in view of the absence of any tungsten spectral lines the erosion rate must be extremely small during the steady state operation, or clusters of tungsten atoms leave the cathode and radiate with a continuous spectrum, or erosion occurs during initiation of the arc when occasional sparks are observed.

A performance parameter often used as a measure of the amount of energy added to the gas by the arc discharge is the average total enthalpy, h_{ta}. This parameter is defined from consideration of the energy balance in the region of the arc discharge. Consider a control volume of gas bounded by surface s as shown in the sketch.

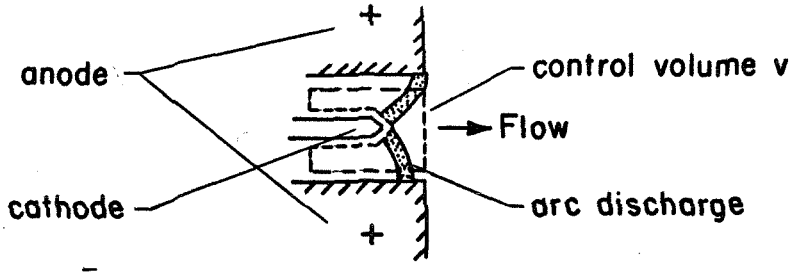

For this simple model the integral energy equation for a gas volume, v, bounded by area s is,

$$\underbrace{\int_s h_t \rho U \cdot \underline{n}\, ds}_{\text{net flux of total enthalpy through the area}} = \underbrace{\int_v \underline{J} \cdot \underline{E}\, dv}_{\text{electrical energy input to the volume}} + \underbrace{\int_s -\underline{q} \cdot \underline{n}\, dx}_{\text{heat transferred to the gas through surface bounding v = -Q.}}$$

where $\underline{n}$ denotes the outward unit normal vector to the fluid. This integral formulation is now applied to the following simple model, in which the incoming enthalpy is negligible. The second term in the equation is rewritten, using Green's theorem, as

$$-\int \nabla \cdot (\phi \underline{J}) dv = -\int \phi\, \underline{J} \cdot n ds = (\phi_{anode} - \phi_{cathode})\, I = VI$$

where $\underline{E} = -\nabla \phi$ and $\nabla \cdot \underline{J} = 0$ have been used.

By defining a mass average total enthalpy as

$$h_{ta} = \frac{1}{\dot{m}_j} \int_s h_t \, \rho \underline{U} \cdot \underline{n} \, ds$$

and denoting the right side of the energy equation as P - Q where P = VI, h_{ta} becomes

$$h_{ta} = \frac{P-Q}{\dot{m}_j}$$

Other performance quantities of interest, the average heat loss to the coolant, Q, and energy transfer efficiency, η, were calculated from the gas flowrate, calorimeter water temperature rise and electrical power measurements as,

$$Q = c_p \dot{m}_c \Delta T_c$$

and

$$\eta = \frac{P-Q}{P}$$

The results of these calculations for h_{ta}, Q, and η, are shown in Figures 14, 15, and 16. Q, h_{ta} and η for the shielded cathode tests are bracketed by the range of these quantities for the unshielded cathode tests in the LVM and HVM. In the HVM the arc voltage, at constant current, was higher for the shielded cathode tests but the heat loss, Q, was substantially higher so that the net effect was to yield higher average total enthalpy and energy transfer efficiency for the unshielded cathode tests. Since, however, arc heater operating stability was far more important than high efficiency, the shielded cathode arc heater is believed to be superior to the unshielded design for purposes of this investigation. Corresponding

to the range of h_{ta}^{*} shown in Fig. 15, an average total temperature, T_{ta}, and species mass fractions for the atoms, c_A, and the singly-ionized ions, c_I, for equilibrium** conditions have been tabulated here for reference purposes. These quantities, shown in the table, were obtained from the equilibrium thermodynamic calculations of Baum and Cann (25) corresponding to our measured values of h_{ta} and plenum pressure, p_c.

	Conditions at lowest input power, Fig. 15			Conditions at highest input power, Fig. 15		
	T_{ta} °K	c_A	c_I	T_{ta} °K	c_A	c_I
LVM and HVM without cathode shield	6300	1.0	10^{-4}	12300	0.5	0.5
HVM with cathode shield	9800	0.9	0.1	11600	0.7	0.3

Ideally it would have been desirable to operate at a negligible ionization level as well as with the shielded cathode arc heater. However this flexibility could have been achieved in this investigation only at the expense of continued operation without the cathode shield and the uncertainty and disruption of the transition from the LVM to the HVM.

*The total enthalpy measured at the centerline of the jet is approximately 3 h_{ta} (see Section III.3.4).

** The extent to which the plasma can be considered to be in equilibrium, i.e., considered to have equal species temperatures, and to have the species composition determined by the law of mass action, is a subject which will be considered later in interpreting the results of the probe measurements.

Since the radial component of current, J_r, crosses the induced azimuthal magnetic field, B_θ, an axial body force acts upon the plasma which can be represented as,

$$F_x = \int_v J_r B_\theta \, dv$$

The integral form of Ampere's law is

$$\int_s (\nabla \times \underline{B}) \cdot \underline{n} \, ds = \int_s \mu_o \underline{J} \cdot \underline{n} \, ds$$

Applying Stokes' theorem to the left hand side, B_θ, becomes

$$B_\theta(r,x) = \frac{1}{2\pi r} \int_s \underline{J}(r,x) \cdot \underline{n} \, dx$$

In order to estimate the size of this body force, two simple discharge models are considered as follows:

Discharge Model for LVM:

Boundary Conditions:

(i) $B_\theta(r,0) = \frac{\mu_o I}{2\pi r}$

$R_c < r < R_o$

(ii) $B_\theta(r,\ell) = 0$

(iii) $\underline{J} = 0 \quad x < 0 \quad r > R_c$

$x > \ell \quad$ for all r

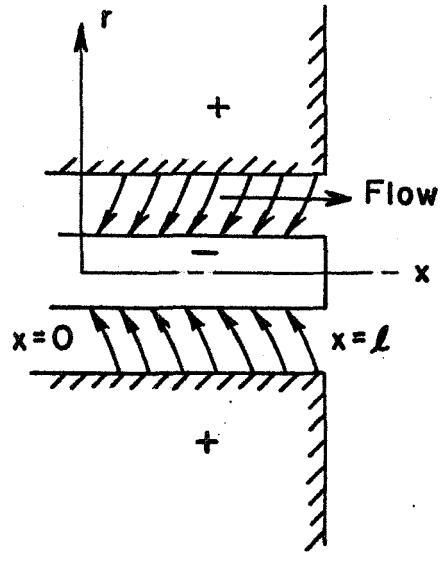

where I is the total arc current and R_c and R_o are the cathode and anode radii respectively.

Discharge Model for HVM:

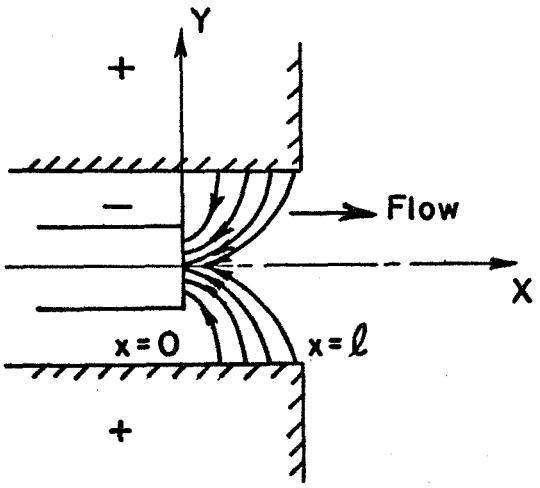

Boundary conditions:

(i) $B_\theta(r,0) = \frac{\mu_o I}{2\pi r}\left(\frac{r}{R_c}\right)^2$

$0 \leq r \leq R_c$

(ii) $B_\theta(r,0) = \frac{\mu_o I}{2\pi r}$

$R_c \leq r \leq R_o$

(iii) $B_\theta(r,\ell) = 0$

(iv) $\underline{J} = 0 \qquad x < 0 \quad r > R_c$

$x > \ell$ for all r

where the current entering the cathode at x = 0 has been assumed to be of constant current density.

From Ampere's law,

$$\mu_o J_r = -\frac{\partial B_\theta}{\partial x}$$

and F_x becomes

$$F_x = -2\pi \int\int \frac{\partial}{\partial x}\left(\frac{B_\theta^2}{2\mu_o}\right) r\,dr\,dx$$

$$= -2\pi \int \frac{B_\theta^2}{2\mu_o}\Bigg|_0^{\ell} r\,dr$$

The body force for the LVM becomes

$$F_x = 2\pi \int_{R_c}^{R_o} \frac{1}{2\mu_o}\left(\frac{\mu_o I}{2\pi r}\right)^2 r\,dr = \frac{\mu_o I^2}{4\pi}\,\ell n\,\frac{R_o}{R_c} \qquad \text{(LVM)}$$

and for the HVM,

$$F_x = 2\pi\left[\int_0^{R_c} \frac{1}{2\mu_o}\left(\frac{\mu_o I}{2\pi r}\right)^2 \left(\frac{r}{R_c}\right)^4 r\,dr + \int_{R_c}^{R_o} \frac{\mu_o I}{2\pi r}\right)^2 r\,dr\right]$$

$$= \frac{\mu_o I^2}{4\pi}\left[\frac{1}{4} + \ell n \frac{R_o}{R_c}\right] \qquad \text{(HVM)}$$

In MKS units, $\mu_o I^2/4\pi$ becomes

$$\frac{\mu_o I^2}{4\pi} = 0.1\left(\frac{I}{1000}\right)^2 \quad \text{Newton's}$$

where I is in amperes. Since $R_o/R_c = 2$, $F_{xHVM}/F_{xLVM} = 1.25$.

The resultant pressure force on this same volume of gas is approximately

$$P_x = \Delta p\pi(R_o^2 - R_c^2)$$

From the results shown in Fig. 13, $\Delta p = p_c - p_{ex} \cong 20$ mmHg at 200 amp and 30 mmHg at 1000 amp and thus P_x ranges from 0.6 to 0.9 Newtons/(meter)^2. The ratio of the $\underline{J} \times \underline{B}$ force to the total force becomes

$$0.006 < F_x/P_x \leqslant 0.1$$

for the conditions of these tests.

III.2. Unheated Free Jet

III.2.1. Physical Model of the Flow Field

Interpretation of the results of the probe measurements is facilitated if first a brief review of the flow field of an underexpanded free jet effluxing from a sonic nozzle is undertaken. From the theoretical and experimental work of a number of investigators (1, 4, 6, 8) , the underexpanded free jet may be modeled schematically as shown in Fig. 17. The main features of the flow field of interest here include the hypersonic source-like variation of flow quantities along rays emanating from the origin ($x = 0$, $r = 0$), the oblique shock and free shear layer surrounding the jet laterally, and the disk (normal) shock which terminates the supersonic flow in the vicinity of the jet axis. The rapid expansion of the gas at the exit plane into a quiescent gas at low pressure, $p_{tank} \ll p_t$, produces the barrel shock. Incipient shock formation occurs at the intersection of the last expansion characteristic from the lip of the nozzle and the first reflected characteristic from the boundary.

The flow field calculations by Ashkenas and Sherman (8) are particularly helpful in determining flow quantities; these authors give simple semi-empirical formulas derived from the results of the method of characteristics solution for the inviscid flow field without shock waves. The relationships for centerline Mach number and radial density distribution are

$$M\left(\frac{x}{D_*}\right) = A\left(\frac{x-x_o}{D_*}\right)^{\gamma-1} - \frac{1}{2}\left(\frac{\gamma+1}{\gamma-1}\right)\left[A\left(\frac{x-x_o}{D_*}\right)^{\gamma-1}\right]^{-1}$$

and

$$\frac{\rho(r,x)}{\rho(0,x)} = \cos^2\theta \cos^2\left(\frac{\pi\theta}{2\phi}\right)$$

where the radial and axial coordinates (r,x) are related to the (ray) distance from the source, R, by $R^2 = r^2 + x^2$. For $\gamma = 5/3$, $A = 3.26$, $x_o/D_* = 0.075$ and $\phi = 1.365$. Other quantities of interest, such as the density and pressure, can be calculated from the compressible flow relationships. In this regard, the compressible flow tables of Wang, Peterson and Anderson (26) and those by Pratt and Whitney Aircraft (27) are helpful for $\gamma = 5/3$.

As can be seen from a simple calculation, the maximum size of the expansion field of an underexpanded source-like jet is related to the pumping speed of the facility. From the momentum equation in hypersonic flow, the static pressure behind the disk shock is approximately

$$p_2 \cong \rho_\infty u_\infty^2$$

For source-like flow in which the streamlines emanate as rays from the origin the continuity equation yields,

$$\rho_\infty u_\infty R_\infty^2 = f(\theta)$$

where θ is the polar angle. For a simple source, $f(\theta)$ is a constant which can be related to the jet flowrate $\dot{m}_j$ as

$$\rho_\infty u_\infty R_\infty^2 = \rho_* u_* R_*^2 = \dot{m}_j/(2\pi) \quad .$$

By combining these results with the energy equation in the same

approximation, $u_\infty \cong \sqrt{2c_p T_t}$, one obtains, for $R_\infty = x_s$, the disk shock position along the jet axis,

$$x_s = (\dot{m}_j/p_2)^{1/2}(\pi)^{-1/2}\left[\frac{\gamma}{2(\gamma-1)}\right]^{1/4}(RT_t)^{1/4}$$

where R is the gas constant per unit mass.

For $\gamma = 5/3$ and $T_t = 522$ R, and the pump characteristic shown in Fig. 12, x_s becomes

$$x_s \cong 3 \text{ in.}$$

for $0 \lesssim \dot{m} \lesssim 0.4$ gm/sec whereas at 0.5 gm/sec, $x_s \cong 2$ in. $\dot{m}/p_2$ is related simply to the volumetric pumping speed, Q, as

$$\dot{m}_j/p_2 = Q/RT_{tank})$$

in the approximation that $p_2 = p_{tank}$.

By evaluating $\dot{m}_j$ at the sonic conditions, one obtains

$$x_s/D_* = \frac{1}{\sqrt{2}}\left[\frac{2}{\gamma+1}\right]^{\frac{1}{2}\left(\frac{1}{2}+\frac{1}{\gamma-1}\right)}\left[\frac{\gamma^2}{2(\gamma-1)}\right]^{1/4}\left(\frac{p_t}{p_2}\right)^{1/2}$$

where D_* is the orifice or sonic nozzle diameter.

For $\gamma = 5/3$ and $p_2 = p_{tank}$, this becomes

$$x_s/D_* = 0.64\,(p_t/p_{tank})^{1/2}$$

whereas Ashkenas and Sherman (8) found experimentally for argon, air, and nitrogen that

$$x_s/D_* = 0.67\,(p_t/p_{tank})^{1/2}$$

which was independent of γ for pressure ratio, p_t/p_{tank}, ranging from 10 to 10,000, and thus verified the results of Bier and Schmidt (6) for argon, hydrogen, nitrogen and carbon dioxide, for pressure ratios ranging from 10 to 1,000.

Bier and Schmidt (6) also made extensive measurements of the disk shock diameter, D_s, and the maximum barrel shock diameter, D_b, for pressure ratios, p_t/p_{tank}, between about 10 and 200. Of interest here are their results for argon at $p_t/p_{tank} = 10^2$ for which $D_s/x_s \cong 0.51$ and $D_b/x_s \cong 0.63$. As a check with air, there is good agreement between their results, $D_s/x_s = 0.62$, and Sherman's (7) results, $D_s/x_s = 0.59$ at this same pressure ratio. For argon at $p_t/p_{tank} = 20$, Bier and Schmidt's (6) results yield D_s/x_s about 37% below those reported at $p_t/p_{tank} = 10^2$.

As remarked earlier in Section II.1, $x_s \cong 3$ in. and $D_s \cong 1.5$ in. for the unheated jet investigated here. The heated jet was about twice this size.

A few measurements were made in the cold flow free jet (arc heater power off) with and without the cathode. The purpose of the measurements made without the cathode was to determine the centerline flow field at several axial positions and compare it to existing theory. In addition this flow field was used to calibrate the mass flux probe shown in Fig. 5 . The purpose of the measurements made with the cathode was to determine a reference set of radial impact pressure profiles for comparison to the hot flow profiles described later on in Section III.3.

III.2.2. Centerline Impact Pressure and Mass Flux Measurements Without the Cathode

In order to establish the centerline flow field of the cold jet using only the plenum (stagnation) chamber pressure, p_c, and temperature, T_c, and impact pressure measurements, p_i, the cathode was removed, thereby eliminating the cathode wake and providing an adiabatic-isentropic flow between the plenum and the probe. The Mach number distribution between $\bar{x} = 1$ and the disk shock was determined from the p_i and p_c measurements and is shown in Fig. 18 The free jet theory of Ashkenas and Sherman (8) is shown for reference. These measurements cover a 10 to 1 range in probe tip diameter and a 5 to 1 range in jet Reynolds number based on sonic conditions and anode diameter $D_* = 3/4''$. Typical probe Reynolds number, $Re_{id_p} \equiv \frac{\rho u d_p}{\mu_i}$, based on probe diameter, d_p, free-stream ρu, and impact conditions downstream of the shock, range between about 5 and 400 over the Mach number range shown. The viscosity* for atomic argon at room temperature and below was evaluated from the Sutherland viscosity law (28, p. 225; with the Sutherland constant equal 147°K). The scatter in the experimental data seem to have obscured any trend due to probe size or Reynolds number which might have occurred. Indeed it was shown in Appendix E that with the exception of the effect of strong axial Mach number gradient for

---

* The transport properties of argon are discussed in Appendix D.

the 0.335'' tip data, for which the correction applied to M at $\bar{x} = 1$ was about 10%, neither the Mach number gradient correction nor the viscous correction to p_i exceeded about 4% which was within the scatter of the data and hence was neglected. The scatter in the data is believed to be caused primarily by the lack of stability of the pressure transducer reference vacuum (tank ambient pressure) and the repeatibility of the vacuum pressure gauge as discussed in Section II.3.4. The results are in good agreement with the theory except for the Mach number at $\bar{x} = 1$ which is consistently 20% higher than the theory of Ashkenas and Sherman (8). This discrepancy may be caused by the difference in initial conditions at the exit plane between theory and experiment.

The mass flux measurements, ρu, in cold flow were made without the cathode and were confined to the region of supersonic cone flow along the axis. By combining this measurement with the stagnation pressure, p_c, and temperature, T_t, which were measured in the plenum, free stream Mach number, M, could be calculated and compared to the known Mach number distribution (shown in Fig. 18) obtained from the impact pressure and plenum pressure measurements. This calibration procedure was used in order to verify the probe sampling model used to calculate the operating range for the steady state and collector tank sampling techniques discussed in Appendix A. On the basis of this verification in cold flow the probe sampling model was extended to the hot flow jet conditions. Fig. 19 shows a comparison of the Mach number distribution obtained in cold flow (without the cathode) from the impact pressure measurements,

from ρu measurements using the calculated operating range, and the free jet theory of Ashkenas and Sherman (8). The steady state sampling technique yields results which generally predict higher Mach numbers (lower ρu) than the collector tank method. However a detailed comparison between the two techniques was not made. The results do show that either sampling technique appears to be valid within about a 10% scatter band about the mean of the measurements. The operating range calculated for the steady state sampling technique provided a good estimate of the operating boundary. However the operating range calculated for the collector tank sampling technique was too pessimistic, as discussed in Appendix A, Section A.3.

After using both sampling techniques in hot flow, it was found that the collector tank method (Section A.3) always measured substantially ($\leq 40\%$) larger ρu's than the steady state sampling method. The largest disagreement occurred at $\bar{x} = 1$.

This difference in sampling range may be accounted for in the following way. If in fact the shock wave was inside the probe, in the aft position shown in Fig. 20 , the operating range of the collector tank sampling technique would be extended but that for the steady state sampling technique would be reduced and in fact marginal at $\bar{x} = 1$. With the shock in the aft position at higher Mach number the pressure loss is larger than that proposed in the original model for the shock wave at the tip. Although this loss reduces the line pressure drop it also reduces the overall pressure differences between the tip and either the collector tank whose initial pressure is 0.1 μ Hg or the pump inlet pressure whose pressure is constant for a given

flowrate. The sum of the pump inlet pressure and line losses is quite close to the pressure downstream of the shock and the steady state sampling technique is marginal for the heated jet at $\bar{x} = 1$. After checking the mass balance (Section III.3.3) by integrating the mass flux profiles at $\bar{x} = 1$, it was clear that the collector tank sampling technique was correct. This method was then used for all ρu measurements in hot flow.

III.2.3. Radial Impact Pressure Profiles with the Cathode

A reference set of impact pressure profiles were made in cold flow with the cathode in place for comparison to the hot flow profiles discussed later on in Section III.3.2. The profiles shown in Fig. 21 extend from x = 1 to 22. The impact pressure decreases rapidly with both axial and radial distance as expected in a supersonic source-like flow field until either the disk shock ($M \cong 6.6$) is crossed, for flow near the axis, or the flow is turned by the curved oblique shock wave, which bounds the core flow laterally. This region of the flow field is qualitatively the same as that described earlier for the free jet in Section III.2.1. and shown schematically in Fig. In this region the impact pressure, p_i, achieves a relative maximum as the lateral shock and free shear layer is crossed. An impact pressure recovery and a stagnation pressure loss occur across the oblique shock wave, e.g., at $\bar{x} = 3$, $M_1 \cong 6$ and $\beta = 20^\circ$, $\frac{(p_{t2})_2}{(p_{t2})_1} = 2.1$ and $\frac{(p_{t1})_2}{(p_{t1})_1} = 0.18$. [$(\ )_1$ and $(\ )_2$ refer to quantities upstream and downstream of the oblique shock wave, respectively.] Downstream of the wave the Mach number rises slowly and the stagnation pressure rises rapidly so that the impact pressure continues to rise until M

and p_t peak; then M, p_t and p_i (= p_{t2}) decrease rapidly to their edge values of M = 0 and $p_t = p_i = p_{tank}$. That a relative maximum in total pressure is achieved between the shock and the quiescent gas can be visualized by observing that the inviscid solution yields the isentropic (plenum) stagnation pressure at the jet boundary and the shocked stagnation pressure at the shock boundary whereas the development of the free shear layer lowers this stagnation pressure maximum as well as moves it radially inward. Since the static pressure is constant in this region the Mach number reflects the same variation as the stagnation pressure. Near the exit where the oblique shock strength is negligibly small and free shear layer very thin the stagnation pressure and impact pressure rise rapidly from their ambient condition to the inviscid jet edge condition.

Just downstream of the disk shock the Mach number is about 0.46. The periphery of the disk shock forms the intersection point of the lambda shock as shown in Fig. 17 . The gas above this slip line but somewhat inside the outer edge of the external free shear layer is supersonic. The slip line (discontinuity in velocity) created at this intersection causes another free shear layer to develop which reaccelerates the strongly shocked core flow along the axis to low supersonic speeds, e.g., $M \cong 1.4$ at $\bar{x} = 22$.

A discussion of the effect of the cathode wake will be given when the heated jet profiles are compared to the unheated profiles in Section III.3.2.

Downstream of the influence of the cathode, which generates a relative minimum of impact pressure, the impact pressure profiles

are qualitatively similar to those measured by Chow (5) and Sherman (7) who operated air free jets effluxing from a sonic nozzle.

Although this set of profiles gives a good overall description of the free jet expansion, asymmetries in the magnitude of maximum impact pressure on either side of the centerline monotonically increase from a negligible value at $\bar{x} = 1$ to a maximum of 25% at $\bar{x} = 7$, and then decrease again to zero as the locus of impact pressure maxima move toward the centerline of the jet. Careful realignment of the cathode to the anode reduced the asymmetry to less than about 5% in subsequent tests.

III.3 Heated Free Jet

III.3.1 Physical Model of the Flow Field

The arc heated jet investigated here and shown in Figs. 22 and 23 bears a remarkable resemblance to the arc heated free jet of Sherman and Talbot (29) (as discussed by Grewal and Talbot (30)) using argon and to the cold free jet investigated by Collins (31) who used a nitrogen afterglow flow visualization technique with nitrogen and argon in the Jet Propulsion Laboratory low-density facility described by Ashkenas and Sherman (8). In particular the bulb-like incandescent central region extending from the orifice, the dark region surrounding this "bulb", and the rather sharp outer boundary (or barrel shock) terminating the dark region are the most important features visually observed. The color photograph (Fig. 23) exaggerates the blue part of the emission spectra from the jet. To the unaided eye, the jet appears white. The jet shown in Figs. 22 and 23 was operated at a total pressure of about 23 mm Hg. and an average total enthalpy

of 7000 BTU/lb m, for an arc discharge at 600 amp. and 26 v. Based on equilibrium stagnation conditions the average total temperature is about 12,000°K and the ion mass fraction about 0.25.

An estimate of the recombination rate was obtained in Appendix F by use of Petschek and Byrons' (32) ionization rate and the equilibrium constant. The resulting expression for n_E was integrated, holding T_E constant, to yield the reaction time necessary to achieve 70% of the initial number density. By combining these results with the measured jet velocity of about 25,000 ft/sec, and hence a typical flow time of about 10^{-6} sec. based on the anode diameter, the upper curve shown in Fig. 24 was obtained. The results show that recombination is negligible for any position in the jet. For this condition, $t_{recomb}/t_{flow} >> 1$, and the flow field is said to be chemically frozen, or that frozen flow prevails.

The frozen flow Mach number may be as much as 12 prior to the normal shock along the centerline. Since the compression ratio across the shock wave is about 200 and the tank pressure is about 250 μHg. the pressure just upstream of the shock, $p_{\infty 1}$, is about 1 μHg. Using a frozen flow model and $T_{\infty 1} \cong 300°K$, these conditions correspond to a mean free path of $\lambda_{\infty 1}$, about 10^{-4} cm for the ion-ion, ion-electron and electron-electron collisions.

Not only are there too few collisions to maintain chemical equilibrium, but after about one anode diameter from the exit plane there are too few collisions to maintain kinetic equilibrium between the ions and the electrons as shown by the lower curve of Fig. 24.

As can be seen by considering one encounter between two particles of large mass disparity (see also pp. 80-81 of Spitzer (33)) about 10^5 electron ion collisions are required to equilibrate their energy (or temperature) difference. Thus, if the electron temperature remained constant throughout the expansion for the same conditions described earlier, the electron-ion and electron-electron mean free path would be about 1 mm. immediately upstream of the shock.

The flow visualization observed in this jet is caused by the density and temperature dependent radiation processes involved in recombination for radiative transition between excited states whose energy levels are separated by less than about 4 ev. This radiation is in the visible spectrum. The strong inverse temperature dependence of this recombination process led Grewal and Talbot (30) to conclude from their analysis of the normal shock wave structure of a slightly ionized gas that upstream conduction of heat by the electrons behind preheated the electrons and quenched the radiation in the darker region separating the "bulb" and the barrel shock. This situation is in contrast to the treatment of the atom-ion shock which undergoes conventional Rankine-Hugoniot jump conditions for all quantities. From the impact pressure measurements made in the present investigation the barrel shock (atom-ion shock) is observed to correspond to the sharp outer boundary of the dark region, so that the location of the dark region also observed by Grewal and Talbot (30) for a slightly ionized gas may also be the same for a highly ionized gas as well.*

* However, from the estimates made here, $T_E \cong$ constant throughout this region. Hence it is not at all clear that the dark region is caused by the mechanism described by Grewal and Talbot (30) for the conditions of this investigation.

In fact the analysis by Jukes (34) and Jaffrin and Probstein (35) for a fully ionized gas also predict the rather broad region of elevated electron temperature which extends upstream of the compression zone of the shock.

Features of these models (30, 34, 35) which are essential to the explanation of the "dark space" is that "far" upstream and downstream of the shock wave $T_E = T_I$ and the heat fluxes vanish, $\nabla . \underline{q_E} = \nabla . \underline{q_I} = 0$. However, an analysis of the electron energy equation (Appendix F) applied to the flow field here indicates that these constraints are not a good approximation to the conditions observed in this free jet. Beginning at about one anode diameter downstream of the exit plane both inelastic and elastic energy transfer processes are negligible; after about two diameters the electron heat conduction term, $\nabla . \underline{q_E}$, dominates the convective terms as well. The solution of the energy equation for this case, $\nabla . \underline{q_E} = 0$, yields a T(x) which decreases as a weak function of x. Because of their isolation from the ions, which undergo an adiabatic expansion to first approximation, and the weak decay of T_E with x, the electrons are at an elevated temperature, $T_E > T_I$, for $x/D \geq 2$. For these conditions the electrons probably undergo an isothermal compression through the disk shock. Thus $T_E(x)$ is at best a very weakly decreasing function of x throughout the bulb-like region of interest here. The initial levels (at x = 0) of T_E and T_I, for which T_E may already be larger than T_I, are the result of a rather complicated, non equilibrium heating process in the arc discharge which has not been studied here.

For the largest probe* (0.47 in. tip dia.) used in this investigation a dark space just upstream of the shock wave was visible for $x/D_* \leq 4$ as shown in Fig. 25. This phenomenon was also observed by Sherman and Talbot (29) [shown photographically in the work of Grewal and Talbot (30)] for end on flow over a 5/8 in. dia. cylinder in a weakly ionized flow of arc heated argon from a conical nozzle at stagnation conditions of 300 mm Hg., 5000°K and ion mass fraction of 0.006.

The flow field of the arc heated free jet was investigated by making impact pressure, mass flux and total enthalpy measurements. The stagnation point heat transfer measurements discussed later on in Section III.3.5 are compared to theory which is based upon knowledge of the flow field gained by the first three measurements discussed in this section.

III.3.2 Impact Pressure Measurements

The impact pressure was measured with a water cooled probe having either a conduction-radiation cooled sharp tungsten or carbon tip (D_p = 0.15 inch, tip thickness $\cong$ 0.001-0.002 inch) or a hemisphere cylinder geometry (D_o = 0.148, D_i = 0.042 inch) which was completely water cooled. These probes and the instrumentation have been described in Section II and are shown in Figures 4 and 5. A typical set of impact pressure profiles taken with the sharp tip

---

* The probes used in this investigation were not biased to either electrode but were allowed to achieve a floating potential for which no net current is received from the plasma. For operation at I = 1000 amp. and V = 24 v. (anode potential) the probe potential, V_p, was 20 v. for all probe positions in the plasma (for I = 200 amp., V = 42 v. and V_p = 40 v.). The cathode was at zero potential.

probe is shown in Fig. 26 for a 200 and 1000 amp. test. By comparison to the profiles of Fig. 21 for the cold flow jet which was discussed and compared in Section III. 2 to the "classical" underexpanded free jet of Ref. 8, the differences are in fact what one might expect for a heated jet at low Reynolds number. The cathode wake is not observed in hot flow and the off axis impact pressure peak has progressively less strength throughout the flow. As will be discussed later, the gas effluxing from the heated jet has a strong radial total enthalpy gradient and is probably chemically frozen. The exit plane Reynolds number, Re_D^*, ($Re_{D^*} \cong 2500$) based on anode diameter and the centerline properties of a nearly full singly ionized flow is of the same order as Re_{D^*} for the corresponding cold flow. This result, along the centerline, is caused by the decrease in μ associated with the larger (Coulomb) collision cross section for a fully singly ionized gas. The Reynolds number of the much cooler gas at the periphery of the anode which forms the oblique shock wave is much smaller because μ is much larger. (The decrease in μ due to lower temperature is offset by the increase of μ attributed to the smaller atom-atom collision cross section.) At a fixed axial position the effect of lowering Re is to increase the cathode wake thickness and decrease the velocity defect. The result is that the centerline dip in the impact pressure observed for the cold jet is not present in the heated jet, and the presence of the cathode wake is not distinguished by this measurement. The off centerline impact pressure rise is less in hot flow than cold flow probably because the free shear layer is merged with the

lateral shock wave and no total pressure recovery, which would further increase p_i, is observed beyond the shock as discussed in Section III.2 for cold flow. The barrel shock configuration is larger due to a larger pressure ratio, p_t/p_{tank} (larger p_t), for the heated tests but in other respects the heated jet appears to be a free jet which is unaffected by the electromagnetic phenomena of the arc heater discharge. Fig. 27 shows the ratio of centerline impact pressure p_i, to stagnation pressure, p_t, for typical 0, 200, and 1000 amp tests. p_i/p_t obtained from the free jet theory of Ashkenas and Sherman (8) is also shown. In cold flow, (0 amp.) two sets of data are shown: one with and one without the cathode in place. p_t was measured in the plenum chamber in the absence of the cathode shield for the cold flow data only. In hot flow, p_t was calculated from the semi-empirical relationship given by Ashkenas and Sherman (8), $x_s/D_* = 0.67(p_t/p_{tank})^{1/2}$ which relates shock position to jet pressure ratio. x_s was obtained from the axial impact pressure distribution shown in this figure and p_{tank} was measured with the McLeod gauge. For these tests the total enthalpy ranges over a factor of about 500 or from about 65 to 32,000 BTU/lb.

The measured p_i/p_t distribution varies approximately as $\bar{x}^{-2.2}$ for both current levels whereas $p_i \sim \bar{x}^{-2.0}$ in the hypersonic source flow approximation and in the theory of Ashkenas and Sherman (8) for $\bar{x} \geq 2$, $M_\infty \geq 4.5$. Their (8) measurements show that $p_i \sim \bar{x}^{-2.07}$ for the $\bar{x}$ range between about 2 and 100. The percent difference in slope is within the maximum scatter of the p_i

measurements. This agreement further substantiates the belief that the flow is frozen and hypersonic.

At $x/D_* = 1$ the scatter in the hot and cold flow data is less than 10% and the mean of the data are about 15% below this theory. Further downstream, $2 \leq x/D_* \leq x_s/D_*$, differences between the two sets of cold flow data first increase and then decrease as the impact pressure minimum or disk shock is approached. Shock position and pressure ratio are in good agreement for the cold flow data and thus these quantities appear to be independent of the presence of the cathode. Differences in p_i/p_t downstream of the shock are caused primarily by the larger tank pressure, p_{tank}, for Test 104 as compared to Test 81. Over this same range of x/D_*, the two sets of hot flow data remain within about 25%. However, the hot flow data drop substantially below the theory for $x/D_* \geq 3$. This result is probably obtained for the following reasons. Since the total enthalpy decreases rapidly with radial distance away from the centerline, neighboring streamlines achieve progressively lower adiabatic limit velocity. Viscous shear forces decrease the centerline velocity and hence the impact pressure.

From the approximate relationship derived in Section III.2.1 shock position, x_s, for constant γ and flowrate, $\dot{m}_j$, varies as $x_s \sim h_t^{1/4}(p_{tank})^{-1/2}$. Using this relationship to calculate the shock position for the cold and hot flow data yields values of x_s which are 50, 5, and 7% lower than those measured with the impact pressure probe for the 0, 200 and 1000 amp. data respectively at $\dot{m}_j = 0.52$ gm/sec. For the hot flow data, the total enthalpy used in this

expression was the frozen total enthalpy deduced from the impact pressure and mass flux measurements to be discussed in Section III.3.4. The agreement in hot flow is good but in cold flow rather poor. Somewhat better agreement in cold flow is obtained by using the empirical relationship of Ashkenas and Sherman (8), $x_s/D_* = 0.67\ (p_t/p_{tank})^{1/2}$ valid for $p_t/p_{tank} > 15$, which yields a value of x_s about 20% below that which was measured.

Radial impact pressure profiles at $x/D_* = 1$ for 0, 200, and 1000 amp. are shown in Fig. 28. The total pressure was obtained for the hot flow as described earlier for Fig. 27 whereas p_t was taken as the arc plenum pressure, p_c, in cold flow, which was conducted without the cathode shield and with and without the cathode. The gross features of the cold and hot flow profiles including the presence of the cathode wake and distinct barrel shock in cold flow as compared to hot flow were discussed earlier with regard to Figs. 21 and 26. The predicted impact pressure profiles shown in Fig. 28 were derived for hypersonic flow starting with the momentum equation across a normal shock wave as

$$p_i \cong \rho_\infty u_\infty^2$$

For a given axial position, x, p_i may be related to its centerline value as

$$\frac{p_i(r,x)}{p_i(0,x)} = \frac{\rho(r,x)}{\rho(0,x)}$$

Ashkenas and Sherman (8) have determined this density ratio empirically from the method of characteristics solution as

$$\frac{\rho(r,x)}{\rho(0,x)} = \cos^2\theta \cos^2 a\theta$$

where $a = \pi/(2\phi)$ (= 1.15 for $\gamma = 5/3$) and $\theta = \tan^{-1} r/x$. Normalizing p_i by the total pressure, p_t, and using the density ratio just discussed, the momentum equation becomes,

$$\frac{p_i(r,x)}{p_t} = \frac{p_i(0,x)}{p_t} \cos^2\theta \cos^2 a\theta$$

where $\frac{p_i(0,x)}{p_t}$ depends on M and γ only.

Based on the solution of Ashkenas and Sherman (8), M depends on x/D and γ. Because of the presence of the cathode, the correct value of D may be somewhat less than the anode diameter, $D_* = 0.75$ in. Since x = 0.75 for these profiles, $x/D_* = 1$ and M = 2.44; however, on the basis of an equivalent diameter, D_e, which is based on the area of the annulus bounded by the anode and cathode, $\pi D_e^2/4 = \pi(D_*^2 - D_c^2)/4$, $D_e = 0.65$ in., $x/D_e = 1.15$ and M = 2.85. The prediction is shown at both Mach numbers.

Of marked significance in Fig. 28 is that the hot flow profiles are generally in far better agreement with the free jet theory than is the cold flow profile which remains substantially above both the theory and the hot flow data. The effect of the cathode on the cold flow field alters the profile shape and magnitude from the free jet theory at $\bar{x} = 1$. For $\frac{x_s}{D_*} \geq \frac{x}{D_*} \geq 2$ the profile shape is in agreement with theory but not its magnitude whereas the position of the disk shock (Fig. 27) is unaffected by the presence of the cathode.

Inevitably the question of the viscous correction to the impact

pressure measurement arises. Probe Reynolds number, Re_{id_p}, based on tip diameter, measured ρu and the viscosity prediction of Chapman (36) for a fully singly ionized gas, evaluated at p_i and the calculated frozen total temperature, ranges from approximately 220 to 6 for 200 amp. and from 35 to 0.5 for 1000 amp. between $\bar{x} = 1$ and the disk shock. Although there exist no data or theory for the combined ionization and viscous correction to impact pressure, estimates based on the data of Ashkenas and Sherman (8) and Potter and Bailey (37), discussed in Appendix E, suggest that the correction to the data at 200 amp. is no more than 3% but would reduce p_i by as much as a factor of two at the disk shock for the 1000 amp. tests. By comparison, p_i measured at 1000 amp. with the total enthalpy probe tip shown in Fig. 6 shows that for a factor of three larger Re_{id_p}, differences between the two probes could not be differentiated from the scatter of the measurements which is within about 10%. According to the above sources a factor of three in Re_{id_p} in the region $Re_{id_p} \cong 1$ causes a 30% change in impact pressure correction which however the measurements do not confirm.* In addition, results given later on when p_i and ρu are used to obtain u_∞ will not support viscous corrections of a factor of two. In view of these arguments it is believed that the viscous corrections determined at lower stagnation temperatures without ionization cannot be extended in a simple way to the results obtained here nor is

* It is not really clear that Re_{id_p} is the "correct" Reynolds number to correlate the viscous correction for the case of a highly cooled wall. The possibility of reconciling this apparent contradiction by choosing a Reynolds number evaluated at the arithmetic mean temperature between the stagnation and wall conditions, is discussed in Appendix E.

this correction crucial to the interpretation of p_i. Therefore, no viscous correction was applied to the impact pressure measurements.

The impact pressure variation with the average total enthalpy is shown in Fig. 29. This information is needed for the stagnation point heat transfer predictions used in Section III.3.5. The pressure ratio, p_t/p_{tank} controls the disk shock location and thus some of these data may have been taken in the region within the disk shock where the impact pressure has a minimum.

III.3.3 Mass Flux Measurements

Mass flux, ρu, measurements were made in the supersonic portion of the hot free jet using the transient sampling technique described and used in Section III.2 for the centerline ρu measurements in the cold jet. The combined impact pressure, mass flux, total enthalpy probe shown in Fig. 5 and described in Section II.3.2 was used to make the hot-flow measurements. Near the exit of the jet, for $\bar{x} = 1$ and 2, the shock position around the probe was generally visible so that a marked difference in shock wave location was observed when the sample was taken. As the sampling valve was opened, the curved detached shock wave moved downstream to a position close to the probe body and appeared to be attached at the leading edge. This observation provided additional evidence that the shock wave was "swallowed" and that the undisturbed streamtube having the frontal area of the probe was captured. For $\bar{x} \geq 3$ the shock wave became very diffused and difficult to see because of low density, and validity for streamtube capture rests on the

operating range criterion established for the cold flow measurements and described in Appendix A. The ρu samples were confined to the supersonic region within the barrel shock whose position was established by the impact pressure measurements prior to sampling.

For steady, inviscid, adiabatic flow for which the velocity is constant, $u_\infty = u_{max}$ in hypersonic flow, the continuity equation yields a simple, axisymmetric radial source flow solution

$$\rho \sim 1/R^2$$

which is valid within the barrel shock. By introducing the jet flow rate and measured ρu, this becomes

$$\frac{\left(\frac{\dot{m}_j}{2\pi R_o^2}\right)}{\left(\frac{\rho u}{\cos\theta}\right)} = \left(\frac{R}{R_o}\right)^2$$

where $\cos\theta$, $\theta = \tan^{-1}\frac{r}{x}$, corrects ρu for angle of attack, and R_o is the anode radius. In an attempt to show the deviation of the ρu data from a simple source distribution, the above expression is shown in Figs. 30 and 31 for the 200 and 1000 amp. tests. The agreement with the source flow solution is good. Part of the scatter in the data arises from tests in which the probe tips had eroded due to melting or sublimation of the tip material. This erosion caused blunting of the sharp tip and changed the sampling area somewhat. The tip diameter and thickness were measured with an optical comparator before and after each test so that a probe tip area correction could be applied to the results in those instances in which erosion

occurred.

Profiles of ρu normalized by their centerline values are shown in Fig. 32 for $\bar{x}$ from one to six. In this instance, rather than correcting ρu for angle of attack effects as before, this correction was included in the simple source flow curve shown as $\cos^3\theta$ where $\theta = \tan^{-1}\frac{r}{x}$. Included also in this figure is a more general, axisymmetric radial source flow distribution of the form $\rho = g(\theta)/R^2$ for which Sherman (10) empirically determined the function $g(\theta) = \cos^2\frac{\pi\theta}{2\phi}$ from the method of characteristics solution for the free jet. ϕ is a function of γ alone so that $\pi/2\phi = 1.15$ for $\gamma = 5/3$. No conclusion can be drawn about which distribution is correct; however the trend for large r/x shows that the 200 amp. data are in better agreement with the simple source distribution, whereas the 1000 amp. data are in better agreement with the more general source distribution.

The validity of these source flow distributions depends on the assumption that the velocity is radial and constant (the adiabatic limit) throughout the free jet. From these assumptions the free jet is irrotational and inviscid, and hence isentropic throughout. According to the discussion of the electron energy equation in Appendix F, heat conduction is almost certain to be important several anode diameters downstream of the exit plane and is probably the dominant term in the electron energy equation in the vicinity of the disk shock. Further, it will be evident from the total enthalpy measurements, discussed later on, that the total enthalpy is not uniform across the jet at $x/D_* = 1$. The extent to which these two non ideal effects might have modified the source distribution was not specifically

studied in the present investigation.

At $x/D_* = 1$, where the free shear layers are small, the mass flux integral, $\dot{m}_j = \int \rho \underline{U} \cdot \underline{n} ds$, was calculated by using a curve fit to the radial ρu profiles shown in Fig. 32. For the 200 amp. and 1000 amp. tests, the total flowrate* calculated in this way was 4 and 19% lower than the metered total flowrate. Based on these results, the ρu sampling technique is believed to be working moderately well in this extreme environment.

The variation of centerline ρu measurements with average total enthalpy is shown in Fig. 33 at 200 and 1000 amp. for $1 \leqslant \bar{x} \leqslant 7$. The data were taken up to an $\bar{x}$ within about one diameter, D_*, of the disk shock which occurred at about an $\bar{x}$ of 6 and 8 for the 200 and 1000 amp. tests respectively. The dashed curves represent a best fit straight line through the data and will be used in Section III.3.5 in obtaining Reynolds number for the stagnation point heat transfer correlation. A 5 to 20% increase in ρu over the enthalpy range is believed to be caused by the increased $\underline{J} \times \underline{B}$ body force present at 1000 amp., as compared to the 200 amp., which has components that radially pinch and axially accelerate the effluxing ionized gas (Section III.1).

III.3.4 Total Enthalpy Probe

The total enthalpy measurements were made with a water-cooled probe having a conduction-radiation cooled sharp leading

---

*These results depend upon the location of the jet boundary (for the limits of integration) which is not too well defined from the impact pressure measurements.

edge carbon or tungsten tip (D = 0.47 in.) shown in Fig. 5 and discussed in Section II.3.2. A common wall separates the inner passage for calorimeter coolant from the outer passage for heat shield coolant, and heat leakage across the wall between the two had to be estimated and entered as a correction to the measured total enthalpy. Because of the numerous assumptions and uncertainties of an analytical heat transfer model, an experimental calibration would be far superior; however, no calibrated low-density, high-enthalpy flow field was available for this purpose. Thus, the enthalpy probe heat transfer model discussed in Appendix B was devised to determine the probe correction, which appears as a function of probe Reynolds number, Prandtl number, the inner ($\dot{m}_c$) and outer ($\dot{m}_e$) coolant passage flow rates and the tip temperature, T_p. By varying $\dot{m}_c$ and $\dot{m}_e$ at one location ($\bar{x}$, Re, Pr, and T_p fixed), the internal consistency of the probe correction model could be checked by demanding that the corrected total enthalpy be the same. In this way, one would not be assured of having the correct model, but this too could be checked in an integral sense through energy conservation, as will be done later on for the data at $\bar{x} = 1$. The results of such an attempt are shown in Fig. 34. The error band which is centered at the average of the corrected measurements widens prohibitively beyond $\bar{x} = 1$ and thus points to the incorrectness of the model in view of the measurement repeatibility which is generally within about ± 10 per cent. This scatter is believed to be due to one or all of three sources. The first is

the fact that the calorimeter signal decreases rapidly as $\bar{x}$ increases so that any heat leaks within the calorimeter not accounted for in the present model become more important as the probe moves downstream. Secondly, the heat transfer through the gas at the probe tip could become a very serious source of error as Re decreases rapidly. Then, finally, the simple models of heat transfer from the gas and water to the walls used for the calorimeter are suspect. The last source of error can be eliminated by redesigning the probe by making it similar to the stagnation point heat transfer probe in which the calorimeter was isolated from the external coolant passages. This possibility was considered at the outset of this investigation but was rejected because the resulting probe would have been about twice its present size.

The total enthalpy profiles across the jet at $\bar{x} = 1$ are shown in Fig. 35 for the 200 and 1000 amp. tests. The data are normalized by the averaged centerline total enthalpy shown in the legend for both current levels. These data have been corrected for calorimeter heat leakage as discussed earlier. The corrections reduced the measured total enthalpy by 6 to 14 per cent for the 1000 amp. tests and ranged from reducing to augmenting the measurements by 13 to 12 per cent respectively for the 200 amp. tests. Valid measurements for $r/x > 1$ were complicated by low thermocouple calorimeter signals introducing repeatibility problems. With strong total enthalpy gradients present, h_t may vary by as much as 30 per cent across the probe diameter. Under these conditions of maximum gradient, the probe measurements overestimate the total enthalpy

by less than 10 per cent, whereas the centerline total enthalpy is underestimated by about 4 per cent. These error estimates are based upon flow models for which ρu and h_t vary linearly in the region of maximum gradient and parabolically near the centerline. Using these flow models the total enthalpy measured by the probe, h_{tp}, was calculated as

$$h_{tp} = \frac{1}{\dot{m}_p} \int_A \rho \, \underline{U} \cdot \underline{n} \, h_t dA$$

and compared to the probe centerline enthalpy at the probe tip. The integration was carried out over the sampling area of the probe. $\dot{m}_p$ is the aspirated gas flowrate. In view of the rather limited data comprising this profile and the other uncertainties present in the total enthalpy measurement, no correction for finite probe size was made.

An energy integral, $P\text{-}Q = \int \rho h_t \, \underline{U} \cdot \underline{n} \, ds$, was calculated to check the energy balance at $x/D_* = 1$. By curve fitting the ρu profiles from Fig. 32 and the h_t profiles from Fig. 35, the energy balance closed within about 20% at 200 amp. and 10% at 1000 amp.

In the hypersonic flow approximation ($M_\infty^2 \to \infty$) the impact pressure is approximately equal to the free-stream momentum flux.

$$p_i \cong \rho_\infty u_\infty^2$$

With the independent measurements of p_i and ρu, discussed previously, u_∞ can be obtained. Since the typical flow time is much shorter than the time required for recombination, $t_{flow}/t_{recomb} \ll 1$, (Fig. 24) the composition of the expanding gas will be fixed or

"frozen" throughout and u_∞ will be a constant. In the approximation of steady, inviscid and non-radiating flow, the energy equation yields constant total enthalpy along a streamline which provides a simple energy integral for the centerline flow properties,

$$h_t = c_{pA}\left(1 + \frac{n_E}{n_o}\right) T_\infty + \frac{u_\infty^2}{2} + h_I$$

where $h_I = \Sigma c_i h_i^{(0)}$ and the energy due to electronic excitation has been neglected. Now for frozen flow and $M_\infty^2 \to \infty$, ($T_\infty \to 0$ and $u_\infty \to$ constant) this may be rewritten,

$$h_{tf} \equiv \frac{u_\infty^2}{2} = h_t \left[1 - \frac{h_I}{h_t}\right]$$

where the second term in the brackets is the frozen ionization energy fraction. h_{tf} has been calculated from the p_i and ρu measurements and is shown to be constant in Fig. 36 for the 200 and 1000 amp. tests. The measured values of h_t at $\bar{x} = 1$, from the enthalpy probe, are also shown in the legend as well as h_I/h_t calculated from the equation above. For purposes of comparison, $(h_I/h_t)_{Equil.}$ was calculated at the stagnation equilibrium conditions. These values of h_I/h_t, calculated in these two ways, show good agreement. In fact, the agreement is within the scatter in the data used to deduce these results. It is believed that the results shown in Fig. 36 convey the fact that the flow is hypersonic and frozen and that the ionization energy fraction can be estimated by assuming an equilibrium condition at the anode exit plane ($\frac{x}{D_*} = 0$). Corresponding to these equilibrium conditions at 200 amp. and 1000 amp., the species mass fraction ranges from 0.2 for the atoms and 0.8 for the singly-ionized

ions, to 0.8 for the singly-ionized ions and 0.2 for the doubly-ionized ions respectively. At the sonic conditions ($x/D_* \cong 1/2$) these results correspond to electron number densities of about 1.6×10^{15} cm^{-3} at 200 amp. and 2.4×10^{15} cm^{-3} at 1000 amp.

III.3.5 Stagnation Point Heat Transfer Measurements

From the results of the impact pressure, mass flux and total enthalpy measurements and the discussion of the flow field given in Section III.3 the stagnation point heat transfer measurements made here can be brought into proper perspective. The flow field along the axis of the free jet is highly ionized, chemically frozen and hypersonic. Within about one or two anode diameters from the exit plane the electrons become isolated energetically from the ions and are believed to remain at nearly constant temperature throughout the region of interest in the free jet. On the other hand, the ions undergo an adiabatic expansion to the first approximation. The ions and electrons are in close proximity, in order to preserve charge neutrality ($n_E \cong n_I$) and the ions are moving at the adiabatic limit velocity corresponding to the frozen total enthalpy. Primarily due to the small electron mass, and thus large speed of sound, $a_E = a_I \sqrt{\frac{m_I}{m_E} \frac{T_E}{T_I}} \geq 270\, a_I$, the electrons are moving at low subsonic speed throughout.

The presence of a body in the flow field, e.g., the stagnation point heat transfer probe, must now be considered. As mentioned earlier, the probes used in this investigation were not biased to either electrode but were at floating potential so that no current was drawn from the plasma. A sketch of the stagnation point flow field is shown on the next page in order to facilitate the following discussion. For reasons similar to those already mentioned, for probe locations in which $x/D_* > 2$, the electrons are believed to undergo an isothermal compression through the probe bow shock wave. This compression decreases the electron-ion and electron-electron mean

Stagnation Point Flow*

$T_{I_\infty} \ll T_{E_{\infty\infty}} \cong$ constant throughout the boundary layer as well

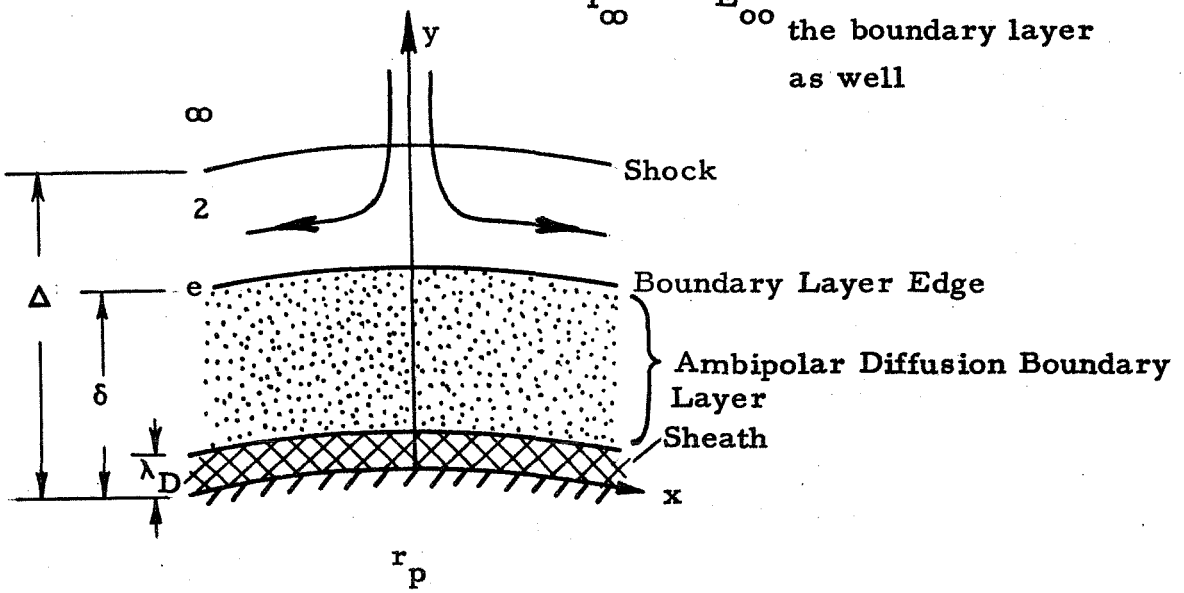

$\frac{x}{D_*}$	M_∞	Re_∞ cm^{-1}	Re_2 cm^{-1}	$\frac{\delta}{r_p}$	$\frac{\Delta}{r_p}$	$(\lambda_{E-E})_\infty$ cm	$(\lambda_{I-I})_\infty$ cm	$(\lambda_{EE})_e$ cm	$(\lambda_{I-I})_e$ cm	λ_D cm
1	2.4	10^3	10^2	0.1	1/4	10^{-2}	10^{-3}	10^{-3}	10^{-3}	10^{-5}
8	13	10^4	1	1	1/4	0.5	10^{-4}	10^{-1}	10^{-1}	10^{-4}

* Estimates of the flow quantities shown below the sketch are based on frozen flow of fully singly-ionized argon from a free jet having stagnation number density and temperatrue of $0.6 \times 10^{15} cm^{-3}$ and $20,000^oK$ respectively.

free path from about 1 mm upstream of the shock to about 0.1 mm downstream of the shock. For nearly all conditions, the ions are compressed adiabatically and exhibit the conventional Rankine-Hugoniot shock jump conditions corresponding to frozen flow for a monatomic gas. Because of the inverse square temperature dependence of the coulomb cross section, the ion-ion mean free path ranged from between about 10^{-3} cm upstream of the shock to as large as 0.1 cm downstream of the shock.

What happens in the boundary layer must also be explained from consideration of a two fluid model of weakly interacting electrons and ions. Except for the low range of Reynolds number* the velocity boundary layer is distinct from the shock wave. In this case an ambipolar diffusion model may be valid; in this model electron-ion pairs diffuse to the surface through counterdiffusing atoms which come from the surface. However account must be taken of the elevated electron temperature ($T_E > T_I = T_A$) in the diffusion model.

In the thin sheath ($<< r_p$) near the wall, charge neutrality is not preserved. For the case of interest here, (probe current $J_p = 0$) the probe potential is somewhat less than the plasma potential. A large fraction of the electrons which enter the sheath is repelled from the surface so that the electron and ion particle fluxes reaching the surface are equal. An estimate of the thickness of the sheath based on the Debye length, λ_D, is about 10^{-5} - 10^{-4} cm for

* Reynolds number behind the shock wave was based on the measured ρu and viscosity from the Fay mixture rule (38) (see Appendix D) based on the frozen stagnation temperature and the measured impact pressure.

the conditions here. The mean free path of the ions is smaller and that of the electrons larger than this sheath thickness, i.e., the sheath is collision dominated for the ions and collision free for the electrons.

A reasonable model then for stagnation point heat transfer in the first approximation is shown in the sketch above. The electron temperature is assumed constant throughout and in general unequal to the ion temperature at the edge of the boundary layer, $(T_I)_e \neq (T_E)_e$. The boundary layer and the shock wave may be assumed to be distinct over much of the operating range. The flow through the shock wave and into the boundary layer is fully singly-ionized and chemically frozen. In this region heat transport occurs by ambipolar diffusion of species and by conduction. A thin sheath at the surface of the probe screens a large fraction of the "hot" electrons from the wall where the electrons and ions recombine.

Even for this simplified model no solution exists at present. This problem has all the difficulties of the stagnation point Langmuir probe problem and is further complicated by the uncertainty in the values of the transport properties. However, before discussing the results of the stagnation point heat transfer measurements made here, three theoretical predictions, which are related to the present problem, will be discussed briefly. These predictions apply to the following cases:

Geometry and Flow	Conditions in the Boundary Layer	Source
1. Stagnation Point For partially ionized argon and helium.	1a Equilibrium Flow 1b Frozen Flow Equilibrium edge conditions; no sheath at the wall	Finson and Kemp (39)
2. Shock Tube End Wall For partially ionized argon.	2a. Equilibrium Flow 2b. Frozen Flow Equilibrium edge conditions; no sheath at the wall. 2c. Frozen Flow with no Ionization Frozen Flow Edge Condition	Fay and Kemp (40)
3. Shock Tube End Wall For partially ionized argon.	3a. Frozen Flow with $T_E \neq T_I$ Equilibrium edge condition; sheath included with probe current $J_p = 0$.	Camac and Kemp (41)

Finson and Kemp (39) solved the stagnation point boundary layer equations using variable fluid properties, Pr, $C = \rho\mu/\rho_e\mu_e$, Le, and an ambipolar diffusion model over a range of freestream ionization fraction between 0 and 16% for argon and between 2 and 67% for xenon. They considered the limits of equilibrium and frozen flow in the boundary layer having equilibrium edge conditions for an electrically neutral, equal electron, ion, and atom temperature gas and did not consider a sheath region. Transport properties were evaluated by applying the Fay mixture rule (38). The boundary layer

similarity transformations of Fay and Kemp (40) were used to reduce the non-linear partial differential equations to non-linear ordinary differential equations, which were then solved numerically. The freestream conditions of interest were chosen so as to allow a comparison with the measurements of Rutowski and Bershader (42) for the hemisphere in argon, and Reilly (43) for the two dimensional body (circular cylinder) in argon and xenon. For the axisymmetric body the agreement is good at low degrees of ionization, but the theory is about 20% above the mean of the radiation-corrected data points at higher degrees of ionization. For the two dimensional body the agreement between experiment and theory (particularly for xenon) is not nearly as good. The scatter in the data is large; the mean of the experimental data at M = 8 where the degree of ionization is about 2% is about 40% below the prediction. However as pointed out by Finson (44) this result may be caused by a faulty heat transfer gauge. The frozen and equilibrium boundary layer heat transfer predictions are within 30% of each other.

Fay and Kemp (40) have calculated the convective heat transfer to a shock-tube end-wall from reflected shock heated argon for 1) equilibrium and frozen boundary layer models for which the boundary layer edge is in ionization equilibrium and 2) frozen boundary layer with no ionization in the boundary layer for which the edge conditions are just those of a shock heated (un-ionized) frozen gas which exists at the end-wall prior to the onset of ionization. They then compared these predictions to the measurements of Camac and Feinberg (45). The duration of measurement was sufficiently

sufficiently long that first the un-ionized and then the ionized gas was exposed to the end-wall. The measured heat transfer rates did not change as a result of the relaxation process. Before as well as after the onset of ionization the measurements agreed reasonably well with the heat transfer prediction for the un-ionized gas as compared to the frozen and equilibrium predictions, which are low by as much as 40 and 30% respectively. (Note also a point misplotted for 2F4E' of the frozen prediction at $U_s = 3$ in Fig. 2, p. 670, Ref. 40.) Fay suggests that the effect of unequal electron and atom-ion temperatures may be the unknown factor which would account for this anomaly.

Camac and Kemp (41) have predicted the effect of unequal electron and ion-atom temperature on heat transfer for the end-wall shock tube problem for a special case. They used the continuum boundary layer equations with ambipolar diffusion up to the edge of the sheath, where a molecular description was matched to the continuum description. The boundary layer edge condition was taken to be in equilibrium and the end-wall was assume d to be at the floating potential for which $J_p = 0$. With either temperature or chemical non-equilibrium present complete similarity was not possible; however a local similarity approach was believed to be satisfactory provided the nonsimilar terms containing time varied slowly so that time could be treated as a parameter. Their solution represented one external condition in time, with two different values of the elastic collision rate constant, 0 and ∞, and gas phase recombination neglected. The conditions behind the reflected shock were

$T \cong 16,000^{\circ}K$

$p \cong 2.5$ atm

$\alpha \cong .6$

$T_w \cong 300^{\circ}K$

Since a few collisions exist in the sheath they varied the ion velocity at the sheath edge from the maximum drift velocity $4\sqrt{\kappa T_e/m_I}$ to the collision dominated equilibrium value based on the wall temperature $\sqrt{\frac{8}{\pi}\kappa T_w/m_I}$. When the elastic energy exchange between the electrons and the heavy species was neglected, the range in ion velocity at the sheath edge resulted in only a 6% difference in heat transfer. These results ranged between 5 and 10% respectively below the case for which complete temperature equilibration throughout the boundary layer was specified. Because of the negative sheath potential the electrons are insulated from the wall, and in fact the electron temperature drops to only one-half its edge value at the sheath when the collision rate constant is zero. For the case of equal temperatures at the edge of the boundary layer, the effect of unequal temperatures in the shock-tube end-wall boundary layer has a small effect on heat transfer, at least for the one condition investigated there. However in the present case $(T_E)_e \neq (T_I)_e$ in general.

Axial heat transfer profiles taken between $1 \leq x/D_* \leq 12$ in axial intervals of the anode radius $R_o = 3/8$ in. are shown in Fig. 37 for 5 operating conditions of the arc heater, I = 200, 400, 600, 800 and 1000 amps. The conditions of operation of the arc heater were such as to provide about a factor of two in total enthalpy, $18,300 \leq h_t \leq 32,200$ BTU/lb_m, as the ionization fraction, α, ranged between

.78 and 1.0^+. $\alpha = 1.0^+$ means that complete single ionization of argon is completed at the two highest currents. According to the energy estimates of Section III.3, there may be 20% by mass of doubly-ionized argon present. Estimates of h_t, and subsequently T_{tf} and α, shown in Fig. 37 at I = 400, 600, and 800 amps. were obtained by assuming that the centerline total enthalpy depended linearly on the average total enthalpy h_{ta}, between 200 and 1000 amps. where h_t was measured. h_{ta} could be monitored continuously during each test. The frozen total enthalpy, h_{tf}, comprising the random thermal energy and kinetic energy, was obtained in a similar way.

The stagnation point heat transfer measurement was made over a 30^o half-angle spherical cap which comprised the calorimeter sensor of the stagnation point heat transfer probe shown in Fig. 7. The heat transfer distribution over this sensor was assumed to obey the distribution proposed by Lees (46) for the hemisphere,

$$\frac{q(\theta)}{q_s(0)} = 1 - (0.722 - \frac{0.667}{\gamma_\infty M_\infty^2})\,\theta^2$$

which has been verified by Kemp, Rose and Detra (47) and Hickman and Giedt (47a). The integration of this distribution over the sensor area, including the effect of angle-of-attack, to relate the average heat flux measured by the probe to the stagnation point value, is carried out in Appendix C. For measurements along the axis, this correction, the ratio of average to stagnation point heat transfer rate, was taken to be $q_a/q_s = 0.88$ corresponding to $M_\infty^2 \to \infty$. At $M_\infty = 2$, $q_a/q_s = 0.89$. The heat transfer rate is seen to decrease

rapidly with x/D_* or approximately as $\sqrt{p_i}$ (or $x/D_*)^{-1}$ for hypersonic source flow) until a small relative maximum* in the profile occurs at each current level, e.g., at $x/D_* \cong 6$ and 8 for the 200 and 1000 amp. conditions respectively.

The level of T_E was not measured in this investigation. However the measurements of T_E (and estimates of T_I) by Kelly, Nerheim, and Gardner (15) (discussed in Section III.3) show that T_E is significantly higher than T_I near the exit plane ($x/D_* \cong 1.3$) of a similar arc-produced free jet. These observations are the basis of a plausibility argument explaining the differences in the heat transfer rates measured here at 200 and 1000 amp. From the more recent measurements by Nerheim (20) it is observed that T_E is nearly independent of arc current, i.e., T_E variations with current are within the uncertainty band given for T_E between 1000 and 1600 amp. at $m_j = 0.3$ gm/sec for $\frac{1}{2} \lesssim x/D_* \lesssim 3$. Indeed this type of argument seems to be supported by the data here. If we scale the heat flux as

$$q \sim \frac{k\Delta T}{\delta_{thermal}}$$

where

$$\frac{\delta_{thermal}}{\ell} \sim \frac{1}{\sqrt{RePr}}$$

and replace the temperature difference by the total enthalpy, we

*This point is where the disk shock was visually observed to be from the distinct changes in luminosity of the gas. As observed and discussed in Section III.3 the minimum of the impact pressure occurred at this same point.

obtain

$$q_{BL} \sim \frac{\sqrt{p_i k_i (1+\alpha)}\, h_t}{(h_{tf})^{1/4}}$$

and

$$q_{BL} \sim \frac{\sqrt{p_i (1+\alpha)}\, T_E^{5/4} h_t}{(h_{tf})^{1/4}}$$

where the Spitzer thermal conductivity (33) has been used. Thus if the value of T_E is invariant with arc current,

$$\frac{q_{BL}}{q_{BL}}_{200\ \text{amp.}} \cong \sqrt{\frac{10.5}{20}\,\frac{1.78}{2}}\ \left(\frac{13,500}{5,530}\right)^{1/4}\ \left(\frac{18,300}{32,200}\right)$$

$$= 0.48 \ (\text{at } x/D_* = 1)$$

whereas the measured ratio is 0.57 (Fig. 37) or about 15% higher than predicted. The fact that the measured q at 1000 amp ($x/D_* = 1$) appears somewhat low (in Fig. 37) makes this argument even stronger. For equal electron and ion temperature, for which the conductivity was evaluated at the frozen total temperature of the mixture (~30,000°K at 1000 amp. and ~14,000°K at 200 amp.), the heat flux ratio would have been 0.18 or about a factor of 3 lower than the measurements. If these arguments are carried one step further, the data can be correlated in a somewhat more conventional manner. In particular, the data can be compared to the frozen boundary layer prediction by Finson and Kemp (39) in the same spirit of the calculations just made. The effect of elevated electron temperature would have to be reflected

in lowering the Prandtl number because their theory does not include the effect of unequal temperatures. Use of the numerical solutions by Finson and Kemp (39) is facilitated by the work of Back (48).

Back (48) predicted the laminar boundary layer heat transfer on a flat plate from a partially ionized monatomic gas for constant freestream velocity for equilibrium and frozen boundary layer models using constant transport properties* and the ambipolar diffusion assumption. By comparing his constant transport properties prediction to the variable transport properties solution of Finson and Kemp (39) at the stagnation point, Back was able to obtain a simple curve fit to the exact solution as shown in Fig. 38. For $Pr \leq 0.05$, two new curves have been drawn to better approximate the exact solution.

For the case of the fully catalytic cold wall ($z_{Iw} \cong 0$, $g_w \cong 0$) axisymmetric stagnation point ($\frac{g'_w}{1-g_w} = .495$) the prediction for the entire Pr_e range is

$$q_{BL} = \frac{C_l}{\sqrt{r_p}} (\rho_e \mu_e)^{1/2} \left(\frac{du_e}{d\theta}\right)^{1/2}_{\theta=0} h_t \left[1 + \frac{\alpha I}{h_t}(Le^{.63} - 1)\right] \quad (1)$$

where

$$C_l = 0.86\, Pr_e^{-1/3} \quad \text{Valid for frozen and equilibrium boundary layers for } Pr_e \gtrsim .05 \text{ (Back, 48)} \quad (2)$$

* The validity of using heat transfer predictions based on constant transport properties depends upon the success of determining the correct reference conditions in the boundary layer at which the properties are to be evaluated so that agreement with exact solutions is obtained. This technique has been successful for a number of boundary layer heat transfer problems (e.g., 46, 49, and 50).

$$C_l = 0.60\ Pr_e^{-0.46} \quad \text{Valid for the frozen boundary layer for } Pr_e \lesssim .05 \qquad (3)$$

$$= 0.39\ Pr_e^{-0.61} \quad \text{Valid for the equilibrium boundary layer for } Pr_e \lesssim .05 \qquad (4)$$

The modified Newtonian approximation for the pressure distribution on hemispheres seems to be adequate (51, at least to $Re_{2r_p} \cong 28$ and $0 \leq \theta \leq 70^\circ$) in low Reynolds number flows of argon so that the velocity gradient may be approximated as

$$\frac{1}{u_\infty} \left(\frac{due}{d\theta}\right)_{\theta=0} \cong \sqrt{\frac{\gamma-1}{\gamma}}$$

in the hypersonic approximation, $M_\infty^2 >> 1$. γ was taken to be 5/3.

Shown in Fig. 39 are the data normalized by the heat flux calculated by using the frozen boundary prediction, Eqs. 1 and 3, with the following assumptions:

(i) Transport properties evaluated at p_i, T_{tf}, and α (except the Δ data points in Fig. 39) by using the Fay mixture rule (38). (See application of this mixture rule to argon in Appendix D).

(ii) Velocity gradient based on $u_\infty = \sqrt{2h_{tf}}$ instead of $u_\infty = \sqrt{2h_t}$

(iii) h_t is constant along the axis for $1 \leq x/D_* \leq 8$; measured values of h_t at $x/D_* = 1$ were used.

The impact pressure, p_i, was measured; α was deduced from the results shown in Fig. 36 and is given in Fig. 37; and the frozen total temperature, T_{tf}, was calculated from the measured frozen total

enthalpy, h_{tf} (derived from the measured p_i and ρu as discussed in Section III.3) as

$$T_{tf} = \frac{h_{tf}}{c_{pA}(1+\alpha)}$$

where

$$c_{pA} = \frac{\gamma}{\gamma-1} \frac{\kappa}{m_A}$$

The open circles and solid triangles apply to the data for which all species are at the frozen total temperature, T_{tf}, at the edge of the boundary layer. The 200 amp data, compared in this way, lie nearly 2.5 times above the 1000 amp. data, as observed earlier. For the 1000 amp. data the Prandtl number is seen to take on its fully singly-ionized value for argon. (See the transport properties discussion in Appendix D.)

If the data at 200 amp. are correlated by using the Prandtl number for a fully-ionized gas (see the open triangles in Fig. 39) the data compare favorably with the 1000 amp. data. (Note that good agreement is also observed with the data collected by Cheng (52) for this same Reynolds number range.) One way of interpreting this result is as follows: although the gas is not fully ionized, elevated electron temperature $(T_E)_e > (T_I)_e$ would have the effect of lowering Pr_e, i.e., from simple kinetic theory arguments,

$$P_r(T_E \neq T_I) \cong \left(\frac{T_I}{T_E}\right)^{5/2} Pr(T_E = T_I) .$$

In this way $(T_E)_e$ at 200 amp. was estimated to be 23,000°K or about

a factor of 1.5 larger than $(T_I)_e$. The electron temperature at 1000 amp. corresponds to the ion temperature $(T_E)_e = (T_I)_e \cong 30,000^oK$. The electron temperature at these two current levels differs only by about 30%. This result seems consistent with the measurements of Kelly, Nerheim, and Gardner (15) and Nerheim (20). Their measurements, made at 1000 and 1600 amp., show that T_E is insensitive to changes in current level. However, the electron temperatures estimated here range between 5,000 and 10,000°K higher than they measured.

Although the arc heater used in this investigation was identical to that used by them without the cathode shield (see Fig. 3 and discussion in Section II.2) operation with the cathode shield could be quite different. For instance, conditions at 1000 amp. and $m_j = 0.5$ gm/sec were:

(Private communication Ref. 24) Heater Used in Refs. 15 and 20)	Heater Used Here
I = 1000 amp.	I = 1000 amp.
V = 17.1 - 18.3 v	V = 24-26 v
h_{t^a} = 5600 - 6400 BTU/lb_m	h_{ta} = 9200-9800 BTU/lb_m

Thus, on the average, our average total enthalpy, h_{ta}, is one-and-one-half times their value. (It is observed that h_{ta} scales approximately as the arc voltage drop, V.) This differential in h_{ta} is equivalent to raising the temperature of a fully singly-ionized argon gas of equal species temperature by 8,000°K.

The energy added to the electrons by the electric field, E,

varies directly as E at constant current density. If T_E were scaled in this way, where $E \sim V/L$, one would expect T_E to be about a factor of 1.5 higher for the tests conducted here at 1000 amp.

As a result of these plausibility arguments, it is believed that the electron and ion temperatures are substantially higher than those reported in Refs. 15 and 20. What is not understood is why $T_E \cong 23,000^{\circ}K$ at 200 amp. and $\cong 30,000^{\circ}K$ at 1000 amp.

Radial profiles of stagnation point heat flux, q_m, are shown in Fig. 40 for the arc heater operating at 200 and 1000 amp. for $\bar{x} = x/D_*$ between 1 and 12. Corrections applied to the measured (average) heat flux, q_a, to obtain q_m, were for the effect of finite sensor area and angle-of-attack and were developed in Appendix C and shown in Fig. 41. Heat flux measurements were made over a radial distance of about 4 in. at each axial position; however, the profiles shown for $1 \leq x \leq 6$ were terminated in the data reduction scheme when the angle of attack, α, became 40° in order to be consistent with the approximation made in Appendix C that $\alpha^4 << 1$.

Only one-half of the profile is shown for each current level. Entire profiles (not shown here) at one current level were symmetric up to about the disk shock location ($x = 6$ and 8 at 200 and 1000 amp. respectively). Beyond this point asymmetries in q_m of 10-20% were not uncommon. In addition a radial shift as large as 5% was observed between the geometric axis aligned with the arc heater and the measured maximum in q_m.

The trend established for q_m along the centerline shown here

as well as in Fig. 37, for which q_m at 200 amp. is about one-half q_m at 1000 amp., continues to be true for the radial profiles. Any effect of the barrel shock wave on heat transfer is either small or has been smoothed out by the use of this large stagnation point heat transfer probe (r_p = 1/4 in.).

IV. SUMMARY OF RESULTS AND SUGGESTIONS FOR FUTURE WORK

IV.1 Summary of Results

The work carried out in this experimental investigation includes the building of a low density, high enthalpy continuous-flow test facility; the development of a probe which can be used for measurements of impact pressure, mass flux and total enthalpy and a stagnation-point heat-transfer probe to withstand an extremely hostile plasma environment; and the use of these probes in an attempt to define the flow field of a highly ionized, supersonic free jet.

Test Facility

The test facility has the flexibility of operating at low gas flowrates (< 0.5 gm/sec) when using the diffusion-ejection pumping system and operating at higher flowrates when the wind tunnel compressor facility is used. One version of the so-called Magneto-Plasma-Dynamic arc heater was used to heat the gas to average total enthalpies ranging from between about 5000 to 10,000 BTU/lb_m. Operation of the arc heater at 0.5 gm/sec argon flowrate, over a range of current from 200 to 1000 amp., provided a stable discharge and a flow field of high purity. The atom-ion number density was about 10^{15} cm^{-3} at the exit plane of the arc heater.

Probe Development

All probes were water cooled to allow continuous operation in the hostile plasma environment encountered here. Probe tips made of molybdenum, tungsten and carbon were used for the combined impact pressure, mass flux and total enthalpy probe, in order to maintain a sharp leading edge. This feature was necessary to

insure swallowing of the shock wave while making the mass flux measurements in supersonic flow. It also delays the onset of viscous effects which complicate the interpretation of pressure measurements. The mass flux sampling technique was developed in the supersonic flow field of an unheated free jet.

An important feature incorporated into the design of the stagnation point heat transfer probe was a 0.001 in. "air" gap which thermally isolated the outer heat shield cooling passage from the inner calorimeter. Stagnation point heat transfer rates ranged as high as about 13 BTU/in^{2}sec.

Heated Free Jet Investigation

These probes were used in an attempt to define the flow field of a highly ionized arc heated free jet. Based upon the Chapman (36) viscosity for a fully-ionized gas, the Reynolds number was about 2500 at the exit plane and remained at about this value along the centerline of the free jet. The total pressure ranged between about 20 and 35 mmHg. The impact pressure and mass flux measurements indicated that the flow was source-like, chemically frozen, and in other details very much like the underexpanded free jet flow of a perfect gas. Near the exit plane, $x/D_* = 1$, where the free shear layer is small, the validity of the ρu measurements was demonstrated.

The enthalpy measurements made on the centerline, at $x/D_*=1$, ranged from between 18,000 BTU/lb$_m$ at 200 amp. to 32,000 BTU/lb$_m$ at 1000 amp. These values are about a factor of 10 higher than those reported by others, who used this size probe or smaller (0.47 in.

dia. inlet), in supersonic flow. These centerline values were approximately three times the mass average total enthalpy deduced from a heat balance on the arc heater. Thus, use of the average total enthalpy to infer local flow field quantities in the free jet, is completely misleading.

By combining these total enthalpy measurements with the impact pressure and mass flux measurements just mentioned, the fraction of the total energy contained in ionization was shown to range between 0.7 at 200 amp. and 0.6 at 1000 amp. Using equilibrium conditions for reference purposes, the total temperature ranges from between 12,000° at 200 amp. to 20,000°K at 1000 amp. For this same current range, the species mass fraction ranges from 0.2 for the atoms and 0.8 for the singly-ionized ions, to 0.8 for the singly-ionized ions and 0.2 for the doubly-ionized ions respectively. Reasonable approximation to other flow quantities along the centerline is obtained by assuming that the gas is fully singly-ionized and chemically frozen to recombination, and that the flow is hypersonic. The electron energy equation was examined, and it was concluded that within a few diameters from the exit the electrons become energetically isolated from the ions and the electron heat conduction term dominates. These conclusions substantiate the results of electron temperature (T_E) measurements made (by others (15 and 20)) at the exit plane and 3 diameters downstream, which show that to a first approximation, $T_E \cong$ constant. Solution of the electron heat conduction equation, for this simple case, indicates a very weak decay of T_E along the axis.

Radial profiles of stagnation point heat transfer were obtained between one and twelve diameters downstream of the exit plane. No theory exists which accounts for the effect on heat transfer of unequal species temperature for the conditions encountered here. A preliminary attempt to correlate the results along the axis in the supersonic region ($1 \leq x/D_* \leq 8$), shows that the electron temperature ($T_E \neq T_I$ in general) plays an important role. If it is assumed that T_E is nearly independent of current level, the data at the two current levels correlate quite well. Elevated electron temperature was taken into account in the evaluation of the thermal conductivity (in the Prandtl number) in order that the data could be compared to the heat transfer prediction by Finson and Kemp (39). Their prediction is only strictly valid for equal species temperatures throughout and chemical equilibrium at the edge of the boundary layer. In this regard, the one fluid model cannot provide the exact solution to this problem; however, it may establish the trend of the data as a result of unequal temperature.

IV.2 Suggestions for Future Work

As a result of the present investigation, a number of problems are suggested for future work:

(1) An experimental investigation to determine the electron temperature and density in the supersonic portion of the free jet used here. Near the exit plane ($x/D_* \lesssim 3$) the electron temperature can be measured spectroscopically. For all locations the possibility exists for measuring T_E and n_E by swinging a small uncooled Langmuir probe through this jet.

(2) A theoretical and a continued experimental investigation to solve the stagnation point heat transfer problem. In particular a two-fluid model must be used to determine the effect on the stagnation point heat transfer rate of unequal species temperature and of probe potential which is, in general, different from the plasma potential.

(3) An experimental investigation of the dark space which exists upstream of the disk shock (see Fig. 15) in the free jet as well as upstream of the bow shockwave from the total enthalpy probe (see Fig. 25). With regard to the former instance, the Langmuir probe measurements (suggested as (1) above) in this region and through the disk shock of the free jet should answer some fundamental questions about the variation of electron temperature. Of particular interest, in the latter instance, is the possibility of altering the structure of this dark space by changing the potential on the body.

REFERENCES

1. Bier, K. and Hagena, O. "Influence of Shock Waves on the Generation of High-Intensity Molecular Beams by Nozzles", Rarefied Gas Dynamics, edited by J. A. Laurman, Academic Press, New York, 1963.

2. Fenn, J. B., and Deckers, J. "Molecular Beams from Nozzle Sources", Rarefied Gas Dynamics, edited by J. A. Laurman, Academic Press, New York, 1963.

3. French, J. B. "Continuum Source Molecular Beams", AIAA Jour., Vol. 3, No. 6, pp. 993-1000, June 1965.

4. Love, E. S., Grigsby, C. E., Lee, L. P. and Woodling, M.J.: "Experimental and Theoretical Studies of Axisymmetric Free Jets", NASA TR R-6, 1959.

5. Chow, R. R.: "On the Separation Phenomenon of Binary Gas Mixture in an Axisymmetric Jet", Univ. Calif. Berkeley. Institute of Engineering Research Report No. HE-150-175, Nov. 4, 1959.

6. Bier, Von K. and Schmidt, B.: "Zur Form der Verdichtungstösse in frei expandierenden Gasstrahlen", Zeitschrift für angewandte Physik, Vol. 13, No. 11, pp. 495-500, Nov. 1961.

7. Sherman, F. S.: "Transition Flow" (A Survey of Experimental Results and Methods for the Transition Region of Rarefied Gas Dynamics) Univ. Calif. Berkeley. Institute of Engineering Research, TR HE 150-201, Aug. 15, 1962. Also in Advances in Applied Mechanics, Supplement 2, vol. 2, 1963 Rarefied Gas Dynamics, Academic Press.

8. Ashkenas, H. and Sherman, F. S.: "The Structure and Utilization of Supersonic Free Jets in Low Density Wind Tunnels", Rarefied Gas Dynamics, vol. 2, 1966, Academic Press, Inc., New York

9. Owen, P. L., and Thornhill, C. K.: "The Flow in an Axially Symmetric Supersonic Jet from a Nearly Sonic Orifice into a Vacuum", Aeronautical Research Council, United Kingdom, R and M 2616, 1948.

10. Sherman, F. S.: "Self-Similar Development of Inviscid Hypersonic Free-Jet Flows", Lockheed Missiles and Space Company Technical Report: Fluid Mechanics 6-90-63-61, May 23, 1963, Sunnyvale, Calif.

11. Chou, Y. S., and Talbot, L.: Source-Flow Expansion of a Partially Ionized Gas into a Vacuum", AIAA Paper No. 67-99 AIAA 5th Aerospace Sciences Meeting, New York, New York, Jan. 1967.

12. Ducati, A. C., Giannini, G. M., and Muhlberger, E.: "Experimental Results in High Specific-Impulse Thermo-Ionic Acceleration", AIAA Journ. Vol. 2, No. 8, pp. 1452-1454, Aug. 1964.

13. John, R. R., Bennett, S., and Conners, J. F.: "Experimental Performance of a High Specific Impulse Arc Jet Engine", AIAA Paper No. 64-669, AIAA Fourth Electric Propulsion Conference, Philadelphia, Pa., Aug. 31-Sept. 2, 1964.

14. Cann, G. L.; "Annular Magnetic Hall Current Accelerator", AIAA Paper No. 64-670, AIAA Fourth Electric Propulsion

Conference, Philadelphia, Pa., Aug. 31-Sept. 2, 1964.

15. Kelly, A. J., Nerheim, N. M., Gardner, J. A.: "Electron Density and Temperature Measurements in the Exhaust of an MPD Source", AIAA Journal, vol. 4, Number 2, pp. 291-295, Feb. 1966.

16. Jahn, R. G.: "Design and Development of a Thermo-Ionic Electric Thrustor", Interim Report 5QS085-968, Giannini Scientific Corporation, Santa Ana, Calif., Aug. 1965.

17. Powers, W. E.: "Measurement of Current Density Distribution in the Exhaust of an MPD Arcjet", AIAA Jour. Vol. 5, No. 3, pp. 545-550, Mar. 1967.

18. Patrick, R. M., and Schneiderman, A. M.: "Axial Current Distribution in the Exhuast of the Magnetic Annular Arc", AVCO Everett Res. Lab. Report 231, July 1966.

19. Cann, G. L., Lenn, P. D., and Harder, R. L.: "Hall Current Accelerator", Electro-Optical Systems Incorporated Quarterly Progress Report, EOS Report 5470-Q-3, Pasadena, Calif., Mar. 1965.

20. Nerheim, N. M.: "Space Programs Summary No. 37-35, Vol. IV" Aug. 1, 1965 to Sept. 30, 1965, pp. 174-180, Jet Propulsion Laboratory, Calif. Inst. of Technology, Oct. 31, 1965.

21. Grey, J., Jacobs, P. F., and Sherman, M. P.: "Calorimetric Probe for the Measurement of Extremely High Temperature," Rev. of Scientific Instruments, Vol. 33, No. 7, pp. 738-741, July 1962.

22. Welsh, W. E.: Jr. "V. Liquid Propellant Propulsion, Part C.1.c: Heat Transfer and Fluid Mechanics; Propellant Heat Transfer; Water", Jet Propulsion Laboratory Research Summary 36-3, Vol. 1, Part 2, April 1, 1960 to June 1, 1960, pp. 29-30, June 15, 1960.

23. Conversion Tables for Thermocouples, No. 077989 Issue 2, Leeds and Northrup Company. The tables in this booklet are taken from NBS Circular 561.

24. Nerheim, N. M.: Private Communication.

25. Baum, E. and Cann, G. L.: "Thermodynamic Properties of Argon", ARL 63-133, Electro-Optical Systems, Inc., Pasadena, Calif., Aug. 1963.

26. Wang, C. J., Peterson, J. B., Anderson, R.: "Gas Flow Tables", Report No. GM-TR-154, Space Technology Laboratories, Inc., March 14, 1957.

27. Pratt and Whitney Aircraft: "Tables of Compressible Flow Functions", United Aircraft Corporation, East Hartford, Conn., 1960.

28. Chapman, S., and Cowling, T. G.: The Mathematical Theory of Non-Uniform Gases, Cambridge University Press, 1961.

29. Sherman, F. S., and Talbot, L.: "Diagnostics of a Low Density Arc Heated Wind Tunnel Stream", Progress in Aeronautics and Rocketry, vol. 7, Ed. by F. R. Riddell, Academic Press, pp. 581-598, 1961.

30. Grewal, M. S., and Talbot, L.: "Shock Wave Structure in a Partially Ionized Gas". Journal Fluid Mech., Vol. 16 No. 4,

pp. 573-594, 1963.

31. Collins, D. J.: "Visualization of a Free-Expansion Jet at Low Densities", Jet Propulsion Laboratory Space Program Summary No. 37-30, Vol. IV for the period Oct. 1, 1964 to Nov. 30, 1964, pp. 186-191, Dec. 31, 1964.

32. Petscheck, H., and Byron, S.: "Approach to Equilibrium Ionization Behind Strong Shock Waves in Argon", Annals of Physics: vol. 1, pp. 270-315, 1957.

33. Spitzer, L., Jr.: Physics of Fully Ionized Gases, Interscience Publishers, Inc., New York, New York, 1956.

34. Jukes, J. D.: "The Structure of a Shock Wave in Fully Ionized Gas", Jour. of Fluid Mech., Vol. 3, pp. 275-285, 1957.

35. Jaffrin, M. Y. and Probstein, R. F.: "Structure of a Plasma Shock Wave", Jour. of Fluid Mech., Vol. 7, No. 7, pp. 1658-1674, Oct. 1964.

36. Chapman, S.: "The Viscosity and Thermal Conductivity of a Completely Ionized Gas", Astrophysical Journal, vol. 120, No. 1, pp. 151-154, 1954.

37. Potter, J. L. and Bailey, A. B.: "Pressures in the Stagnation Regions of Blunt Bodies in the Viscous-Layer to Merged-Layer Regimes of Rarefied Flow." AEDC-TDR-63-168 von Karman Gas Dynamics Facility, ARO, Inc., Sept. 1963, (AD416004).

38. Fay, J. A.: Hypersonic Heat in Air Laminar Boundary Layer, in High Temperature Aspects of Hypersonic Flow, Ed. by W. C. Nelson, Macmillan Co., New York, New York,

pp. 583-605, 1964.

39. Finson, M. L. and Kemp, N. H.: "Theory of Stagnation Point Heat Transfer in Ionized Monatomic Gases," Physics of Fluids, vol. 8, No. 1, pp. 201-204, Jan. 1965.

40. Fay, J. A. and Kemp, N. H.: "Theory of Heat Transfer to a Shock-Tube End-Wall from an Ionized Monatomic Gas", Journal of Fluid Mechanics, vol. 21, Part 4, pp. 659-672, April 1965.

41. Camac, M. and Kemp, N. H.: "A Multitemperature Boundary Layer", AIAA Paper No. 63-460, presented at AIAA Conference of Physics of Entry into Planetary Atmospheres, Aug. 1963. Also found in AVCO Everett Research Laboratory Research Report 184, Aug. 1964.

42. Rutowski, R. W., and Bershader, D.: "Shock Tube Studies of Radiative Transport in an Argon Plasma", Phys. Fluids, vol. 7, Part 4, 1964, pp. 568-577, April 1964.

43. Reilly, J. A.: "Stagnation Point Heating in Ionized Monatomic Gases", Physics of Fluids, Vol. 7, No. 12, Dec. 1964, pp. 1905-1912.

44. Finson, M. L.: "Theory of Stagnation Point Heat Transfer in Ionized Gases", Thesis Mechanical Engineering Dept., Massachusetts Institute of Technology, June 1964.

45. Gamac, M., and Feinberg, R.M.: "Thermal Conductivity of Argon at High Temperatures", Jour. of Fluid Mechanics, vol. 21, Part 4, April 1965, pp. 673-688.

46. Lees, L.: "Laminar Heat Transfer Over Blunt-Nosed Bodies at Hypersonic Flight Speeds", Jet Propulsion, vol. 26, pp. 259-269, April 1956.

47. Kemp, N. H., Rose, P. H., Detra, R. W.: "Laminar Heat Transfer Around Blunt Bodies in Dissociated Air", Journal of Aero-Space Sciences, vol. 26, July 1959, pp. 421-430.

47a. Hickman, R. S., and Giedt, W. H.: "Heat Transfer to a Hemisphere-Cylinder at Low Reynolds Numbers", AIAA Jour., Vol. 1, No. 3, pp. 665-672, March 1963.

48. Back, L. H.: "Laminar Boundary-Layer Heat Transfer from a Partially Ionized Monatomic Gas". To be published Phys. of Fluids, April 1967.

49. Fay, J. A. and Riddell, R. R.: "Theory of Stagnation Point Heat Transfer in Dissociated Air", Journal of Aeronautical Sciences, vol. 25, No. 2, pp. 73-85, Feb. 1958.

50. Back, L. H. and Witte, A. B.: "Prediction of Heat Transfer from Laminar Boundary Layers. With Emphasis on Large Free-Stream Velocity Gradients and Highly Cooled Walls", Transactions of the ASME Journ. of Heat Transfer, vol. 88, Series C, No. 3, pp. 249-256, August 1966.

51. Potter, J. L. and Bailey, A. B.: "Pressure in the Stagnation Regions of Blunt Bodies in the Viscous-Layer to Merged-Layer Regimes of Rarefied Flow", AEDC-TDR-63-168 AD 416004, Sept. 1963.

52. Cheng, H. K.: "The Blunt Body Problem in Hypersonic Flow at Low Reynolds Numbers", Cornell Aeronautical Laboratory,

Inc., CAL Rept. No. AF-1285-A-10, June 1963.

53. Grey, J.: "Enthalpy Probes for Arc Plasmas--Second Status Review", Report to Section 3 (Thermal Ablation) Subcommittee VI, Committee E-21 ASTM, May 3, 1967.

54. Brown, A. C., Smith, E. C., Jr., Kramer, R. L., and McAdams, E. E., Jr.: "The Use of Mass-Flow and Total Enthalpy Probes in Supersonic Flow", Lockheed Missiles and Space Company Rept. B-07-64-1, Sept. 1964, Sunnyvale, Calif.

55. Carden, W. H.: "Heat Transfer in Nonequilibrium Hypersonic Flow with Surface Catalysis and Second-Order Effects", AIAA Journal, vol. 4, No. 10, Oct. 1966.

56. Potter, J. L., Arney, G. D., Jr., Kinslow, M., and Carden, W. H.: "Gasdynamic Diagnosis of High-Speed Flows Expanded from Plasma States", AEDC-TDR-63-241, Nov. 1963.

57. Chapman, D. R., and Rubesin, M. W.: "Temperature and Velocity Profiles in the Compressible Laminar Boundary Layer with Arbitrary Distribution of Surface Temperature", JAS, Vol. 16, No. 9, pp. 547-565, Sept. 1949.

58. Witte, A. B.: "Analysis of One-Dimensional Isentropic Flow with Tables for Partially Ionized Argon", Technical Report No. 32-661, Jet Propulsion Laboratory, Pasadena, Calif., Sept. 30, 1964.

59. Tables of Thermal Properties of Gases, Circular 564, National Bureau of Standards, pp. 75-137, 1955.

60. Bonilla, C. F., Wang, S. J., Weiner, H.: "Viscosity of Steam, Heavy-Water Vapor, and Argon at Atmospheric Pressure up to High Temperatures", ASME Transactions, Vol. 78, pp. 1285-1289, 1956.

61. Carneval, E. H., Larson, G. S., and Lynnworth, L.C.: "Experimental Determination of Transport Properties of High Temperature Gases", 7th Quarterly Progress Report Contract NASw-549, Parametrics, Inc., Waltham, Massachusetts, Sept. 8, 1964.

62. Back, L. H.: "Laminar Boundary-Layer Heat Transfer from a Partially-Ionized Monatomic Gas by the Similarity Approach", Technical Report No. 32-867, Jet Propulsion Laboratory, Calif. Inst. of Tech., Pasadena, Calif., Feb. 1966.

63. Hirschfelder, J. O., Curtiss, C. F., and Bird, R. B.: Molecular Theory of Gases and Liquids, John Wiley and Sons, Inc., New York, New York, 1954.

64. Smiley, E. F.: "The Measurement of the Thermal Conductivity of Gases at High Temperature with a Shock Tube; Experimental Results in Argon at Temperatures Between 1000° and 3000°K", Ph.D. Thesis, Catholic University of America, 1957.

65. Lauver, M. R.: "Evaluation of Shock-Tube Heat-Transfer Experiments to Measure Thermal Conductivity of Argon 700° to 8600°K, NASA TN D-2117, Feb. 1964.

66. Amdur, I., and Mason, E. A.: "Properties of Gases at Very High Temperatures", Physics of Fluids, vol. 1, No. 5,

pp. 370-383, Sept.-Oct. 1958.

67. de Voto, R. S.: "Transport Properties of Partially Ionized Monatomic Gases", Dept. of Aeronautics and Astronautics SUDAER 207, Stanford University, Sept. 1964.

68. de Voto, R. S.: "Transport Properties of Ionized Gases", Phys. of Fluids, Vol. 9, No. 6, pp. 1230-1240, June 1966.

69. de Voto, R. S.: "Argon Plasma Transport Properties", Dept. of Aeronautics and Astronautics SUDAER No. 217, Stanford University, Feb. 1965.

70. Athye, W. F.: "A Critical Evaluation of Methods for Calculating Transport Coefficients of Partially and Fully Ionized Gases", NASA TN D-2611, Ames Research Center, Moffett Field, Calif., Jan. 1965.

71. Liboff, R. L.: "Transport Coefficients Using the Shielded Coulomb Potential", Phys. of Fluids, Vol. 2, No. 1, pp. 40-51, Jan.-Feb. 1959.

72. Arave, R. J. and Husby, O. A.: Aerothermodynamic Properties of High Temperature Argon, Document No. D2-11238 (with revisions), Boeing Co., Seattle, Wash., Feb. 1962.

73. Cann, G. L. and Ducati, A. C.: "Argon Mollier Diagram", Rept. No. PLR-55 Plasmadyne Corp., Santa Ana, Calif., Feb. 1959.

74. Drellishak, K. S., Aeschliman, D. P., and Cambel, A. B.: "Tables of Thermodynamic Properties of Argon, Nitrogen, and Oxygen Plasmas", Arnold Engineering Development Center, AEDC-TDR 64-12, Jan. 1964.

75. Drellishak, K. S., Knopp, C. F., and Cambel, A. B.: "Partition Functions and Thermodynamic Properties of Argon Plasma", Arnold Engineering Development Center, AEDC-TDR-63-146, Aug. 1963.

76. de Voto, R. S.: Private Communication.

77. de Voto, R. S.: "Simplified Expressions for Transport Properties of Ionized Monatomic Gases", Dept. of Aeronautics and Astronautics SUDAER No. 283, Stanford University, July 1966. Also issued as SU-IPR Report No. 82 of the Institute for Plasma Research, Stanford University.

78. Lin, S. C., Resler, E. L, and Kantrowitz, A.: "Electric Conductivity of Highly Ionized Argon Produced by Shock Waves", Jour. of Appl. Phys., Vol. 26(1), Jan. 1955.

79. Hayes, W. D., and Probstein, R. F.: Hypersonic Flow Theory, Academic Press, New York and London, 1959.

80. Bailey, A. B., and Sims, W. H.: "The Shock Shape and Shock Detachment Distance for Spheres and Flat-Faced Bodies in Low-Density, Hypervelocity, Argon Flow", AEDC-TDR-63-21, Feb. 1963.

81. Potter, L. J., and Bailey, A. B.: "Pressures in the Stagnation Regions of Blunt Bodies in Rarefied Flow", AIAA Tech. Note, Vol. 2, No. 4, pp. 743-745, April 1964.

82. Bailey, A. B.: "Further Experiments on Impact-Pressure Probes in a Low-Density, Hypervelocity Flow", AEDC-TDR-62-208, Nov. 1962.

83. Daum, F. L., Shang, J. S., and Elliott, G. A.: "Impact Pressure Behavior in Rarefied Hypersonic Flow", AIAA Tech. Note, Vol. 3, No. 8, Aug. 1965.

84. Daum, F. L., Shang, J. S., and Elliott, G. A.: "Rarefaction Effects on Impact Pressure Probes in Hypersonic Flow", ARL 65-176, AD 631477, Sept. 1965.

85. Ashkenas, H.: Private Communication from the Jet Propulsion Laboratory, May 5, 1965.

86. Matthews, M. L.: "An Experimental Investigation of Viscous Effects on Static and Impact Pressure Probes in Hypersonic Flow", GALCIT, Memorandum No. 44, June 2, 1958.

87. Sherman, F. S.: "New Experiments on Impact Pressure Interpretation in Supersonic and Subsonic Rarefied Air Streams", NACA TN 2995, Sept. 1953.

88. Enkenhus, K. R.: "Pressure Probes in Low Density", UTIA Report No. 43, Jan. 1957.

89. Arney, G. D., Jr., and Bailey, A. B.: "An Investigation of the Equilibrium Pressure Along Unequally Heated Tubes", AEDC-TDR-62-26, Feb. 1962.

90. Arney, G. D., Jr. and Bailey, A. B.: "Addendum to an Investigation of Equilibrium Pressure Along Unequally Heated Tubes", AEDC-TDR-62-188, Oct. 1962.

91. Howard, W. H.: "An Experimental Investigation of Pressure Gradients Due to Temperature Gradients in Small Diameter Tubes", GALCIT Memorandum No. 27, June 10, 1955.

92. Bates, D. R., Kingston, A. E., and McWhirter, R.W.P.: "Recombination Between Electrons and Atomic Ions I. Optically Thin Plasmas", Proc. of the Royal Society 267A (1962) pp. 297-312.

93. Bates, D. R., Kingston, A. E. and McWhirter, R.W.P.: "Recombination Between Electrons and Atomic Ions. II. Optically Thick Plasmas", Proc. of the Royal Society 270A 1962, pp. 155-167.

94. Bates, D. R., and Kingston, A. E.: "Properties of a Decaying Plasma", Planet. Space Sci., 1963, vol. 11, pp. 1-22, Pergamon Press, Ltd.

95. Makin, B. and KeckJ. C.: "Variational Theory of Three Body Electron-Ion Recombination Rates", Phys. Review Letters, vol. 11, No. 16, Sept. 15, 1963, pp. 281-283.

96. Talbot, L., Chou, Y. S. and Robben, F.: "Expansion of a Partially-Ionized Gas Through a Supersonic Nozzle", Report No. AS-65-14, Institute of Engineering Research, University of Calif., Berkeley, Calif., Aug. 1965.

APPENDIX A: MASS FLUX SAMPLING TECHNIQUES

A.1 Mass flux measurement

Mass flux, ρu, can be measured in a supersonic stream if the shock wave can be "swallowed" in the diffusor section of a probe thereby capturing the undisturbed streamtube bounded by the probe tip perimeter. This technique has been used successfully by several investigators (54, 55, 56) who measured ρu in much lower enthalpy flows than reported here. The probe must have a sharp leading edge of small enough included angle so as to insure shock attachment while taking the mass sample thereby eliminating mass spillage at the tip. In addition the vacuum supply for the probe must have sufficient pumping capacity, with line losses included, so that the pressure at the probe tip, at the required flowrate, is less than the static pressure downstream of the shock. Both a steady-state sampling technique using a vacuum pump and a transient sampling technique using a 4 ft^3 evacuated collector tank were employed.

The purpose of this appendix is to establish the operating range of the ρu sampling technique in hot flow. To do this, models of the two sampling techniques used here are developed to allow calculation of their operating ranges in terms of jet conditions and sampling conditions. The centerline ρu measurements made in the known flow field of the cold free jet are shown to be valid as long as conditions fall within the calculated operating range. This same model of the sampling technique is then used to predict the ρu probe operating range in hot flow.

Since the mass flux measurement involves flowrates

typically between 10^{-8} and 10^{-5} lbm/sec, the probe line Reynolds number range between 10^{-2} to 10/in. Knudsen number based on probe tip conditions is no greater than about .01. Thus the Hagen-Poiseuille laminar flow result is used to relate probe line pressure drop to flowrate. This solution is,

$$Q = \frac{\Delta p}{L} \frac{\pi D^4}{128\mu} .$$

To introduce mass flowrate, $\dot{m}$, and to account for the change in density the expression is rewritten in terms of the average density $\bar{\rho} = \frac{1}{2} \frac{(p_1+p_2)}{R\,T}$, as,

$$\dot{m} = c\eta(p_2^2-p_1^2)$$

where $\eta = \frac{D^4}{L}$ and

$$c = \frac{\pi}{256\mu\, R\, T} = 1.30 \frac{\text{lbm}}{\text{sec}} \cdot \frac{\text{ft}}{(\text{lb}_f)^2}$$

for argon at 522°R.

Now if this result is applied to a series of 3 tubes of different lengths L_0, L_1, L_2 and diameters D_0, D_1, D_2, the result is,

$$\dot{m} = c \frac{\eta_2\eta_1\eta_0}{\eta_2\eta_1+\eta_1\eta_0+\eta_0\eta_2} (p_2^2-p_0^2)$$

A.2 Steady State Mass-flux Measurement Technique

With valves A and B open and valve C closed (see Fig. 6) the mass flux sample is pumped from the probe inlet, through the probe lines, through the vacuum pump and finally into an inverted water-filled calibrated beaker. The time elapsed to displace the water from the calibrated beaker to the free surface of the water

reservoir was recorded with a stop watch. For instance at $\bar{x} = 1$ and $D_{probe} = .149''$ a 250 ml beaker was filled typically in 2 min. whereas at $\bar{x} = 5$ a 50 ml beaker was filled in 10 min. From this measurement and knowledge of the gas sample volume and its density at 1 atm the flowrate and hence the mass flux was calculated for a given tip diameter. When valve B was closed, the output of the pump was immeasurable over a 30 minute period indicating that the pump was not leaking in any external air.

The operating range was calculated by using the modified Poiseulle relationship in which the resistance of the circuit between valves A and B is negligible so that the result is,

$$\dot{m} = c \frac{\eta_2 \eta_1}{\eta_2 + \eta_1} (p_2^2 - p_1^2) \qquad (1\text{-A})$$

where p_2 is the pressure at the probe tip and p_1 is the pump inlet pressure corresponding to the pump performance at $\dot{m}$. Thus for given tube diameters and lengths and vacuum pump characteristic the results can be plotted as shown in Fig. 42, curve 1. For a given probe diameter and static pressure behind the shock, p_2, the actual mass flowrate must fall below and to the right of the pump performance curve, otherwise the pump capacity will be exceeded, the shock will not be swallowed, and the mass flowrate measured in this way will be too low. The impact pressure measurements in cold flow (Fig. 18) showed that for purposes of estimating the operating range, the impact pressure distribution predicted by Ashkenas and Sherman (Ref. 8) could be used. Thus for any given total pressure, total temperature and probe size, the probe flowrate could be

plotted as a function of p_2, the static pressure behind the shock. In Figure 42, for instance, curves 2 and 3 are shown at the same total pressure for probe diameters .035 and .149" in cold flow (T_t = 522°R). Whereas the .035 in. dia. probe, curve 2, can be operated for $\bar{x}$ = 3, the .149 diameter probe is satisfactory at $\bar{x}$ = 1 and in question at $\bar{x}$ = 2. In fact experimentally ρu was measured at $\bar{x}$ = 2 in cold flow. The Mach number obtained from this ρu and the measured total pressure was about 60% higher than that shown in Fig. 42 for $\bar{x}$ = 1. From this example, and others not given here, the model used to predict the operating range is believed to be reliable. Comparison of these results to the known cold flow field is discussed in Section III.2.2. The operating range criterion of the sampling technique appears to be valid in cold flow.

Preliminary results obtained by flow field v sualization and impact pressure measurements given in Section III.3.2 indicated that the hot jet was remarkably similar in structure to the cold jet. The operating range criterion for the ρu measurements for the hot flow was then calculated on the basis of the free jet solution given by Ashkenas and Sherman (8) and the measured impact pressure measurements. Thus, for a given $\bar{x}$, ρu in hot flow was taken equal to ρu in cold flow; however, the total jet pressure and temperature was higher in hot flow (the total gas flowrate was kept constant at .5 gm/sec for both cases). Curves 4 and 5 of Fig. 42, which were calculated in this way, show that the effect of heating the jet is to increase the operating range of the ρu measurement technique.

In fact, whereas the .149 dia. tip probe could not be used for $\bar{x} = 1$ in cold flow, the operating range in hot flow was extended to include the entire supersonic flow field of the jet.

A.3 Collector Tank Mass Flux Measurement

In this method of measuring ρu the collector tank, Fig. 6 was evacuated to about 0.1 μHg. Then valve B was closed and valve A was opened for a measured time period during which the gas was collected in the collector tank. The collector tank pressure was then measured with a McLeod gage again and the mass entering the probe was calculated from the simple mass balance,

$$M = \frac{V\Delta p}{RT} - \frac{p_i V}{RT} + \frac{p_{if} V}{RT}$$

↑ Mass of gas collected by collector tank.

↑ Mass of gas contained initially in the probe line at the impact pressure. This gas does not enter the probe as part of the gas sample but does enter the collector tank and must be subtracted from the collected mass.

↑ Residual mass of gas contained in the probe line when valve A is closed. This gas enters the probe but does not enter the collector tank and must be added to the collected mass.

When the mass flux probe operates correctly, it intercepts the oncoming undisturbed streamtube so that the flow rate is constant in time. Thus, when the above expression is converted to mass flux and rewritten slightly, it becomes,

$$\rho u = \frac{1}{At} \cdot \frac{V\Delta p}{RT} \left[1 - \frac{\Delta p_i}{\Delta p} \frac{v}{V}\right]$$

where

ρu = mass flux, $\frac{\text{lbm}}{\text{ft}^2\text{sec}}$

V = collector tank volume plus the line volume between value C and B · ($4.35\ \text{ft}^3$)

v = probe line volume between valve A and the probe tip · ($.0387\ \text{ft}^3$)

Δp = collector tank pressure rise, μHg.

Δp_i = $p_i - p_{if}$, where p_{if} is the final pressure of the probe line just prior to closing valve A and p_i is the impact pressure, mm Hg.

t = sample time, i.e., time that valve A is open, sec.

A = area of probe tip, ft^2.

R = gas constant for argon, $38.7\ \frac{\text{ft-lb}_f}{\text{lbm}}$

T = collector gas temperature, 70°F.

With the units prescribed above, ρu becomes,

$$\rho u = 0.602 \times 10^{-6} \frac{\Delta p}{At} \left[1 - \frac{8.88\ \Delta p_i}{\Delta p}\right] .$$

The second term in the bracket ranges typically from about .05 to .25.

The operating range for this ρu measurement technique must now be determined. The essential idea is the same as before. The shockwave must be swallowed to allow stream tube capture. The pressure at the probe tip must be less than the static pressure downstream of the shock, p_2, while the constant flowrate sample is taken. Thus for a given sample flowrate, $\dot{m}$, and static pressure behind the shock, p_2, the maximum collector tank pressure, p_{ctmx}, which is associated with the maximum sampling time, becomes, from

Eq. 1-A where the pump inlet pressure has been replaced by p_{ctmx},

$$p_{ctmx} = \left[p_2^2 - \frac{\dot{m}}{c\bar{\eta}}\right]^{\frac{1}{2}}$$

where $\bar{\eta} = \frac{\eta_1 \eta_2}{\eta_1 + \eta_2}$.

The minimum collector tank pressure, at t = 0, is

$$p_{ctm} = p_{cti} + p_i \frac{v}{V}$$

where the last item is the pressure contribution of the probe line gas which is assumed to be swept instantaneously into the collector tank as valve A is opened at t = 0. p_{cti}, the initial collector tank pressure, was typically between 0.1 and 1 μHg. whereas $p_i \frac{v}{V}$ ranged from 180 μHg. at $\bar{x}$ = 1 to 1 μHg. at $\bar{x}$ = 6. The maximum sampling time is that associated with the pressure rise between p_{ctm} and p_{ctmx}.

The rate of collector tank pressure rise is related to gas sample flowrate through the perfect gas law as,

$$\dot{p}_{ct} = \dot{m} \frac{RT}{V}$$

$\dot{m}$ is then eliminated from Eq.1-A and the result is integrated to obtain the sample time as,

$$t = \frac{\bar{c}}{2p_2} \ell n \left[\frac{(p_2+p_{ctmx})(p_2-p_{ctm})}{(p_2+p_{ctm})(p_2-p_{ctmx})}\right]$$

where

$$\bar{c} = \frac{V}{RTc\bar{\eta}} = 153 \text{ sec.}$$

when t and p are in seconds and lb_f/ft^2 respectively. (p_2 is the static pressure behind the shock.)

In order to calculate the probe operating range for given jet conditions it was assumed, as discussed previously, that the free jet character of the inviscid flow field is not changed radically by gas heating. The results of these calculations for the probe operating range are shown in Fig. 20 for the .149" diameter probe tip with the jet operating 1000 amperes and 1/2 gm/sec total flowrate. However in addition to using the free jet theory of Ashkenas and Sherman (8), the hypersonic approximation ($M_\infty^2 \rightarrow \infty$) was applied to their theory to provide the hypersonic source flow model to calculate the operating range also shown in Fig. 20 . Experimentally it was found that the operating range calculated in this way was too pessimistic in both cold and hot flow. For instance in hot flow at $\bar{x} = 1$ the permissible sampling time was from two to three times longer than the calculated sampling time, probably because the theory overpredicts ρu at $\bar{x} = 1$. However if at this highest Reynolds number condition ($Re_{id_p} = 400$) the shock is not at the tip but rather in the aft position shown in Fig. 20 , the operating range is extended by about a factor of 3, as shown for the two calculated points. The less favorable pressure recovery for the aft shock position decreases the sampling line pressure drop and thus increases the sampling time.

APPENDIX B: TOTAL ENTHALPY PROBE CORRECTION

The total enthalpy probe correction alluded to earlier in section III.3.4 is described briefly in this appendix. Inter coolant passage heat transfer which occurs across as well as along the walls of the probe is considered by combining the one-dimensional heat conduction equation in the outer, dividing, and inner walls with the energy equation for the coolant. The heat transfer between the water and the wall is approximated by an appropriate film coefficient, temperature difference product which is valid for fully developed laminar flow in an annulus. A model for the gas side heat transfer which accounted for low Reynolds number effects in a simple way was added to complete the set of equations. The details of the computer solution which was solved on the computer are not included here. The solution sought was the response of the calorimeter, Q_c, to an input (energy/time), Q_g, from the gas for fixed outer, $\dot{m}_e$, and inner, $\dot{m}_c$, coolant passage flowrates, Reynolds number and probe (tungsten) tip temperature, which was measured with an optical pyrometer and entered as a boundary condition. Fig. 38 is typical of the solution obtained for several Q_c and one set of coolant flowrates as a function of RePr. Since the measured total enthalpy is obtained from the calorimeter energy input Q_c and measured gas flowrate $\dot{m}_g$, as $h_t = Q_c/\dot{m}_g$, the corrected total enthalpy is calculated as,

$$h_{t\,corr'd} = \frac{h_{t\,meas'd}}{Q_c/Q_g}$$

Because of the prohibitive scatter in the corrected data (Fig.34 for $\bar{x} > 1$) this model does not appear to be adequate beyond $\bar{x} = 1$. A discussion of this result and the probable errors of this correction model is given in Part I, section III.3.4.

APPENDIX C: CORRECTION FOR THE EFFECT OF FINITE SENSOR AREA AND ANGLE OF ATTACK ON THE STAGNATION POINT HEAT TRANSFER MEASUREMENTS

Measurements made with the stagnation point heat transfer probe shown in Fig. 40 were corrected for the effect of finite sensor area and angle of attack. At locations several anode radii downstream of the exit plane of the jet, negligible error is made by assuming that the free stream flow is both radial (source-like) and constant across the sensor for a given probe location.

The applicability of the stagnation point heat flux distribution given by Lees (46) for a hemisphere has already been discussed in Section III.3.5. This distribution, the ratio of local-to-stagnation point heat flux, can be written,

$$\frac{q(\bar{\theta})}{q_s} \cong 1 - C\bar{\theta}^2 \qquad (\bar{\theta}^4 \ll 1)$$

$$\text{where } C = 0.722 - \frac{0.667}{\gamma_\infty M_\infty^2} \qquad \text{(C-1)}$$

$\bar{\theta}$ is the polar angle ($\bar{x}$ the polar axis) for a coordinate system $(\bar{x},\bar{y},\bar{z})$ centered at the origin of the hemisphere; $\bar{x}$ passes through the stagnation point and the origin of the jet source and is thus inclined at angle α to the jet axis which is parallel to the x axis or probe axis.

The total heat transferred to the probe becomes,

$$Q = \int_{\theta=0}^{\theta_p} \int_{\phi=0}^{2\pi} q(\theta,\phi)\, R^2 \sin\theta d\theta d\phi \qquad \text{(C-2)}$$

where θ and ϕ are the polar and azimuthal angles corresponding to the (x,y,z) axes.

The heat flux distribution in $\bar{\theta}$, Eq. C-1, must be transformed to a function of θ and ϕ in order that the simple integration limits in Eq. C-2 be retained. The two coordinate systems are related by

$$\bar{x} = x \cos\alpha + y \sin\alpha$$

$$\bar{y} = x \sin\alpha + y \cos\alpha$$

where x and y may be eliminated by

$$x = R \cos\theta$$

$$y = R \sin\theta \cos\phi$$

to obtain, where $R = \bar{R}$,

$$\frac{\bar{x}}{\bar{R}} = \cos\theta \cos\alpha \, (1 + \cos\phi \tan\theta \tan\alpha) \qquad \text{(C-3)}$$

By noting that

$$\bar{\theta} = \tan^{-1} \frac{\sqrt{\bar{y}^2 + \bar{z}^2}}{\bar{x}}$$

and that

$$\bar{R}^2 = \bar{x}^2 + \bar{y}^2 + \bar{z}^2$$

one obtains

$$\bar{\theta} = \tan^{-1} \sqrt{\left(\frac{\bar{R}}{\bar{x}}\right)^2 - 1} \qquad \text{(C-4)}$$

By substituting Eq. C-3 into C-4 and expanding both sides, dropping terms of fourth order or higher, i.e., $\bar{\theta}^4$, θ^4, α^4, $\ll 1$, one obtains

$$\overline{\theta}^2 \cong \theta^2 + \alpha^2 - 2\alpha\theta\cos\phi \qquad \text{(C-5)}$$

Substituting this relationship into Eq. C-1 and integrating Eq. C-2 with $\sin\theta \cong \theta - \theta^3/6$, the ratio of average to stagnation point heat flux becomes

$$\frac{q_a}{q_s} = 1 - \frac{\theta_p^2}{2}\left(C + \frac{1}{6}\right) - C\alpha^2 \qquad \text{(C-6)}$$

where the average heat flux over the sensor (spherical cap of radius R_p and half angle θ_p) area is defined as

$$q_a = \frac{Q}{2\pi R_p^2 \left(\frac{\theta_p}{2}\right)^2}$$

to the same approximation ($\theta_p^4 << 1$). In this investigation $\theta_p = \frac{\pi}{6}$ rad. (30^o).

When $\gamma_\infty = \frac{5}{3}$ and $\alpha = 0$, $0.88 \leq \frac{q_a}{q_s} \leq 0.89$ for $2 \leq M_\infty \leq \infty$. The effect of angle of attack, α, on this ratio, shown in Fig. 41, is seen to be quite important as is the effect of M_∞ for large α. The corrections applied to the data were taken from Fig. 41 corresponding to $M_\infty \to \infty$.

APPENDIX D: TRANSPORT PROPERTIES OF IONIZED ARGON

One limitation on the prediction of heat transfer rates from ionized gases is the uncertainty in the values of transport properties such as viscosity, thermal conductivity and diffusion coefficient which enter the Prandtl number, Lewis number and Chapman-Rubesin (57) function ($C = \rho\mu/\rho_e\mu_e$). In Part II of this thesis (computor printout given in Ref. 58) it was shown that for temperatures above about 7,000 to 8,000°K, ($\alpha = 2.6 \times 10^{-4}$ and 1.6×10^{-3} respectively at 1 atm.), the thermally and calorically perfect gas assumptions for equilibrium argon must be modified to account for ionization effects on flow quantities. As will be seen later, the predicted effect of ionization on equilibrium transport properties becomes significant for thermal conductivity at 7,000°K or somewhat less, depending on the pressure. The purpose of this appendix is to discuss and compare the results of two current theories which were used to predict transport properties for ionized argon. These properties were used in the heat transfer predictions which are discussed in Section III.3.5.

The experimental problem of measuring transport properties directly becomes difficult at temperatures far below that for which significant ionization occurs. In this regard the NBS (59) tables provide values of viscosity from 50 to 1,500°K and thermal conductivity from 90 to 1,500°K at 1 atm, which were obtained by a correlation of experimental data from many sources for argon. Except for the viscosity measurements of Bonilla (60) from 270 to 2,070°K with a capillary efflux viscometer, and the sound absorption and speed measurements by Carneval et al. (61) between 300-8,100°K,

even the viscosity for atomic argon is not known with certainty above about 1,500°K, as shown by Back (62) at 0.1 atm. The overall trend of the viscosity data ($250 \leq T \lesssim 8,000$°K) is however predicted fairly well by the theory of Amdur and Mason (66) who calculated transport properties for rare gases and nitrogen between 1,000 and 15,000°K by the Chapman-Enskog procedure (63) using force laws from molecular beam scattering data. They considered only translational degrees of freedom and hence neglected electronic excitation and ionization for argon.

Back (62) also shows the shock tube heat transfer measurements of thermal conductivity by Smiley (64), 1,000-3,000°K, and Lauver (65), 700-8,600°K, for atomic argon. Again, the overall trend of the data is fairly well predicted by Amdur and Mason (66) from 250 to 8,000°K. Camac and Feinberg (45) used shock tube endwall heat transfer measurements behind the reflected shock for freestream temperatures ranging from 20,000 to 75,000°K to measure thermal conductivity before ionization begins. They showed good agreement, over the entire temperature range, with the 3/4 power temperature dependence of the thermal conductivity as predicted by Amdur and Mason (66) for $1,000 \leq T \leq 15,000$°K for atomic argon.

As can be seen from this brief review of transport property measurements, available data are insufficient to establish any trends of these properties at temperatures for which ionization effects are believed to be important. Thus, one must rely upon theoretical predictions for transport properties. Two of these predictions which are in current use are the Fay (38) mixture rule, which is based on

simple kinetic theory arguments, and the theory by de Voto (67), which entails the Chapman-Enskog procedure (63).

The Fay (38) mixture rule has the advantage of indicating the role of individual species contribution to the transport properties of the mixture, and of being readily amenable to calculating transport properties for cases in which a solution by the more rigorous Chapman-Enskog procedure (63) is not available, e.g., the cases of ionization nonequilibrium (frozen boundary) and unequal species temperatures (41). On the other hand, the mixture rule (38,67) has to be modified to include the Coulomb cross section when charged species are present so that the correct results are obtained in the limit of full ionization as discussed in Refs. 38, 68 and 70. Although the mixture rule, so modified, is correct in the limits of no ionization and full ionization, the values of the transport properties in the intermediate range must be used with caution. For this reason, the transport property calculations by de Voto (69) for argon are discussed next and compared later with those calculated by the Fay (38) mixture rule, which has been formulated for argon by Fay and Kemp (40) and Finson (44). In this way the validity of the approximate method (38) may be assessed for equilibrium argon.

de Voto (69) studied the rate of convergence of consecutive orders of approximation of the Chapman-Enskog procedure (63) to the transport coefficients for ionized argon. He used the fourth order approximation for thermal conductivity and thermal diffusion coefficient, and the third order for viscosity and electrical conductivity, in order to show that the third order and second order approximations,

respectively, were adequate for these quantities for equilibrium argon. Whereas the third approximation of the thermal conductivity joins smoothly to the Spitzer (33) value at 1 atm. and 15,000°K, the second order approximation is too low by more than a factor of two. The poor agreement of the second approximation with Spitzer's (33) thermal conductivity was also noted by Athye (70) who attributed this behavior to Spitzer's (33) neglect of the contribution of ion-ion interactions.

In addition, de Voto (69) calculated the transport coefficients for argon by including the next higher order terms in the charged-particle cross sections. Following an approximate method developed by Liboff (71), de Voto (69) used the Coulomb potential for close encounters and a shielded Debye potential for the more distant encounters. One of the interesting results of this procedure was that the third order approximation to the thermal conductivity (including the higher order cross section terms) is consistently higher than the Spitzer's (33) value, e.g., 3.80×10^{-3} compared to 3.05×10^{-3} cal/(cm sec °K) at 15,000°K and 1 atm.

The Fay (38) mixture rule applied to argon by Fay and Kemp (40) and Finson (44) and used here to calculate transport properties will be outlined briefly. The thermal conductivity, k, and viscosity, μ, are represented by a sum of the contributions due to each species present,

$$k = \sum_i \frac{X_i k_i}{\sum_j X_j G_{ij}} \qquad \text{(D-1)}$$

$$\mu = \sum_i \frac{X_i \mu_i}{\sum_j X_j G_{ij}} \tag{D-2}$$

where

$$G_{ij} = \left(\frac{2m_j}{m_i+m_j}\right)^{1/2} \frac{Q_{ij}}{Q_{ii}} \text{ , and} \tag{D-3}$$

X_i, k_i, μ_i, Q_{ij} and m_i are the species mole fraction, pure species thermal conductivity and viscosity, effective hard-sphere collision cross section between species i and j and the species mass respectively. In this regard, k_i and μ_i are

$$k_i = \frac{75}{64} \frac{\kappa}{Q_{ii}} \left(\frac{\pi \kappa T}{m_i}\right)^{1/2}, \tag{D-4}$$

$$\mu_i = \frac{5}{16} \frac{1}{Q_{ii}} (\pi \kappa m_i T)^{1/2} \tag{D-5}$$

and the binary diffusion coefficient, D_{ij}, is

$$D_{ij} = \frac{3}{16} \frac{1}{(n_i+n_j)} \frac{1}{Q_{ij}} \left[\frac{2\pi(m_i+m_j)}{m_i m_j} \kappa T\right]^{1/2} \tag{D-6}$$

The expressions for k_i and μ_i and the expression for D_{ij} are given in equation (10.21,1) and equations (9.81,1 and 10.22,2) respectively of Chapman and Cowling (28).

If the mixture rule is to be valid in the limiting cases of no ionization ($\alpha = 0$) and full ionization ($\alpha = 1$), then its a priori formulation must be altered. Often this amounts to altering the hard-sphere, temperature-independent collision cross sections so that k (for instance) takes on the value of atomic argon for negligible ionization and ionized argon for a fully singly-ionized gas. The details of this

procedure are given by Fay (38), Fay and Kemp (40), and Finson (44).

For the thermal conductivity of argon Fay and Kemp (40) give

$$k = \frac{k_A}{1+\left(\frac{\alpha}{1-\alpha}\right)\left(\frac{Q_{IA}}{Q_{AA}}\right)} + \frac{k_s}{1+\left(\frac{2m_E}{m_A}\right)^{1/2}\left(\frac{1-\alpha}{\alpha}\right)\left(\frac{k_s}{k_A}\right)\left(\frac{Q_{EA}}{Q_{AA}}\right)} \qquad \text{(D-7)}$$

where k_A and k_s are the thermal conductivities of atomic argon (Amdur and Mason (66)) and fully singly-ionized argon (Spitzer (33)), respectively. Since $k_i \sim (m_i)^{-1/2}$, k_I was neglected relative to k_E in the formulation of k. Use of the Lorentz (33, p. 87) conductivity for the electron gas in the mixture rule would overestimate the Spitzer (33) conductivity by about a factor of four in the limit of full ionization. Agreement with the Spitzer (33) conductivity as $\alpha \to 1$ was achieved by defining the electron thermal conductivity as

$$k_E = (1 + \sqrt{2})\, k_s \ .$$

(Note that $k_{E_{LORENTZ}} \cong 10\, k_s$ for a singly-ionized gas).

By applying the mixture rule in a similar way for the viscosity, Finson* (44) and Back (62) give

$$\mu = \frac{\mu_A}{1 + \left(\frac{\alpha}{1-\alpha}\right)\left(\frac{Q_{IA}}{Q_{AA}}\right)} + \frac{\mu_I}{1 + \left(\frac{1-\alpha}{\alpha}\right)\left(\frac{\mu_I}{\mu_A}\right)\left(\frac{Q_{IA}}{Q_{AA}}\right)} \qquad \text{(D-8)}$$

where the μ_A and μ_I refer to the atomic and ionic values of viscosity

*In the first term on the right-hand side of Eq. 3.22 of Finson (44) a factor of α has been omitted; however in subsequent equations it has been included.

for argon. Since $\mu_i \sim (m_i)^{1/2}$ the contribution of the electrons was neglected relative to the heavy species. By introducing a constant species Prandtl number, $Pr_i = 2/3$, Eq. D-8 can be rewritten in terms of species thermal conductivity rather than species viscosity as

$$\mu = \frac{4}{15}\,\frac{m_A}{\kappa}\left[\frac{(1-\alpha)k_A}{(1-\alpha)+\frac{Q_{AI}}{Q_{AA}}\alpha} + \frac{\alpha k_s(1+\sqrt{2})\left(\frac{m_E}{m_I}\right)^{1/2}}{(1-\alpha)\frac{Q_{IA}}{Q_{AA}}\left(\frac{m_E}{m_I}\right)^{1/2}(1+\sqrt{2})\frac{k_s}{k_A}+\alpha}\right] \tag{D-9}$$

The calculations of Amdur and Mason (66) for the thermal conductivity for atomic argon was approximated by a power law as

$$k_A = 5.8 \times 10^{-7}\, T^{3/4}\ \frac{cal}{cm.sec^{o}K} \tag{D-10}$$

The thermal conductivity of a fully singly-ionized gas is given by Spitzer (33, pp. 87-88) as

$$k_s = \frac{4.4 \times 10^{-13} T^{5/2}}{\ell n\,\Lambda}\ \frac{cal}{cm\ sec^{o}K} \tag{D-11}$$

where Λ is the ratio of the Debye distance to the impact parameter for a 90° deflection of an electron-ion encounter given by Spitzer (33, p. 18) as

$$\Lambda = \frac{3}{2}\left[\frac{(\kappa T)^3}{\pi n_E e^6}\right]^{1/2} = \frac{1.24 \times 10^4 T^{3/2}}{n_E^{1/2}} \tag{D-12}$$

where T is in ^{o}K and n_E is in cm^{-3}. For low temperature and high electron density, the Debye distance is less than the average electron spacing, $n_E^{1/3}$, and should be replaced by the latter in determining Λ(40, p. 664), giving

$$\Lambda' = \frac{3\kappa T}{\epsilon^2 n_E^{1/3}} = \frac{1800T}{n_E^{1/3}}$$

which should be used as long as $\Lambda' \leq 12\pi$. For all the calculations made here using the mixture rule, the Debye length was greater than $n_E^{1/3}$, so that Λ rather than Λ' was used in Eq. D-11 for thermal conductivity.

Fay and Kemp (40) approximate the cross section ratios over the temperature range of interest by

$$\frac{Q_{AE}}{Q_{AA}} = 1.5 \times 10^{-2}$$

and (D-13)

$$\frac{Q_{AI}}{Q_{AA}} = 1.44T^{0.16}$$

where T is in ^{o}K.

The Prandtl number was calculated as

$$Pr = \frac{c_{pA}(1+\alpha)\mu}{k} \qquad \text{(D-14)}$$

where k and μ are given by Eqs. D-7 and D-9 respectively.

Consideration of the momentum equation for a quiescent gas, in which binary diffusion of atoms and ion-electron pairs takes place, is given by Fay and Kemp (40) to define the ambipolar diffusion coefficient as

$$D_{amb} = \frac{2}{1+\alpha} D_{AI} \qquad \text{(D-15)}$$

where D_{AI} is the atom-ion diffusion coefficient. The Lewis number,

based on the ambipolar diffusion coefficient, is

$$Le = \frac{\rho c_{pA}(1+\alpha)D_{amb}}{k} \qquad (D\text{-}16)$$

By substituting Eq. D-15, with D_{AI} taken from Eq. (D-6), into Eq. D-16 the Lewis number becomes,

$$Le = \frac{8}{5}\,\frac{\frac{k_A}{k}}{\frac{Q_{AI}}{Q_{AA}}} \quad , \qquad (D\text{-}17)$$

where k, k_A and Q_{AI}/Q_{AA} are given in Eqs. D-7, D-10 and D-13 respectively.

For equilibrium conditions the ion mass fraction, α, was obtained from Arave (72) and Part II of this thesis up to about 16,000°K and from Cann and Ducati (73), Baum and Cann (25), and Drellishak, et al. (74,75), at higher temperatures.

In Figs. 44, 45, 46 and 47 thermal conductivity, viscosity, Prandtl number and Lewis number, calculated from the Fay (38) mixture rule, and obtained from de Voto (76)*, are shown as a function of temperature for pressures ranging in atmospheres from 10^{-4} to 1.0 atm. and 10^{-2} to 1.0 atm. for each model respectively. These transport properties are also tabulated in Tables D.1 and D.2. Although the first and second ionization potentials for argon are separated by about 12 electron volts, incipient double ionization occurs

* de Voto calculated these transport properties as outlined in Ref. 77, with the exception that here he included the next higher order terms (terms of order unity) in the charged particle cross sections.

before all atoms are first singly-ionized, so that in fact the fully singly-ionized gas is hypothetical in this case. In this regard, the transport properties calculated from the Fay (38) mixture rule were terminated somewhat arbitrarily at that temperature, for a given pressure, at which the electron number density, n_E, was equal to the combined number density of the "heavy" species or nuclei, i.e., $n_E = n_A + n_I + n_{II}$, as determined from the thermodynamic calculations of Baum and Cann (25). Since $n_E = n_I + 2n_{II}$, this cutoff may also be written as $n_A = n_{II}$. The terminal points of the curves correspond to an ion mass fraction, α, ranging from 0.991 at 13,000°K and 10^{-4} atm. to 0.964 at 20,000°K and 1 atm.

For purposes of convenience, the transport properties calculated by means of the Fay (38) mixture rule and those obtained from de Voto (76), calculated by the Chapman-Enskog procedure (63,68), will be denoted as $(\ )_{Fay}$ and $(\ )_{de\ Voto}$ respectively.

For reference purposes the thermal conductivity of atomic argon (66) given here as Eq. D-10 was included in Fig. 44. Two effects of ionization on thermal conductivity are related to the Coulomb cross section of the ionized species. Initially, for small degrees of ionization at low temperature, k decreases as T increases because of the increasing importance of the electron-ion (Coulomb) cross section which is much larger than the electron-atom cross section. This effect is especially noticeable at the lowest pressures where the $T^{3/4}$ dependence of k_A is completely obliterated. At somewhat higher degree of ionization the inverse square temperature dependence of the Coulomb cross section gradually changes the

temperature dependence of k to $T^{5/2}$, which is necessary to match the Spitzer (33) thermal conductivity for a fully-ionized gas. The degree of ionization, α, at which these effects occur is shown along with k_{Fay} and $K_{de\ Voto}$ in tabular form in Table D.1. The least favorable comparison of k_{Fay} to $k_{de\ Voto}$ occurs at the lowest temperature shown (6,000°K), where $k_{de\ Voto}$ and k_A are in agreement but k_{Fay} is about 15 to 20% high. It can be shown as the results indicate in the table below, that even before the gas is "fully singly-ionized", k_{Fay} may be quite close to $k_{Spitzer}$. Conditions for which $0.95 \leq k_{Fay}/k_{Spitzer} \leq 1.0$:

p atm	T °K	α
10^{-4}	10,000	.90
10^{-3}	11,000	0.86
10^{-2}	12,000	0.76
10^{-1}	13,000	0.60
1	14,000	0.39

The values of $k_{de\ Voto}$ (76) shown in Fig. 44 correspond to the de Voto calculations which included the next higher order terms in the charge-particle cross sections, so that $k_{de\ Voto}$ lies above $k_{Spitzer}$ (and hence k_{Fay}) by about 15 to 20% in the limit of a fully singly-ionized gas, as discussed previously. However, de Voto shows (69, Figs. 13 and 15) that k calculated to third order in the conventional manner, without the higher order terms in the cross sections, agrees with $k_{Spitzer}$ as $\alpha \to 1$.

The variation of viscosity with temperature and pressure for argon is shown in Fig. 45 for the same range of pressure and temperature and for the two transport property models discussed before for thermal conductivity. The initial rise of μ at low temperature and high pressure is in good agreement with the $T^{3/4}$ dependence of μ_A calculated by Amdur and Mason (66) and approximated by a power law as $\mu = 3.1 \times 10^{-6} T^{3/4}$ gm/(cm sec) with T in ^{o}K. The subsequent decrease of μ can be visualized by considering μ to vary inversely with some effective collision cross section which is Q_{AA} initially and Q_{II} finally where $Q_{AA} < Q_{IA} < Q_{II}$. The initial decrease in μ for $\alpha = 10^{-3} - 10^{-2}$ is caused by the increasing number of atom-ion collisions for which $Q_{IA}/Q_{AA} \cong 5$ (Eq. D-13) at 6,000^{o}K. The value of μ continues to decrease rapidly at higher temperature where more ions are present so that the still larger ion-ion or Coulomb cross section becomes important. Then as the gas becomes nearly fully singly-ionized and Coulomb encounters dominate, the inverse-square temperature dependence of Q_{II} causes μ to rise rapidly as $T^{5/2}$.

Except for the conditions at 1 atm. where μ_{Fay} is as much as 25% below $\mu_{de\ Voto}$, the agreement between these theories is good. That only the second approximation for $\mu_{de\ Voto}$ was required may be the reason for the somewhat better agreement between the viscosities than for the thermal conductivities shown in Fig. 44.

The Prandtl number variation with temperature and pressure is shown in Fig. 46. Pr decreases rapidly from about 2/3 to 0.0085 as α varies from 0 to 1. This decrease is caused by the joint rapid

decrease of μ and increase of k caused by the ionization effects already mentioned. At 6,000°K Pr_{Fay} is low by about 30%. This discrepancy is caused primarily by the over estimation of k by k_{Fay} as discussed earlier. For $\alpha \cong 1$, and 0.01 atm., $Pr_{Fay} \cong$ 0.011 whereas $Pr_{de\ Voto} \cong .0085$.

The variation of Lewis number, $\rho Dam\ c_{p_A}(1+\alpha)/k$, with temperature and pressure is shown in Fig. 47. Because of rapid increase of thermal conductivity with temperature the Lewis number decreases from about 0.5 at room temperature to about 3.5×10^{-2} at 20,000°K and 1 atm. Le_{Fay} varies from a value about 30% low at 6,000°K to about 30% high at 20,000°K. Since the ambipolar diffusion coefficient, D_{amb}, increases with temperature and varies inversely with pressure (Eqs. D-6 and D-15) Le decreases less rapidly than Pr and exhibits an inverted pressure dependence compared to Pr.

Comparisons made between the transport properties calculated from the Fay (38) mixture rule and the Chapman-Enskog procedure (63) used by de Voto (69) show that the mixture rule predicts the trends in the transport properties for argon caused by the effects of ionization quite well. With certain exceptions, the mixture rule generally predicts the transport properties to within 15 or 20%. On the basis of this fair agreement with the more rigorous theory for the equilibrium transport properties, the mixture rule was used in Section III.3.5 for those cases for which chemical non equilibrium was present (frozen boundary layer edge conditions).

The variation of electrical conductivity, σ, with temperature and pressure is shown in Fig. 48. In Part II, σ was calculated by

using the theory of Lin, et al. (78) (shown as points in Fig. D.5) who suggest a parallel conductance approximation, $\frac{1}{\sigma} = \frac{1}{\sigma_c} + \frac{1}{\sigma_s}$ which combines the conductivity, σ_c, for a slightly ionized gas which is governed by close range electron-atom encounters, with the Spitzer (33) conductivity, σ_s, which is valid for the fully-ionized gas. The curves represent the third approximation to σ by the Chapman-Enskog procedure (63) calculated by de Voto (69) in which the higher order terms in the charged particle collision cross sections have been ignored. When these higher order terms are retained, σ can be as much as about 10% higher as shown in Fig. 12 of de Voto (69) at 1 and 100 mm Hg for $5,000 \leq T \leq 20,000^{\circ}K$. The theory of Lin et al. (78) is in good agreement with de Voto (69) for the higher temperatures but is as much as a factor of 3 too high at $6,000^{\circ}K$ and 0.1 atm. As pointed out by de Voto (69, p. 46), the mean free path conductivity, σ_c, is essentially related to the first approximation to the electron-ion diffusion coefficient for which he shows that the fourth approximation is required at lower temperatures.

TABLE D.1

Variation of Transport Properties with Temperature at 1.0 atm for Argon Calculated by Fay Mixture Rule Outlined in Appendix D

$T \times 10^{-3}$ ^{o}K	α	k $\frac{cal}{cm\ sec\ ^{o}K}$	μ $\frac{gm}{cm\ sec}$	Pr	Le
6	2.388-5*	0.4670-3	2.121-3	0.5651	0.2339
7	2.572-4	0.6898-3	2.378-3	0.4288	0.1735
8	1.564-3	0.9278-3	2.608-3	0.3503	0.1411
9	6.478-3	1.185-3	2.767-3	0.2924	0.1171
10	2.048-2	1.461-3	2.765-3	0.2404	0.1011
11	5.305-2	1.739-3	2.482-3	0.1869	0.0898
12	1.179-1	2.027-3	1.951-3	0.1339	0.0812
13	2.299-1	2.410-3	1.341-3	0.8514-1	0.0715
14	3.942-1	2.710-3	8.339-4	0.5336-1	0.0664
15	5.862-1	3.126-3	5.145-4	0.3247-1	0.0600
16	7.543-1**	3.578-3	3.427-4	0.2090-1	0.0545
17	0.8950	4.060.3	2.446-4	0.1420-1	0.0497
18	0.9417	4.564-3	2.328-4	0.1232-1	0.0457
19	0.9619	5.090-3	2.415-4	0.1158-1	0.0424
20	0.9635	5.659-3	2.649-4	0.1144-1	0.0393

---

* $2.388\text{-}5 = 2.388 \times 10^{-5}$

** For $\alpha \leq \alpha^{**}$, α from Ref.

For $\alpha > \alpha^{**}$, α from Ref.

TABLE D.1

Variation of Transport Properties with Temperature at 10^{-1} atm for Argon Calculated by Fay Mixture Rule as Outlined in Appendix D

$T \times 10^{-3}$ ^{o}K	α	k $\frac{cal}{cm\ sec\ ^{o}K}$	μ $\frac{gm}{cm\ sec}$	Pr	Le
6	7.553-5	0.5093-3	2.121-3	0.5182	0.214
7	8.133-4	0.6979-3	2.370-3	0.4228	0.171
8	4.945-3	0.8889-3	2.557-3	0.3595	0.146
9	2.048-2	1.081-3	2.554-3	0.3001	0.128
10	6.463-2	1.247-3	2.187-3	0.2322	0.118
11	1.657-1	1.395-3	1.507-3	0.1566	0.112
12	3.514-1	1.579-3	8.425-4	0.08968	0.104
13	0.5984	1.822-3	4.203-4	0.04586	0.0946
14	0.8049	2.112-3	2.266-4	0.02409	0.0852
15	0.9163	2.440-3	1.581-4	0.01545	0.0768
16	0.9642	2.794-3	1.416-4	0.01238	0.0697
17	0.9792	3.174-3	1.482-4	0.01150	0.0636
18	0.9721	3.579-3	1.706-4	0.01169	0.0583

TABLE D.1

Variation of Transport Properties with Temperature at 10^{-2} atm for Argon Calculated by Fay Mixture Rule as Outlined in Appendix D

$T \times 10^{-3}$ ^{o}K	α	k $\frac{cal}{cm\ sec\ ^{o}K}$	μ $\frac{gm}{cm\ sec}$	Pr	Le
6	2.388.4	0.5194-3	2.118-3	0.5073	0.210
7	2.572-3	0.6826-3	2.347-3	0.4288	0.175
8	1.564-2	0.8276-3	2.406-3	0.3672	0.156
9	6.465-2	0.9244-3	2.028-3	0.2905	0.150
10	0.2007	0.9762-3	1.233-3	0.1887	0.151
11	0.4692	1.0691-3	5.411-4	0.09252	0.145
12	0.7648	1.238-3	2.118-4	0.03755	0.133
13	0.9114	1.458-3	1.162-4	0.01895	0.118
14	0.9739	1.707-3	8.811-5	0.01268	0.105
15	0.9906	1.982-3	8.983-5	0.01122	0.0945
16	0.9962	2.281-3	9.911-5	0.01079	0.0854

TABLE D.1

Variation of Transport Properties with Temperature at 10^{-3} atm for Argon Calculated by Fay Mixture Rule as Outlined in Appendix D

$T \times 10^{-3}$ ^{o}K	α	k $\frac{cal}{cm\ sec\ ^{o}K}$	μ $\frac{gm}{cm\ sec}$	Pr	Le
6	7.553-4	0.5301-3	2.113-3	0.4963	0.206
7	8.133-3	0.6533-3	2.274-3	0.4366	0.183
8	4.939-2	0.7229-3	2.011-3	0.3630	0.119
9	0.2007	0.7073-3	1.145-3	0.2419	0.196
10	0.5436	0.7315-3	3.935-4	0.1033	0.202
11	0.8593	0.8504-3	1.185-4	0.03223	0.184
12	0.9663	1.019-3	6.208-5	0.01490	0.161
13	0.9912	1.215-3	5.656-5	0.01153	0.142
14	0.9973	1.431-3	6.225-5	0.01081	0.126

TABLE D.1

Variation of Transport Properties with Temperature at 10^{-4} atm for Argon Calculated by Fay Mixture Rule as Outlined in Appendix D

$T \times 10^{-3}$ ^{o}K	α	k $\frac{cal}{cm\ sec\ ^{o}K}$	μ $\frac{gm}{cm\ sec}$	Pr	Le
6	2.388-3	0.5212-3	2.094-3	0.5010	0.210
7	2.571-2	0.5985-3	2.064-3	0.4401	0.200
8	0.1545	0.5548-3	1.260-3	0.3261	0.233
9	0.5437	0.5104-3	3.621-4	0.1362	0.272
10	0.8986	0.5866-3	7.920-5	0.03190	0.252
11	0.9827	0.7174-3	3.950-5	0.01358	0.218
12	0.9965	0.8709-3	3.883-5	0.01107	0.189

TABLE D.2

Variation of Transport Properties with Temperature

at 1.0 atm for Argon Calculated by de Voto (75)

$T \times 10^{-3}$ ^{o}K	α	$k \times 10^{3}$ $\frac{cal}{cm\ sec\ ^{o}K}$	$\mu \times 10^{4}$ $\frac{gm}{cm\ sec}$	Pr	Le	σ $\frac{mhos}{cm}$
3	2.330-12	0.2437	13.0	0.6635	0.307	4.79-7
4	6.937-9	0.2962	15.8	0.6637	0.302	9.91-4
5	8.978-7	0.3440	18.4	0.6654	0.298	8.12-2
6	2.398-5	0.3966	20.8	0.6525	0.290	.867
7	2.595-4	0.4778	23.1	0.6015	0.264	3.77
8	1.584-3	0.6307	25.2	0.4979	0.217	10.1
9	6.598-3	0.8911	27.1	0.3808	0.166	19.2
10	2.099-2	1.249	28.1	0.2857	0.126	29.8
11	5.469-2	1.677	27.1	0.2120	0.0994	41.3
12	0.1221	2.14	23.1	0.1507	0.0822	53.2
13	0.2382	2.65	16.8	0.9762-1	0.0697	64.9
14	0.4061	3.20	10.8	0.5903-1	0.0607	75.8
15	0.5971	3.80	6.64	0.3471-1	0.0533	85.2
16	0.7454	4.40	4.50	0.2220-1	0.0478	92.9
17	0.8596	4.99	3.25	0.1507-1	0.0438	99.8
18	0.9182	5.61	2.81	0.1195-1	0.0403	106.
19	0.9466	6.24	2.72	0.1056-1	0.0375	112.
20	0.9662	6.90	2.73	0.9678-2	0.0350	117.
25	0.9865	10.70	3.79	0.8752-2	0.0260	146.

TABLE D.2

Variation of Transport Properties with Temperature at 0.1 atm for Argon Calculated by de Voto (75)

$T\times10^3$ °K	α	$k\times10^3$ $\frac{cal}{cm\ sec\ ^oK}$	$\mu\times10^4$ $\frac{gm}{cm\ sec}$	Pr	Le	σ $\frac{mhos}{cm}$
3	7.368-12	0.2437	13.0	0.6635	0.307	1.52-6
4	2.193-8	0.2962	15.8	0.6637	0.302	3.12-3
5	2.840-6	0.3440	18.4	0.6654	0.298	.210
6	7.585-5	0.4061	20.8	0.6373	0.283	1.72
7	8.184-4	0.5184	23.0	0.5525	0.244	6.53
8	4.988-3	0.7215	25.1	0.4349	0.190	14.0
9	2.073-2	0.9914	26.0	0.3331	0.149	22.4
10	5.728-2	1.261	23.9	0.2492	0.123	31.0
11	1.685-1	1.51	17.6	0.1695	0.111	39.5
12	0.3566	1.78	10.2	0.9674-1	0.0990	47.5
13	0.6028	2.12	5.10	0.4797-1	0.0872	54.6
14	0.7992	2.48	2.72	0.2454-1	0.0781	60.4
15	0.9087	2.87	1.79	0.1480-1	0.0705	65.5
16	0.9561	3.30	1.50	0.1106-1	0.0638	70.4
17	0.9762	3.73	1.47	0.9686-2	0.0585	75.1
18	0.9839	4.18	1.56	0.9210-2	0.0541	79.8
19	0.9887	4.68	1.68	0.8880-2	0.0501	84.6
20	0.9908	5.21	1.84	0.8748-2	0.0464	89.4
25	0.9946	8.31	2.84	0.8475-2	0.0335	114.

TABLE D.2

Variation of Transport Properties with Temperature at 0.01 atm for Argon Calculated by de Voto (76)

$T \times 10^{-3}$ °K	α	$k \times 10^{3}$ $\frac{cal}{cm\ sec\ ^{o}K}$	$\mu \times 10^{4}$ $\frac{gm}{cm\ sec}$	Pr	Le	σ $\frac{mhos}{cm}$
3	2.330-11	0.2437	13.0	0.6635	0.307	4.79-6
4	6.937-8	0.2962	15.8	0.6637	0.302	9.69-3
5	8.978-6	0.3464	18.4	0.6608	0.296	0.456
6	2.398-4	0.423	20.8	0.6118	0.272	3.23
7	2.581-3	0.573	23.0	0.5005	0.221	9.22
8	1.574-2	0.776	24.2	0.3942	0.177	16.0
9	6.516-2	0.944	21.8	0.3059	0.155	22.6
10	0.2023	1.044	14.0	0.2006	0.150	29.0
11	0.4719	1.19	6.32	0.9723-1	0.140	34.8
12	0.7646	1.41	2.43	0.3783-1	0.125	39.8
13	0.9171	1.67	1.19	0.1699-1	0.111	44.0
14	0.9688	1.95	0.892	0.1121-1	0.0997	47.9
15	0.9854	2.26	0.869	0.9496-2	0.0893	51.8
16	0.9913	2.60	0.935	0.8908-2	0.0810	55.8
17	0.9940	2.96	1.04	0.8716-2	0.0737	59.8
18	0.9951	3.34	1.15	0.8545-2	0.0678	63.8
19	0.9954	3.75	1.29	0.8539-2	0.0625	67.9
20	0.9962	4.18	1.43	0.8495-2	0.0579	72.1
25	0.9980	6.81	2.27	0.8288-2	0.0409	93.8

APPENDIX E

IMPACT PRESSURE PROBE CORRECTIONS

Potentially the three mode important corrections to the impact pressure measurements are those caused by probe displacement, low Reynolds number effects, and thermal transpiration. Based upon the results for un-ionized flows, these corrections, except for isolated conditions, are estimated to be within the scatter of the measurements and thus, except for the effect of probe displacement at $x/D_* = 1$ in cold flow, no corrections were applied to the impact pressure measurements.

In a supersonic flow field which has a strong Mach number gradient, the free stream Mach number, M_∞, (and hence the impact pressure) may vary significantly over the shock wave standoff distance. The measured impact pressure corresponds to M_∞ at the shock position and not the probe position. In the present case of an accelerating flow the measured value of p_i is too large and the Mach number deduced therefrom must be corrected (increased) approximately as

$$M_p = M_s + \Delta \left|\frac{dM}{dx}\right|$$

$$= M_s \underbrace{\left(1 + \frac{\Delta}{M_s} \left|\frac{dM}{dx}\right|\right)}_{N}$$

where M_p, M_s and Δ are the Mach number at the probe tip location in the undisturbed stream, the shock Mach number, and the shock standoff distance respectively. In cold flow Δ was calculated from

the flat nosed axisymmetric body formula* for inviscid flow, $\frac{\Delta}{R_b} \cong .43$ for $\epsilon = 0.1$, for constant free stream Mach number given by Hayes and Probstein (79, p. 201) and $\frac{1}{M}\left|\frac{dM}{dx}\right|$ was estimated from Ashkenas and Sherman's (8) Mach number distribution. For example, $\frac{1}{M}\frac{dM}{dx} \cong .6/\text{cm}$ at $x/D_* = 1$ where $M = 2.4$. For the $D_p = 0.335$ in. dia. at $x/D_* = 1$ $N \cong 0.1$ and a 10% correction to M_p was made. Generally for the smaller probe tips, $D_p \leq 0.15$ in., $N \leq 0.03$ at $x/D_* = 1$, and for $x/D_* > 2$, $N \leq .01$ so that the correction to M_p would be about 1% and was therefore neglected for all impact pressure measurements.

In hot flow for large x/D_*, prediction of Δ is very difficult because of the dependence of Δ on the interaction between the shock-wave and the merged viscous layer and possible rarefaction effects. Bailey and Sims (80) have measured shock detachment distances for spheres and flat-nosed bodies in heated argon ($T_t \leq 4020^\circ K$, $25 \lesssim Re_{2D_b} \lesssim 200$, $4 \lesssim M_\infty \lesssim 9$). A value of $Re_{2D_b} \cong 40$, where Δ/R_b rises rapidly (Fig. 3 (80)) with decreasing Reynolds number, corresponds to $x/D_* \cong 4$-5 in the free jet, where $dM/dx \cong 1/2$ per cm or about one-third the value at $x/D_* \cong 1$. For this reason and the fact that the small tips ($D_p \cong .15$ in.) were used in hot flow, no correction to p_i was made.

The second correction deals with the well-known problem of interpretation of impact pressure measurements in low density gas flows, and has received renewed attention with the use of arc-heated

---

* Potter and Bailey (51) have shown experimentally, at one Reynolds number ($Re_{2r_p} \cong 10^6$), that Δ is unaffected by orifice-to-body diameter ratio between 0 and .85 for flat nosed bodies.

low density wind tunnels. In particular the recent work by Potter and Bailey (51, 81) who considered argon and helium besides nitrogen, and others (82, 83, 84) has been helpful in clarifying the role of γ, heat transfer and probe nose geometry on these measurements. Potter and Bailey's (51, 81) range of conditions for argon and helium is $5 \lesssim Re_{2r_p}\sqrt{\rho_2/\rho_\infty} \lesssim 1000$, $4 \lesssim M_\infty \lesssim 16$, $0.1 \leq \frac{T_w}{T_{aw}} \leq 1.0$, $1 \lesssim \frac{\lambda_\infty}{D_p} \lesssim 10^{-4}$, $270 \lesssim Re_\infty \lesssim 50{,}000\ (in)^{-1}$ and $300 \leq T_t \leq 4{,}260^\circ K$. The experimental work with air by Ashkenas (85) (discussed later on), Matthews (86) and Sherman (87) using flat-nosed, externally chamfered, and internally chamfered and source-shaped probes respectively should be mentioned. In this regard it should also be mentioned that the possibility of delaying viscous effects somewhat in cold flow for argon as compared with air appears attractive because of the γ effect on the Re_∞-M_∞ variation shown in Fig. 49 . The asymptotic limit of Re_∞ for large M_∞ is less than 30% below $Re_{\infty max}$ which occurs at $M_\infty \cong 2$, whereas $Re_\infty \to \frac{1}{M_\infty^2} \to 0$ for air. Because of the 5/2 power dependence of viscosity on temperature for a fully singly ionized monatomic gas it can be shown that Re_∞ increases with M_∞, i.e., $Re_\infty \sim M_\infty^2$ for $M_\infty \gg 1$. Since, however, in each case $Re_2 \to 0$, as $\frac{1}{M_\infty^3}$ for argon and as $\frac{1}{M_\infty^5}$ for air, as $M_\infty \to \infty$, viscous effects must become important eventually.

Before discussing some of the results of Potter and Bailey's (51, 81) investigation, it is helpful to recall the variation of measured-to-inviscid impact pressure ratio, $(p_i)_m/(p_i)_I$ with, say, free stream Reynolds number, Re_∞, shown for Ashkenas' (85) air data in Fig. 50 . $(p_i)_I$ is obtained from the Rayleigh supersonic Pitot formula.

In addition to those quantities already mentioned, $(p_i)_m/(p_i)_I$ depends also on the gas temperature in the pressure gauge volume and the length-to-diameter ratio of the impact tube as free molecule flow is attained (88). In fact in that regime the pertinent pressure ratio is p_g/p_∞ where p_g is the pressure in the gauge volume. An explanation of the overall variation of $(p_i)_m/(p_i)_I$ vs. Re_∞ is attempted by Daum, Shang, and Elliott (83,84) and Bailey and Potter ((37), Fig. 16) who use the flow regimes as defined by Hayes and Probstein (79). Briefly, the initial decrease in pressure ratio with decreasing Re_∞ is due to vorticity interaction and viscous effects accompanying the merging of boundary layer and shock wave into a viscous layer region. Subsequently the increase in pressure ratio is caused by rarefaction effects on the shock wave.

As suggested by the analysis of Matthews (86), (Bailey and Potter (51,81)) use is made of $Re_{2rp}\sqrt{\rho_2/\rho_\infty}$ to correlate $(p_i)_m/(p_i)_I$, instead of Re_∞ or Re_2, in an attempt to account for the variation in the data with the free stream Mach number. For convenience in assessing the viscous correction as a function of the variables mentioned earlier, the location and value of the minimum in pressure ratio, denoted as

$$\left[Re_{2rp}\sqrt{\frac{\rho_2}{\rho_\infty}}\right]_{min.} \qquad \text{and} \qquad \left[\frac{(p_i)_m}{(p_i)_I}\right]_{min.},$$

and the location of the unity pressure ratio, denoted as

$$\left[Re_{2rp}\sqrt{\frac{\rho_2}{\rho_\infty}}\right]_{unity}$$

are shown in table E.1 for some data for the flat nosed, externally chamfered, and hemispherical nosed probes taken from Ashkenas (85), and Potter and Bailey (51,81). Much more data than are included in table E.1 are given in Ref. 51. Acting as kind of a "bench mark", it is noted that the data of Ashkenas (85), shown in Fig. 50 here, and Potter and Bailey (51,81) agree for the externally chamfered probes under similar conditions for $\gamma = 1.40$. Further it is seen that the externally chamfered and flat-nosed probes are in good agreement for $T_{pw} = T_{aw}$ and $\gamma = 1.40$ and that the viscous effects occur at much higher Reynolds numbers for the hemispherical nosed probe under similar conditions, as was shown by Sherman (87) for air in which he compared internally chamfered and source-like probes. Finally for flat nosed probes used in argon and helium, the minimum in $(p_i)_m/(p_i)_I$ is about 2% less than that for diatomic gases, and the effect of the cooled probe moves the unity pressure ratio to a higher Reynolds number, which is quite close to the result for the probes at the adiabatic wall temperature in N_2 and air. A further study of the data (81) shows that the inviscid limit for which $(p_i)_m/(p_i)_I = 1$, appears to have occurred for $Re_{2r_p}\sqrt{\rho_2/\rho_\infty} \cong 1000\text{-}2000$ for all gases and probe geometries. No data for monatomic gases exist for $Re_{2r_p}\sqrt{\rho_2/\rho_\infty} \lesssim 5$. As an example of what happens in this low Reynolds number region the data of Ashkenas (85) for air are shown in Fig. 50. The pressure ratio rises rapidly to over 3 in some instances for $Re_{2r_p}\sqrt{\rho_2/\rho_\infty} \cong 0.1\text{-}0.25$ where Reynolds number is no longer the significant variable when rarefied gas effects become dominant. Bailey and Potter (81) point out that variations of

$(p_i)_m/(p_i)_I$ caused by γ and wall cooling effects are less than 3% for a given nose shape at a given Reynolds number.

At present no impact probe calibrations are available which might explain the effect of appreciable ionization, high probe wall cooling, $T_w/T_t \simeq .01$, and viscous effects on $(p_i)_m$ in this same Reynolds number range. In addition the effect of large probe potential, relative to its floating value (electric field effects), on $(p_i)_m/(p_i)_I$ is not known but is almost certain to play an important role.

For the present investigation in cold flow the corrections to $(p_i)_m$ were no greater than about 2%, or within the scatter of the data, so that no correction was applied. In hot flow, $1 \lesssim Re_{2r_p}\sqrt{\frac{\rho_2}{\rho_\infty}} < 100$ and ρ_2/ρ_∞ was taken as $\gamma+1/\gamma-1 = 4$. The effect of relaxation of electronically excited states and recombination tends to increase ρ_2/ρ_∞ so that the Reynolds number shown should provide a lower bound. A 20^o externally chamfered carbon or tungsten tip (see Fig. 5) which had a body-to-tip diameter ratio of 5 was used in hot flow. Down to about a $Re_{2r_p}\sqrt{\rho_2/\rho_\infty}$ of 10, the lower limit to the cooled probe data for argon, $.96 \lesssim (p_i)_m/(p_i)_I \leq 1$. For lower Reynolds numbers, the data of Ashkenas (85) and several data points from Enkenhus (88) shown in Fig. 50 provide an estimate of $(p_i)_I/(p_i)_I$ which ranges from about 1.1 to 1.7 as $Re_{2r_p}\sqrt{\rho_2/\rho_\infty}$ ranges from 65 to 1. As pointed out in Section III.3 a probe tip having 3 times the normal impact pressure probe tip was used to check the change in $(p_i)_m$ over the range of conditions of this investigation. Both probes yielded the same results within the scatter of the hot flow data, which is

about 10%. In particular for the lowest Reynolds number, a factor of three in Reynolds number should produce a variation in $(p_i)_m$ of 30%. It was concluded on this basis and the fact that the determination of h_{tf} from the ρu and p_i measurements seems consistent, that the corrections to $(p_i)_m$ are less than 10% and thus should be neglected because no theory or calibration for the actual flow case is available. That Ashkenas' data shown in Fig. 50 do not seem to provide good estimates of $(p_i)_m/(p_i)_I$ in that region should perhaps not be surprising for any number of reasons already mentioned.*

The last correction to be considered for $(p_i)_m$ is due to the effect of thermal transpiration. Arney and Bailey (89,90) have given the ratio of pressures, p_c/p_h, between the cold and hot end of the impact tube, as a function of Knudsen number, Kn_c, at the cold end, and tube temperature ratio, T_c/T_h. For the most adverse conditions

---

*On the other hand, if the "correct" probe Reynolds number, Re_p, upon which the viscous correction depends, should instead be based on some intermediate or reference temperature, T_r, between the boundary layer edge and wall temperature, the Reynolds number used here, Re_i, would have to be increased as,

$$Re_p = \left[\frac{T_{tf}}{T_r}\right]^{5/2} Re_i$$

for the frozen flow fully ionized gas boundary layer. If T_r were the arithmetic mean temperature between the edge of the boundary layer and the wall,

$$Re_p \cong 6\, Re_i$$

and $(p_i)_m/(p_i)_I$ would decrease from 1.5 to 1 for the lowest Reynolds number, encountered here, $Re_{ir_p} \cong 1$. This result supports the observation made earlier that the viscous correction to impact pressure measurements is within the scatter of the data.

of this investigation, $Kn_c \leq 0.01$ and $T_c/T_h \leq \frac{1}{4}$, $1.0 > p_c/p_h > 0.98$. (A similar calculation made from the data of Howard (91) gives $1.0 > p_c/p_h > 0.99$.) The corrections to $(p_i)_m$, due to thermal transformation, are less than 2% and have been neglected.

TABLE E.1 Impact Pressure Probe Correction Data

Ref.	γ	Gas	Probe type	$\frac{(p_i)_m}{(p_i)_I}$ min.	$\left(Re_{2r_p}\sqrt{\frac{\rho_2}{\rho_\infty}}\right)_{min.}$	$\left(Re_{2r_p}\sqrt{\frac{\rho_2}{\rho_\infty}}\right)_{unity}$
Ashkenas (85) $T_{pw} = T_{aw}$ $2 \leq M_\infty \leq 7$ [also Fig. 6, Bailey and Potter (51)]	1.40	air	Externally chamfered	.98	30	14
Bailey and Potter (51) [Fig.8] $T_{pw} = T_{aw}$ $3.8 \leq M_\infty \leq 5.6$	1.40	N_2	Externally chamfered	.98	28	15
ibid Fig. 3 $3.9 < M_\infty < 6.0$ $T_{pw} = T_{aw}$	1.40	N_2	Flat-nosed probe	.98	32	12
ibid Fig. 10 $T_{pw} = T_{aw}$ $4.4 < M_\infty < 4.7$	1.40	N_2	"Incomplete" Hemispherical-nosed probe	.98	150	50
ibid Fig. 7 $T_{pw} = T_{aw}$	1.67	argon and helium	Flat-nosed probes	.96	24	5

TABLE E.1 (continued)

Ref.	γ	Gas	Probe type	$\frac{(p_i)_m}{(p_i)_I}_{min.}$	$\left(Re_{2r_p}\sqrt{\frac{p_2}{p_\infty}}\right)_{min.}$	$\left(Re_{2r_p}\sqrt{\frac{p_2}{p_\infty}}\right)_{unity}$
ibid Figs. 13 and 15 $T_{wp} = 0.1$ to 0.3 T_t	1.67	argon	Flat-nosed	.96	30	10

* Subscripts min. and unity refer to conditions at the minimum and unity pressure ratio, respectively.

TABLE E.2

Ratio of Measured to Inviscid Impact Pressure for Air by Ashkenas (85)

Using a 1/8 in. o.d., 10° Externally-Chamfered Impact Tube

Re_{2D_p}	M = 2	M = 3	M = 4	M = 5	M = 6	M = 6.5	M = 6.75	M = 7.0
80	1.031	0.998	0.990					
70	1.030	0.996	0.988					
60	1.027	0.994	0.986					
50	1.023	0.989	0.984					
40	1.013	0.983	0.981					
36	1.009	0.981	0.978					
35	1.006	0.978	0.975					
25	1.005	0.978	0.976					
20	1.009	0.981	0.978					
16	1.022	0.990	0.986					
15	1.026	0.994	0.979					
14	1.032	1.000	0.993					
12	1.049	1.013	1.005	1.005				
10	1.073	1.034	1.024	1.025				
8	1.105	1.066	1.056	1.053				
6	1.149	1.117	1.112	1.110	1.050	1.071		
4.5	1.195	1.185	1.179	1.180	1.126	1.128	1.244	

TABLE E.2 (continued)

Re_{2D_p}	M = 2	M = 3	M = 4	M = 5	M = 6	M = 6.5	M = 6.75	M = 7.0
4.0	1.214	1.215	1.209	1.213	1.161	1.155	1.243	
3.5	1.235	1.254	1.245	1.251	1.204	1.196	1.245	
3.0		1.296	1.290	1.300	1.253	1.241	1.253	
2.5		1.337	1.345	1.360	1.313	1.302	1.270	
2.0		1.378	1.417	1.439	1.388	1.381	1.310	
1.8		1.394	1.453	1.479	1.425	1.420	1.342	
1.6		1.410	1.495	1.525	1.469	1.467	1.395	
1.4		1.426	1.542	1.581	1.521	1.520	1.465	
1.2			1.598	1.648	1.587	1.588	1.548	
1.1			1.632	1.689	1.626	1.625	1.598	
1.0			1.669	1.739	1.673	1.670	1.650	1.428
0.9			1.709	1.794	1.729	1.722	1.711	1.562
0.8			1.754	1.862	1.793	1.788	1.779	1.683
0.7				1.934	1.877	1.878	1.858	1.821
0.6				2.010	1.985	2.000	1.962	1.982
0.5				2.086	2.131	2.165	2.136	2.180
0.4				2.166	2.315	2.392	2.400	2.424
0.3				2.239	2.480	2.692	2.758	2.892
0.2					2.621	2.907	3.065	3.301
0.15					2.696	2.931	3.108	3.385
0.10						2.832	3.009	3.340

APPENDIX F: ELECTRON ENERGY EQUATION AND RECOMBINATION TIME

Electron Energy Equation

By starting with the species energy equation derived from the Boltzmann equation (Chapman and Cowling (28)) and using the Newtonian stress-rate-of-strain relationship and Fourier's heat conduction law the electron energy equation becomes

$$\frac{D}{Dt}\rho_E e_E + \rho_E e_E \nabla\cdot\underline{u} + p_E\nabla\cdot\underline{u} + \nabla\cdot\underline{q}_E - (\underline{\tau}_E\cdot\nabla)\underline{u} - \rho_E\underline{V}_E\cdot(\underline{f}_E - \frac{D\underline{u}}{Dt}) = \Delta E_E$$

Neglecting the terms which contain $m_E^{1/2}$ and m_E, and considering steady flow the energy equation becomes,

$$\underline{u}\cdot\nabla\rho_E e_E + \rho_E e_E\nabla\cdot\underline{u} + p_E\nabla\cdot\underline{u} + \nabla\cdot\underline{q}_E + \bar{e}n_E\underline{V}_E\cdot\underline{E} = \Delta E$$

where the body force has been rewritten as $\underline{f}_E = -\frac{\bar{e}\,\underline{E}}{m_E}$ ($\bar{e}$ is the electronic charge). The term containing the electric field can be rewritten by using a simple electron conduction relationship, $-\bar{e}n_E\underline{V}_E = \sigma\underline{E}$ where $\sigma = \bar{e}^2 n_E/m_E\nu_{EI}$. The result is

$$\bar{e}n_E\underline{V}_E\cdot\underline{E} = -n_E m_E \nu_{EI}\underline{V}_E^2$$

which, in the absence of high applied $\underline{E}$ fields is at most of order $m_E^{1/2}$ (since $\nu_{EI}\sim m_E^{-1/2}$) and thus will be neglected.

The energy source term ΔE is comprised of electron-ion elastic and inelastic collisional energy transfer processes. Rather than use the electron-ion elastic energy transfer expression calculated by Petschek and Byron (32), an expression will be derived here which is in excellent agreement with them but is visualized more

simply. Spitzer (33) has shown that the temperature equilibration time, t_{eq}, between electrons and ions, initially at different temperatures, is related to the electron-electron self collision time t_{ee}, by the mass ratio,

$$t_{eq} = (m_I/m_E)t_{EE}$$

This result can be interpreted as meaning that the fraction of initial kinetic energy transferred to the ion (or electron) from an electron (or ion) is about m_E/m_I as can be verified by considering the energy exchange in an elastic collision between two hard spheres of large mass disparity. The elastic energy transferred from the electrons to the ions is,

$$Q_{el} = 3/2\ \kappa\nu_{EI}\ (m_E/m_A)(T_E-T_I)\,n_E$$

where the average random kinetic energy of each specie has been expressed in terms of its internal energy.

The inelastic energy transfer terms are more complicated primarily because the excitation and de-excitation rate processes for ionization and recombination are not well understood. In fact the recombination is believed to be a collisional-radiative process schematically described as

$$A^+ + e + e \rightarrow A^* + e \rightarrow A + e^* + h\nu$$

where the asterisk denotes high electronic excitation of the atom and large electron kinetic energy obtained by collisional de-excitation of the higher quantum levels of the atom, and $h\nu$ denotes energy

emitted by radiative de-excitation of the quantum levels close to the ground state. Bates et al. (92) realized that the overall process could not be adequately expressed by two independent processes, one, a three-body collisional recombination process valid in the limit of $n_E \to \infty$, and two, a two-body radiative recombination process valid in the limit of $n_E \to 0$ (but high ionization fraction). They calculated the recombination coefficients for hydrogen-like*, optically thick and thin plasmas (92,93) as well as the radiation emitted (94). Their rate equation is

$$\frac{-\partial n_E}{\partial t} = n_E n_I \left(\alpha - \frac{S n_A}{n_E}\right)$$

where α and S are the collisional-radiative recombination coefficient and the collisional-radiative ionization coefficient respectively. The term in parentheses is referred to as the collisional-radiative decay coefficient. As stressed by Bates et al. (92,93) the choice of expressing the rate equation as a two body process must not be taken to mean that two body processes predominate. In the supersonic free jet where recombination processes are dominant the plasma is probably characterized as optically thin, except possibly toward lines of the Lyman series. The recombination coefficients may be obtained from Bates et al. (92,93) for either case. However, over the limited range $10^{13} \leq n_E \leq 10^{16}$ cm^{-3}, $8,000 \leq T_E \leq 20,000^{\circ}$K the three body electron-ion recombination rate ($A^+ + e + e \to A + e$) of Makin and Keck

*Hydrogen-like refers to atoms which have the classical electron orbits around a charged core.

(95) generally conservatively describes the rates given by Bates et al. (92, 93) for all their radiation models in addition to those already mentioned and is given in terms of α as

$$\alpha = 2.3 \times 10^{-8} T_E^{-9/2} n_E$$

where α, T, and n_E have the units cm^3/sec, ^oK, and cm^{-3} respectively.

Since the electrons do not receive all the energy of recombination ($-\frac{\partial n_E}{\partial t} I > 0$) the inelastic energy term must include that energy radiated by the radiative de-excitation processes. The inelastic energy transfer becomes

$$Q_{inel} = \frac{-\partial n_E}{\partial t} I - Q_{rad}$$

where $Q_{inel} > 0$ for the recombining plasma and Q_{rad} has been calculated for hydrogen-like atoms by Bates and Kingston (94). Talbot, Chou, and Robben (96) have expressed Q_{inel} similarly, however they curve fitted α, S, and Q_{rad} individually from Bates et al. (92, 93, 94) by a 12 term double series in n_E and T_E. In addition they chose Q_{rad} so that the net energy of recombination given to the free electrons was the same for argon as for hydrogen in the optically thin case.

$$Q_{rad} = Q_{rad\ hydrogen} - (I_{ar} - I_H) \frac{\partial n_E}{\partial t}$$

By collecting all the terms in the electron energy equation the result becomes,

$$\underline{u}\nabla\rho_E e_E + \rho_E h_E \nabla\cdot\underline{u} + \nabla\cdot\underline{q}_E = -n_E \nu_{EI}(m_E/m_I)3/2\ \kappa(T_E - T_I) - \frac{\partial n_E}{\partial t} - Q_{rad}$$

The importance of various terms can be determined by non-dimensionalizing the energy equation.

Let

$$\underline{u} = u_o\bar{\underline{u}}$$

$$T = T_o\bar{T}$$

$$n_E = n_{Eo}\bar{n}_E \quad (\text{where } n_{E_o} = 2\times10^{15}\,\text{cm}^{-3} \text{ when } \bar{x}_o = 1/2 \text{ and scales as } \bar{x}_o^{-2} \text{ for } \bar{x}_o \geq 1/2)$$

$$k_E = k_{Eo}\bar{T}^{+5/2}$$

$$\nabla = \frac{\bar{\nabla}}{L}$$

$$\nu_{EI} = (\nu_{EI})_o(T_o/T)^{3/2}(n_E/n_{Eo}) = (\nu_{EI})_o\frac{\bar{n}_E}{(\bar{T})^{3/2}}$$

where the $(\ )_o$ quantities are reference variables whose values are typical for the free jet operating conditions at a given axial location, $\bar{x}_o$. By noting that $e_E = 3/2\,(\kappa/m_E)T_E$ and $h_E = 5/2(\kappa/m_E)T_E$ and using the nondimensional quantities above, the energy equation becomes

$$\bar{\underline{u}}\cdot\bar{\nabla}\bar{n}_E\bar{T}_E + 5/3\,\bar{n}_E\bar{T}_E\bar{\nabla}\cdot\bar{\underline{u}} - \bar{\nabla}\frac{(\bar{T}_E^{5/2}\bar{\nabla}\bar{T}_E)}{3/5\,Pe_E} + \frac{(\nu_{EI})_o(m_E/m_I)}{(u_o/L)}\frac{\bar{n}_E^{\,2}(\bar{T}_E - \bar{T}_I)}{\bar{T}^{3/2}} = \frac{Q_{inel}}{3/5\,\rho_E u_o c_{pE} T_o}$$

where $Pe_E = \rho_E u_o c_{pE}/k_{Eo}$ is the electron Peclet number which is the ratio of convected to conducted energy flux. By using the result of the ρu measurements discussed in Section III.3 and the source flow

approximation, the Spitzer (33) thermal conductivity (at $T_o = 20,000^oK$ and $\ell n\Lambda = 6$), $u_o = 10^6$ cm/sec, L = 1 cm and the recombination coefficient from Makin and Keck (95), the relative importance of each of the terms can be estimated.

The coefficients of the last three terms are shown in the following table, where the reference variables $(\ )_o$ containing n_{Eo} take on their estimated values at a given $\bar{x}_o$ (but $T_o = 20,000^oK$ $u_o = 10^6$cm/sec, and L = 1 cm remain constant.

$\bar{x}_o$ x_o/D_*	$(t_{flow}/t_{eq})^*$	$\frac{1}{3/5Pe_E}$	$\frac{Q_{inel}}{3/5\rho_E u_o c_{pE} T_o}$
$\frac{1}{2}$	.2	.4	2.6×10^{-2}
1	.05	2	1.6×10^{-3}
2	.01	7	1×10^{-4}
4	3×10^{-3}	28	6×10^{-6}
8	8×10^{-4}	113	4×10^{-7}
12	3×10^{-4}	255	8×10^{-8}

With the exception of the inelastic energy term, which is negligible, the convective, conductive and elastic energy transfer are about of equal importance at $\bar{x}_o = 1/2$. However by $\bar{x}_o \gtrsim 2$ the electron conduction term is dominant. For these conditions $\nabla \cdot \underline{q_E} = 0$ and this expression may be integrated to yield,

* The ratio of particle flow time to equilibration time, $\frac{t_{flow}}{t_{eq}}$, is just $\frac{(\nu_{EI})_o (m_E/m_I)}{u_o/L}$

$$\frac{\overline{T}_E}{\overline{T}_{E1}} = \left[1 - \frac{7}{2} \frac{\overline{q}_{E1}}{\overline{T}_{E1}^{7/2}\overline{R}_1}\left(1 - \frac{1}{\overline{R}/\overline{R}_1}\right)\right]^{2/7}, \quad \overline{R} \geq \overline{R}_1$$

where $\overline{T}_{E1}$ and $\overline{q}_{E1}$ $\left(\equiv \frac{q_{E1}}{\frac{T_o k_{Eo}}{L}}\right)$ are the known temperature and heat flux at a given position, $\overline{R}_1$. Reasonable estimates of $\overline{T}_{E1}$ and $\overline{q}_{E1}$ show that $\overline{T}_E$ is a very weakly decreasing function of $\overline{R}$.

Recombination Time

The atom-electron ionization rate for argon given by Petscheck and Byron (32) is

$$\dot{n}_E = \underbrace{8.4\times10^{-6}\left[\left(\frac{2}{\pi m_E}\right)^{1/2}(\kappa T_E)^{3/2}\right]\left[2 + \frac{T_{ex}}{T_E}\right]e^{-\frac{T_{ex}}{T_E}}}_{k_I} n_A n_E$$

where $T_{ex} = 135{,}000^{\circ}K$ and k_I is the ionization rate constant. The recombination rate, k_R, may be obtained from k_I, through the equilibrium rate equation

$$\dot{n}_I = 0 = k_I n_A n_E - k_R n_I n_E^2 \qquad \text{(at equilibrium)}$$

for the reaction

$$A + e \underset{k_R}{\overset{k_I}{\rightleftarrows}} A^+ + e + e$$

Carrying through the algebra and evaluating the physical constants, one obtains for the recombination rate,

$$\dot{n}_E = -c_2 n_E^3 \left(2 + \frac{T_{ex}}{T_E}\right) e^{(T_i - T_{ex})/T_E}$$

where $c_2 = 0.234 \times 10^{-31}$ $(\frac{cm^{-6}}{sec})$

and $T_i = 182,900^{o}K$.

Holding T_E constant and integrating this expression one obtains,

$$t = \frac{\left(\frac{n_{E_o}^2}{n_E^2} - 1\right)}{2c_2\left(2 + \frac{T_{ex}}{T_E}\right) e^{\frac{T_i - T_{ex}}{T_E}} n_{E_o}^2}$$

The recombination time, t_{recomb}, shown in Fig. 24 and discussed in Section III.3.1, is defined by choosing $\frac{n_E}{n_{E_o}} = \frac{1}{\sqrt{2}}$. For the range of n_E and T_E encountered here, use of the recombination coefficient from Makin and Keck (95) would yield the same results.

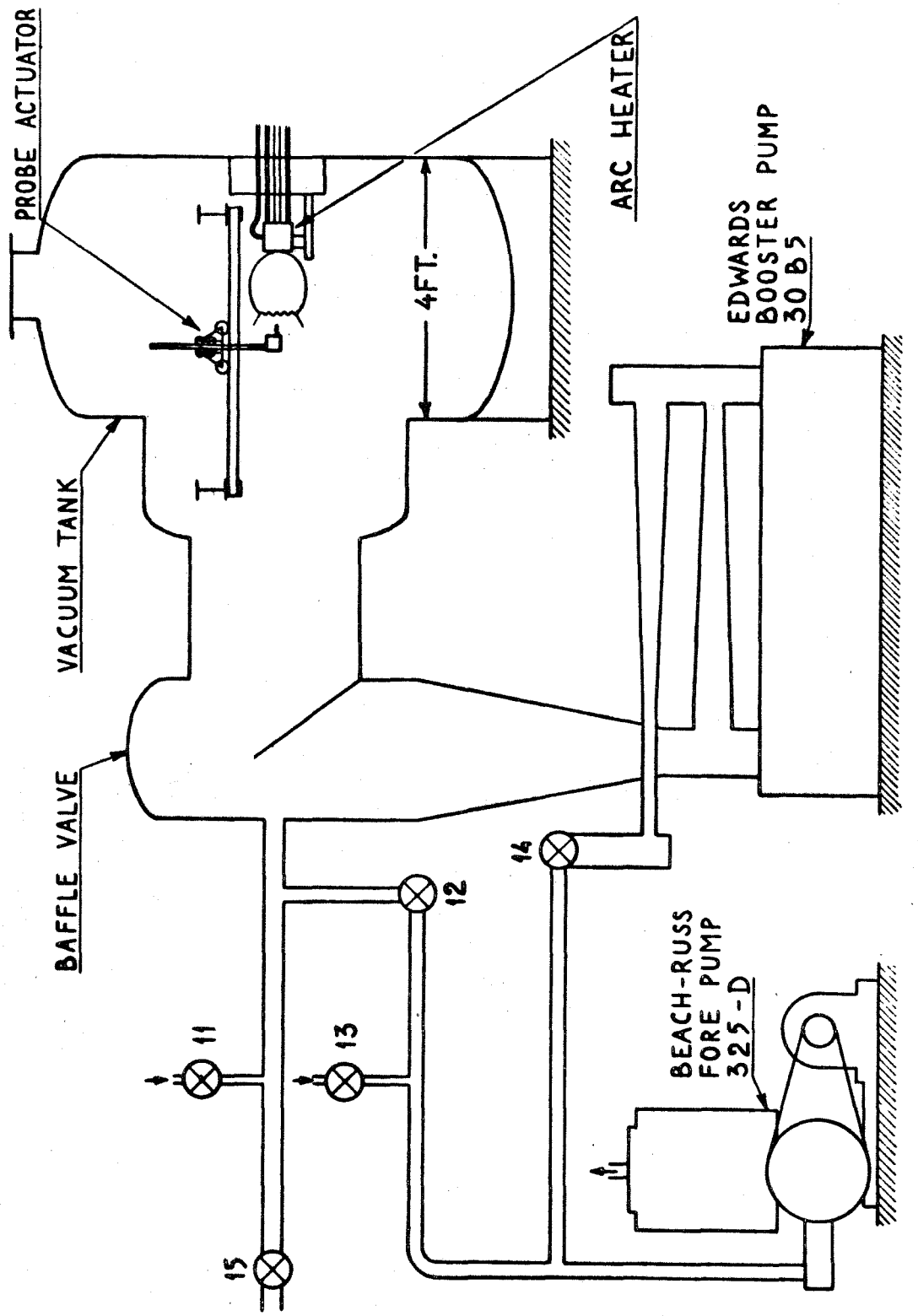

Figure 1. Low Density Facility

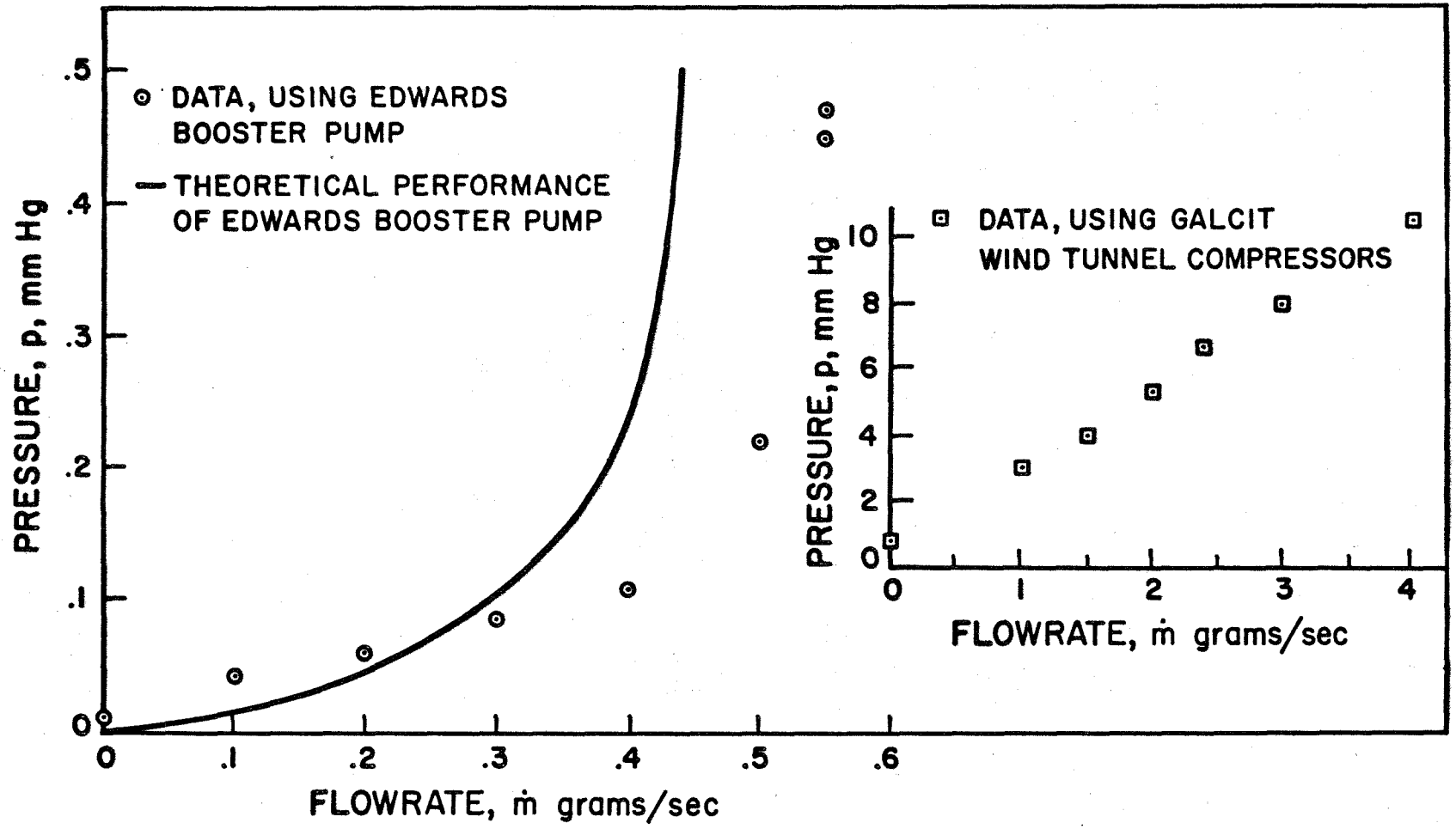

Figure 2. Performance of Low Density Facility with Argon

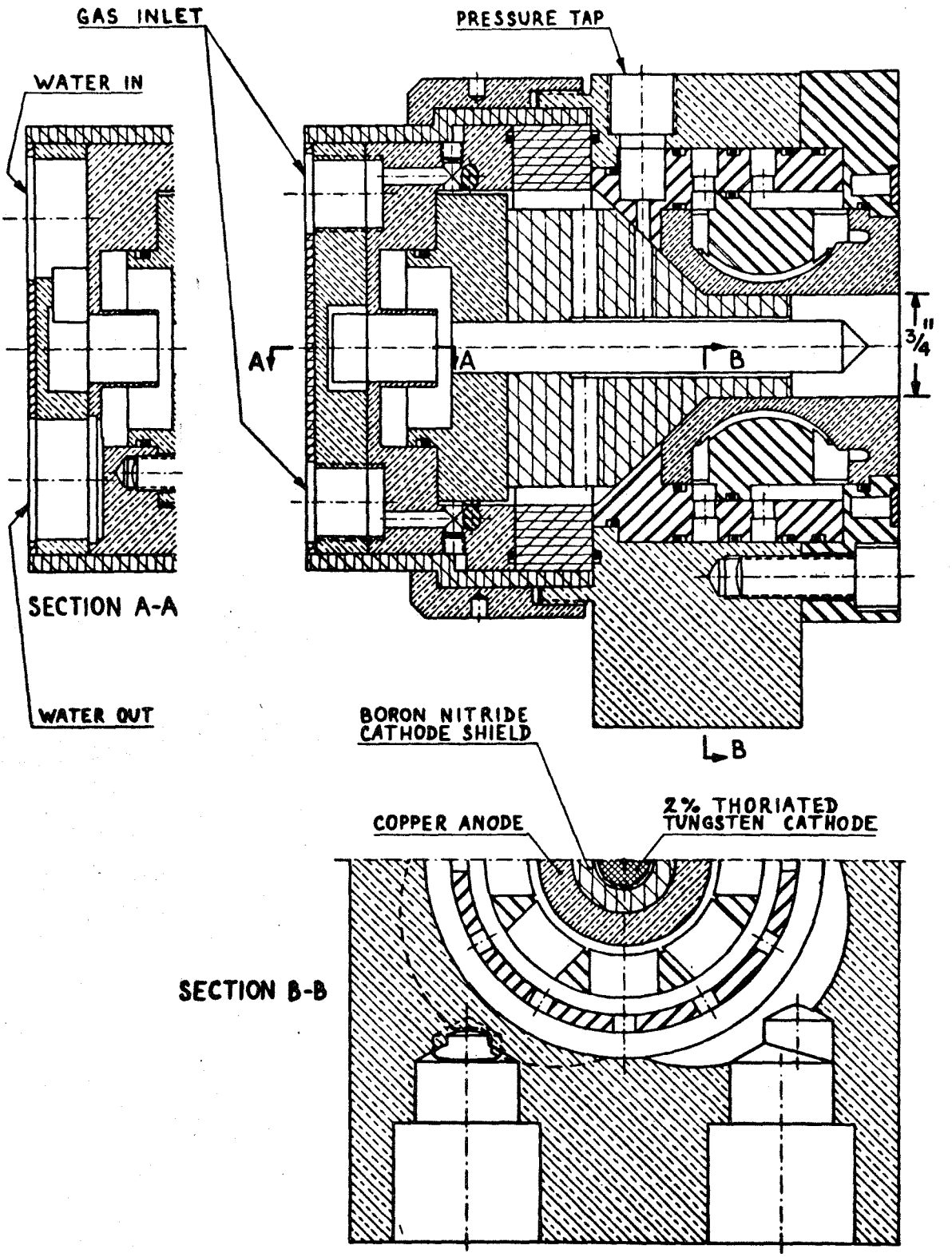

Figure 3. Arc Heater

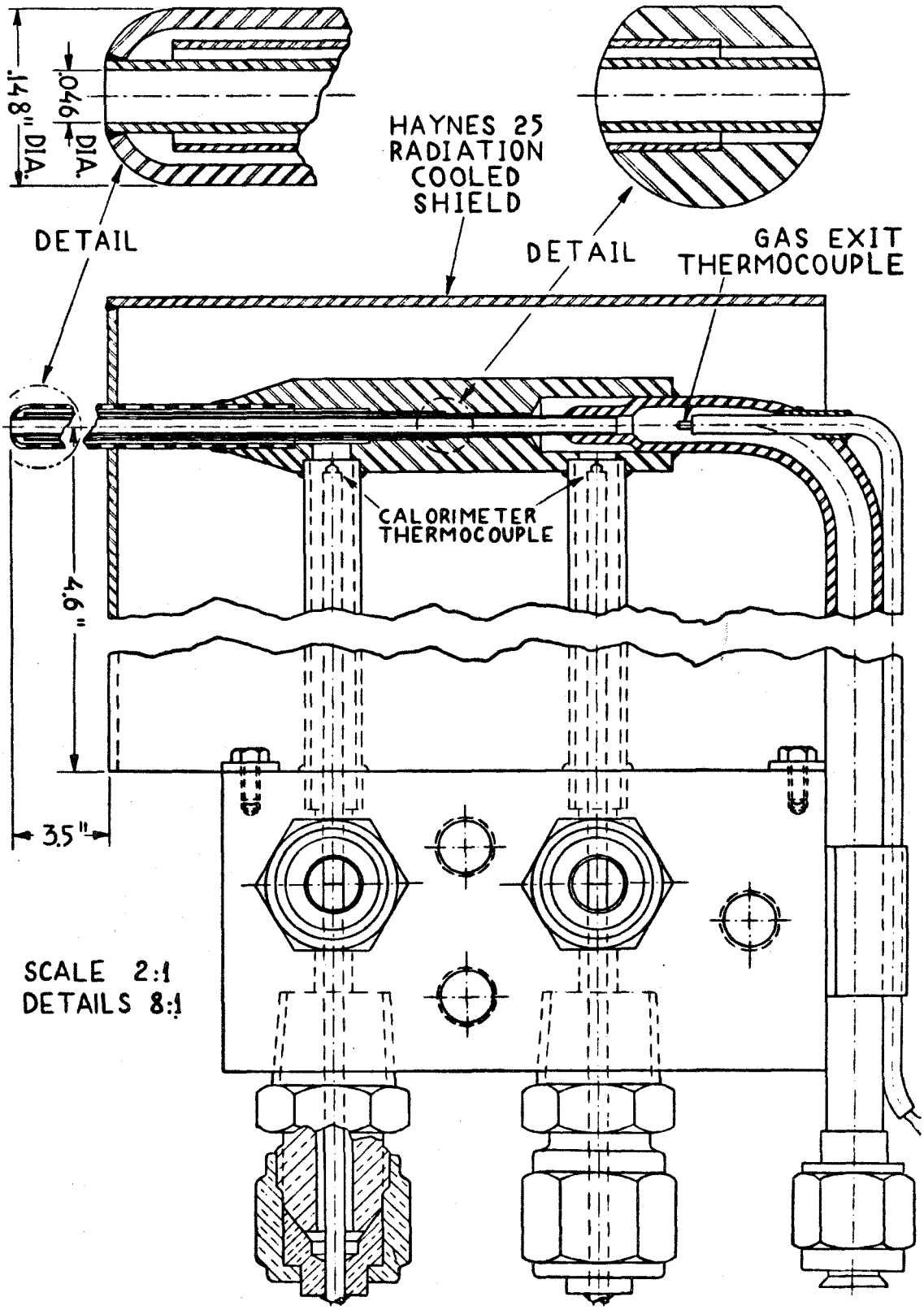

Figure 4. Hemisphere-cylinder Impact Pressure Probe

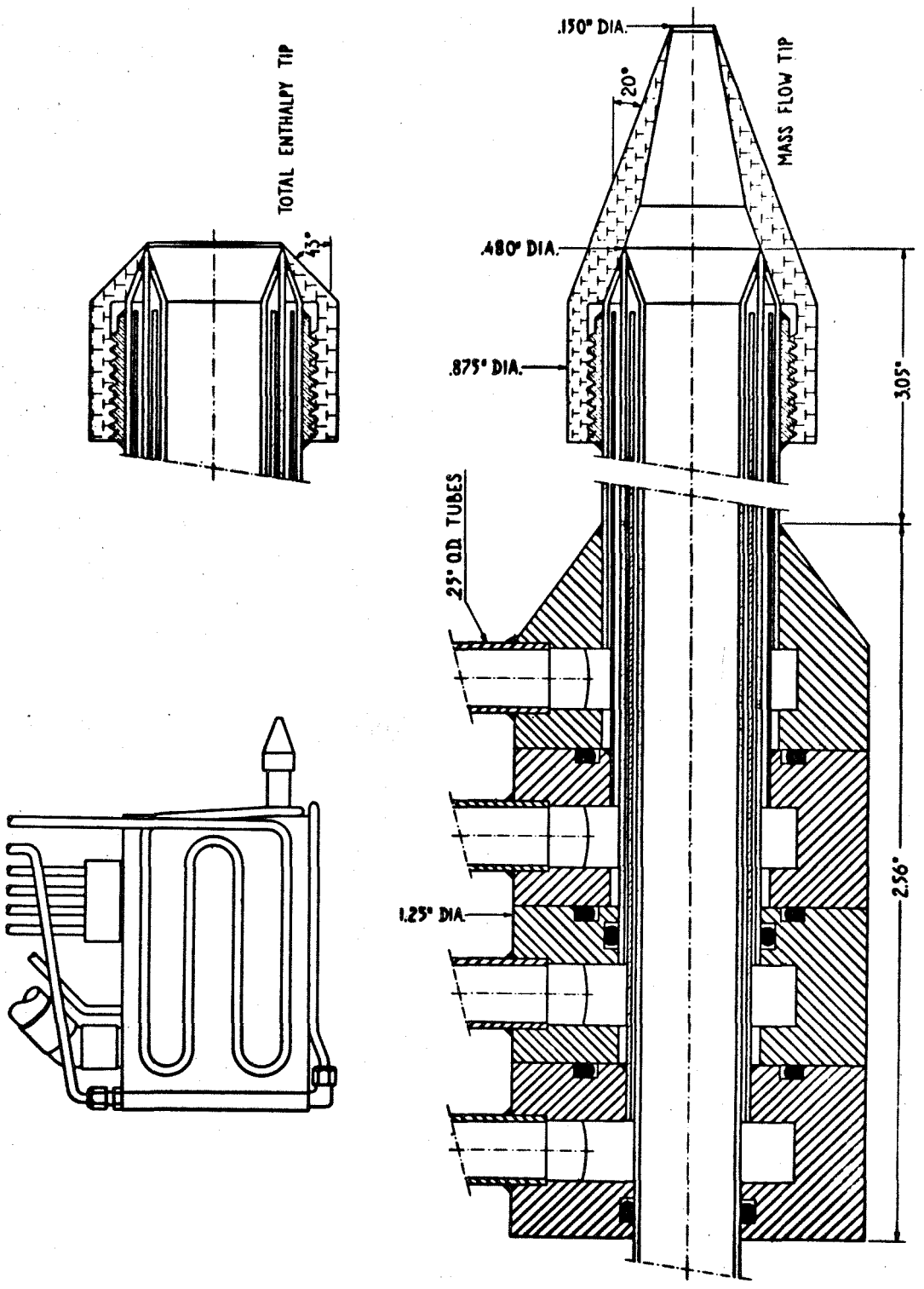

Figure 5. Combined Impact Pressure, Mass Flux and Total Enthalpy Probe

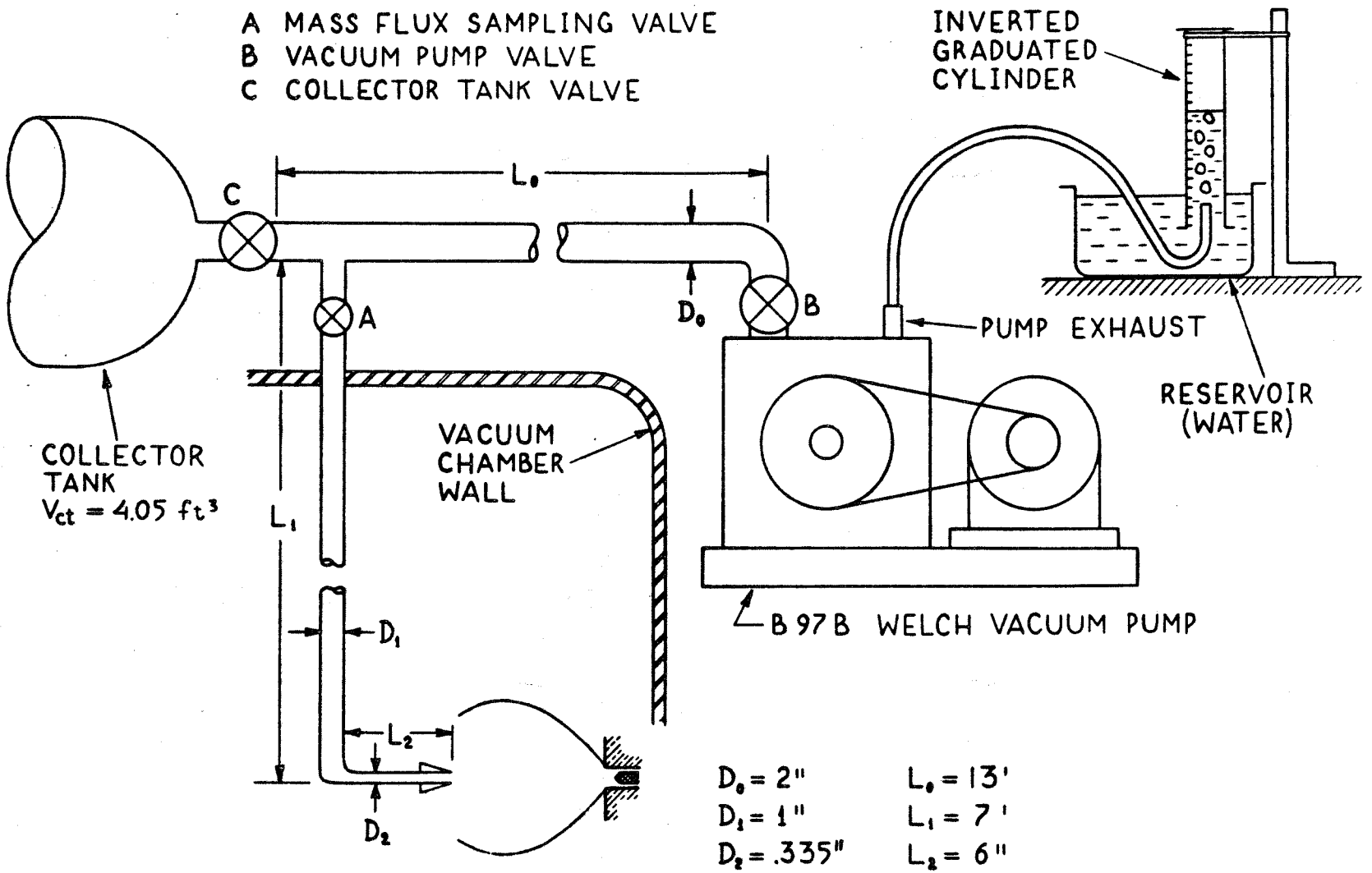

Figure 6. Mass Flux Sampling Apparatus

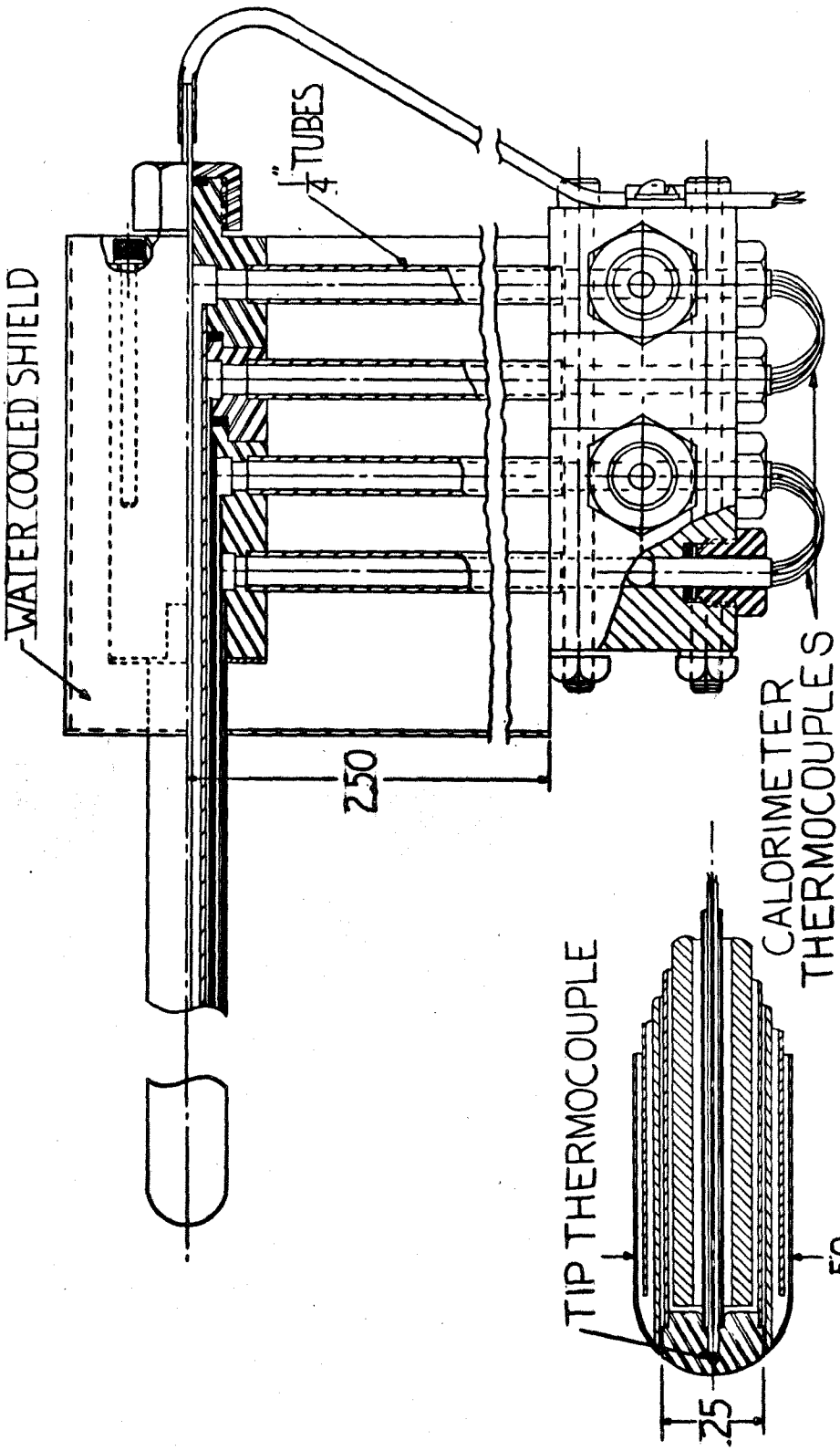

Figure 7. Stagnation Point Heat Transfer Probe

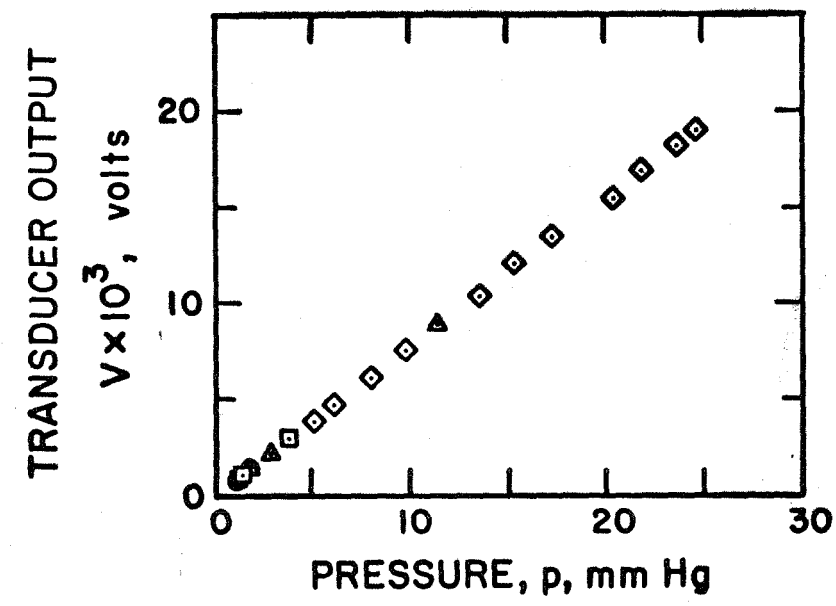

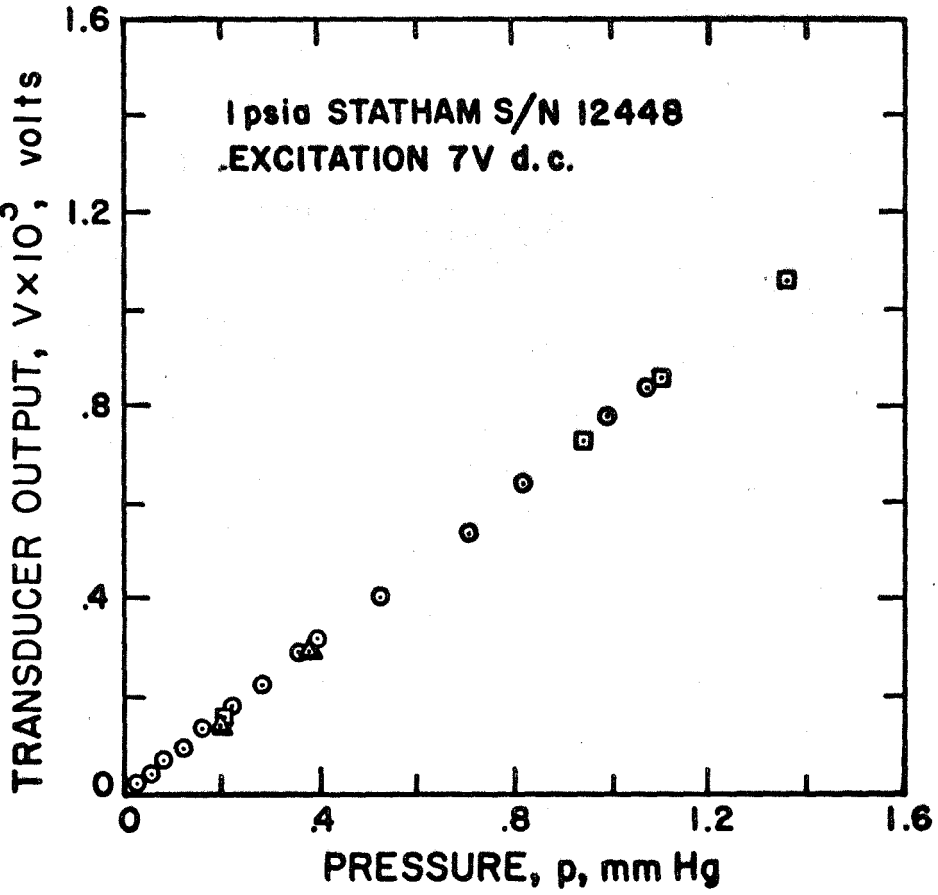

Figure 8. Pressure Transducer Calibration

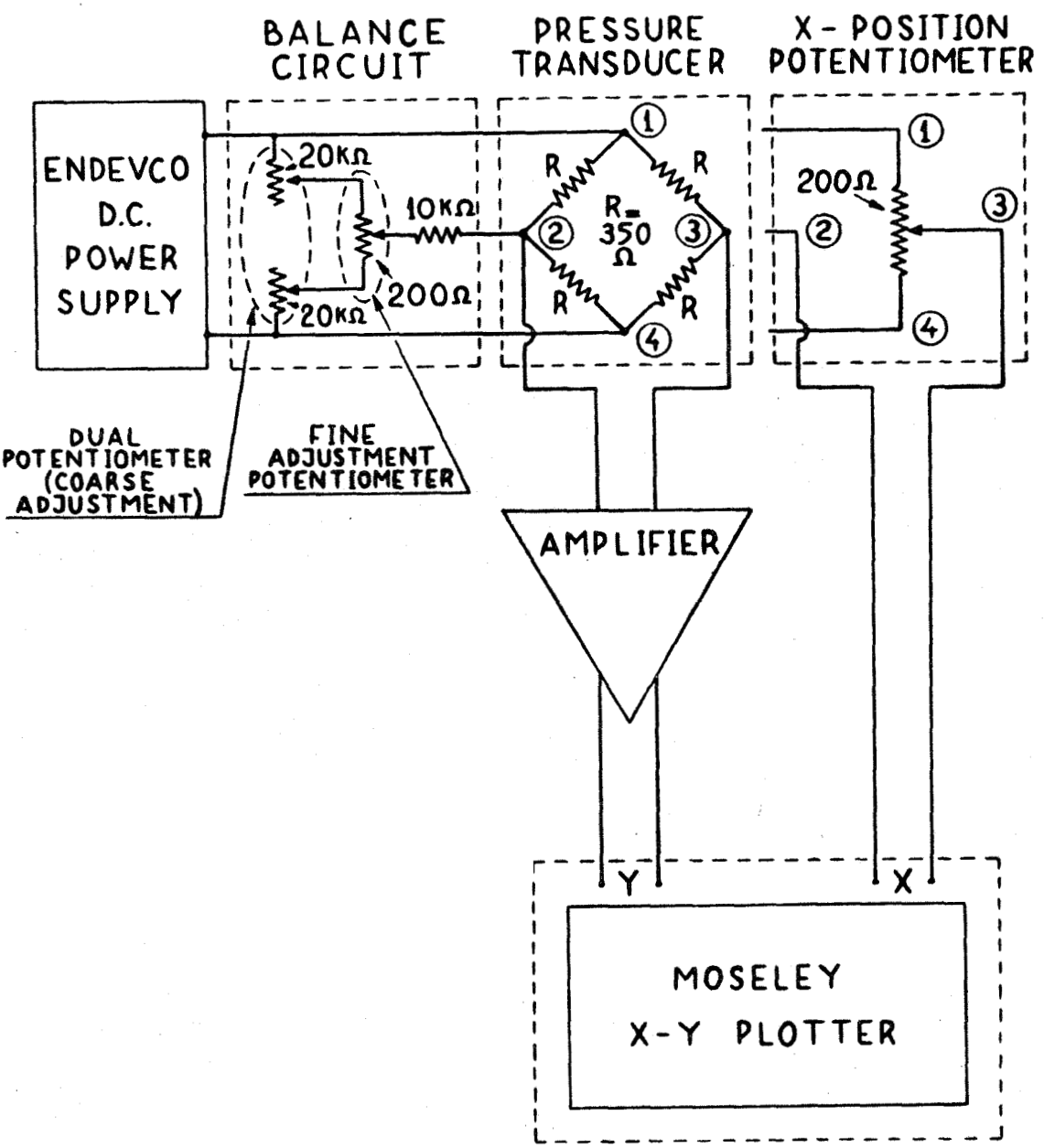

Note:

(i) x-position potentiometer had a separate balance circuit and power supply not shown here.

(ii) Circled numbers indicate pin positions.

Figure 9. Schematic Diagram of Pressure Transducer Circuitry

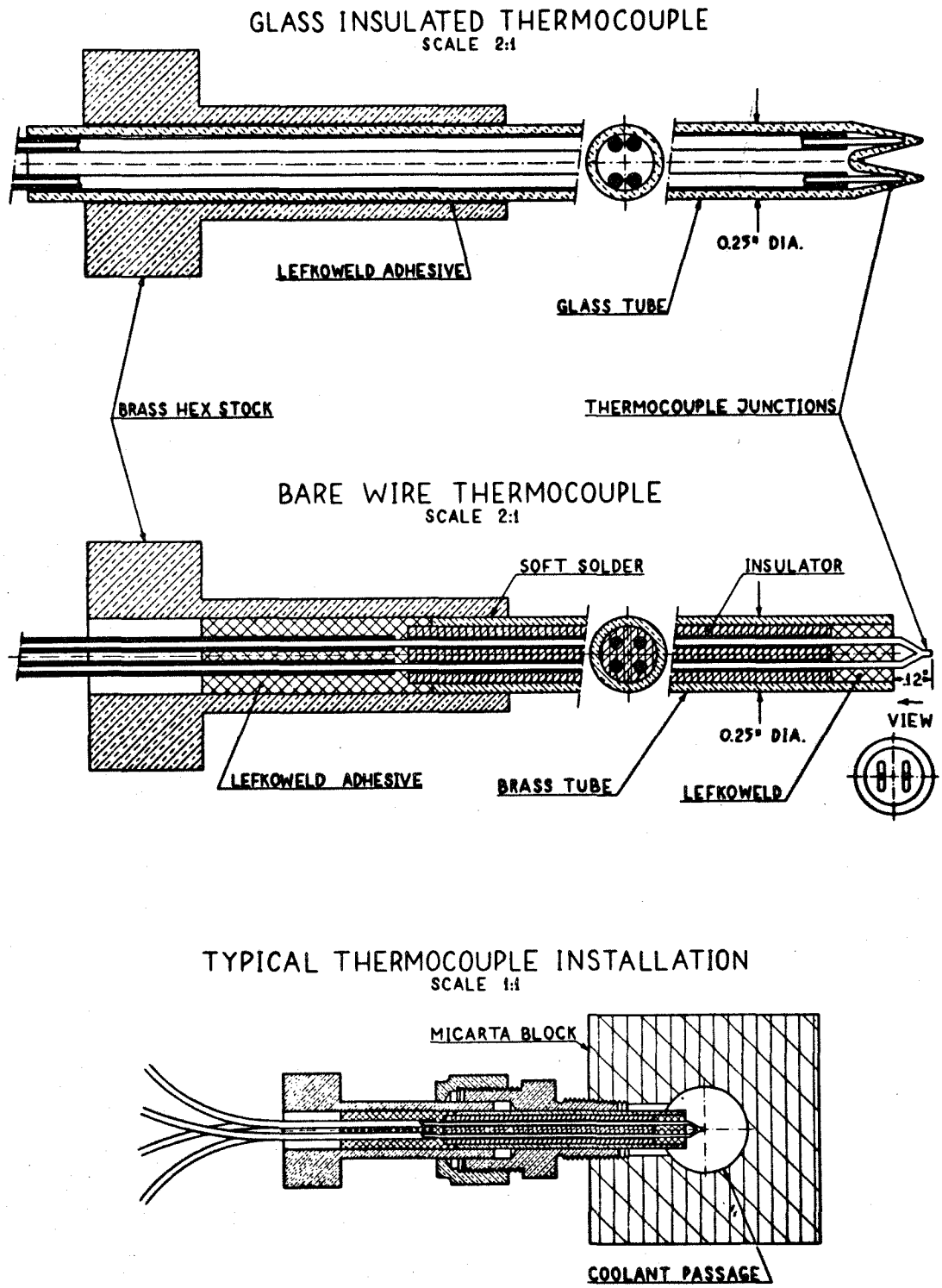

Figure 10. Calorimeter Thermocouple

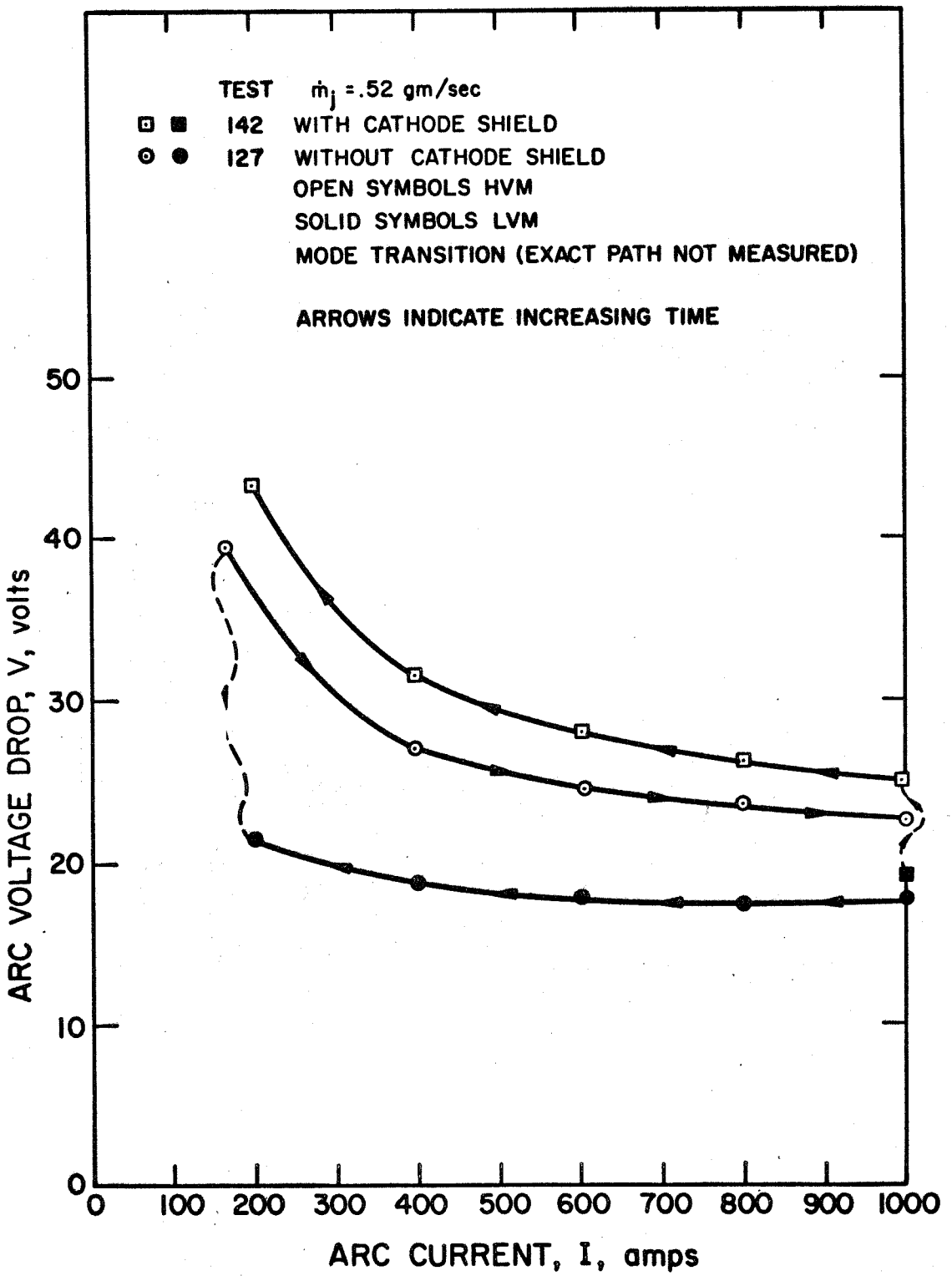

Figure 11. Typical Arc Heater Current-Voltage Drop Characteristics

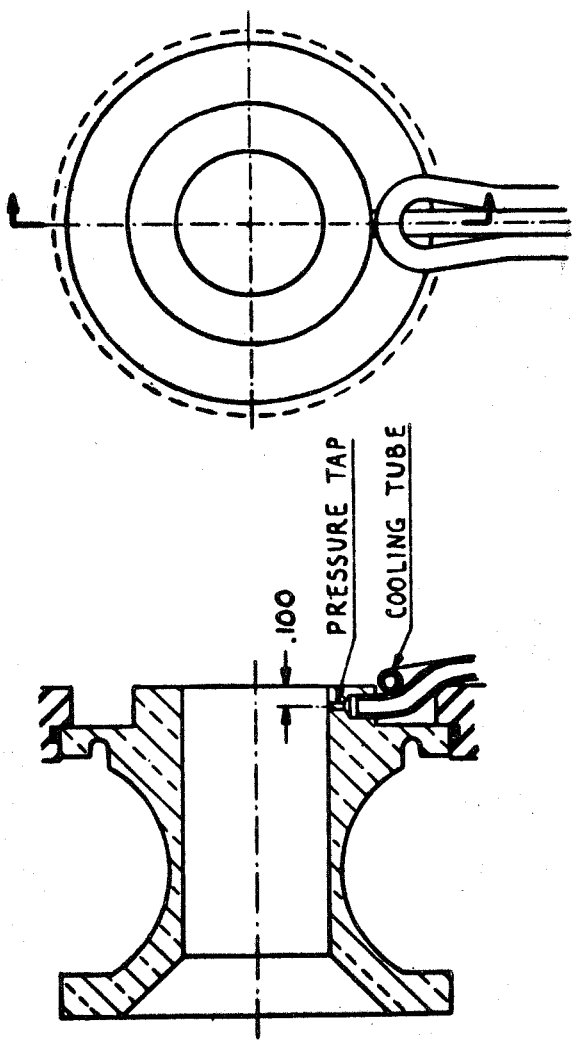

Figure 12. Modified Anode

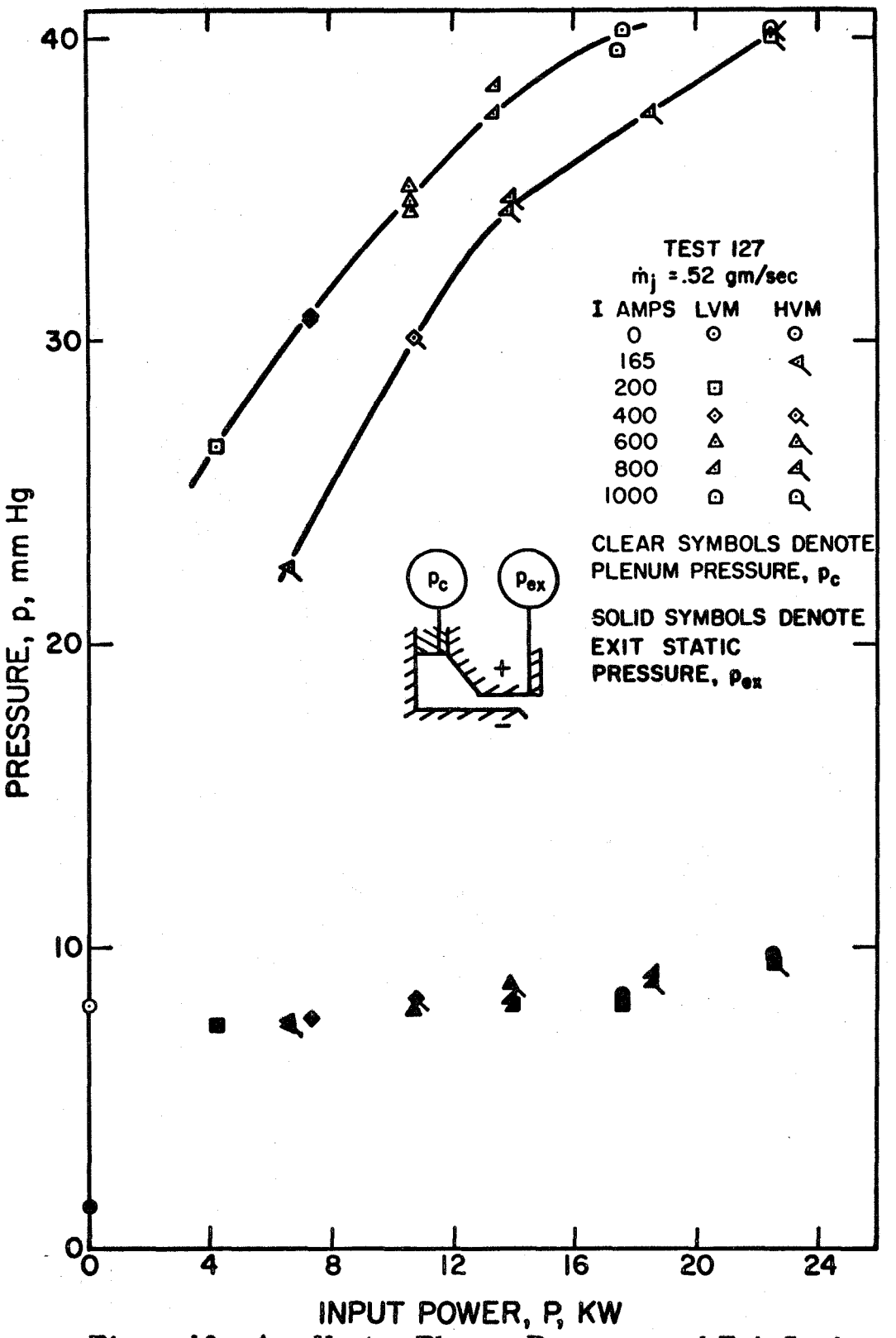

Figure 13. Arc Heater Plenum Pressure and Exit Static Pressure Variation with Power Input

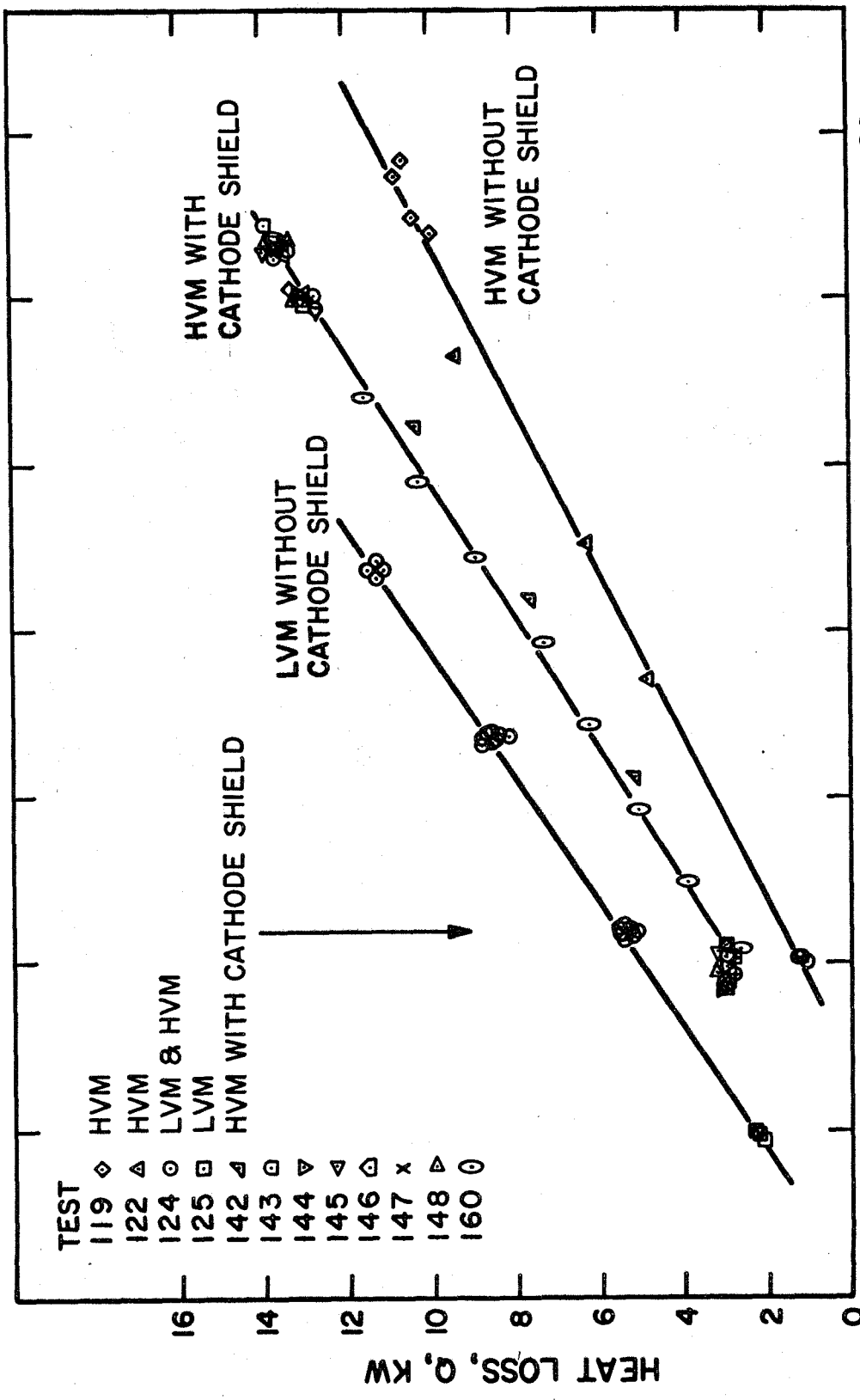

Figure 14. Heat Loss from Gas to Anode-Cathode Coolant

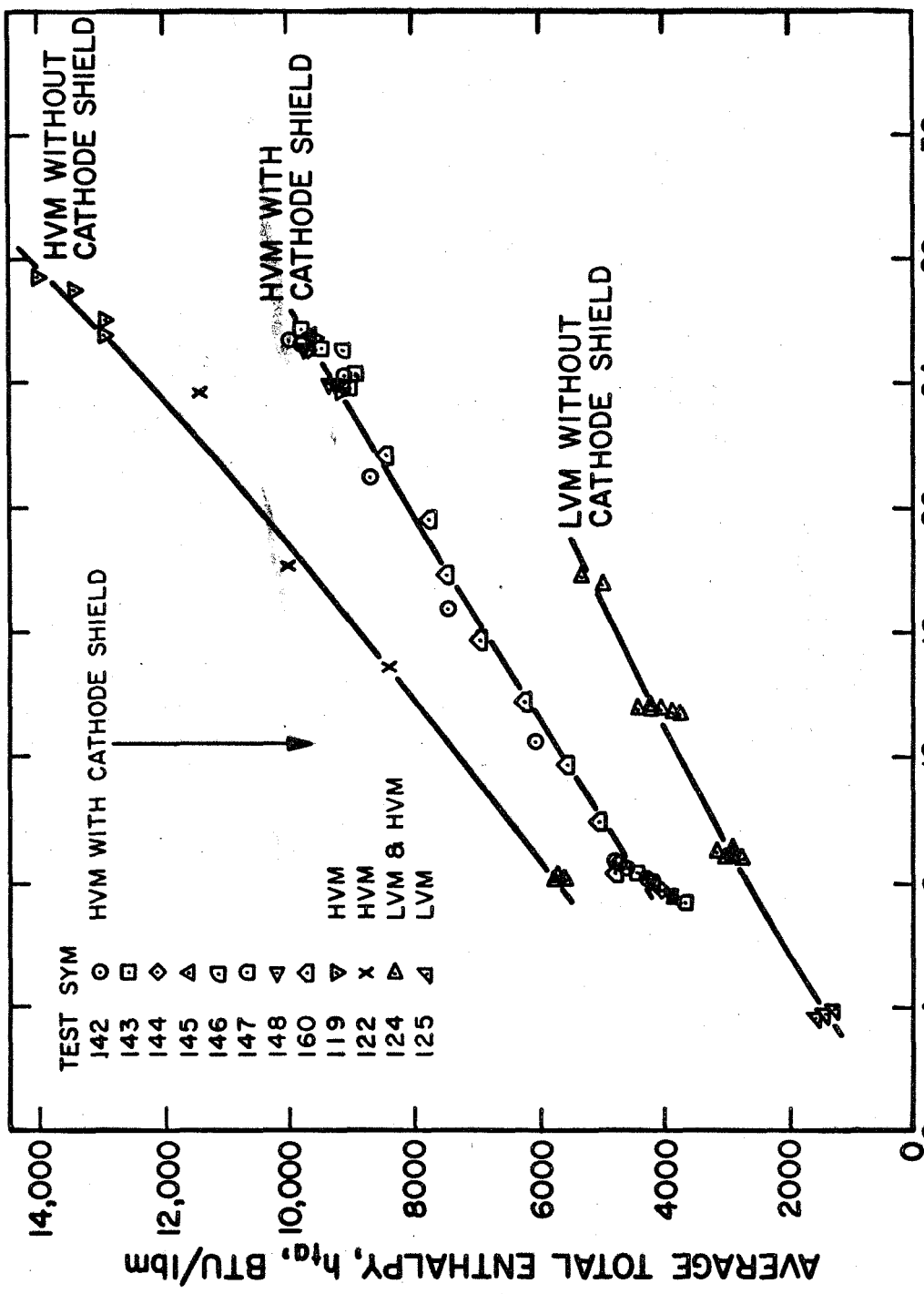

Figure 15. Average Total Enthalpy for Arc Heater

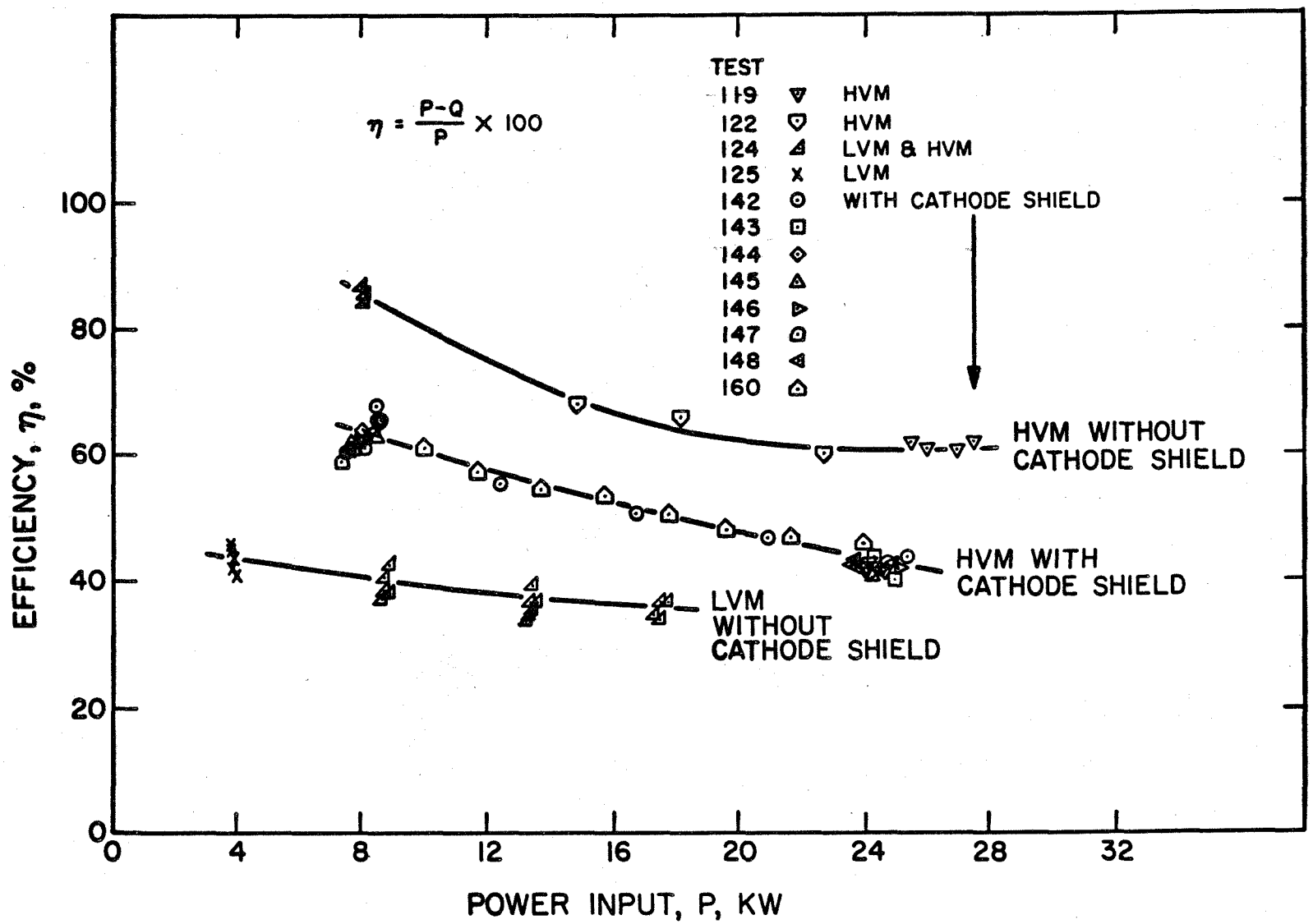

Figure 16. Efficiency for Arc Heater

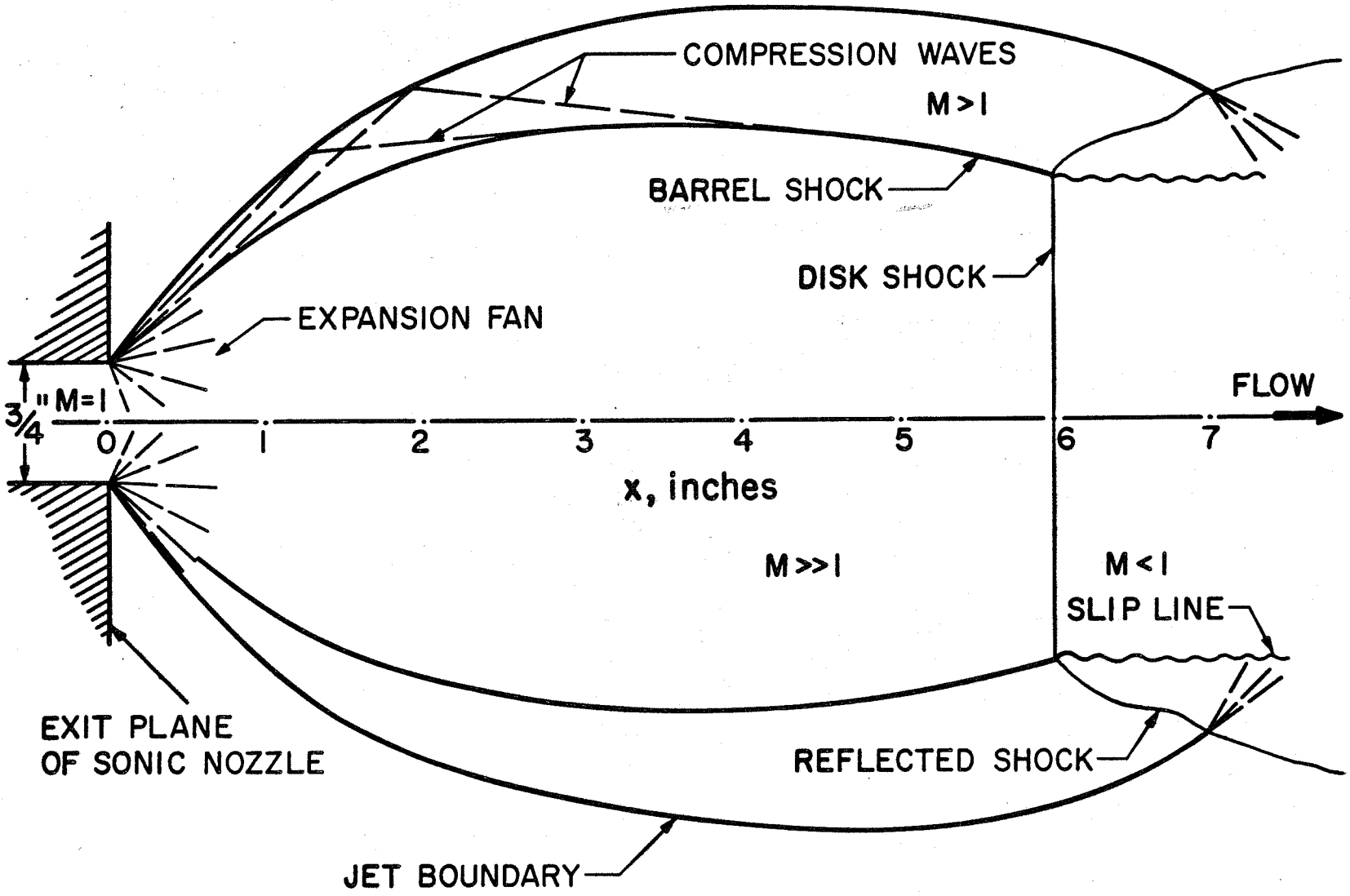

Figure 17. Schematic Diagram of Underexpanded Free Jet

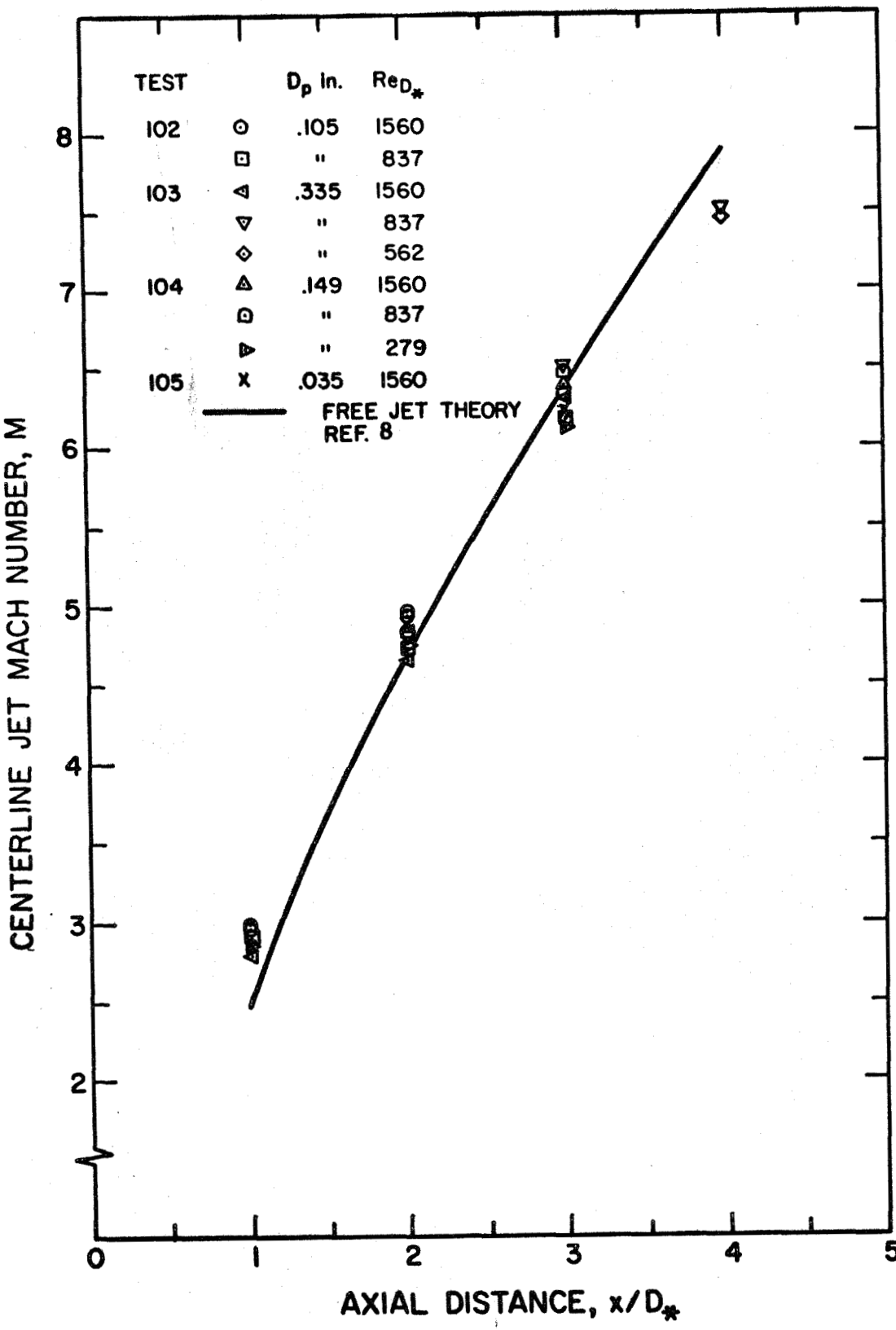

Figure 18. Centerline Jet Mach Number Distribution in Cold Flow

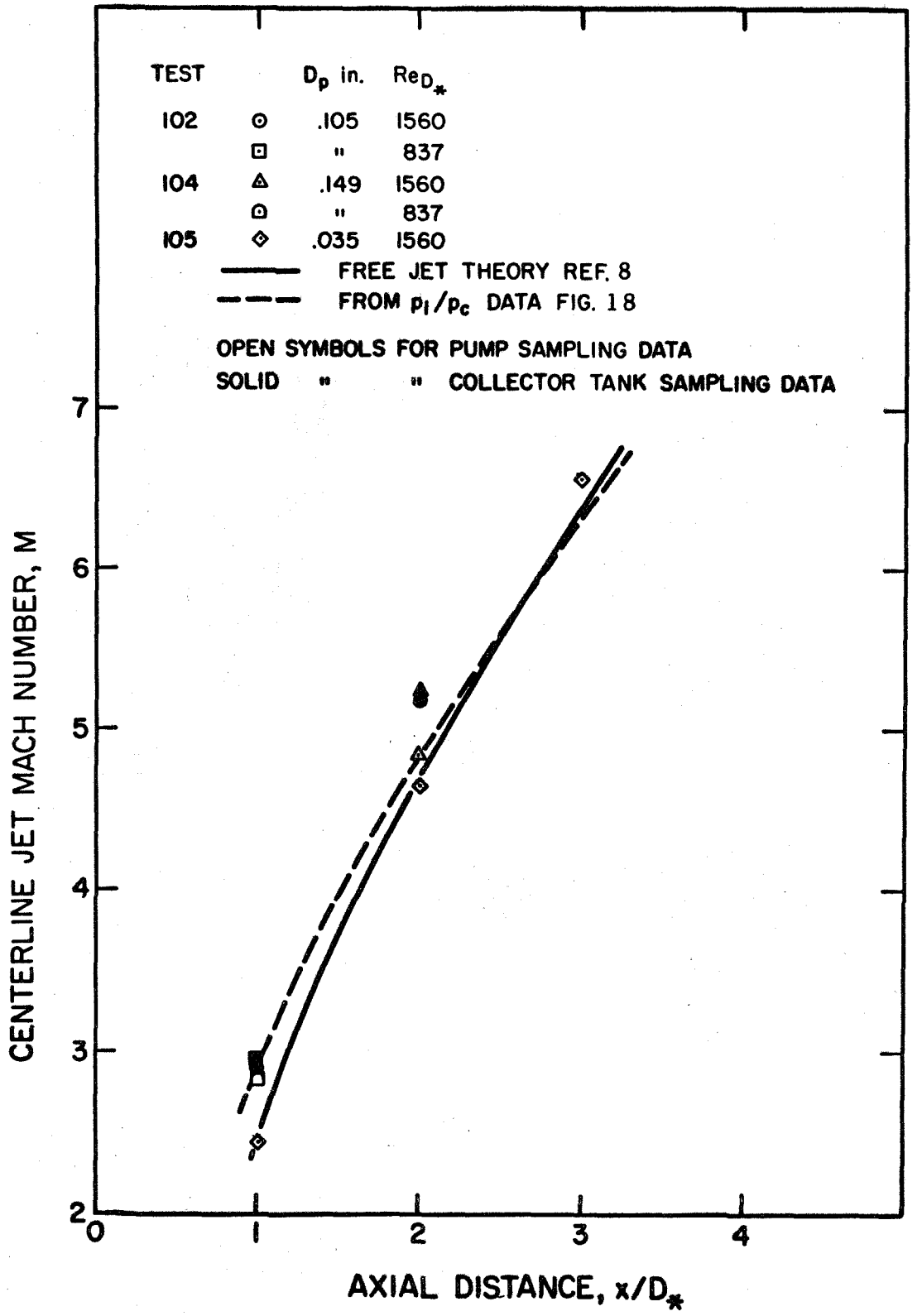

Figure 19. Centerline Mach Number Distribution from Mass Flux Measurements in Cold Flow

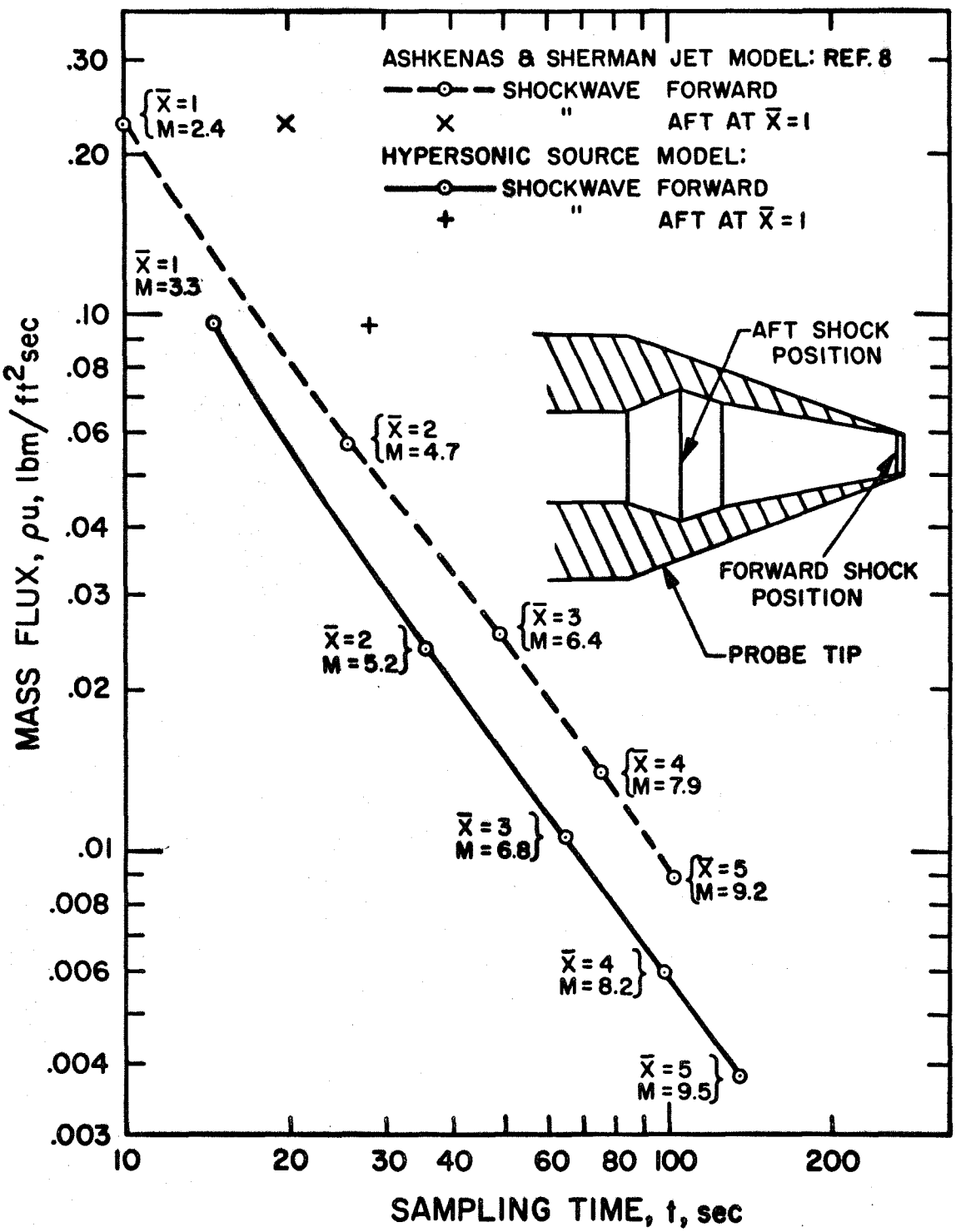

Figure 20. Collector Tank Mass Flux Sampling Operating Range

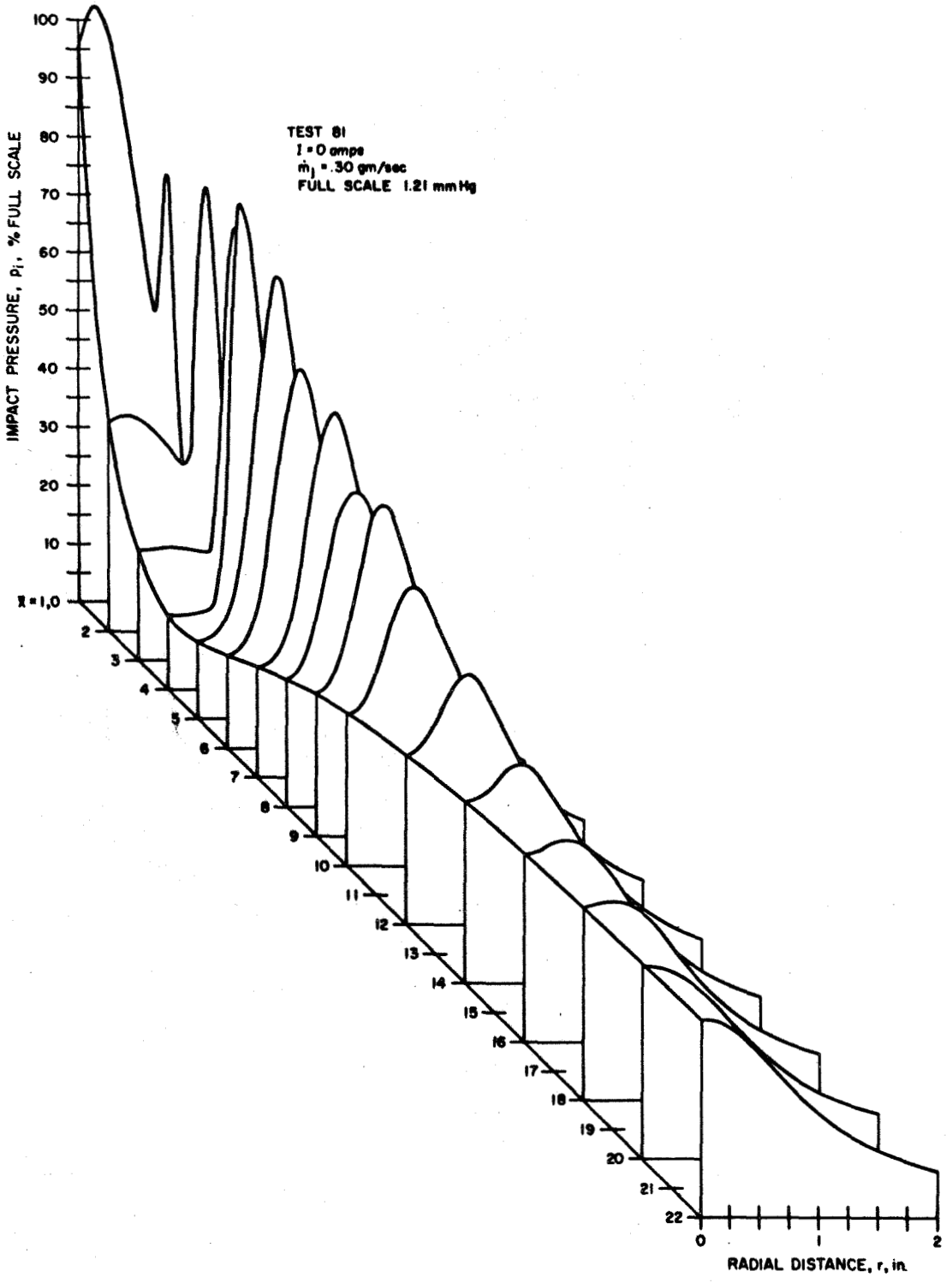

Figure 21. Impact Pressure Profiles in Cold Flow

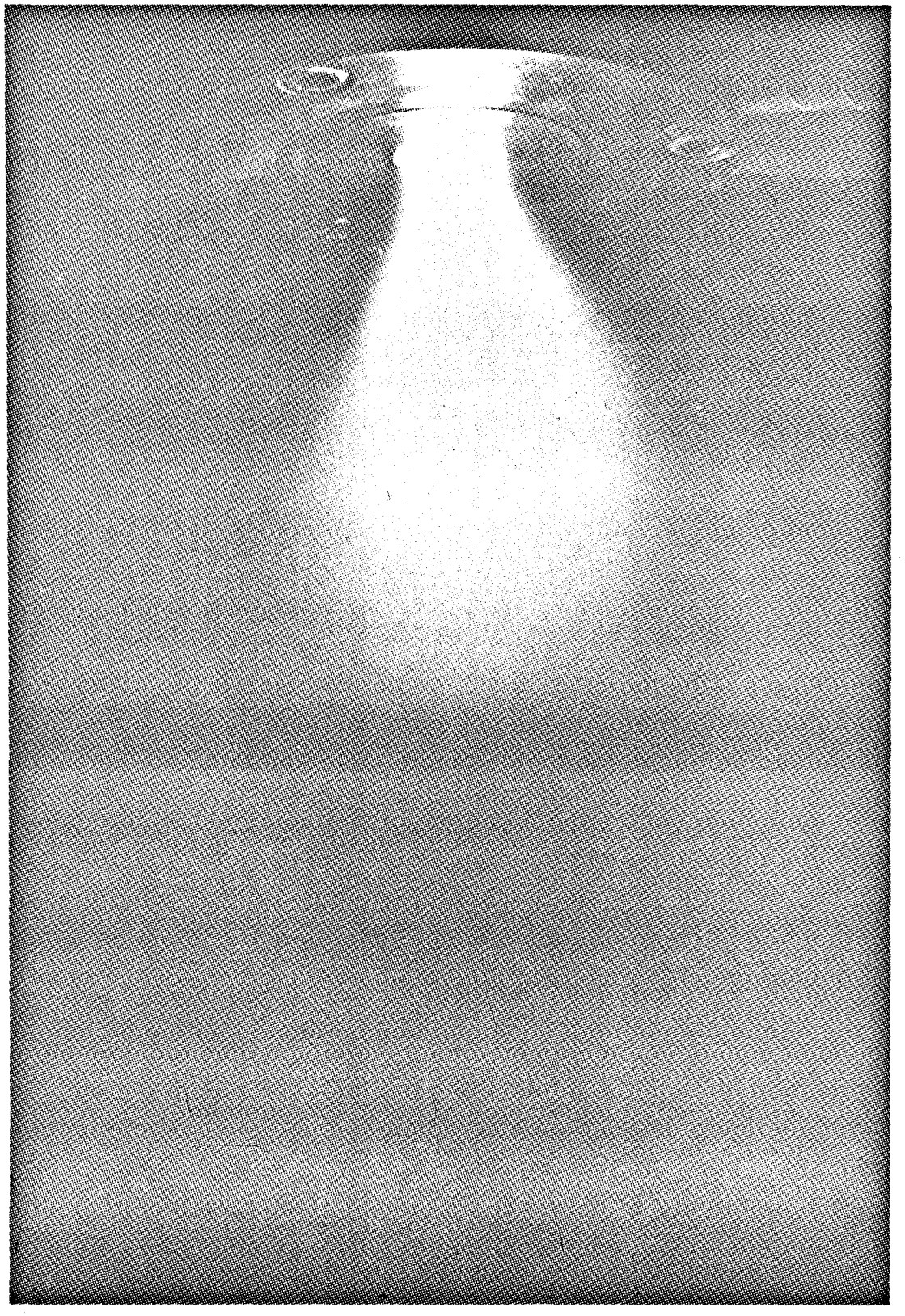

Figure 22. Arc Heated Free Jet

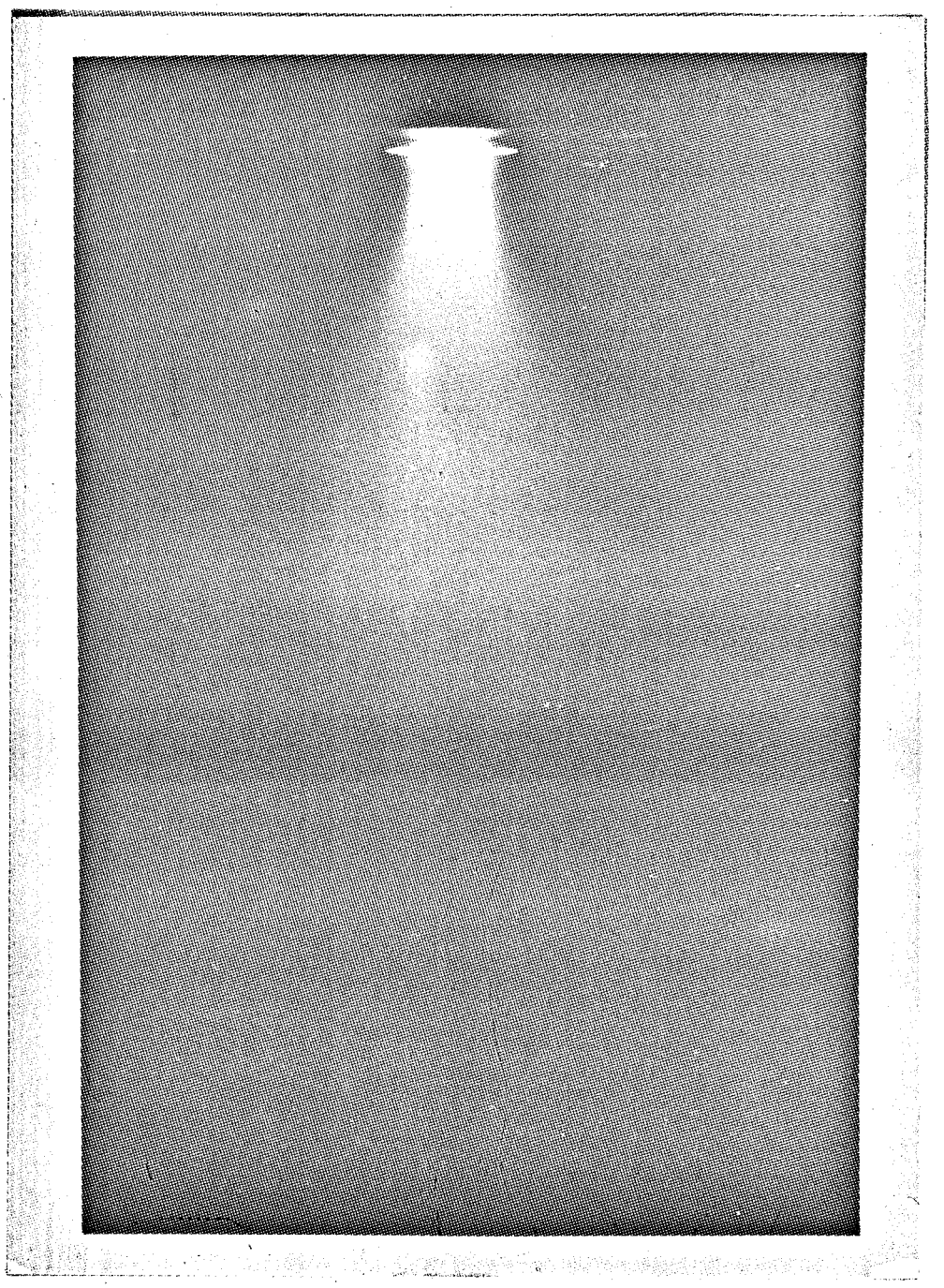

Figure 23. Arc Heated Free Jet

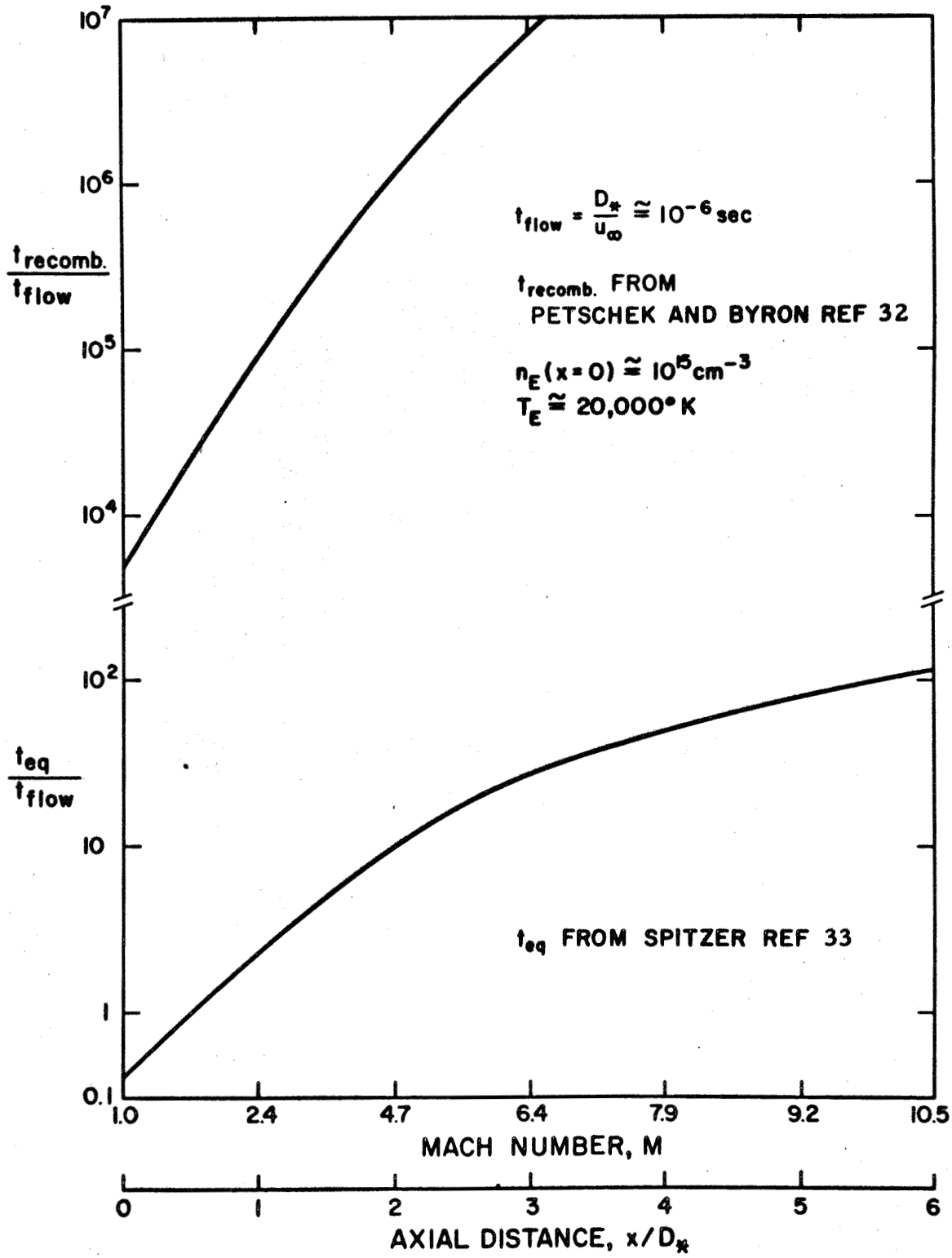

Figure 24. Typical Electron-Ion Recombination and Equilibration Times

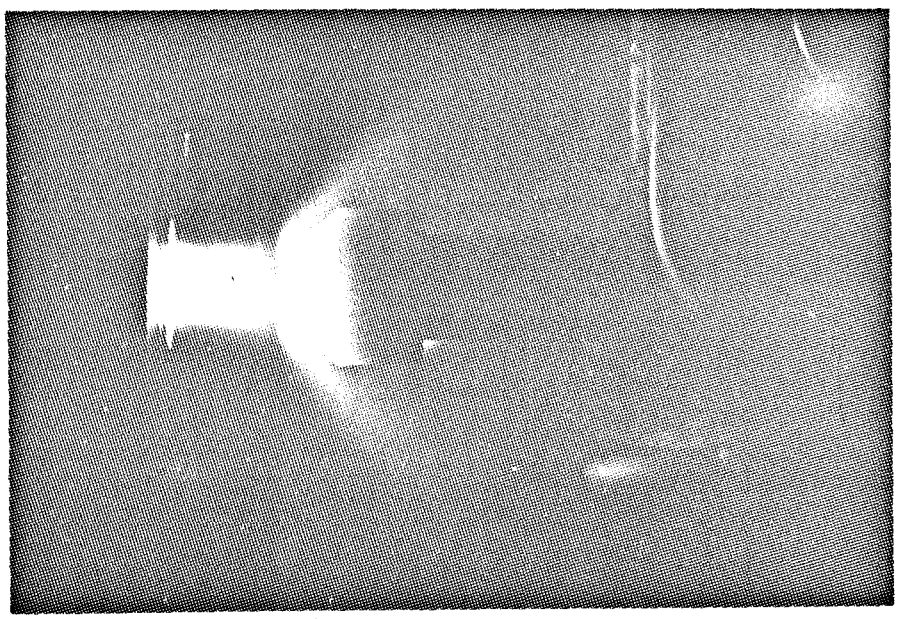

Probe Position $x/D_* = 1$

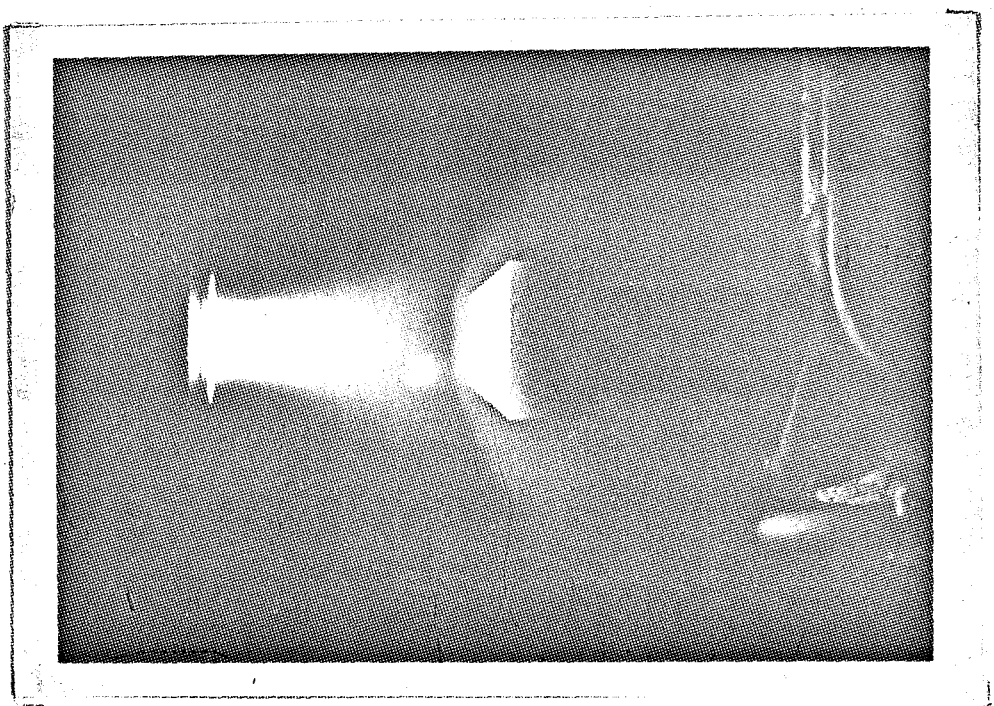

Probe Position $x/D_* = 2$

Figure 25. Dark Space Upstream of Bow Shock on Enthalpy Probe

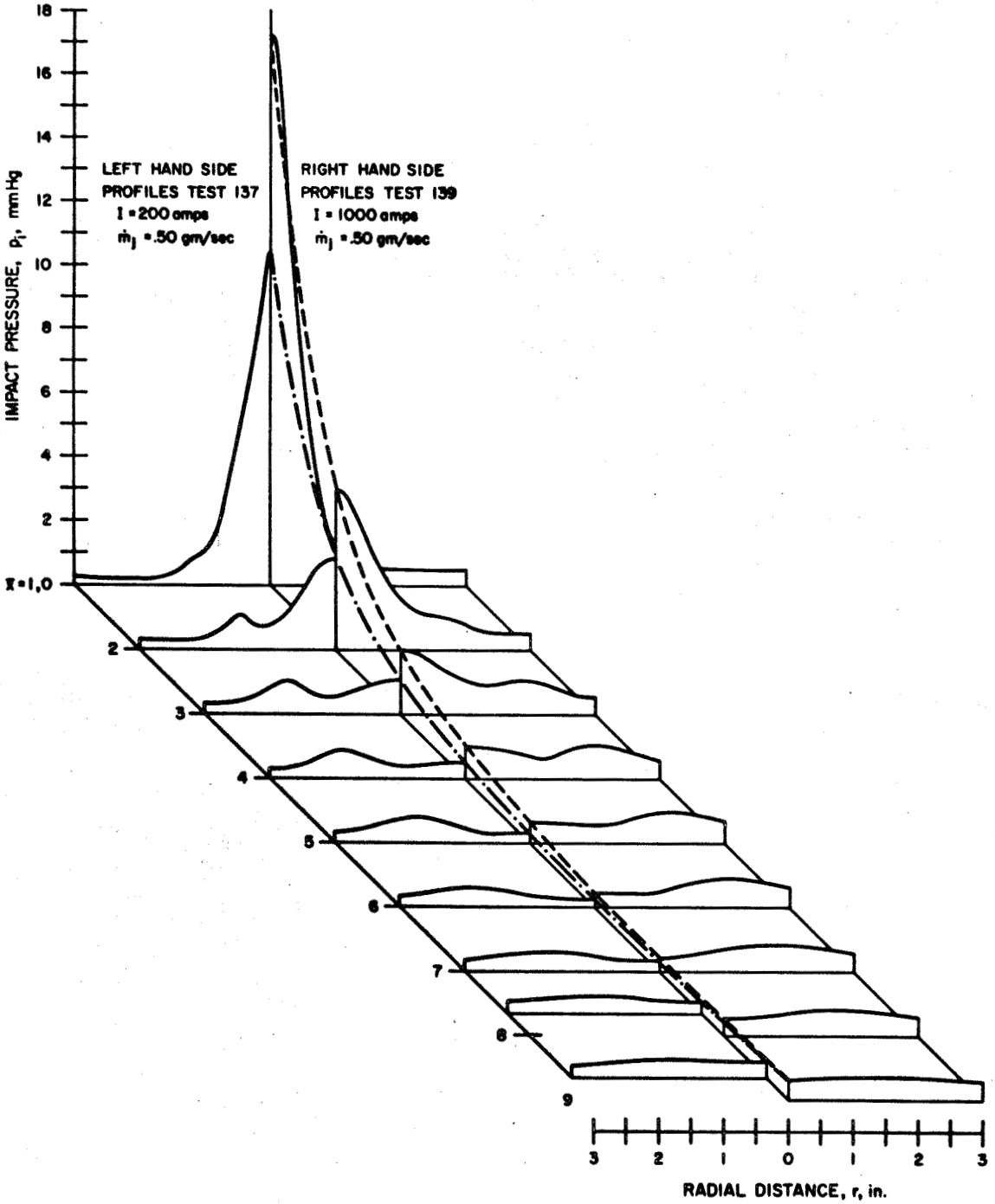

Figure 26. Impact Pressure Profiles in Hot Flow

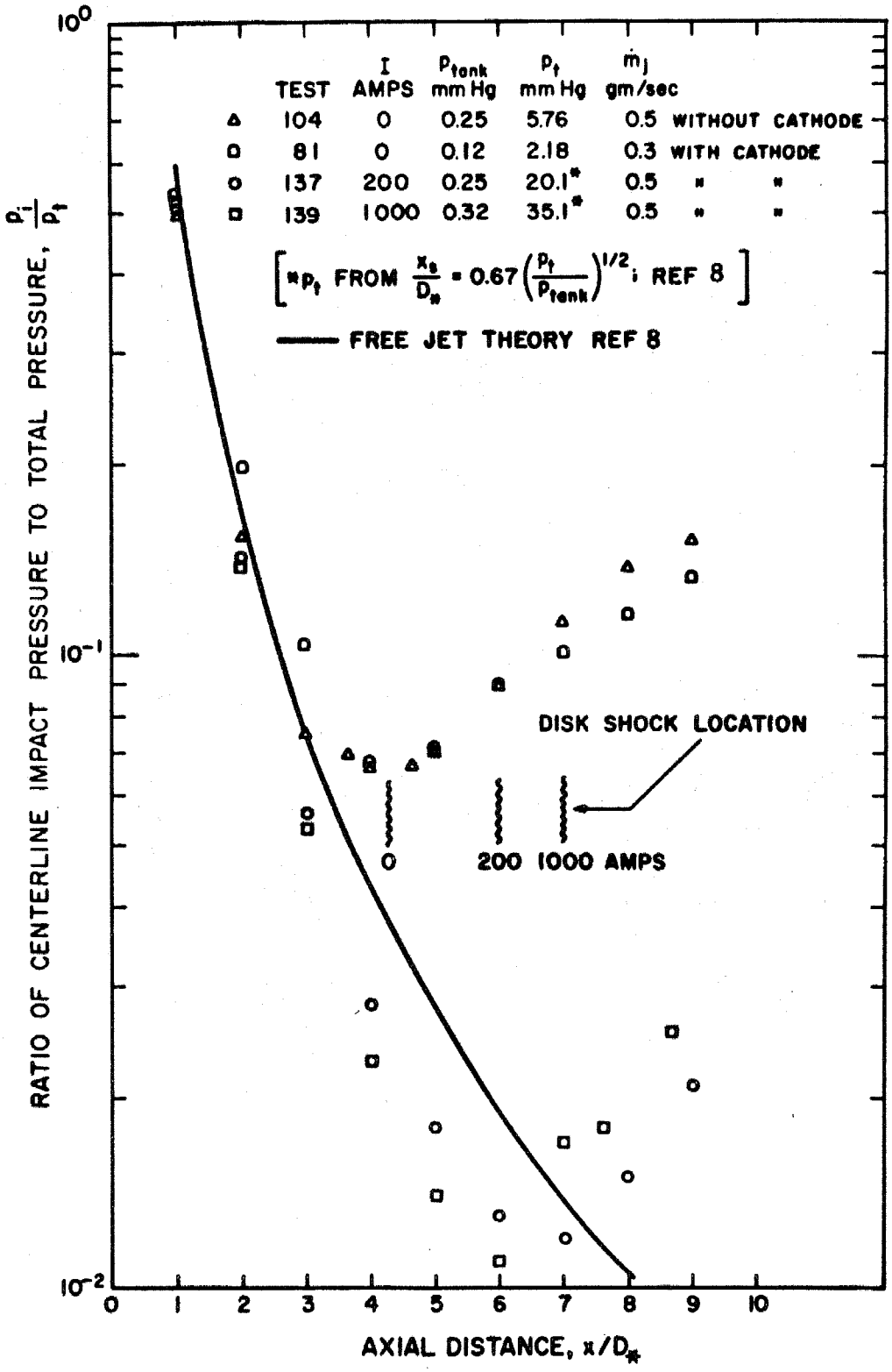

Figure 27. Centerline Impact Pressure Distribution for Unheated and Heated Free Jet

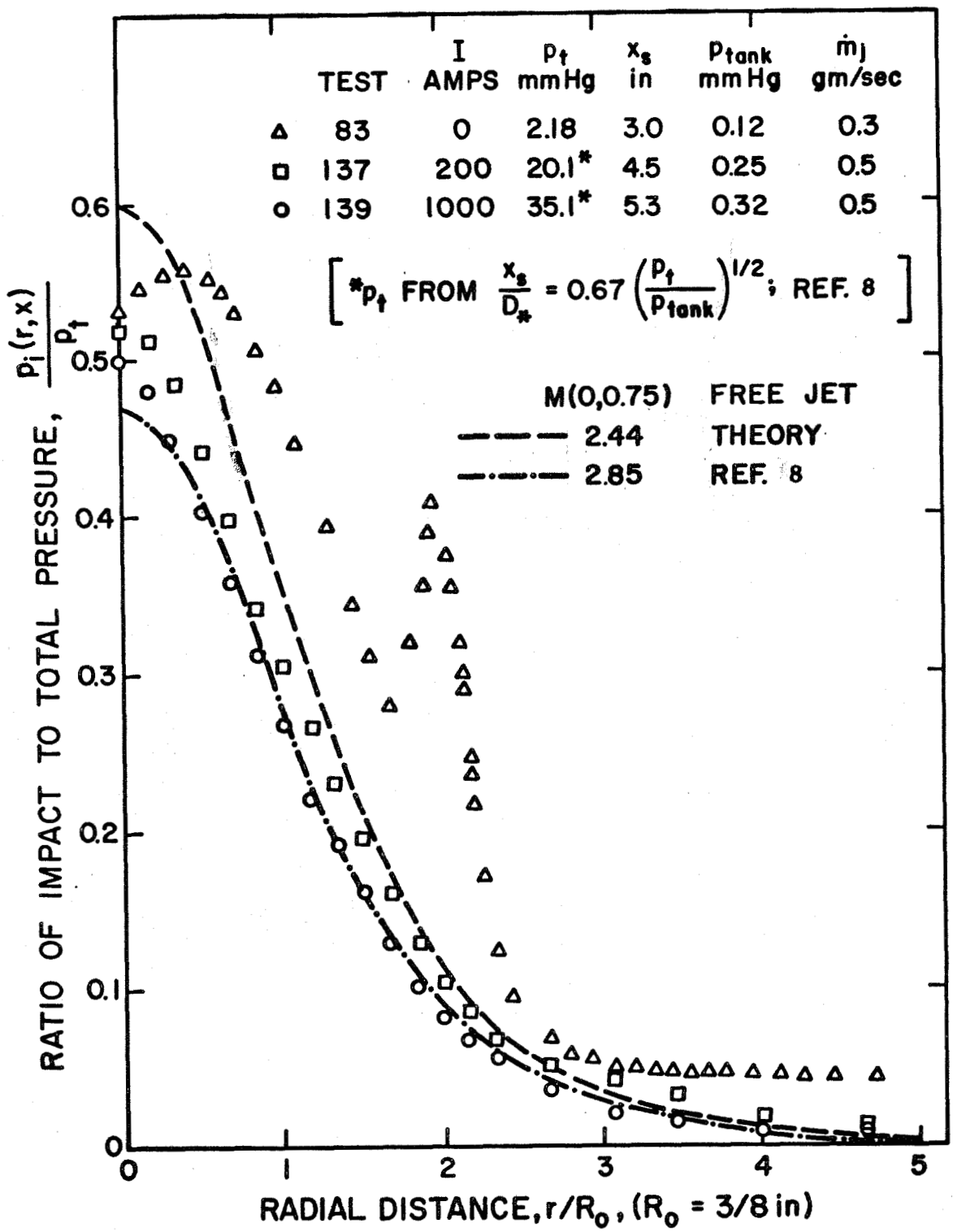

Figure 28. Radial Impact Pressure Distribution for Unheated and Heated Free Jet

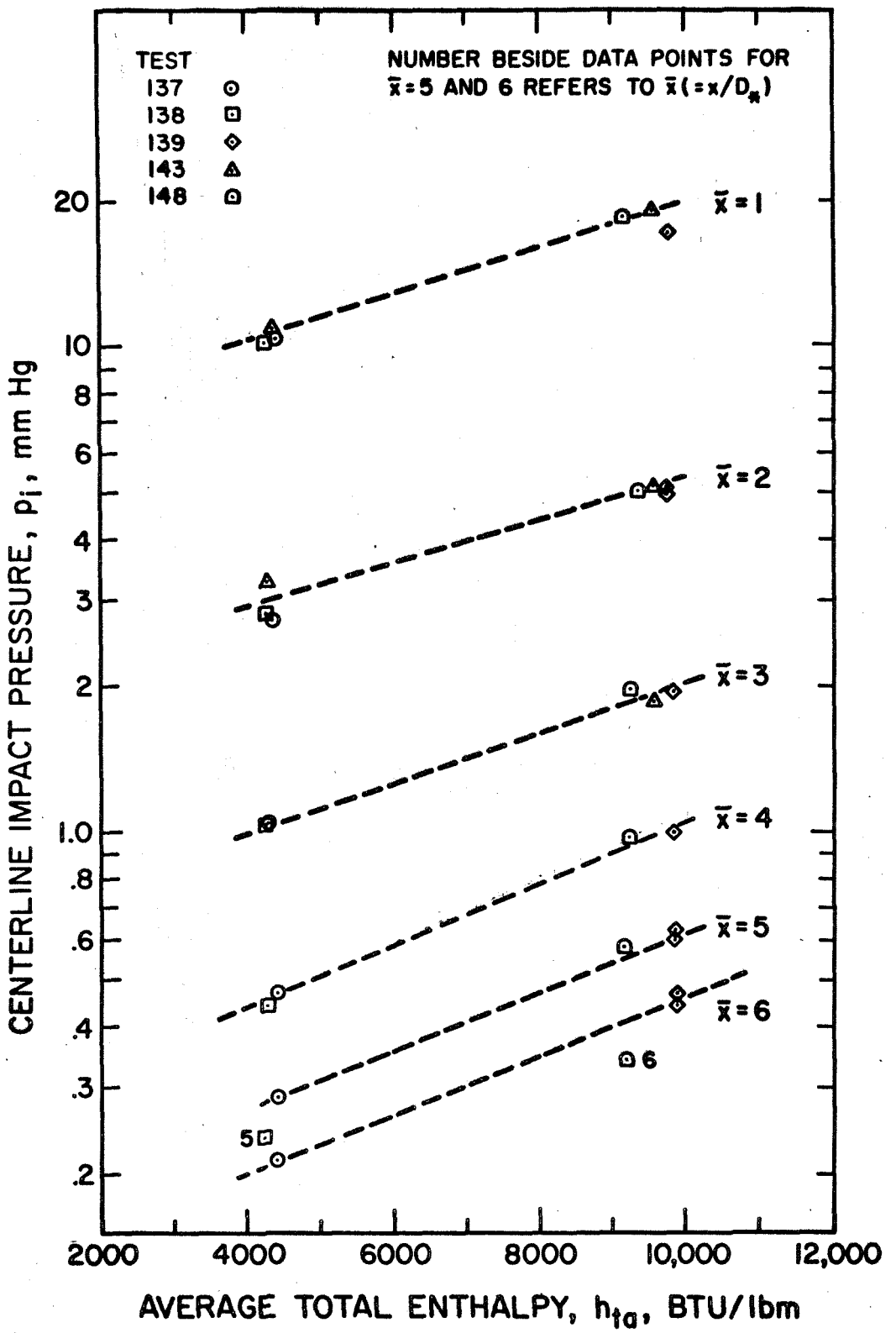

Figure 29. Centerline Impact Pressure versus Average Total Enthalpy

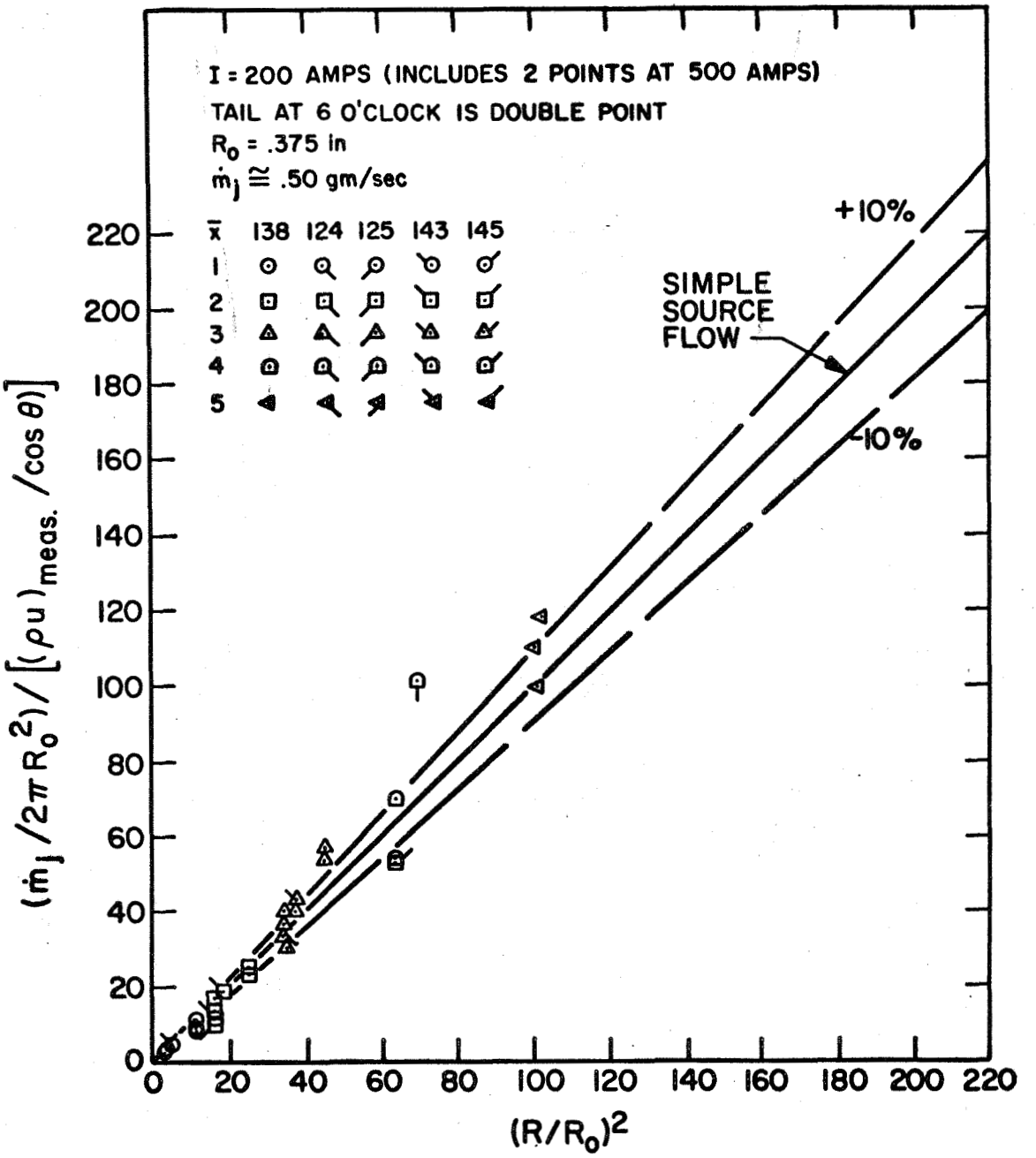

Figure 30. Comparison of Measured Mass Flux to Simple Source Flow Model at 200 amp.

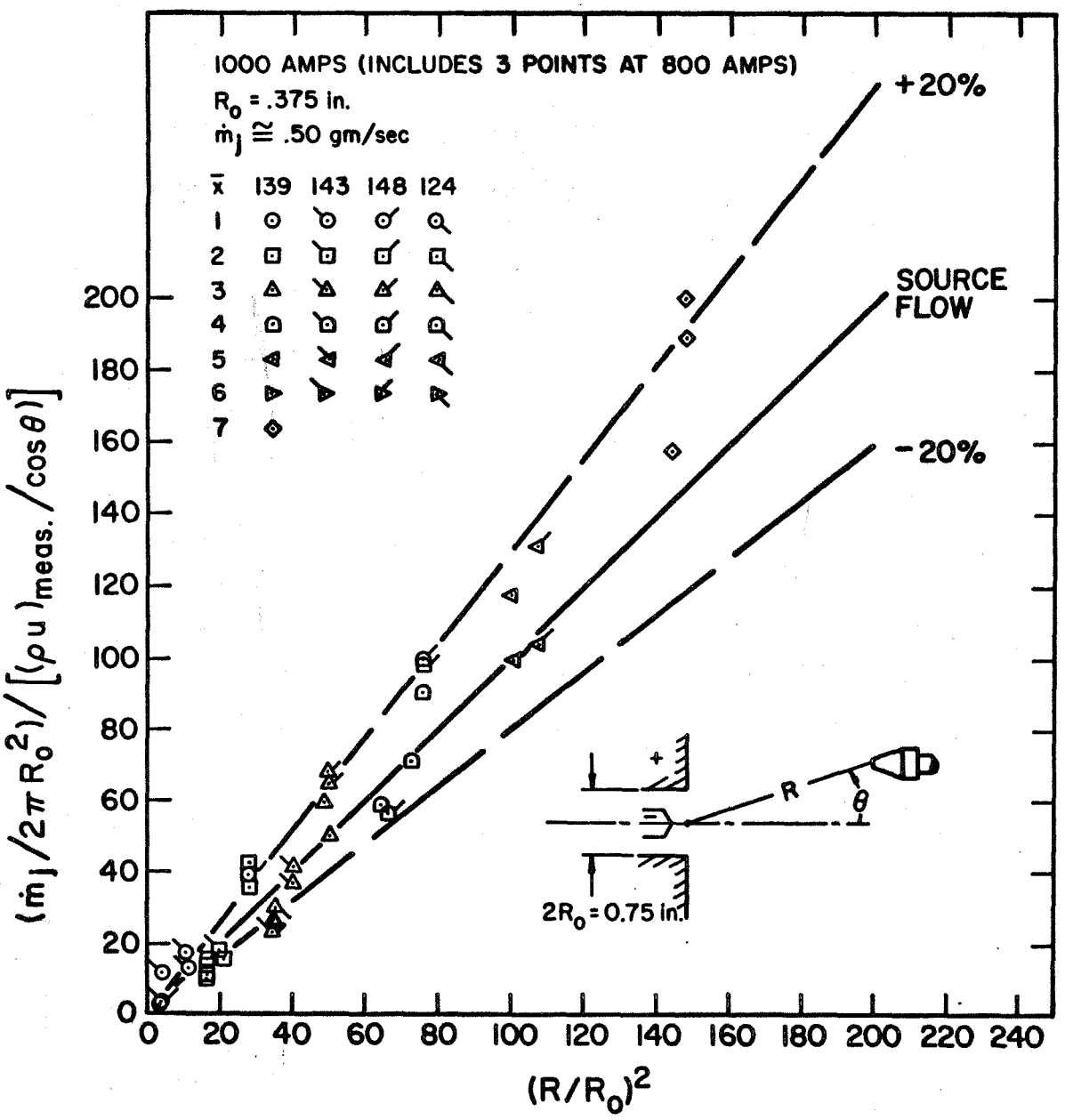

Figure 31. Comparison of Measured Mass Flux to Simple Source Flow Model at 1000 amp.

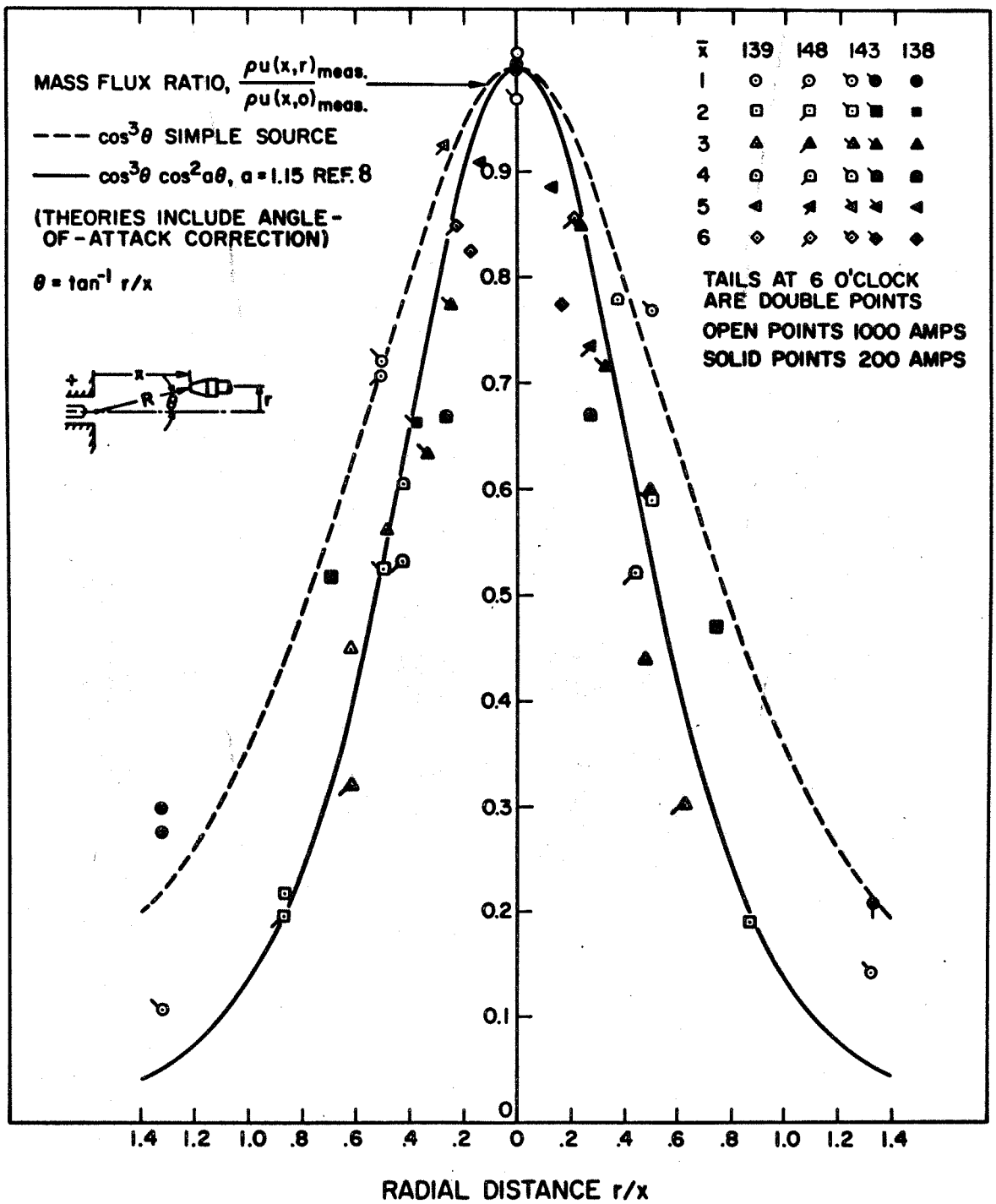

Figure 32. Comparison of Measured Mass Flux Profiles to Sherman's (Ref. 10) Modified Source Flow Model

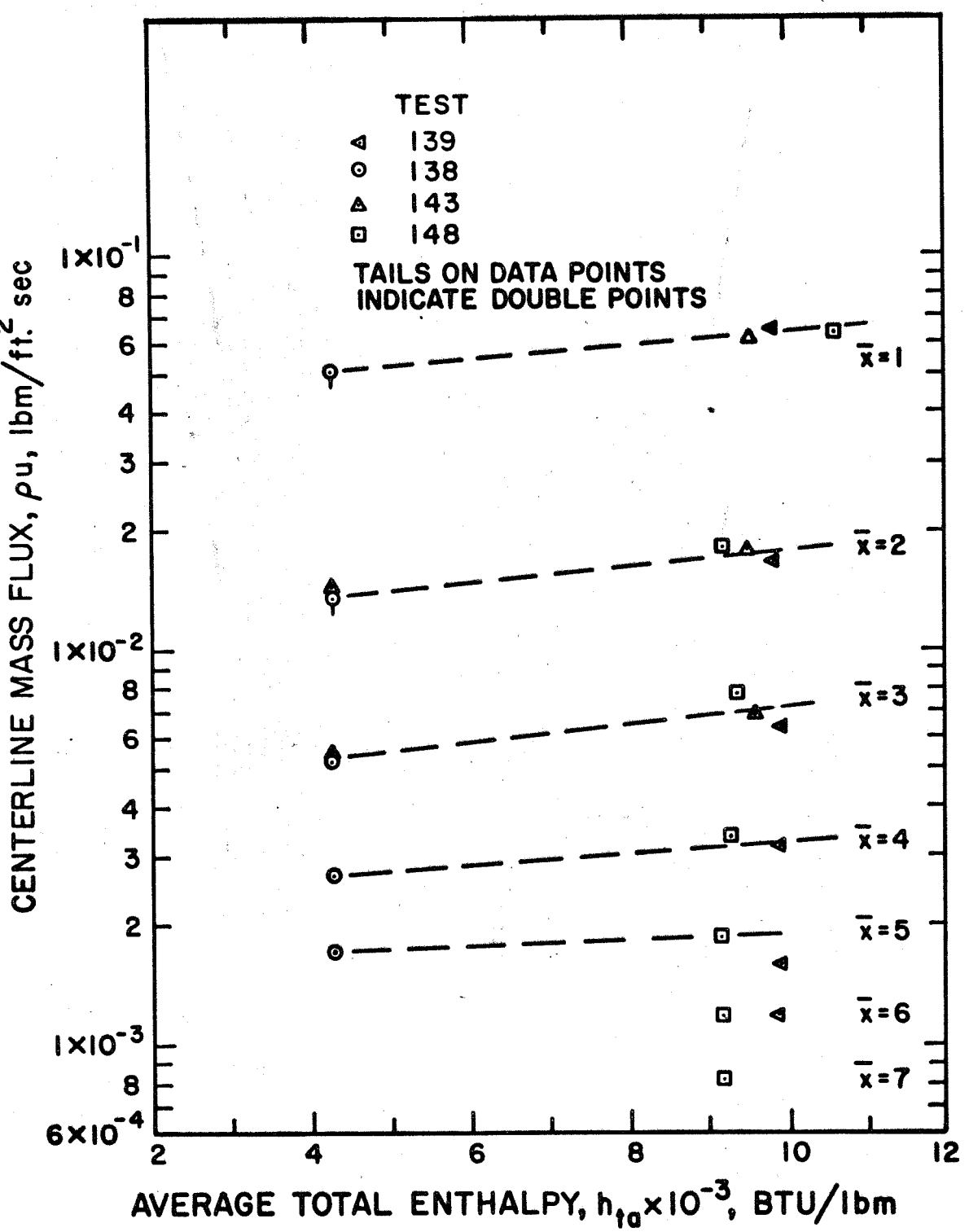

Figure 33. Centerline Mass Flux Distribution Versus Average Total Enthalpy

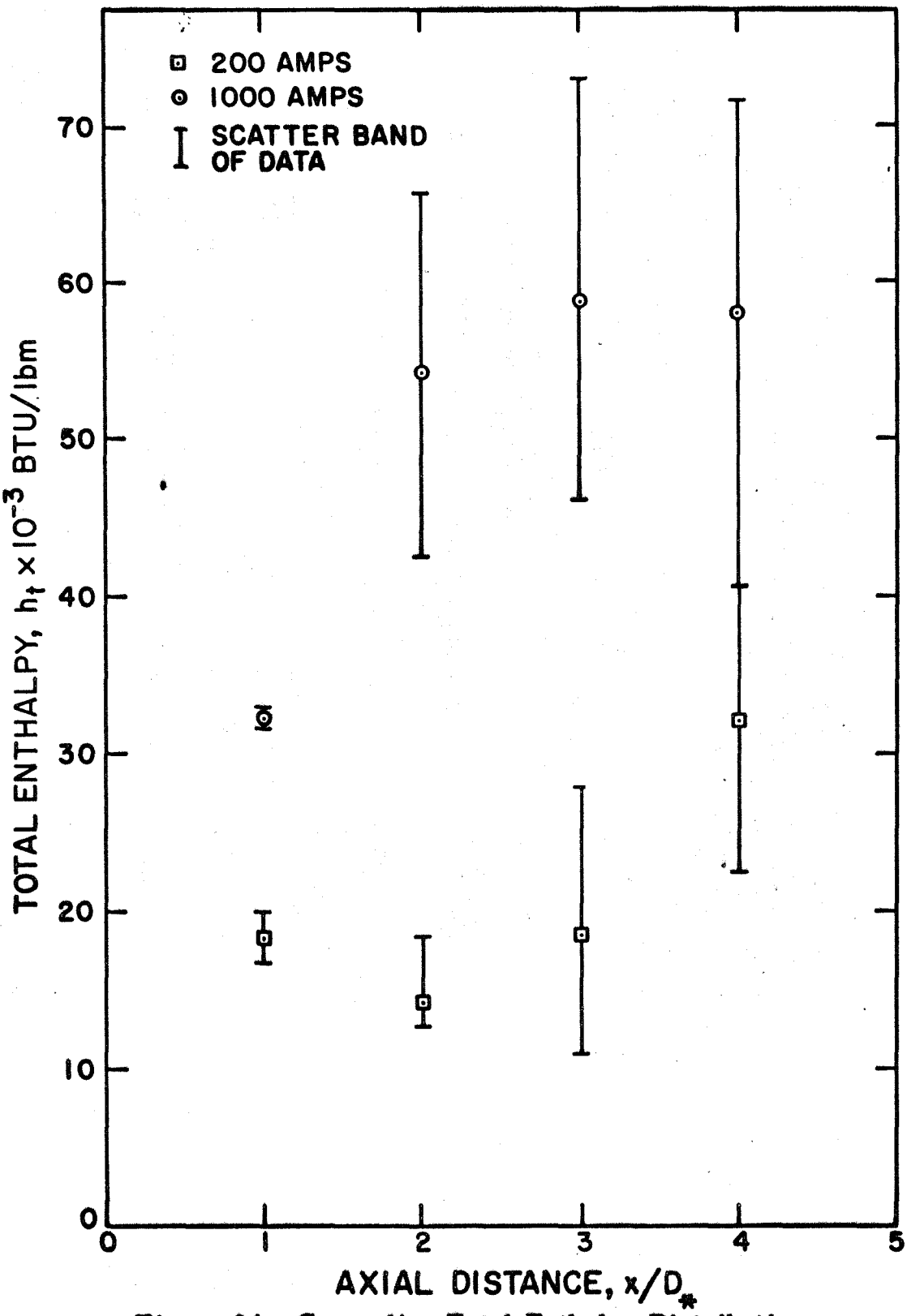

Figure 34. Centerline Total Enthalpy Distribution

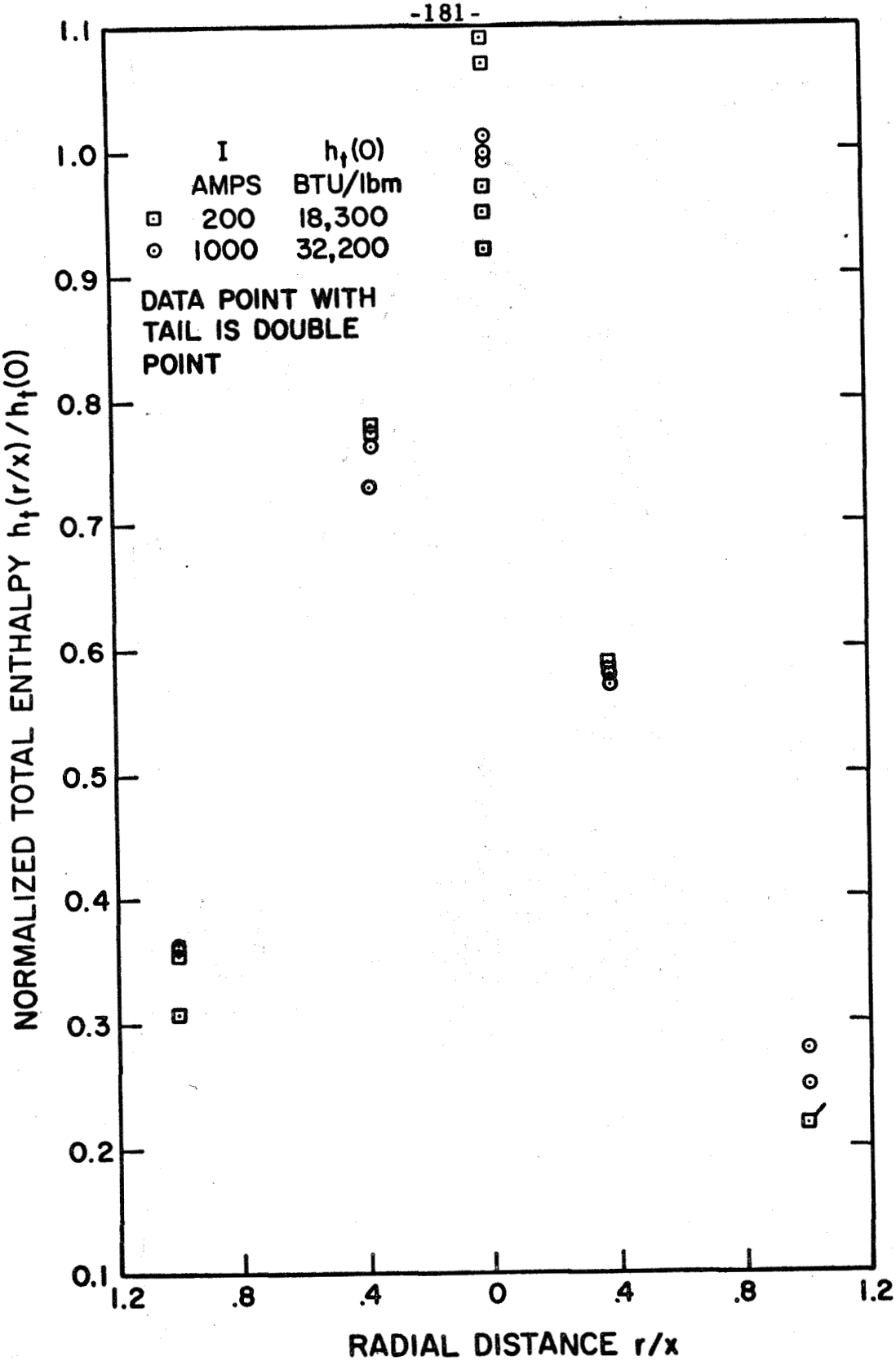

Figure 35. Total Enthalpy Profile at $\bar{x} = 1$

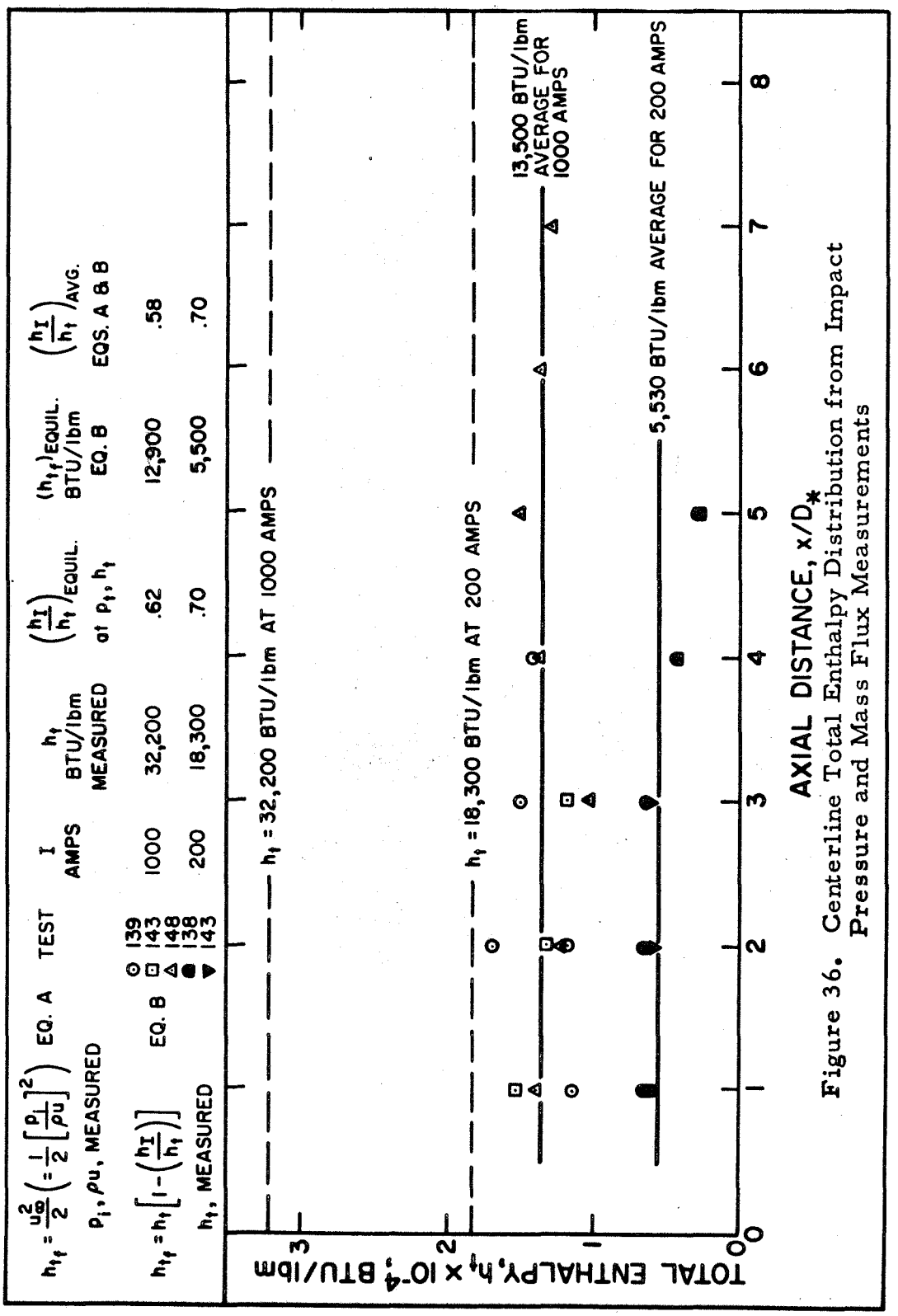

Figure 36. Centerline Total Enthalpy Distribution from Impact Pressure and Mass Flux Measurements

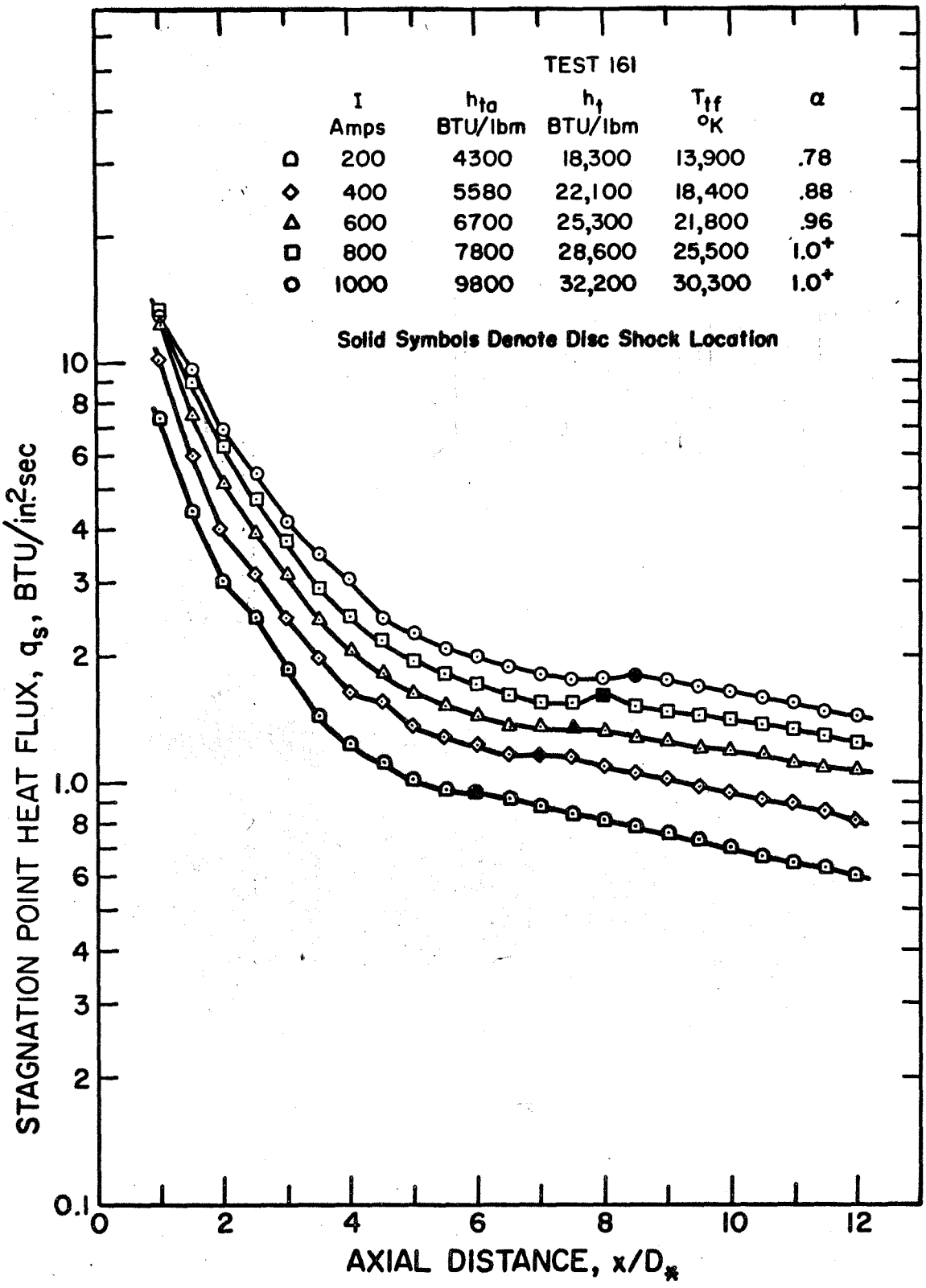

Figure 37. Centerline Stagnation Point Heat Flux Distribution

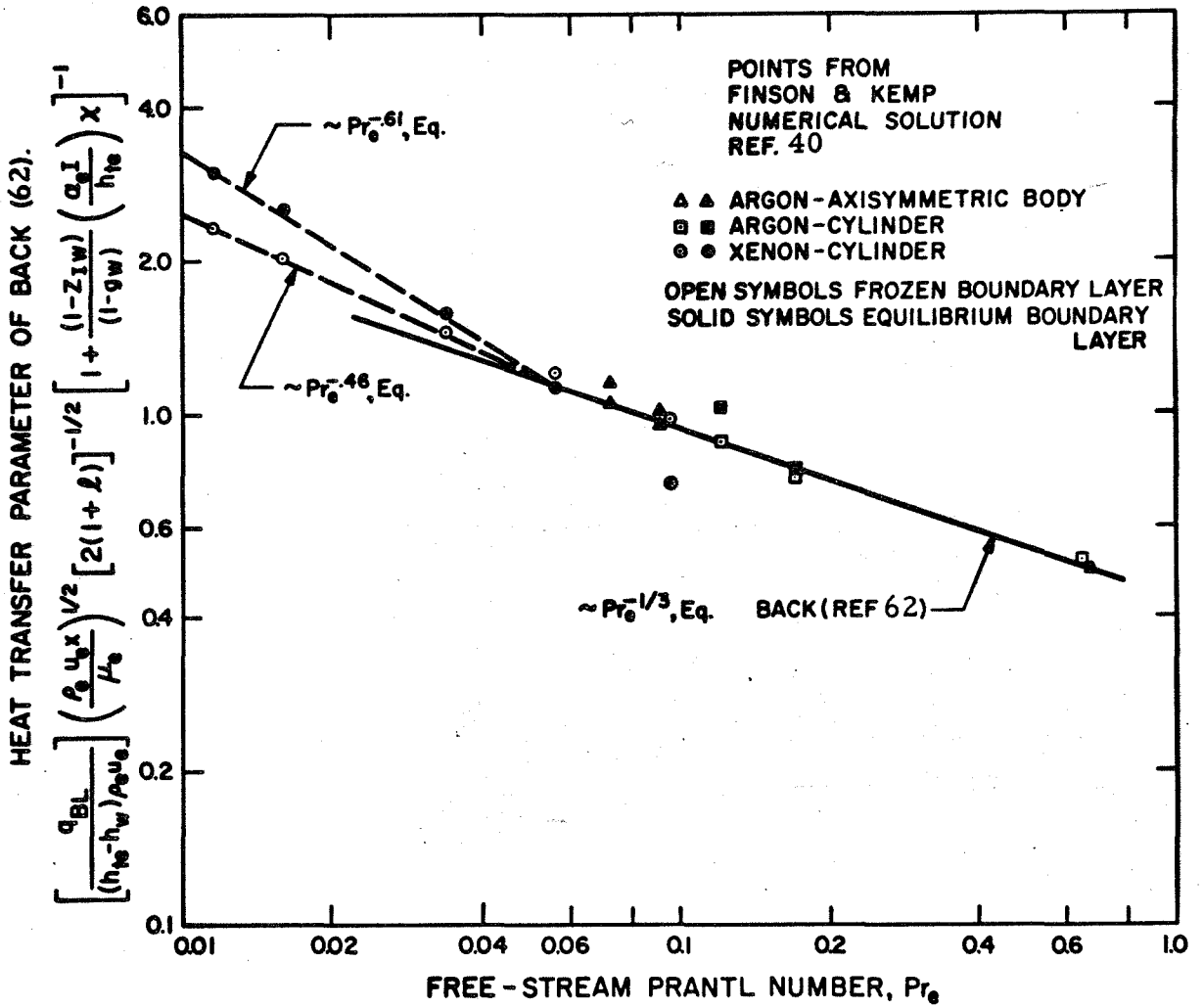

Figure 38. Heat Transfer Parameter versus Prandtl Number

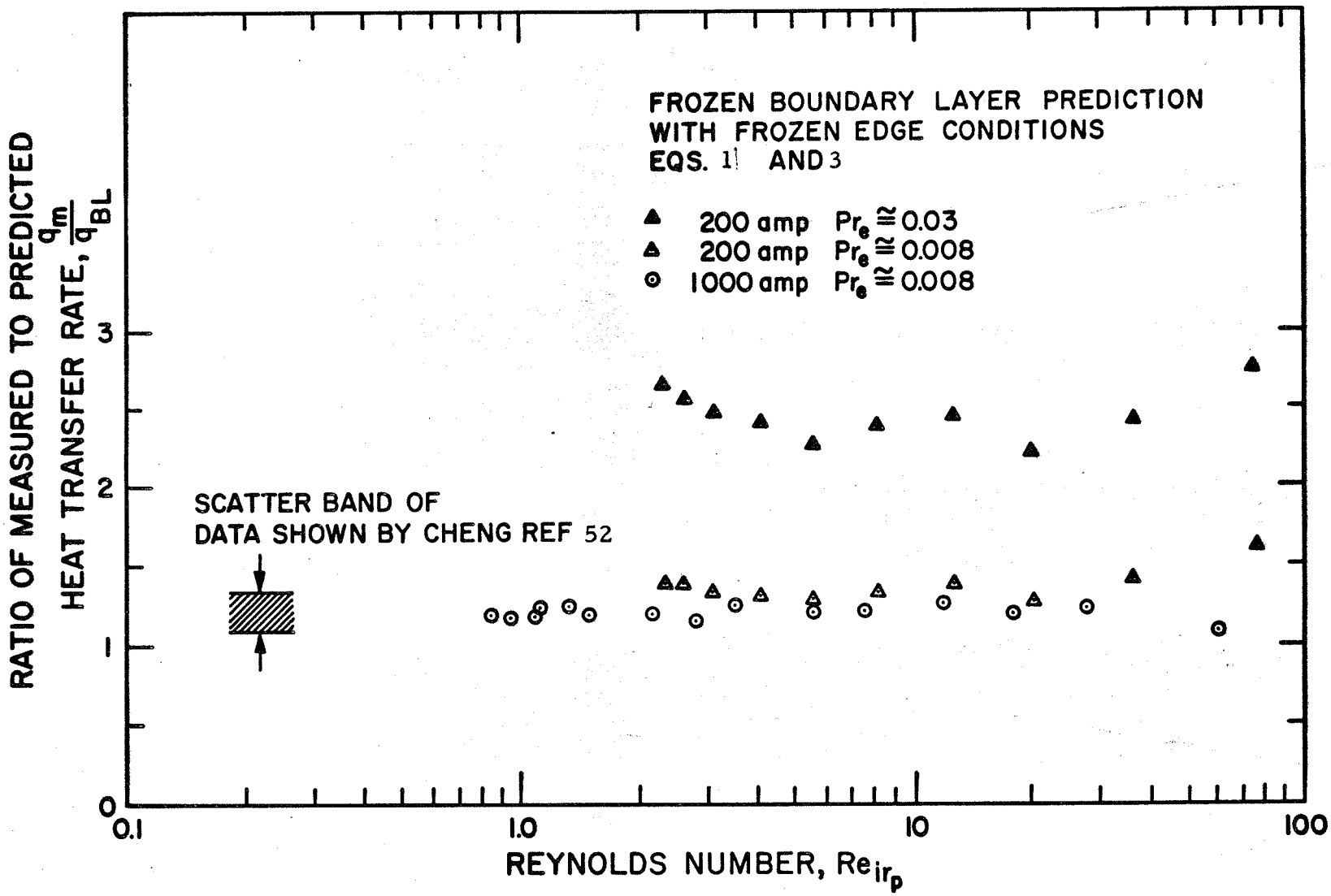

Figure 39. Comparison of Measured Heat Flux to Frozen Flow Boundary Layer Including the Effect of Frozen Flow Boundary Layer Edge Condition

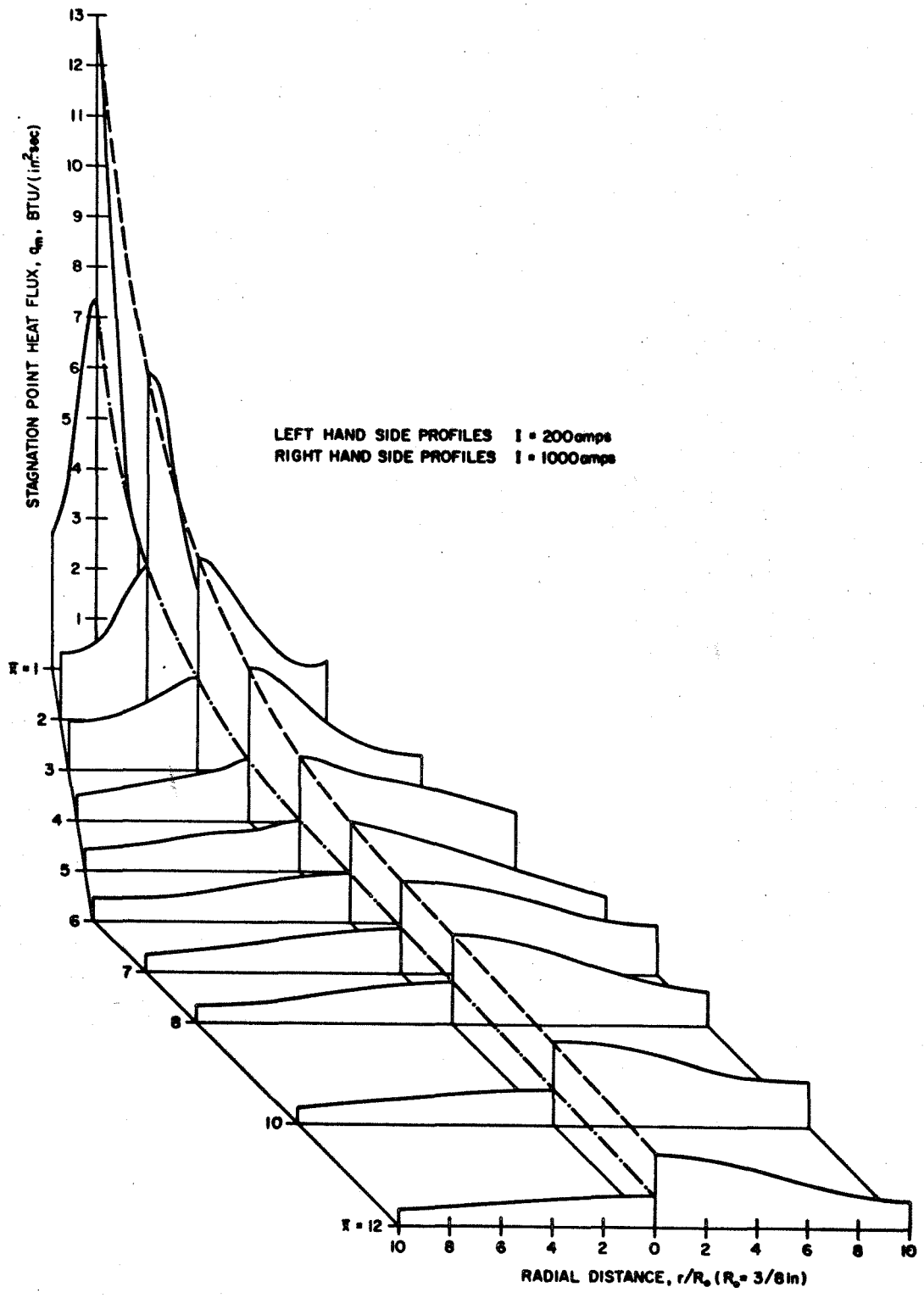

Figure 40. Stagnation Point Heat Flux Profiles for the 200 and 1000 amp. Tests

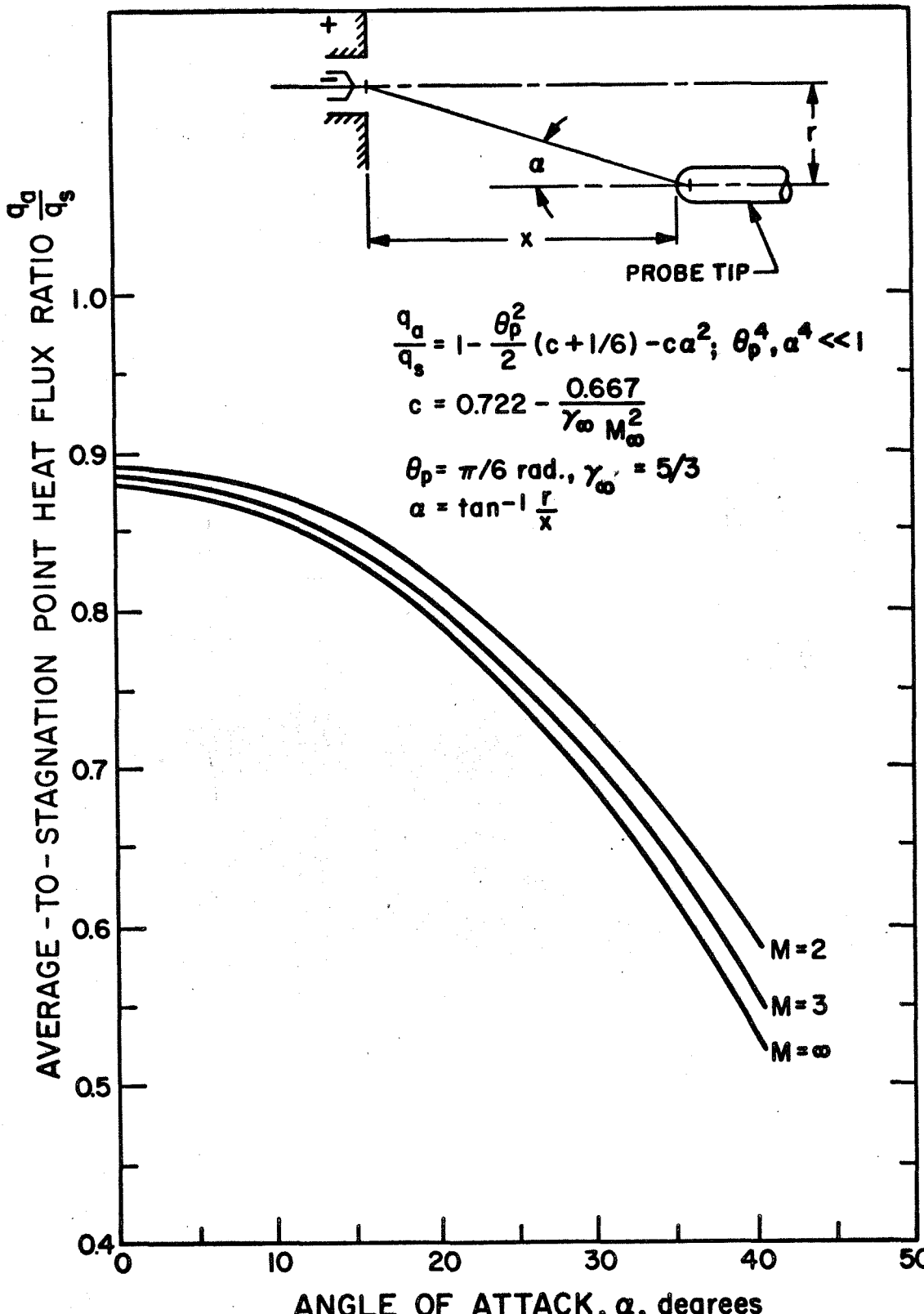

Figure 41. The Effect of Angle-of-Attack on Stagnation Point Heat Transfer Measurements

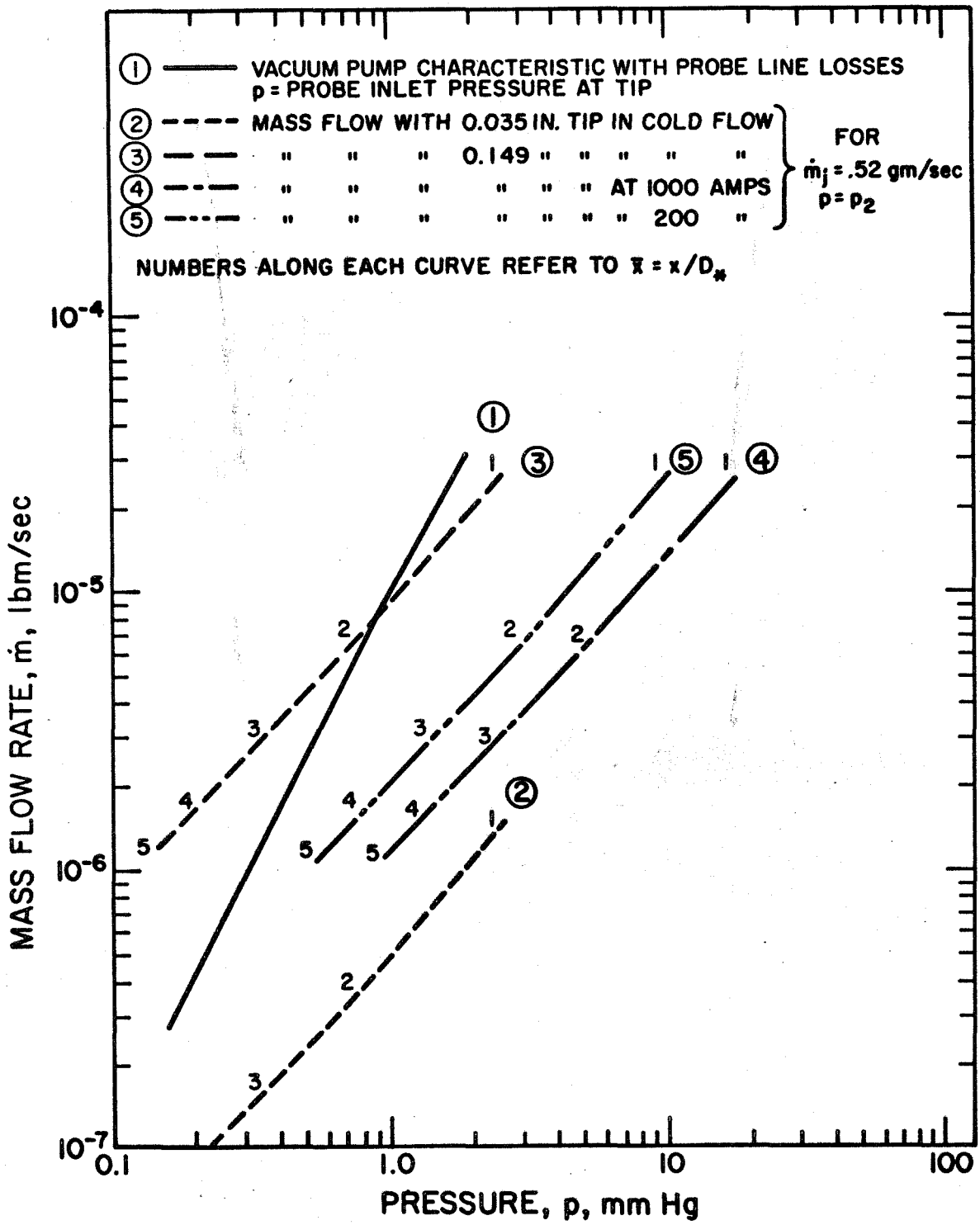

Figure 42. Steady State Mass Flux Sampling Operating Range

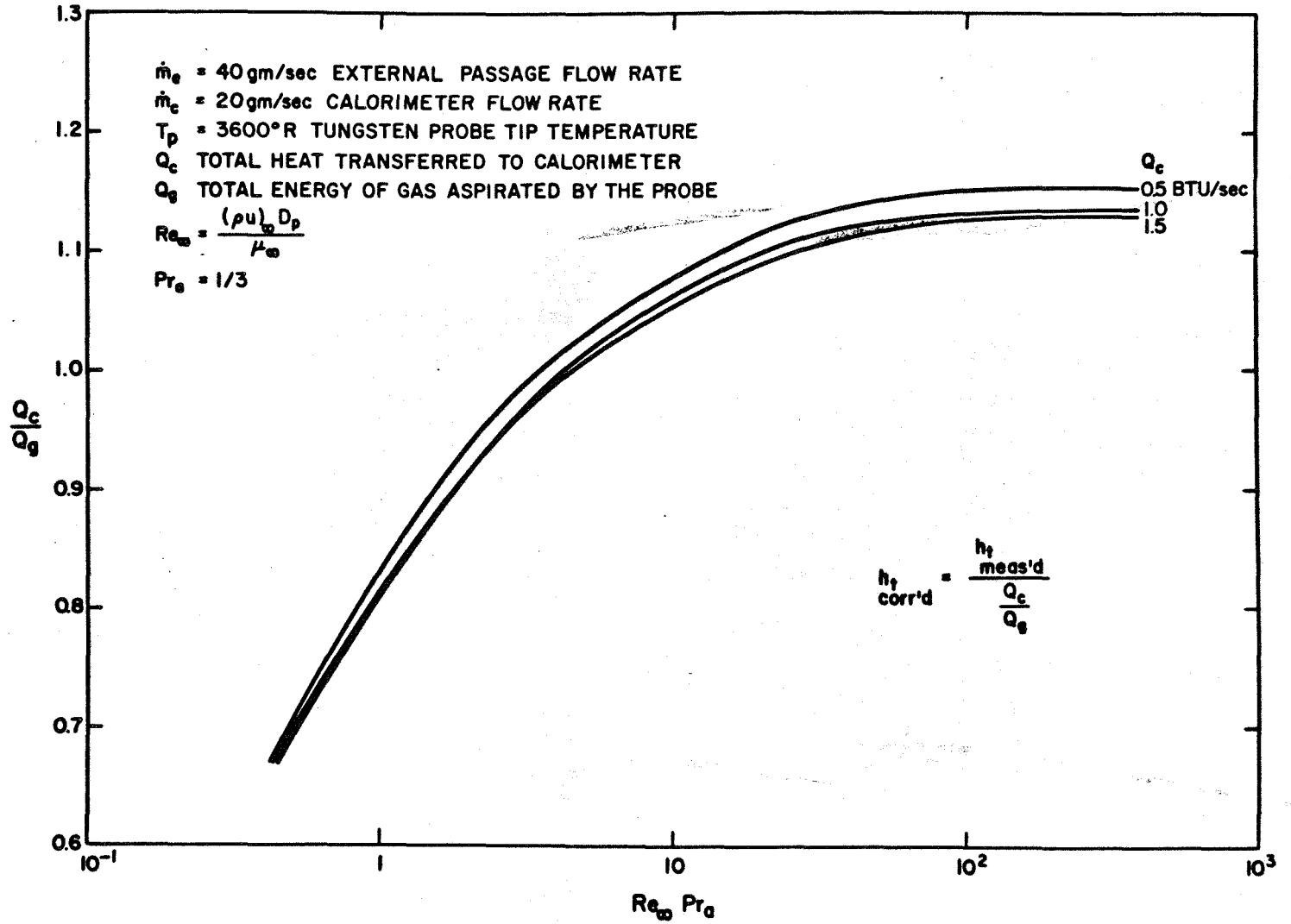

Figure 43. Total Enthalpy Probe Correction

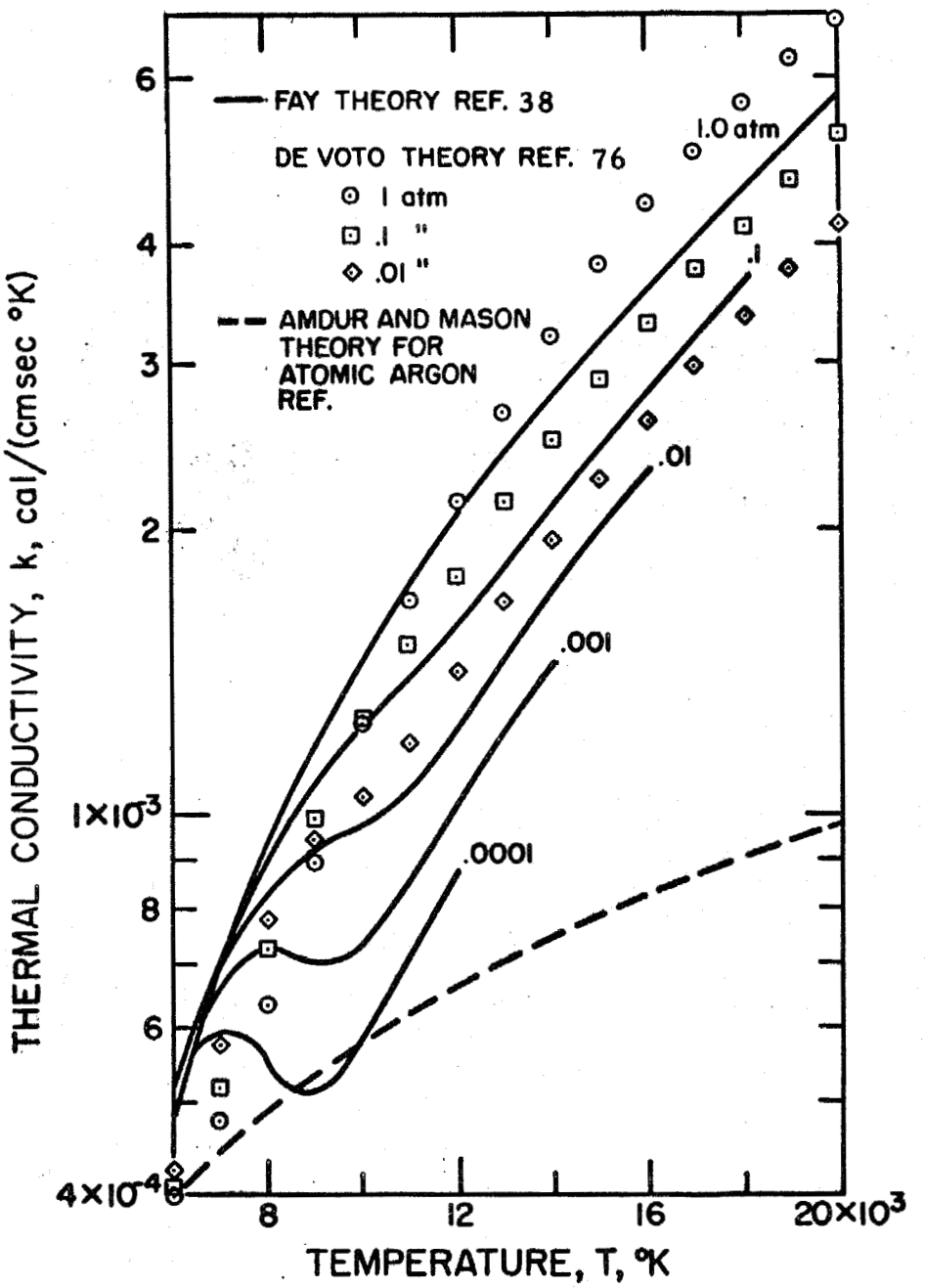

Figure 44. Variation of Thermal Conductivity with Temperature and Pressure for Argon

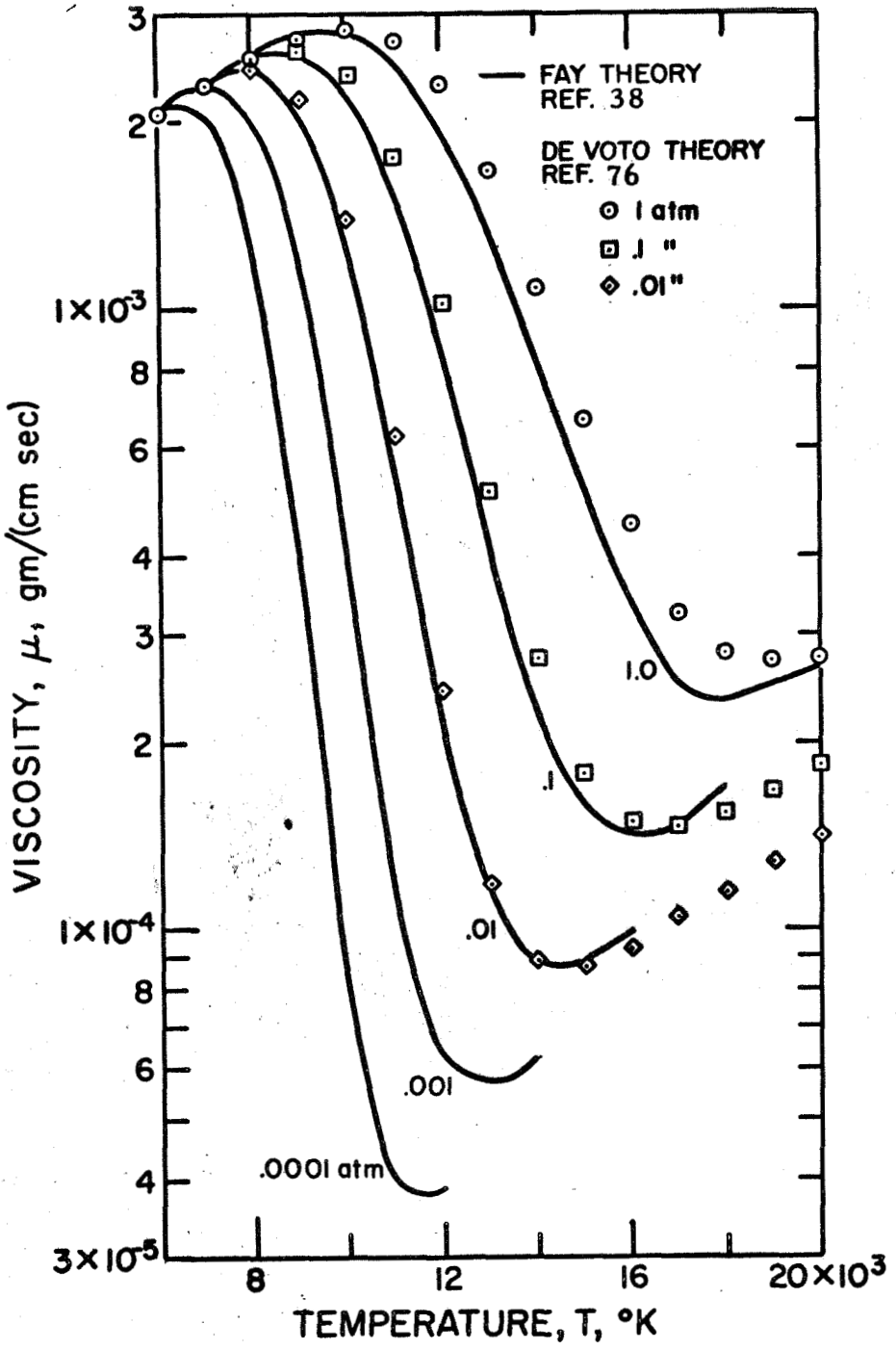

Figure 45. Variation of Viscosity with Temperature and Pressure for Argon

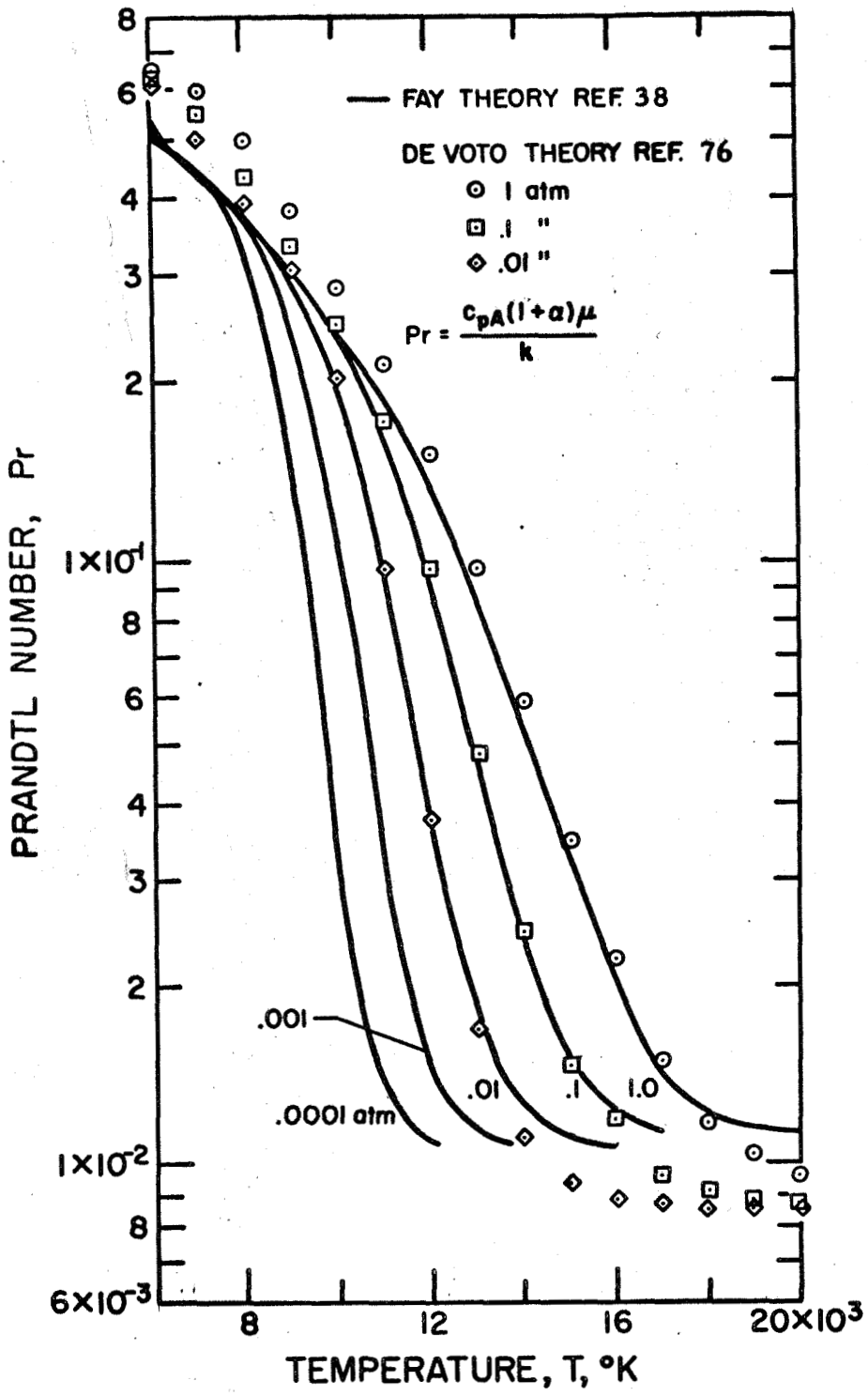

Figure 46. Variation of Prandtl Number with Temperature and Pressure for Argon

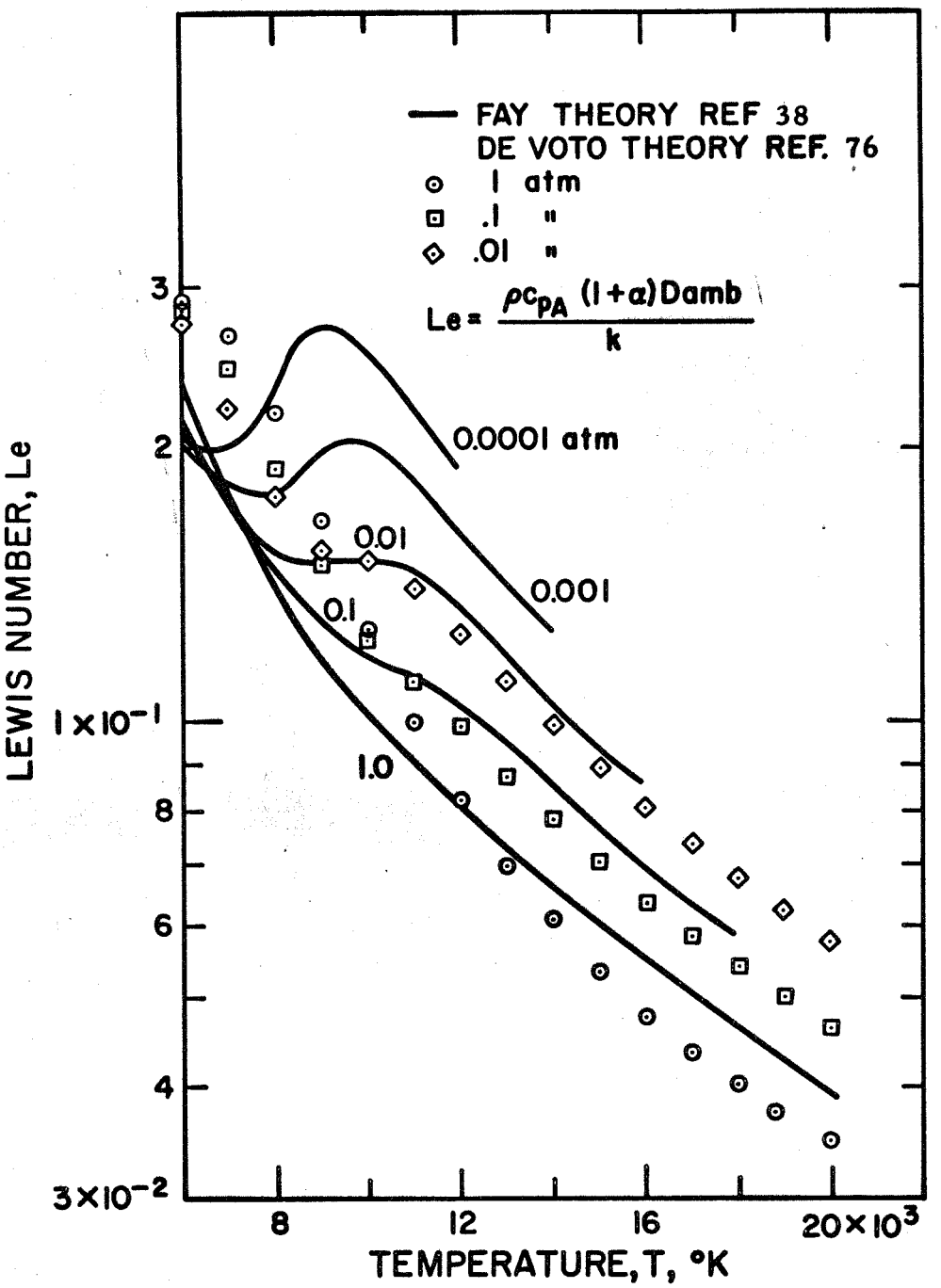

Figure 47. Variation of Lewis Number with Temperature and Pressure for Argon

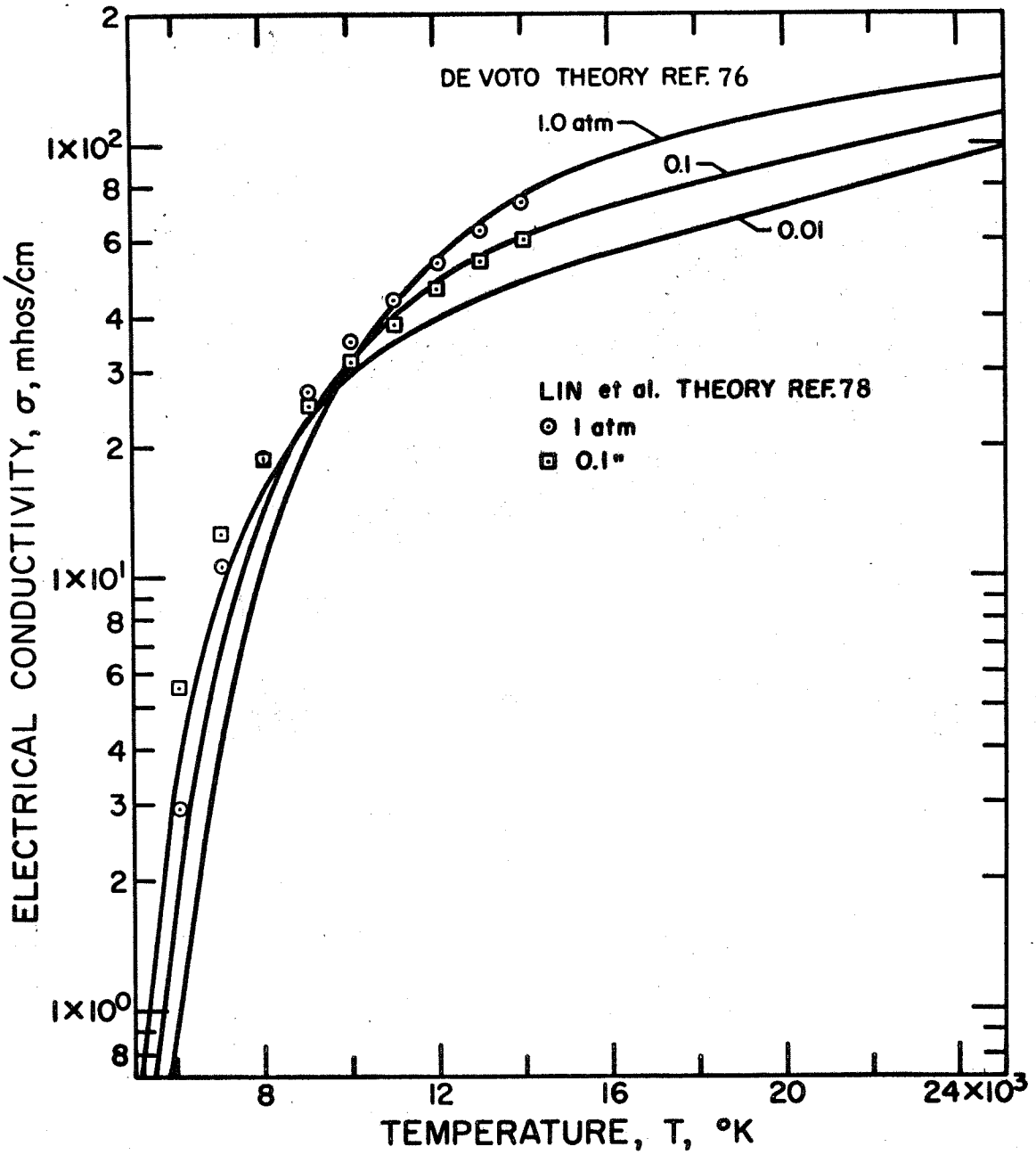

Figure 48. Variation of Electrical Conductivity with Temperature and Pressure for Argon

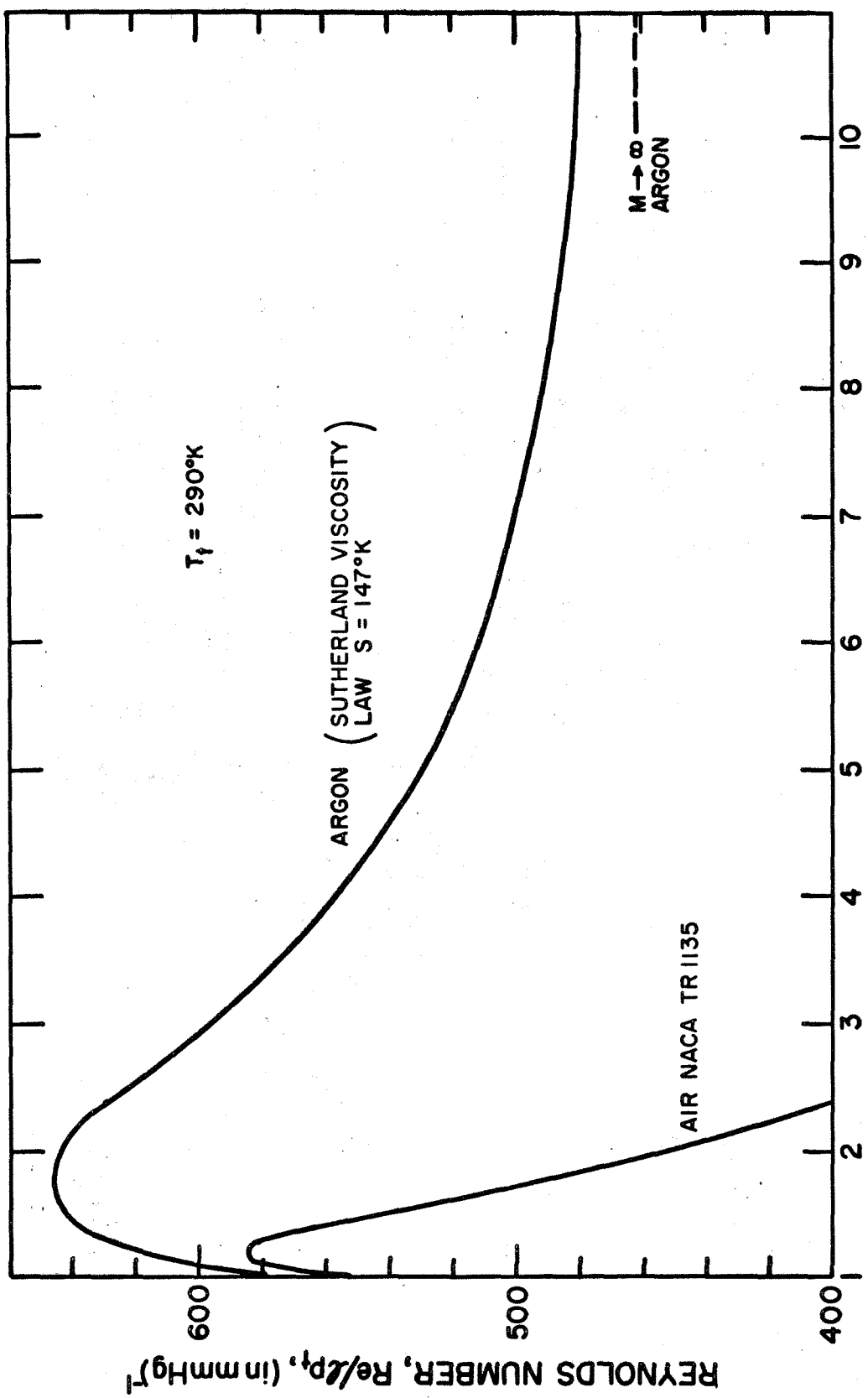

Figure 49. Reynolds Number Variation with Mach Number for Argon

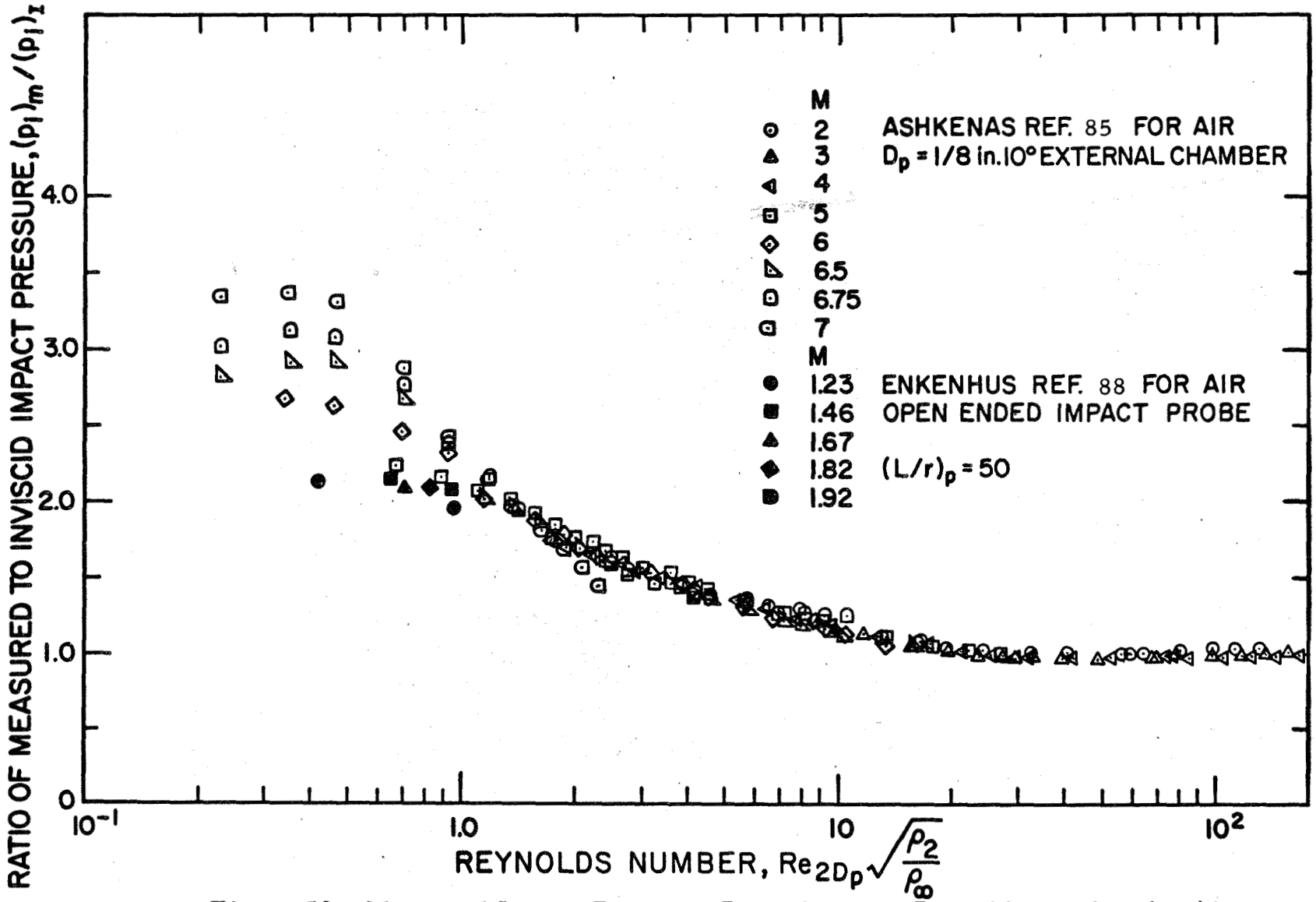

Figure 50. Measured Impact Pressure Dependence on Reynolds Number for Air

I. INTRODUCTION PART II

Argon is used extensively in shock tube, plasma-jet, and plasma-tunnel applications at temperatures that are sufficiently high for electronically excited states and ionization to exist. These effects may cause significant deviation from a perfect gas, in which electronic excitation and ionization are not considered; for instance, thermodynamic properties become a function of pressure as well as temperature. The difficulties encountered in measuring equilibrium thermodynamic properties of gases or plasmas at these temperatures are so great that these properties must be predicted by methods of statistical mechanics. As shown in Section II, the equilibrium thermodynamic properties may be calculated by the partition-function method when the energy levels and degeneracies of the species are known.

The purpose of this investigation was to calculate flow variables for an isentropic expansion of partially ionized argon for stagnation conditions ranging in temperature from 6,000 to 14,000°K and in pressure from 0.1 to 3 atm. Equilibrium properties for argon which have been calculated for this process include the sound speed, entropy, enthalpy, electron concentration, ionization fraction, electrical conductivity, and static-to-stagnation ratios of temperature, pressure, and density. Local values of velocity, mass flux, area ratio, and Reynolds number per centimeter, have also been calculated. The radiation-pressure contribution to the thermodynamic properties is negligible at these temperatures; however, lowering of the ionization potential by electrostatic effects may be significant. The argon

atoms, ions, and electrons are treated as a mixture of perfect gases which obey Maxwell-Boltzmann statistics. However, the mixture is not a perfect gas, because the molecular weight varies and the enthalpy becomes a function of pressure as well as temperature. The author realizes that the equilibrium flow solution is an idealized model of an actual flow process for which reaction rates are indeed finite and particle transit times may be of the order of milliseconds or less. However, the solution of this limiting case does represent an essential step toward the understanding of electronic excitation and ionization effects in the flow of partially ionized argon.

A brief survey of the contributions of other investigations follows. Cann and Ducati (1), using the thermodynamic properties of Gilmore (2), calculated equilibrium thermodynamic properties of argon at temperatures from 1,000 to 14,000°K in 1,000°K increments and pressures from 10^{-4} to 10 atm in 0.5-atm increments of $\log_{10}p$. Their calculations included doubly-ionized atoms. Energy levels corresponding to one electron excited in the n = 5 shell were covered. Their results appear in tabular form as well as on a Mollier diagram.

Bosnjakovic, et al. (3) calculated equilibrium thermodynamic properties of argon, including multiple ionization, for temperatures up to 100,000°K and pressures from 10^{-2} to 10^{2} atm. Insufficient detail relating to the choice of energy levels of the species makes it difficult to assess the validity of the results, which appear as a Mollier diagram.

Knoche (4) made similar calculations at temperatures up to

90,000°K and pressures from approximately 10^{-4} to 10^{2} atm. He included multiple ionization and black-body radiation pressure. At 100,000°K, this radiation contributes an additional partial pressure of 0.25 atm. Again, the choice of pertinent energy levels of the species was not mentioned. The results are presented in several graphs, which include a Mollier diagram.

Arave and Huseby (5) calculated the same properties for temperatures from 3,000 to 16,000°K in increments of 100°K and at pressures from 10^{-4} to 10^{2} atm in increments of 10 atm. Their choice of energy levels of each species is discussed in Appendix A. The results agree very well with the results of Cann and Ducati (1), although only singly-ionized atoms were included in their calculations.

More recently, Baum and Cann (6) as well as Drellishak, Knopp, and Cambel (7) have calculated equilibrium thermodynamic properties of argon, including quadruply-ionized species. The results of Baum and Cann, which appear in tabular form and as a Mollier diagram, range between 1,000 and 25,000°K in 1,000°K increments and between 10^{-4} and 10^{2} atm in 0.5-atm increments of $\log_{10}p$. The findings of Drellishak, Knopp, and Cambel appear in tabular form and range between 5,000 and 35,000°K in 100°K increments for pressures of 0.1, 0.5, 1.0, 2.0, and 5.0 atm. In both investigations, allowance was made for lowering of the ionization potential due to charged-particle field interactions. Olsen (8) used spectroscopic measurements for selecting a best method of treating the plasma corrections lowering the ionization potential, terminating the partition function, and contributing to the total

pressure by means of Debye polarization. Some of the results of these three investigations (and that of Ref. 1) are shown in Table 1 for comparison with thermodynamic properties calculated in this investigation. From the singly-ionized gas model used here, properties are predicted which are within 1% of those cited in the other investigations at 10,000°K; whereas, at 14,000°K and 1 atm, enthalpies are predicted which are 1, 3, and 10% lower than those of Olsen (8), Drellishak, Knopp, and Cambel (7), and Baum and Cann (6), respectively. This departure is apparently a result of lowering the ionization potential, which increases the ion mass fraction and, hence, the energy associated with ionization at a given temperature and pressure. No attempt will be made here to reconcile the 10% spread in predicted enthalpy cited in these investigations. The results of Cann and Ducati (1), including doubly-ionized atoms but not lowering of the ionization potential, are within 0.2% of the results of this investigation and hence show how insensitive the properties of partially ionized argon are to multiple ionization for the limited temperature and pressure range of this study.

Although Mollier diagrams of the type shown in Refs. 1 through 4 are quite versatile in defining the equilibrium state of a gas by following its thermodynamic processes, in published form they do not reflect the accuracy of the state of the art of the present theories, which are generally within 1% agreement below 10,000°K (at 1 atm). Furthermore, time-consuming iterative calculations are required to determine the sonic conditions for the isentropic flow process. The results of the calculations given here facilitate

the use of these flow variables for purposes of analysis. Since there is some experimental and theoretical evidence (Refs. 9 and 10) that certain argon plasma flows near 1 atm pressure and 10,000°K temperature are in thermodynamic equilibrium, information of this kind is quite valuable in arc-jet performance and heat-transfer calculations. At lower pressures, where nonequilibrium conditions may exist, the equilibrium values can serve as a reference.

II. THERMODYNAMIC PROPERTIES DETERMINED BY PARTITION-FUNCTION METHOD

The theory underlying the use of partition functions for calculating thermodynamic properties of a gas is described in Refs. 11 and 12. This method is briefly outlined below and then applied to singly-ionized argon.

For a system of N indistinguishable particles, the internal energy and entropy are related to the partition function as

$$U = kT^2 \left(\frac{\partial \ell n Q_N}{\partial T} \right)_V \tag{1}$$

$$S = k \ell n Q_N + \frac{U}{T} \tag{2}$$

The partition function for a system of N particles, Q_N, is related to the partition function per particle Q as,

$$Q_N = \frac{Q^N}{N!} \tag{3}$$

By choosing one mole of particles, $N = N_0$, and the definition of enthalpy, Eqs. (1), (2) and (3) may be combined to yield the enthalpy and entropy per mole in terms of the partition function per particle,

$$H = \mathcal{R}T^2 \left(\frac{\partial \ell n Q}{\partial T} \right)_V + \mathcal{R}T \tag{4}$$

$$S = \mathcal{R} \ell n \frac{Q}{N_0} + \frac{H}{T} \tag{5}$$

Stirling's formula, $\ell n\, N! \cong N \ell n\, N - N$, has also been used in deriving Eqs. (4) and (5).

By assuming that the translational and internal degrees of freedom are independent, the partition function per particle may be

written as the product of translational and internal parts:

$$Q = Q_{tr} Q_{int} \tag{6}$$

Then, by methods of statistical mechanics, it is found that the translational part is

$$Q_{tr} = \left(\frac{2\pi mkT}{h^2}\right)^{3/2} V \tag{7}$$

where V is the volume occupied by the particle whose temperature and mass are T and m, respectively and h is Planck's constant. Similarly, the internal part of the partition function is found to be

$$Q_{int} = \prod_i Q_{int}^{(i)} \tag{8}$$

where

$$Q_{int}^{(i)} = \sum_{n=0}^{\infty} \exp\left[-\left(\frac{E_n^{(i)} + \mathcal{E}_0^{(i)}}{RT}\right)\right] \tag{9}$$

Equation (9) represents a sum over all internal energy states due to the ith type of internal energy of the particle; i.e., rotational, vibrational, and/or electronic excitational. Only electronic excitation is pertinent to a monatomic gas and, as nuclear effects are negligible, the superscript i will be omitted from $Q_{int}^{(i)}$. Since certain of the electronic energy states E_n are very closely spaced or are, in fact, degenerate, a number g_n of them are counted as degenerate at the nth energy level. Then, Eq. (9) may be written as

$$Q_{int} = \exp\left(-\frac{\mathcal{E}_0}{RT}\right) \sum_{n=0}^{\infty} g_n \exp\left(-\frac{E_n}{RT}\right) \tag{10}$$

Hence, the partition function per particle becomes

$$Q = \left(\frac{2\pi mkT}{h^2}\right)^{3/2} V \exp\left(-\frac{\mathcal{E}_0}{\mathcal{R}T}\right) \sum_{n=0}^{\infty} g_n \exp\left(-\frac{E_n}{\mathcal{R}T}\right) \qquad (11)$$

The energy levels E_n and degeneracies g_n are given in Appendix A. The energy level $\mathcal{E}_0$ is the zero-point energy of the particle above an arbitrarily chosen zero-point energy level for all particles and is also given in Appendix A.

It is desirable to express the volume V in Eq. (11) in terms of pressure and temperature. By combining the first and second laws of thermodynamics for a reversible process and using the definition of the Helmholtz free energy, A = U - TS, the pressure may be calculated as

$$p = -\left(\frac{\partial A}{\partial V}\right) T \qquad (12)$$

The Helmholtz free energy per mole is

$$A = -\mathcal{R}T\left(\ell n \frac{Q}{N_0} + 1\right) \qquad (13)$$

Hence, the equation of state for 1 mole of indistinguishable particles becomes

$$p = \frac{\mathcal{R}T}{V} \qquad (14)$$

The partition function of each species, A, A^+, and e^-, for the argon atom, argon ion, and free electron, proceeds directly from Eq. (11) and Appendix A. Since the logarithm of the partition function divided by Avogadro's number will be used frequently, it is convenient to express the results as

$$\ln \frac{Q(A)}{N_0} = \frac{5}{2} \ln T + 1.866$$

$$+ \ln \left[1 + 12 \exp \left(- \frac{135000}{T} \right) \right] - \ln p \qquad (15)$$

$$\ln \frac{Q(A^+)}{N_0} = \frac{5}{2} \ln T + 1.866 + \ln \left[4 + 2 \exp \left(- \frac{2060}{T} \right) \right.$$

$$\left. + 2 \exp \left(- \frac{156200}{T} \right) \right] - \frac{182900}{T} - \ln p \qquad (16)$$

$$\ln \frac{Q(e^-)}{N_0} = \frac{5}{2} \ln T - 14.24 - \ln p \qquad (17)$$

By combining Eqs. (4) and (11), the enthalpy becomes

$$H = \frac{5}{2} \mathcal{R} T + \frac{\sum_{n=0}^{\infty} g_n E_n \exp \left(- \frac{E_n}{\mathcal{R} T} \right)}{\sum_{n=0}^{\infty} g_n \exp \left(- \frac{E_n}{\mathcal{R} T} \right)} + \mathcal{E}_0 \qquad (18)$$

The last two terms of Eq. (18) represent the contribution of electronic excitation and ionization to the enthalpy of an arbitrary species. The enthalpy of each species may be written at once from Eq. (18) and Appendix A as

$$\frac{H(A)}{\mathcal{R} T} = \frac{5}{2} + \frac{(12)(135000) \exp \left(- \frac{135000}{T} \right)}{T \left[1 + 12 \exp \left(- \frac{135000}{T} \right) \right]} \qquad (19)$$

$$\frac{H(A^+)}{\mathcal{R} T} = \frac{5}{2}$$

$$+ \frac{(2060) \exp \left(- \frac{2060}{T} \right) + (156200) \exp \left(- \frac{156200}{T} \right)}{T \left[2 + \exp \left(- \frac{2060}{T} \right) + \exp \left(- \frac{156200}{T} \right) \right]} + \frac{182900}{T} \qquad (20)$$

$$\frac{H(e^-)}{\mathcal{R}T} = \frac{5}{2} \tag{21}$$

The entropy of each species is calculated from Eq. (5), which is in terms of the species partition function and species enthalpy already calculated. Thus, the entropy per mole of any species i is

$$\frac{S(i)}{\mathcal{R}} = \ell n \frac{Q(i)}{N_0} + \frac{H(i)}{\mathcal{R}T} \tag{22}$$

The partition function for a mixture of gases obeying Maxwell-Boltzmann statistics (12), i.e., for argon atoms and ions and free electrons, is

$$Q_N = \prod_i \frac{Q(i)^{N(i)}}{N(i)!} = \frac{Q(A)^{N(A)} Q(A^+)^{N(A^+)} Q(e^-)^{N(e^-)}}{N(A)!\, N(A^+)!\, N(e^-)!} \tag{23}$$

The total number of particles is

$$N = N(A) + N(A^+) + N(e^-)$$

By substitution of Eq. (23) into Eqs. (1) and (2) and by use of the definition of enthalpy, it can be shown that except for the entropy, the properties per mole of this reacting gas mixture may be simply calculated by summing the species properties previously obtained for a mole of indistinguishable particles. In generalizing Eqs. (1) and (2) to a mixture, the number of each species N(i) is held constant, along with the volume V, in performing the differentiation of Eq. (23). The mixture properties per mole, $N = N_0$, become

$$H = \sum_i X(i)\, H(i) \tag{24}$$

$$S = \sum_i [X(i)S(i) - \mathcal{R}X(i)\,\ell n\, X(i)] \tag{25}$$

where the summation is over the component species A, A^+, and e^-, and the values of H(i) and S(i) are obtained from Eqs. (19), (20), (21), and (22). The second term in the brackets of Eq. (25) is conventionally called the entropy of mixing term. The mole fractions X(i) may be expressed in terms of the ion mass fraction

$$\alpha = \frac{\rho(A^+)}{\rho} = \frac{m(A^+)N(A^+)}{m(A)N(A) + m(A^+)N(A^+) + m(e^-)N(e^-)} \tag{25a}$$

Neglecting the mass of the electron compared to that of the ion, α becomes

$$\alpha = \frac{N(A^+)}{N(A)+N(A^+)} = \frac{N(e^-)}{N(A)+N(A^+)} = \frac{N(e^-)}{N(n)} \tag{26}$$

where N(n) is the number of nuclei in one mole N_0 of the mixture. The second equality in Eq. (26) follows from the fact that the gas is singly-ionized and neutral. Noting that

$$\rho = \sum_i \rho(i)$$

and using Eqs. (25a) and (26), the atom mass fraction becomes

$$1 - \alpha = \frac{N(A)}{N(n)} \tag{27}$$

Using Eqs. (26) and (27) and the definition of mole fraction $X(i) = N(i)/N_0$, the X(i) become

$$X(A) = \frac{N(A)}{N_0} = \frac{(1-\alpha)N(n)}{N(n) + N(e^-)} = \frac{1-\alpha}{1+\alpha} \tag{28}$$

$$X(A^+) = X(e^-) = \frac{\alpha N(n)}{N(n) + N(e^-)} = \frac{\alpha}{1+\alpha} \tag{29}$$

For applications of our interest the enthalpy and entropy per unit mass rather than per mole, is a more convenient quantity. Expressed in nondimensional form and written out in full, they become

$$\frac{\overline{H}}{RT} = (1 + \alpha)\frac{H}{RT}$$

$$\frac{\overline{H}}{RT} = \frac{5}{2}(1 + \alpha) + 182900\frac{\alpha}{T}$$

$$+ (1-\alpha)\left\{\frac{(12)(135000)\exp\left(-\frac{135000}{T}\right)}{T\left[1 + 12\exp -\left(\frac{135000}{T}\right)\right]}\right\}$$

$$+ \alpha\left\{\frac{(2060)\exp\left(-\frac{2060}{T}\right) + (156200)\exp\left(-\frac{156200}{T}\right)}{T\left[2 + \exp\left(-\frac{2060}{T}\right) + \exp\left(-\frac{156200}{T}\right)\right]}\right\} \tag{30}$$

$$\frac{\overline{S}}{R} = (1 + \alpha)\frac{S}{R}$$

$$\frac{\overline{S}}{R} = \frac{\overline{H}}{RT} + \ell n\ \frac{T^{5/2}}{p} - 182900\frac{\alpha}{T}$$

$$+ \ell n\left[\frac{(1 + \alpha)^{1+\alpha}}{(1 - \alpha)^{1-\alpha}}\alpha^{-2\alpha}\right] - 14.24\alpha + 1.866 \tag{31}$$

$$+ (1-\alpha)\ell n\left[1 + 12\exp\left(-\frac{135000}{T}\right)\right]$$

$$+ \alpha\ell n\left[4 + 2\exp\left(-\frac{2060}{T}\right) + 2\exp\left(-\frac{156200}{T}\right)\right]$$

where R is the gas constant per unit mass of argon, T is in degrees Kelvin and p is in atmospheres. In addition, the fact that the ratio of the unionized to ionized gas molecular weights is $(1 + \alpha)$ has also been used in obtaining Eqs. (30) and (31) (see Eq. 37).

The Helmholtz free energy of the mixture needed to calculate the pressure, becomes

$$A = \sum_i [X(i)\, A(i) + \mathcal{R} T\, X(i)\, \ell n\, X(i)] \tag{32}$$

The pressure is calculated from Eq. (12), in which X(i) as well as T is held constant in performing the differentiation. The result is

$$p = \frac{\mathcal{R} T}{V} \sum_i X(i) = \frac{\mathcal{R} T}{V} \tag{33}$$

which is seen to be an expression of Dalton's law of partial pressures for one mole of gas mixture. Rewriting Eq. (33) in terms of the ion mass fraction α, the equation of state becomes

$$p = (1 + \alpha)\, \rho R T \tag{34}$$

The gas constant per unit mass of argon R is written

$$R = \frac{\mathcal{R}}{\mathcal{M}} \tag{35}$$

Since the equation of state may also be written as

$$p = \rho\, \frac{\mathcal{R}}{\overline{\mathcal{M}}}\, T \tag{36}$$

where $\overline{\mathcal{M}}$ refers to the molecular weight of the ionized gas, Eqs. (34), (35), and (36) yield

$$\frac{M}{\overline{M}} = (1 + \alpha) \tag{37}$$

This expression was used in obtaining Eqs. (30) and (31) for the mixture enthalpy and entropy.

As a consequence of applying equilibrium thermodynamics to a reaction, the Gibbs free energy change between the products and reactants in their standard state of unit pressure ΔF^0 is related to the pressure equilibrium constant K as

$$\Delta F^0 = - RT \ln K \tag{38}$$

The Gibbs free energy, defined as F = H - TS, written for $N(i)$ moles of the ith species is derived from the species entropy and enthalpy expressions on a per-mole basis (Eqs. 4 and 5) by replacing N_0 by $N(i)N_0$. The result is

$$F(i) = N(i) RT \left[\ln \frac{Q}{N_0} - \ln N(i)\right] \tag{39}$$

Applying Eqs. (38) and (39) to the ionization reaction, $A \rightleftharpoons A^+ + e^-$, the Gibbs free energy change at unit pressure becomes

$$\begin{aligned} \Delta F^0 &= F^0(A^+) + F^0(e^-) - F^0(A) \\ &= -RT \ln \frac{\frac{Q^0(A^+)}{N_0} \frac{Q^0(e^-)}{N_0}}{\frac{Q^0(A)}{N_0}} \end{aligned} \tag{40}$$

The equilibrium constant in Eq. (38) is, by definition,

$$K = \frac{p(A^+)p(e^-)}{p(A)} \tag{41}$$

The partial pressures in Eq. (41) may be expressed in terms of mole fractions by Dalton's law to obtain

$$K = p\,\frac{\alpha^2}{1-\alpha^2} \tag{42}$$

Combining Eqs. (40) and (42), the equilibrium composition equation becomes

$$\frac{\alpha^2}{1-\alpha^2} = 2\left[\frac{2\pi m(e^-)}{h^2}\,k^{5/3}\right]^{3/2}\,\frac{T^{5/2}Q_{int}(A^+)}{p\,Q_{int}(A)} \tag{43}$$

The argon ion and atom mass have been assumed equal in Eq. (43), and the electron internal partition function which reduces to the spin degeneracy of 2 has been used. By substituting the values of the internal partition function and expressing the constant terms in units consistent with temperature in degrees Kelvin and pressure in atmospheres, Eq. (43) becomes

$$\frac{\alpha^2}{1-\alpha^2} = 0.654\times10^{-6}\,\frac{T^{5/2}}{p}\,\exp\left(-\frac{182900}{T}\right) \times\frac{4+2\exp\left(-\frac{2060}{T}\right)+2\exp\left(-\frac{156200}{T}\right)}{1+12\exp\left(-\frac{135000}{T}\right)} \tag{44}$$

---

* Note that the exponent -13500/T in the denominator of Eq. 44 of Ref. 20 should read -135000/T as shown here in Eq. 44.

III. FLOW EQUATIONS

In this Section, the results of equilibrium thermodynamics obtained in Section II for partially ionized argon are combined with the conservation equations for one-dimensional, varying-area, adiabatic, inviscid flow. As a consequence of these assumptions, the flow is isentropic.

$$\overline{S} = \overline{S}_T \quad \text{(constant)} \tag{45}$$

The conservation equations are as follows:

Continuity:

$$\rho u A = \dot{m} \quad \text{(constant)} \tag{46}$$

Energy:

$$\overline{H} + \frac{u^2}{2} = \overline{H}_T \quad \text{(constant)} \tag{47}$$

The momentum equation is not needed explicitly, since for isentropic flow, it is automatically satisfied by the energy equation.

The Mach number was calculated from its defining relation

$$M = \frac{u}{a_e} \tag{48}$$

The equilibrium sound speed was calculated from

$$a_e^2 = \left(\frac{\partial p}{\partial \rho}\right)_{\overline{s}} \tag{49}$$

The equations in this Section and in Section II were solved simultaneously on an IBM 7090 computer to yield the isentropic flow variables discussed in Section IV.

IV. RESULTS

The computer printout was too lengthy (258 pages) to include here but is included in Appendix D of Ref. 20. Table 1 shows the thermodynamic properties at stagnation conditions and Table 2 contains conversion factors. Briefly, the calculation procedure was as follows:

1. Stagnation pressure and temperature were prescribed for a particular case and, with α obtained from Eq. (44), the entropy was calculated from Eq. (31) and subsequently held constant for the entire computation of the case.
2. A temperature below the stagnation value was then chosen, and the total entropy equation, Eq. (31), was solved simultaneously with Eq. (44) to yield values of pressure and ionization fraction.
3. Step 2 was repeated at consecutively lower values of temperature down to 1,000°K. Hence, the state of the gas was known throughout the isentropic process.
4. A mass-flux (ρu) distribution was computed to locate the maximum ρu, which is also the sonic condition for each case. A Mach number of unity at the sonic condition served as a check for this calculation.

Figures 1 and 2 show the effect of electronic excitation and ionization on temperature ratio and pressure ratio as a function of area ratio for stagnation conditions of 10,000°K and 0.1 and 1.0 atm. At any given area ratio, it may be seen that the temperature

and pressure ratios are above the perfect-gas values for which electronic excitation and ionization are neglected. As stagnation pressure is decreased, the values deviate further from the perfect-gas results. Although not shown on these Figures, the values also deviate further from perfect-gas results as the stagnation temperature is increased. Temperature and pressure ratios are within 1% of the perfect-gas values for stagnation temperatures less than about 7,000°K for the stagnation-pressure range considered.

Figure 3 shows the deviations of maximum mass flux values from those calculated for the perfect-gas conditions. In Fig. 4, the same variables are plotted, except that in this case, the ionization fraction is assumed constant at the stagnation conditions and electronic excitation is neglected. Figure 4 shows that the mass flux ratio appears to be approaching a minimum at the higher temperatures. This trend occurs because the gas is highly singly-ionized (α = 0.2 to 0.8). If the stagnation temperature were increased appreciably above the value which yields $\alpha_T = 1$, the singly-ionized gas model would predict $\alpha^* = 1$ also. (Figure 9 shows the beginning of this trend.) By neglecting the small effect which excitation has on C_p, $(\rho u)^*/(\rho u)_0^*$ would be 1 again because the gas is frozen, with $\alpha = 1$ between the stagnation and sonic conditions. Of course, at the high temperatures at which $(\rho u)^*/(\rho u)_0^* = 1$, the singly-ionized gas model is no longer valid. However, due to the fact that the first and second ionization potentials are separated by about 12 ev, even at 14,000°K and 0.1 atm (α = 0.8), the doubly-ionized ion mass fraction is less than 10^{-4}; hence, the singly-ionized

gas model may be expected to provide valid results even though α is quite large.

The ratio of equilibrium sound speed to frozen-composition sound speed is presented in Fig. 5 as a function of temperature and pressure. The trends shown here are similar to those for the mass flux ratio discussed for Fig. 4. The equilibrium sound speed was calculated from $a_e^2 = (\partial p/\partial \rho)_s$ by differentiation as part of the computer program and from the closed-form approximation given in Appendix B (Eq. B-7). The agreement was excellent for the conditions of the tests. This implies that electronic excitation does not noticeably affect the sound speed for the ionization model and range of conditions considered.

Even though this is an inviscid flow analysis, it is of interest to mention a convenient flow parameter, Reynolds number per centimeter, which is shown in Fig. 6 at the sonic conditions as a function of stagnation temperature and pressure. This flow parameter, evaluated at the local static conditions, lies between 400 and 11,000 cm^{-1} over the range of stagnation temperatures and pressures considered. Because of the marked ionized gas effect on predicted viscosity (5), shown in Fig. 7, the Reynolds number per centimeter attains a minimum value for each stagnation pressure. Had a conventional power-law relation between viscosity and temperature been assumed, $(Re/D)^*$ would have decreased monotonically with increasing temperature.

The ionization fraction, which lies between 1.4×10^{-5} and 0.8 for the range of stagnation conditions considered, is shown as

a function of temperature and pressure in Fig. 8 and a function of area ratio in Fig. 9. A comparison of these values of α (Fig. 8) with those calculated by the method proposed by Saha (13), shows that the Saha equation values of α at 0.1 atm are 30 to 55% of the values of α predicted here between 6,000 and 14,000°K. The Saha equation, which does not include the degenerate energy levels or electronic excitation, can be obtained from Eq. (43) by equating the internal partition-function terms to unity. An improvement to the Saha equation can be made by including the ground-state-degeneracies value of 8 as the sole internal partition-function contribution. The prediction, which includes this correction, yields values of α ranging between 86 and 96% of those calculated by including the excitation terms. Several other investigators include ground-state degeneracies and further assume that the excitation terms are frozen at a temperature typical of the temperature level under consideration. This prediction compares more favorably than the others but has limited utility if deviations larger than 1% are undesirable. From Eq. (44), it is seen that only one of the excitation terms is of importance, so that the composition equation may be written in the following form:

$$\frac{\alpha^2}{1-\alpha^2} = 1.308 \times 10^{-6} \frac{T^{5/2}}{p} \exp\left(-\frac{182900}{T}\right) \times \left[2 + \exp\left(-\frac{2060}{T}\right)\right] \tag{50}$$

where the units are T, °K and p, atm. For the stagnation conditions considered, this equation yields values of α which are within 0.1%

of those predicted by Eq. (44), including all excitation terms. Thus, Eq. (50) may be used instead of the predictions, which are not uniformly valid in this temperature and pressure range.

The question naturally arises as to whether or not the enthalpy and entropy equations (Eqs. 30 and 31) may be similarly reduced in complexity without compromising their validity. Table 1 shows the values of enthalpy and entropy calculated by neglecting excitation but using the composition equation (Eq. 50), which includes the effect of one excited state. A comparison shows that the enthalpy and entropy are less than 0.5 and 1.0% (respectively) lower than those values (reported here as shown in Table 1) calculated by including all excitation terms. The resulting enthalpy and entropy equations are

$$\frac{\overline{H}}{RT} = \frac{5}{2}(1 + \alpha) + 182900\,\frac{\alpha}{T} \tag{51}$$

$$\frac{\overline{S}}{R} = (1 + \alpha)\ell n\,\frac{T^{5/2}}{p} + \ell n\left[\frac{(1 + \alpha)^{1+\alpha}}{(1 - \alpha)^{1-\alpha}}\,\alpha^{-2\alpha}\right]$$

$$- 10.354\alpha + 4.366 \tag{52}$$

where the units are T, ^{o}K and p, atm. Thus, Eqs. (50), (51), and (52) may be substituted for Eqs. (44), (30), and (31) for composition, enthalpy, and entropy of singly-ionized argon when 1% accuracy is sufficient. These values of enthalpy and entropy are shown in Table 1 for purposes of comparison with other predictions. Ionization fraction is not shown, since the agreement between the prediction and the simplified composition equation (Eq. 50) was within 0.1%.

Figure 9 shows the ratio of static-to-stagnation ionization fractions as a function of area ratio for several stagnation temperatures and 1 atm stagnation pressure. At high stagnation temperatures, the static temperature and, hence, the ionization fraction, decrease less rapidly due to the fact that increasing kinetic energy does not occur solely at the expense of decreasing static enthalpy or temperature but includes ionization energy being returned to the flow process. At low stagnation temperatures, ionization fraction decreases rapidly, as does the temperature, since a negligible amount of ionization energy is present.

The electrical conductivity σ, calculated from the results of Ref. 14 given as Eq. (C-1) in Appendix C, is shown as a function of temperature and pressure in Fig. 10. The electrical conductivity lies between 2×10^2 and 8×10^3 mhos/m for the temperature and pressure range considered. In Fig. 11, the electrical conductivity is shown at the sonic conditions σ^* as a function of stagnation temperature and pressure.

In these Figures the electrical conductivity increases directly with α; thus, the trend of σ vs T is similar to that of the ionization fraction shown in Fig. 8. At high temperatures, the pressure dependence is inverted from that at low temperatures. These trends are a consequence of the assumed conductivity model. In this model, the conductivity of a slightly ionized gas, which varies inversely with pressure and is dominant at low temperatures, is combined with the conductivity of a fully ionized gas, which increases monotonically with pressure and becomes dominant at high temperatures.

Table 1 gives the thermodynamic properties at the stagnation conditions for the ionization model used here. Included also are numerous comparisons with other investigations, which, in general, agree quite well with the singly-ionized gas model below 10,000°K.

V. CONCLUSIONS

Thermodynamic properties and one-dimensional, isentropic flow variables of singly-ionized argon have been calculated over the stagnation temperature and pressure ranges of 6,000 to 14,000°K and 0.1 to 3 atm, respectively. Conclusions from these calculations include the following:

1. For the range of stagnation conditions considered here, the singly-ionized gas model of argon provides thermodynamic properties that are generally in good agreement with those of other investigations for which multiple ionization was included. Good agreement below 10,000°K is obtained with the results of those investigations that include lowering of the ionization potential as a result of charged-particle field interactions.
2. Electronic excitation and ionization effects become increasingly important as stagnation temperatures increase and stagnation pressures decrease. However, for the range of this investigation, it was found that, except in the composition equation, electronic excitation could be neglected and the 1% accuracy still retained with those values predicted in which excitation is included. As an example of these effects, static-to-stagnation temperature and pressure ratios are shown to be significantly higher than those calculated by assuming a perfect

gas (or no ionization and electronic excitation) for stagnation conditions of 10,000°K and 1 atm.

3. The mass flux at the sonic conditions differs significantly from both the perfect gas (without ionization or electronic excitation) and frozen composition values calculated for stagnation temperatures above about 7,000°K. Thus, electronic excitation and ionization effects may be expected to influence all area-ratio-dependent quantities significantly.
4. Reynolds number per centimeter at sonic conditions is seen to decrease with decreasing stagnation pressure, then to increase with increasing stagnation temperature as a result of ionized gas effects on viscosity.
5. Ionization fraction and electrical conductivity are observed to decrease rapidly with increasing supersonic area ratio. However, for stagnation conditions at high ionization levels, where translation and ionization energies are of the same order, ionization fraction and conductivity decrease much more slowly with increasing area ratio.

The results clearly indicate that electronic excitation and, particularly, ionization effects are important in nearly every aspect of defining the thermodynamic flow variables of an isentropic,

varying area flow of partially ionized argon.

It should be pointed out that this method of calculation can readily be extended to higher temperatures by including additional energy levels and multiple ionization.

REFERENCES

1. Cann, G. L., and Ducati, A. C., Argon Mollier Diagram, Report No. PLR-55, plasmadyne Corp., Santa Ana, Calif., February 1959.

2. Gilmore, F. R., Equilibrium Composition and Thermodynamic Properties of Air to 24000°K, RM 1543, AD 84052, Rand Corp., Santa Monica, Calif., August 1959.

3. Bosnjakovic, F., Springe, W., Knocke, K. F., and Burgholte, P., "Mollier Enthalpy--Entropy Charts for High-Temperature Plasmas," Thermodynamic and Transport Properties of Gases, Liquids, and Solids, ASME Symposium on Thermal Properties, Purdue University, Lafayette, Ind., February 1959.

4. Knoche, K. F., Thermodynamic Charts for Argon Plasma up to 10^5 °K with Illustrative Examples, Ph.D. Thesis, Institute of Technology, Braunschweig, Germany; Tr. ARL. 171, December 1961.

5. Arave, R. J., and Huseby, O. A., Aerothermodynamic Properties of High Temperature Argon, Document No. D2-11238 with revisions, Boeing Co., Seattle, Wash., February 1962.

6. Baum, E., and Cann, G. L., Thermodynamic Properties of Argon, ARL 63-133, Electro-Optical Systems, Inc., Pasadena, Calif., August 1963.

7. Drellishak, K. S., Knopp, E. F., and Cambel, A. B., Partition Functions and Thermodynamic Properties of Argon Plasma, AEDC-TDR-63-146, Gas Dynamics Laboratory, Northwestern

University, Evanston, Ill., August 1963.

8. Olsen, H. N., "The Measurement of Argon Transition Probabilities and Computation of Thermodynamic Properties of the Argon Plasma," 5th Biennial Gas Dynamics Symposium, Paper No. 63-369, Northwestern University, Evanston, Ill., August 14-16, 1963.

9. Olsen, H. N., "Thermal and Electrical Properties of an Argon Plasma," Physics of Fluids, Vol. 2, No. 6, November-December, 1959.

10. Sherman, M. P., The Degree of Approach to Equilibrium in an Atmosphere-Pressure Arc-Jet Using Argon, Aeronautical Engineering Laboratory Report No. 645, Princeton University Press, Princeton, N. J., April 1963.

11. Mayer, J. E., and Mayer, M. G., Statistical Mechanics, John Wiley and Sons, Inc., New York, 1940.

12. Rossini, F. D., "Thermodynamics and Physics of Matter," Vol. 1, High Speed Aerodynamics and Jet Propulsion, Princeton University Press, Princeton, N.J., 1955.

13. Saha, M. N., "Ionization in the Solar Atmosphere," The Philosophical Magazine, S6, Vol. 40, No. 238, October 1920.

14. Lin, S. C., Resler, E. L., and Kantrowitz, A., "Electrical Conductivity of Highly Ionized Argon Produced by Shock Waves," Journal of Applied Physics, Vol. 26 (1), January 1955.

15. Moore, C. E., Atomic Energy Levels, Vol. 1, National Bureau of Standards Circular 467, 1949.

16. Renard, M. L., "Experimental Investigation of an Arc Heater," Hypersonic Research Project Memorandum No. 64, Guggenheim Aeronautical Laboratories, California Institute of Technology, Pasadena, Calif., March 15, 1962.

17. Chapman, S., and Cowling,T. G., Mathematical Theory of Non-Uniform Gases, Cambridge University Press, London, 1952.

18. Spitzer, L., and Harm, R., "Transport Phenomena in a Completely Ionized Gas," The Physical Review, Vol. 89, pp. 977-981, 1953.

19. Townsend, J. S., and Bailey, V. A., "The Motion of Electrons in Argon," The Philosophical Magazine, Vol. 43, pp. 593-600, 1922; "The Abnormally Long Free Paths of Electrons in Argon," pp. 1127-1128.

20. Witte, A. B., "Analysis of One-Dimensional Isentropic Flow with Tables for Partially Ionized Argon," Technical Report No. 32-661, Jet Propulsion Laboratory, Pasadena, Calif. Sept. 30, 1964.

APPENDIX A

Energy Levels for Ionized Argon

The energy levels of the species were obtained from Moore (15).

Species	$\mathcal{E}_0/\mathcal{R}$, °K	n	g_n	$E_n/\mathcal{R}$, °K
A	0	0	1	0
		1	12	135,000
A^+	182,900	0	4	0
		1	2	2,060
		2	2	156,200
e^-	0	0	2	0

The energy of the first excited state of the argon atom represents an average of five energy levels very near 135,000°K. The infinite series of energy levels contributing to the internal partition function may be cut off after the first few terms because of the relatively low temperatures at which these calculations are made. For instance, the highest energy levels included here contribute terms of order e^{-10} to the internal partition function. The energy levels used in this study were also employed by Arave and Huseby (5) to calculate the thermodynamic properties of singly-ionized argon.

APPENDIX B

Speed of Sound in a Partially Ionized Monatomic Gas

For the pressure and temperature range of this investigation, it was observed that electronic excitation had a negligible effect on the equilibrium speed of sound. By treating a monatomic gas as a mixture of perfect gases comprised of atoms, ions, and electrons, and neglecting electronic excitation, the equilibrium speed of sound may be calculated as a function of the ionization fraction and temperature.

The definition of the equilibrium sound speed a_e is

$$a_e^2 = \left(\frac{\partial p}{\partial \rho}\right)_s \tag{B-1}$$

This may be combined with general thermodynamic relations to obtain

$$a_e^2 = \frac{C_p}{C_p \left(\frac{\partial \rho}{\partial p}\right)_T - \frac{T}{\rho^2}\left(\frac{\partial \rho}{\partial T}\right)_p^2} \tag{B-2}$$

The enthalpy used to eliminate the specific heat in Eq. (B-2) is

$$\overline{H} = \frac{5}{2} RT\,(1 + \alpha) + \alpha I \tag{B-3}$$

The equation of state is

$$p = (1 + \alpha)\,\rho RT \tag{B-4}$$

Combining Eqs. (B-2), (B-3), and (B-4) one obtains

$$\frac{a_e^2}{a_0^2} = \frac{1 + \left(1 + \frac{2}{5}\,\frac{I}{RT}\right)\frac{T}{1+\alpha}\left(\frac{\partial \alpha}{\partial T}\right)_p}{1 + \frac{2}{3}\frac{I}{RT}\frac{p}{1+\alpha}\left(\frac{\partial \alpha}{\partial p}\right)_T + \left(1 + \frac{2}{3}\,\frac{I}{RT}\right)\frac{T}{1+\alpha}\left(\frac{\partial \alpha}{\partial T}\right)_p} \qquad \text{(B-5)}$$

where

$$a_0^2 = \frac{5}{3}\,\frac{p}{\rho}$$

Equation (B-5) was also obtained by Renard (16) by a similar procedure. Unfortunately, a subsequent error in his analysis invalidates his final results. Derivatives of the ionization fraction may be eliminated by the Saha equation,

$$\frac{\alpha^2}{1-\alpha^2} = \text{constant}\ \frac{T^{5/2}}{p}\ \exp\left(-\frac{I}{RT}\right) \qquad \text{(B-6)}$$

Then, the following is obtained:

$$\frac{a_e^2}{a_0^2} = \frac{1 + \frac{5}{4}\left(1 + \frac{2}{5}\,\frac{I}{RT}\right)^2 \alpha(1-\alpha)}{1 + \left[\frac{5}{4} + \frac{I}{RT} + \frac{1}{3}\left(\frac{I}{RT}\right)^2\right]\alpha(1-\alpha)} \qquad \text{(B-7)}$$

Speed of sound was calculated by Eqs. (B-1) and (B-7) and found to give identical results when α was calculated from the computer program which included the effects of electronic excitation. When α was calculated from the Saha equation (Eq. B-6), the agreement was within 1%. This indicates that the effect of electronic excitation on sound speed for the conditions in this investigation is negligible.

APPENDIX C

Electrical Conductivity of Argon

The electron mobility and, hence, the electrical conductivity are dictated by close encounters between the electrons and neutral atoms for a slightly ionized gas as a result of the inverse fourth power interaction potential, and by distant encounters between electrons and ions for a completely ionized gas in which the Coulomb interaction is dominant. Lin et al. (14) suggest that the intermediate range between a slightly ionized gas and a completely ionized gas can be approximated by a series-resistance expression,

$$\frac{1}{\sigma} = \frac{1}{\sigma_c} + \frac{1}{\sigma_d}$$

where σ_c and σ_d represent the conductivities due to the close and distant encounters for a slightly ionized and completely singly-ionized gas, respectively.

Following Ref. 14, the electrical conductivity of a slightly ionized gas of rigid spherical atoms was taken from Chapman and Cowling (17) and that of a completely ionized gas from Spitzer (18). After some algebra one obtains

$$\frac{1}{\sigma} = 8.210 \times 10^{8} \left(\frac{T}{10^3}\right)^{\frac{1}{2}} \frac{S}{\alpha} + 0.2063 \times 10^{-2} \frac{1}{\left(\frac{T}{10^3}\right)^{3/2}} \ln \frac{0.1022\left(\frac{T}{10^3}\right)^2}{(\alpha p)^{\frac{1}{2}}} \qquad \text{(C-1)}$$

The units are σ, mhos/meter; T, ^{o}K; p, atm; and S, cm^2. The

variation of the effective electron-atom cross-section S with electron temperature was obtained from a curve in Ref. 14, which was originally obtained by Townsend and Bailey 19).

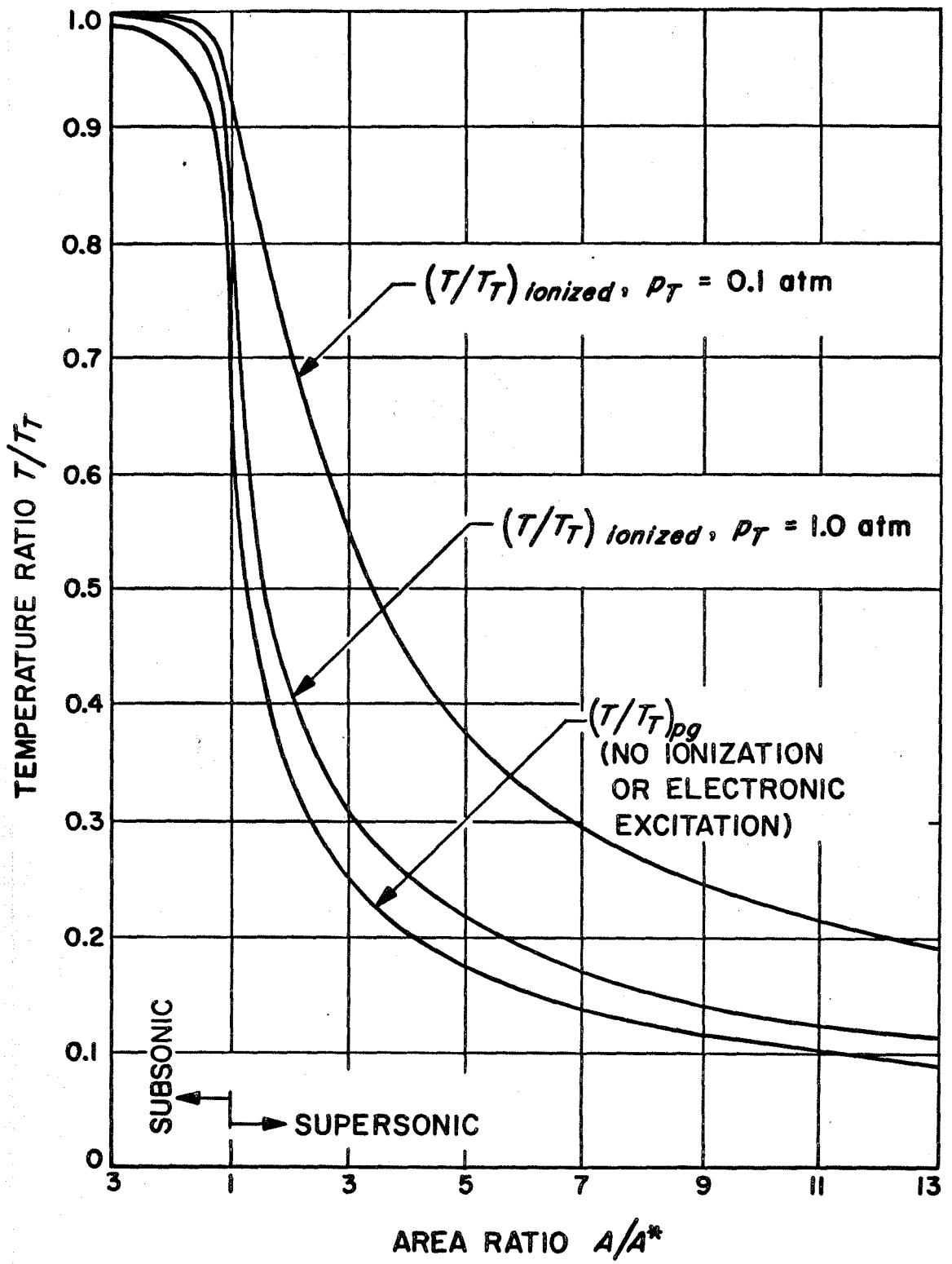

Figure 1. Static-to-stagnation-temperature Ratio as a Function of Area Ratio at 10,000°K Stagnation Temperature

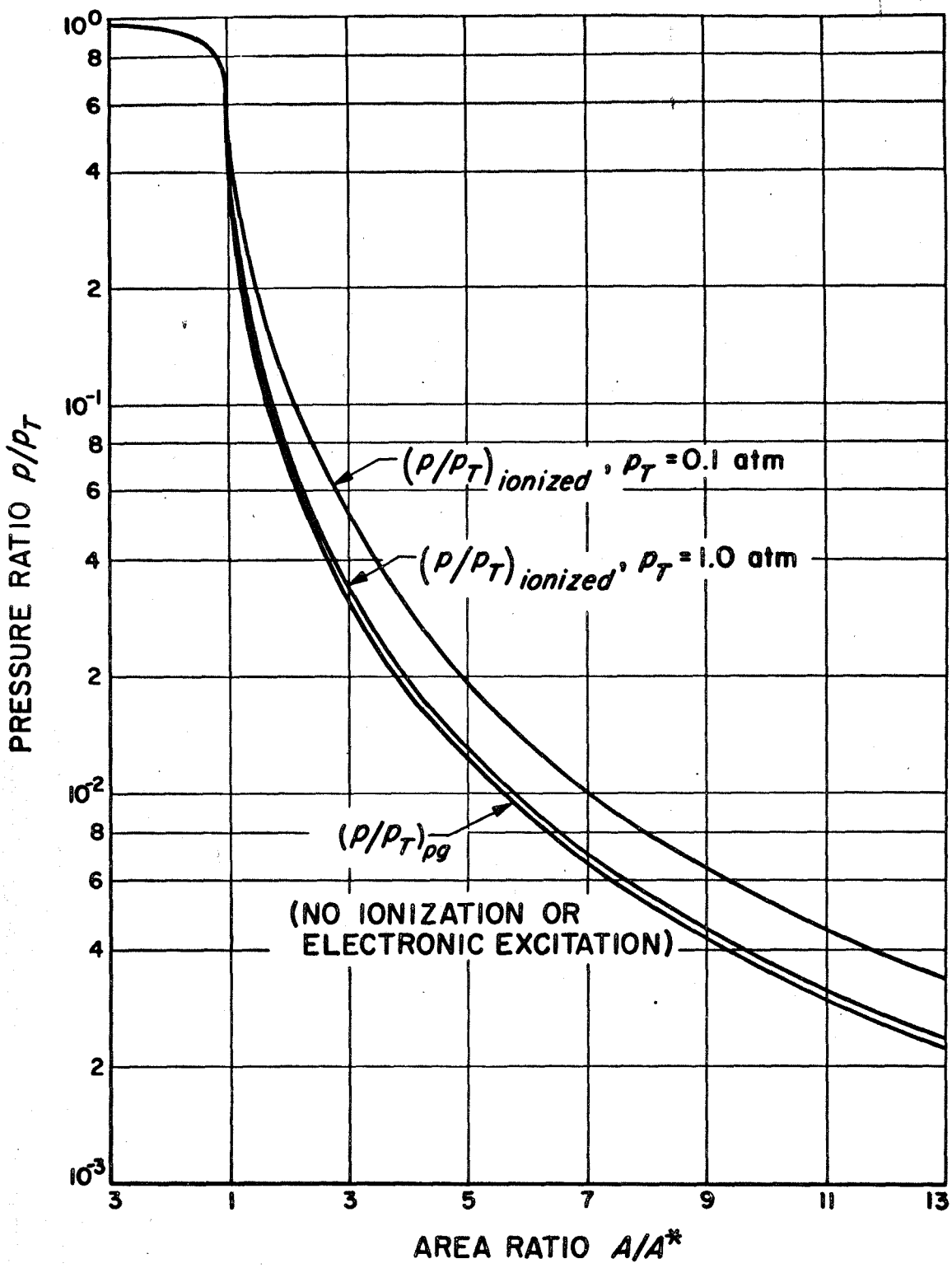

Figure 2. Static-to-stagnation-pressure Ratio as a Function of Area Ratio at 10,000°K Stagnation Temperature

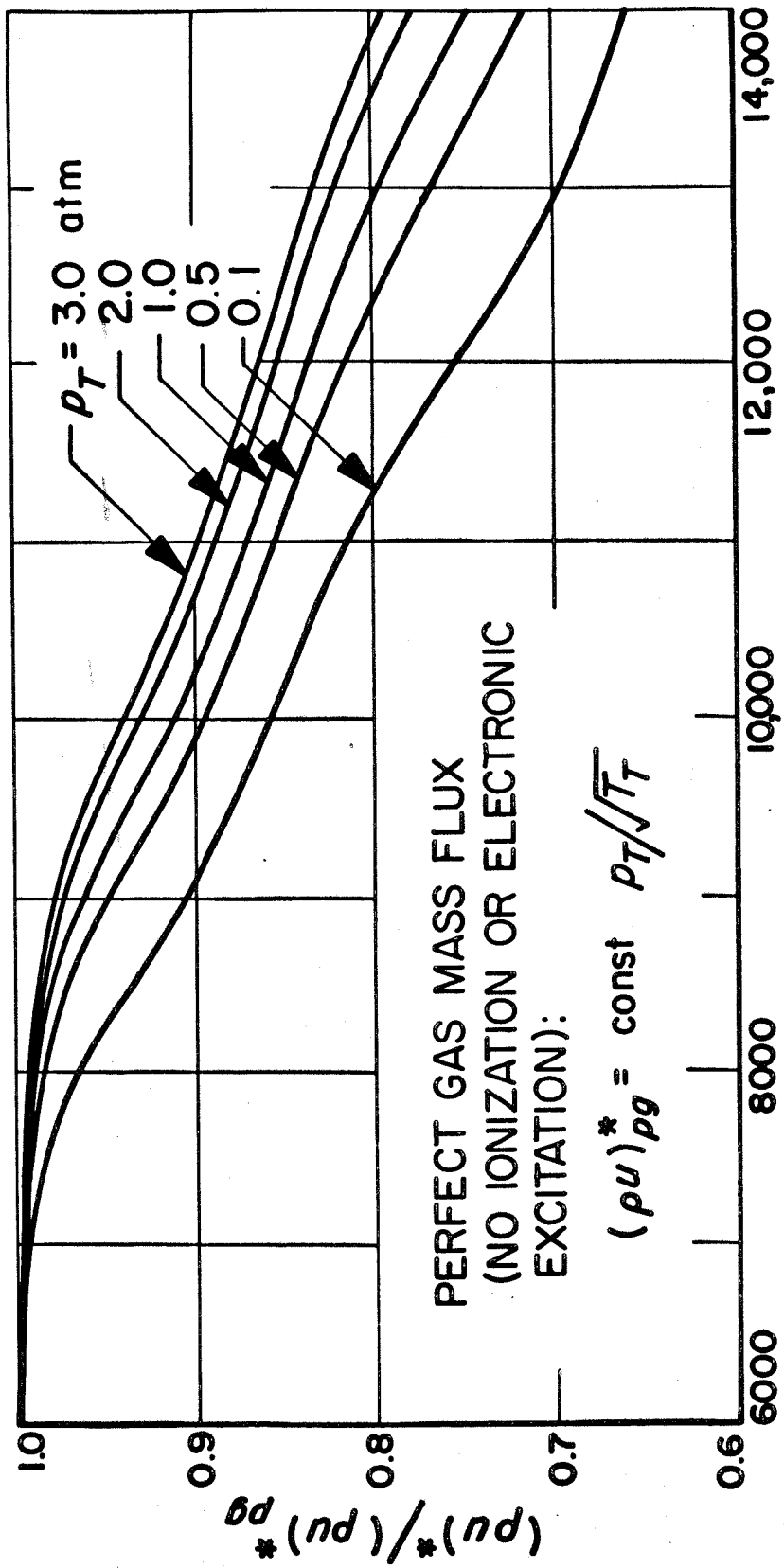

Figure 3. Ratio of Ionized-gas to Perfect-gas Maximum Mass Fluxes as a Function of Stagnation Temperature and Pressure

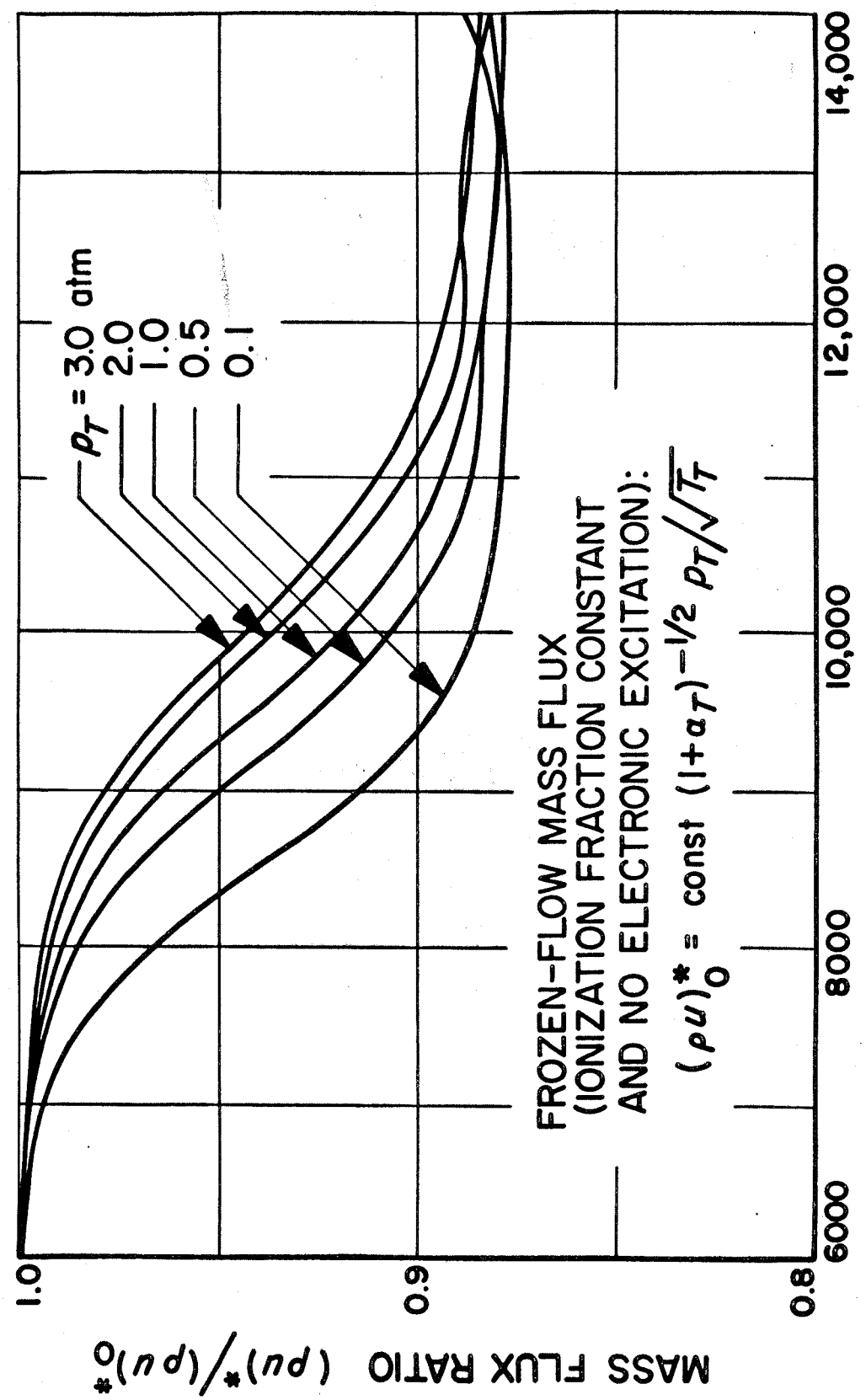

Figure 4. Ratio of Equilibrium Ionized-flow to Frozen-flow Gas Maximum Mass Fluxes as a Function of Stagnation Temperature and Pressure

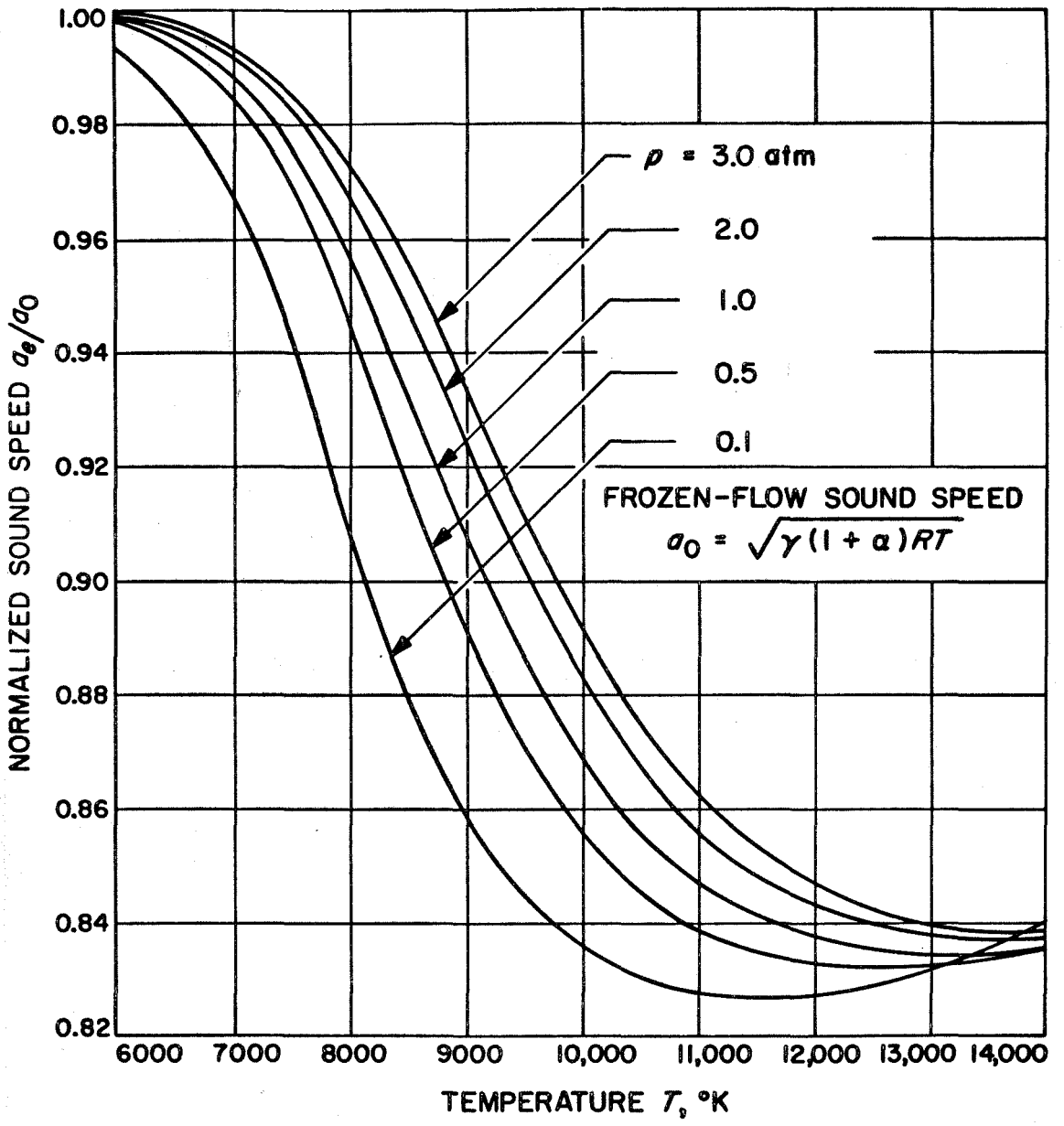

Figure 5. Ratio of Equilibrium to Frozen-flow Sound Speed as a Function of Pressure and Temperature (Eq. B-7)

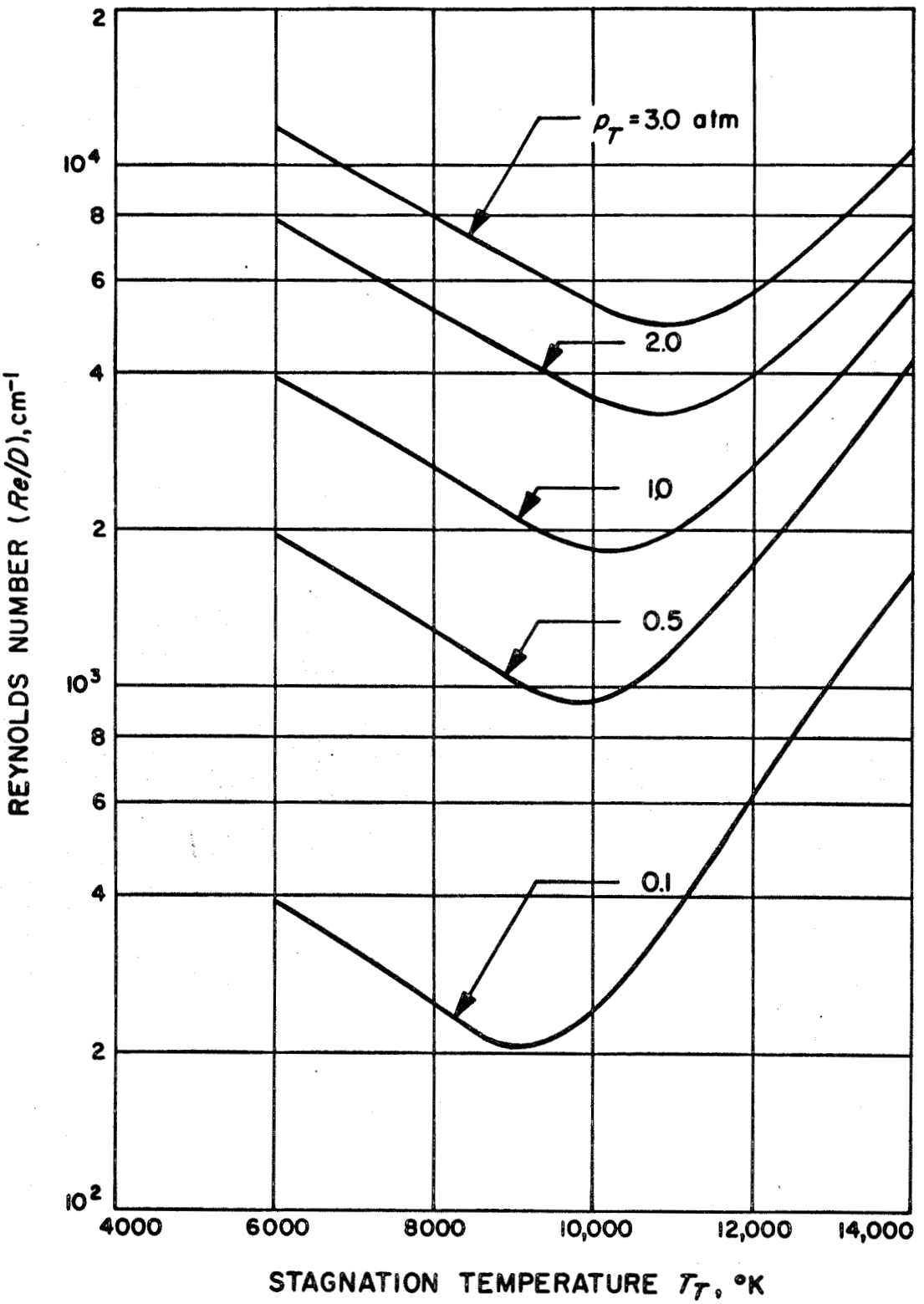

Figure 6. Reynolds Number per Centimeter at the Sonic Condition as a Function of Stagnation Temperature and Pressure

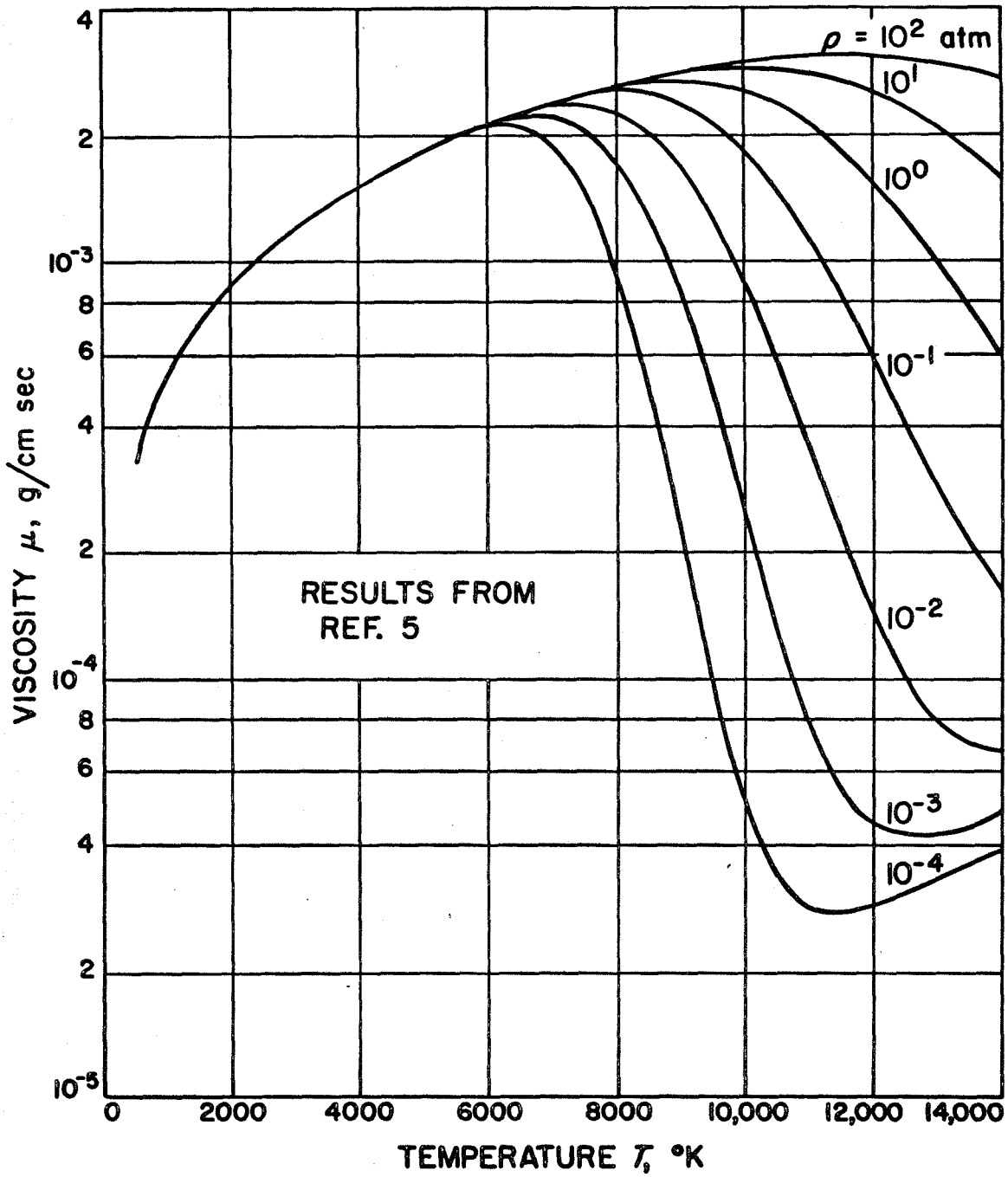

Figure 7. Viscosity of Argon as a Function of Temperature and Pressure

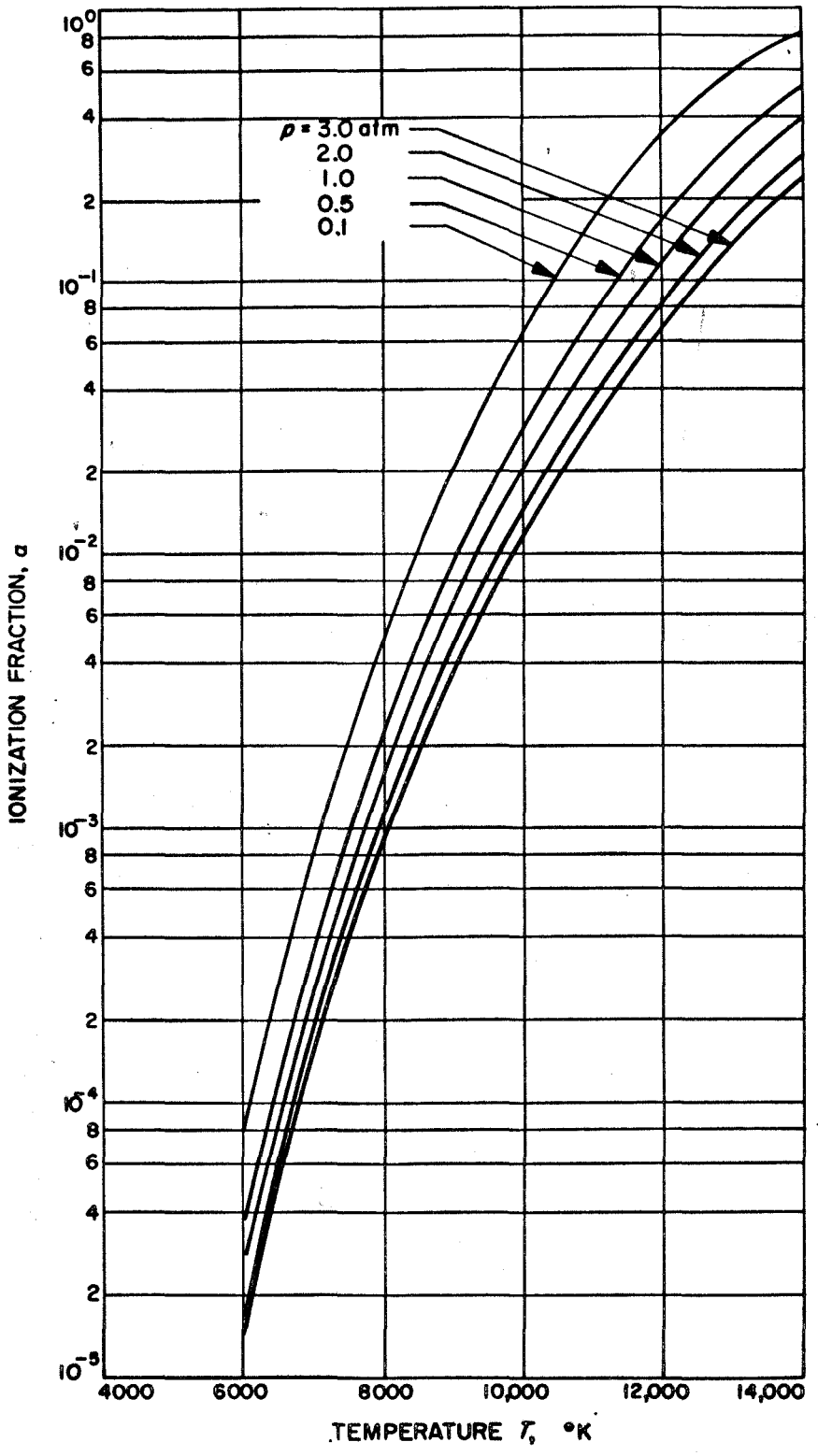

Figure 8. Ionization Fraction as a Function of Temperature and Pressure (Eq. 44)

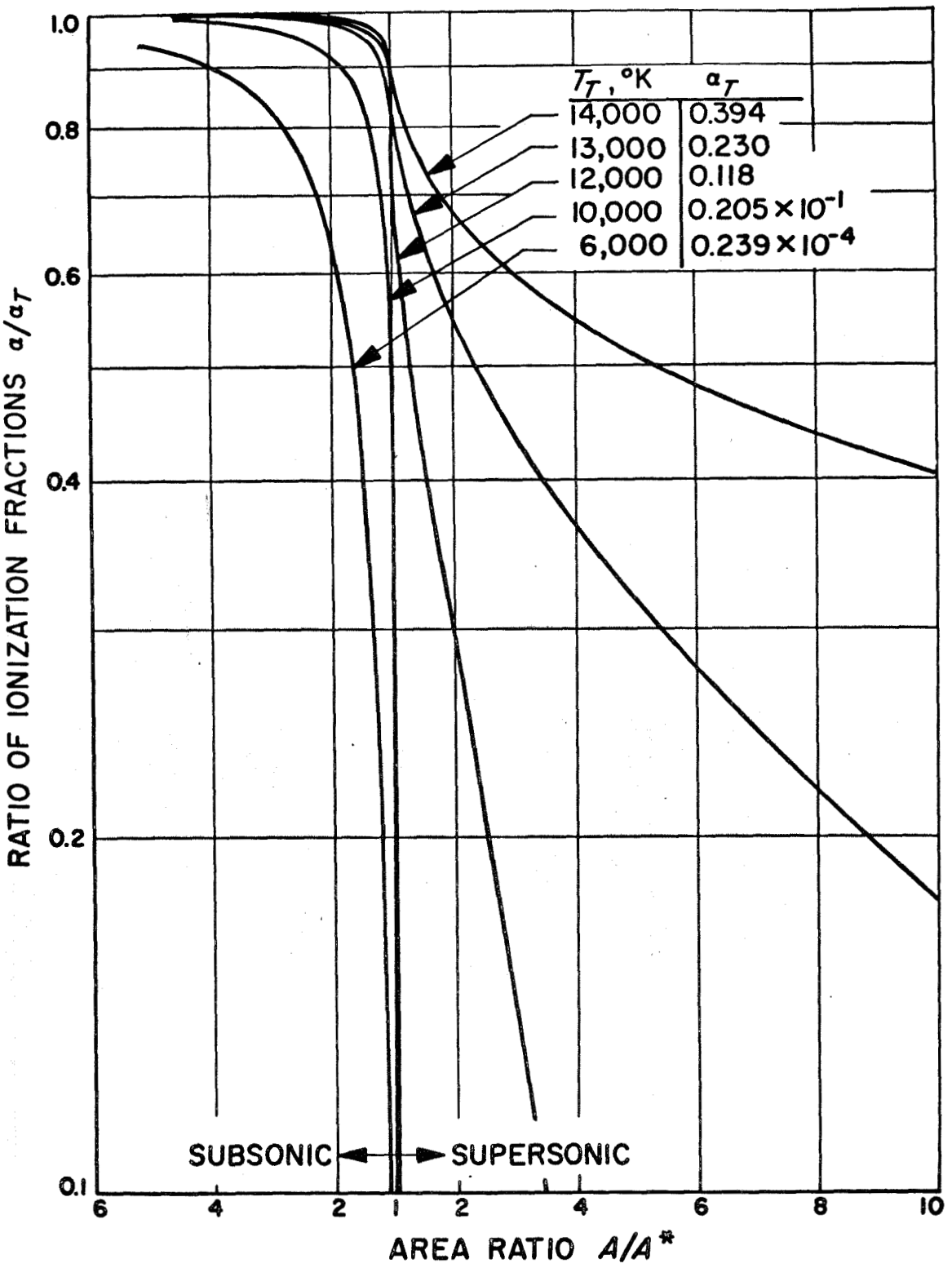

Figure 9. Ratio of Static-to-stagnation Ionization Fraction as a Function of Area Ratio for a Stagnation Pressure of 1.0 atm.

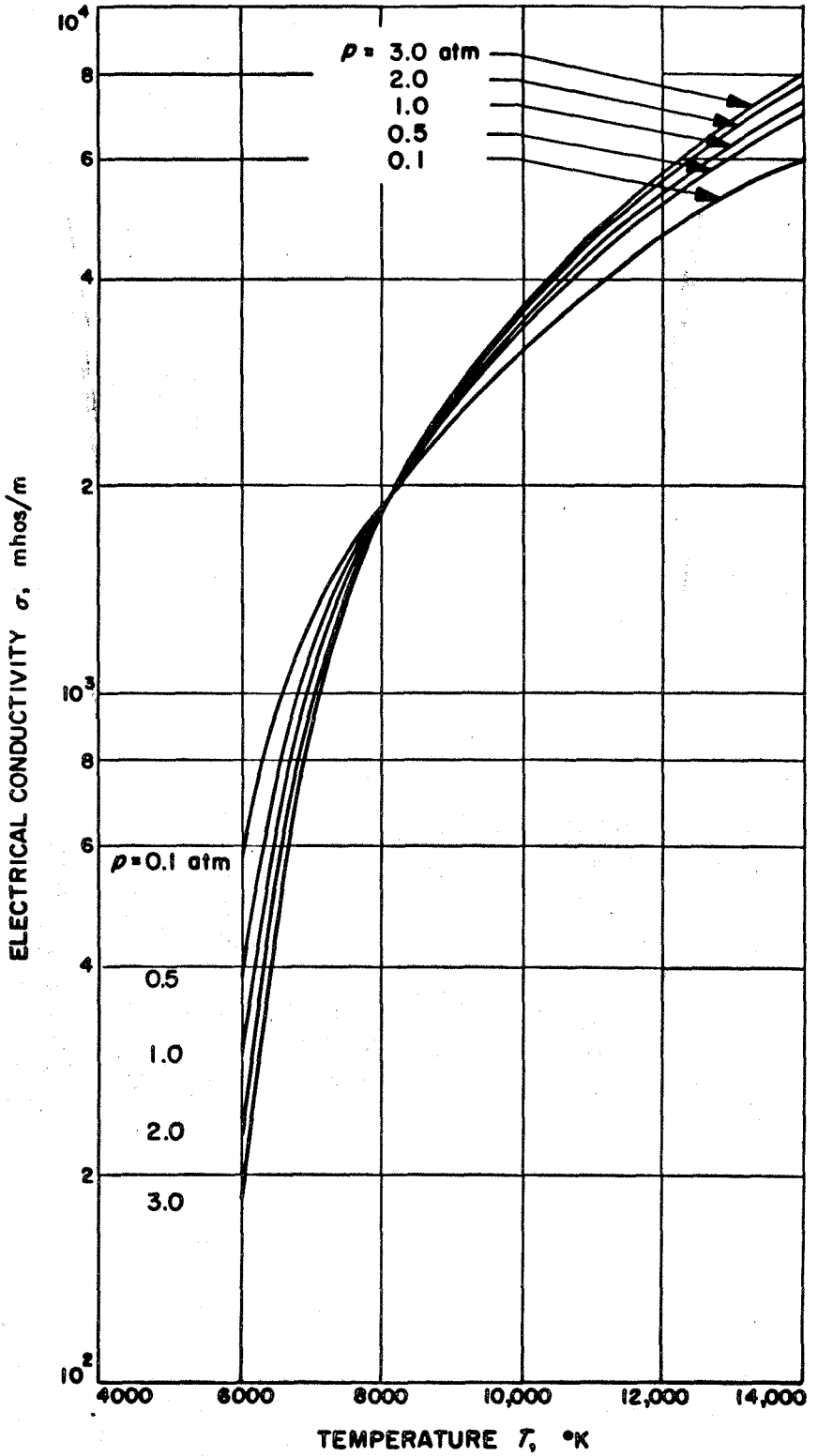

Figure 10. Electrical Conductivity as a Function of Temperature and Pressure (Eqs. 44 and C-1)

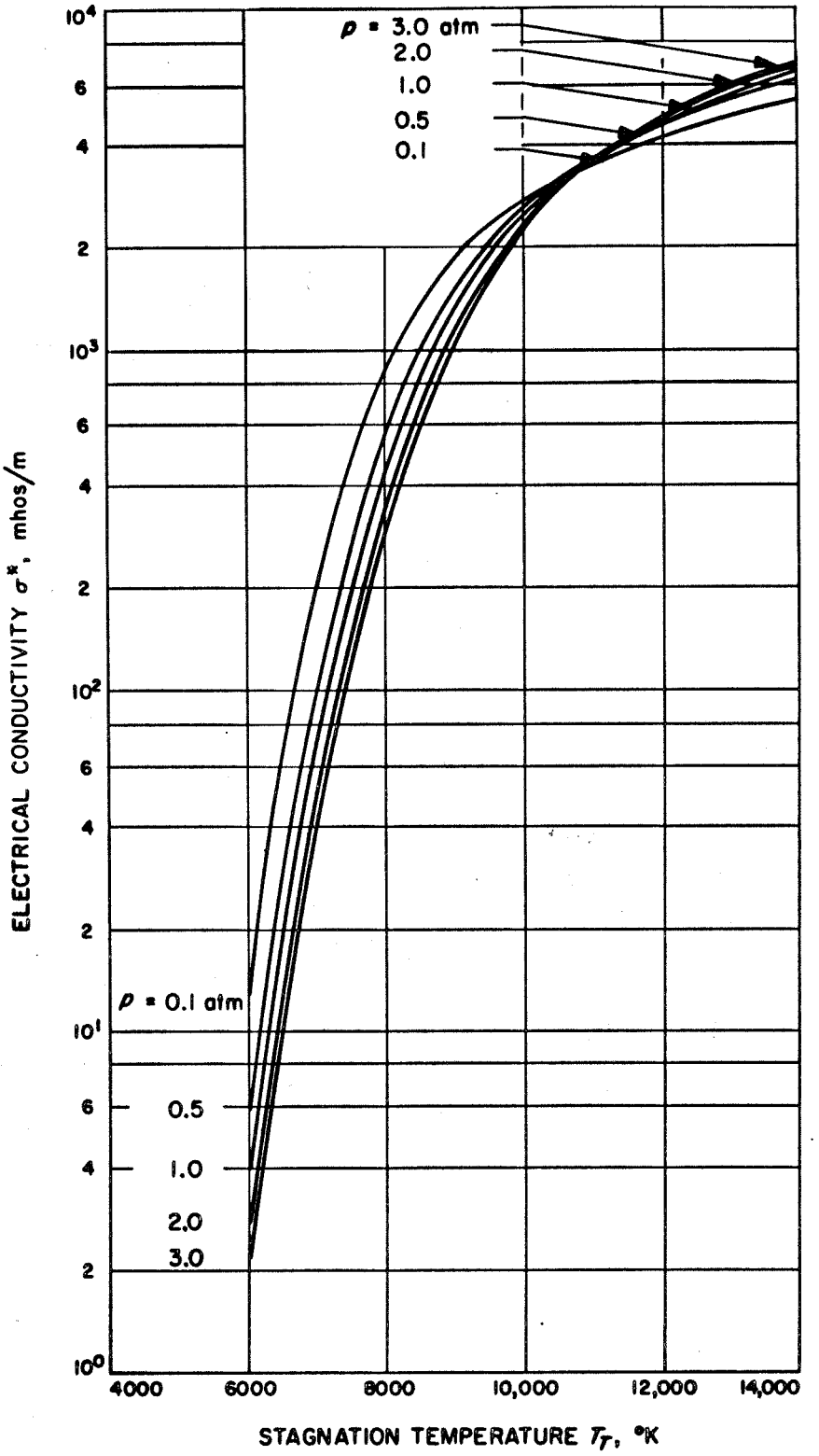

Figure 11. Electrical Conductivity at the Sonic Condition as a Function of Stagnation Temperature and Pressure

Table 1. Properties of argon

Singly ionized gas model								Multiple ionized gas models														Eq. (51) × T/T_0	Eq. (52)
								Cann and Ducati (Ref. 1)			Baum and Cann (Ref. 6)				Drellishak, Knopp and Cambel (Ref. 7)				Olsen (Ref. 8)					
ρ/ρ_0, atm	T, °K	$\bar{H}/RT_0$	$\bar{S}/R$	ρ, kg/m³	α	σ, mhos/m	a_r, m/sec	$\bar{H}/RT_0$	$\bar{S}/R$		$\bar{H}/RT_0$	$\bar{S}/R$	α	a_r, m/sec	$\bar{H}/RT_0$	$\bar{S}/R$	α	a_r, m/sec	$\bar{H}/RT_0$	$\bar{S}/R$	α	$\bar{H}/RT_0$	$\bar{S}/R$
0.1	6000	0.5500×10^2	0.2842×10^2	0.8109×10^{-3}	0.7553×10^{-4}	0.5527×10^2	0.1433×10^4	0.5497×10^2	0.2842×10^2	0.7×10^{-4}	0.5496×10^2	0.2841×10^2	0.7720×10^{-4}	0.1434×10^4	0.5508×10^2	0.285×10^2	0.766×10^{-4}	0.1444×10^4				0.5500×10^4	0.2842×10^2
0.1	7000	0.6470×10^2	0.2883×10^2	0.6945×10^{-2}	0.8133×10^{-3}	0.1246×10^4	0.1509×10^4																
0.1	8000	0.7695×10^2	0.2927×10^2	0.6052×10^{-2}	0.4945×10^{-2}	0.1854×10^4	0.1518×10^4																
0.1	9000	0.9787×10^2	0.2994×10^2	0.5298×10^{-2}	0.2048×10^{-1}	0.2473×10^4	0.1532×10^4																
0.1	10000	0.1409×10^3	0.3117×10^2	0.4570×10^{-2}	0.6463×10^{-1}	0.3139×10^4	0.1605×10^4	0.1409×10^3	0.3118×10^2	0.6×10^{-1}	0.1451×10^2	0.3129×10^2	0.7064×10^{-1}	0.1605×10^4	0.1425×10^3	0.313×10^2	0.654×10^{-1}	0.1614×10^4					
0.1	11000	0.2288×10^3	0.3345×10^2	0.3795×10^{-2}	0.1657	0.3856×10^4	0.1746×10^4															0.1408×10^3	0.3115×10^2
0.1	12000	0.3848×10^3	0.3714×10^2	0.3000×10^{-2}	0.3514	0.4604×10^4	0.1963×10^4																
0.1	13000	0.5926×10^3	0.4168×10^2	0.2342×10^{-2}	0.5984	0.5324×10^4	0.2232×10^4																
0.1	14000	0.7726×10^3	0.4533×10^2	0.1926×10^{-2}	0.8049	0.5951×10^4	0.2488×10^4	0.7720×10^3	0.4534×10^2	0.8	0.7864×10^3	0.4574×10^2	0.8307	0.2510×10^4	0.7713×10^3	0.454×10^2	0.791	0.2456×10^4					
0.5	6000	0.5497×10^2	0.2681×10^2	0.4054×10^{-3}	0.3378×10^{-4}	0.3649×10^2	0.1440×10^4															0.7707×10^3	0.4500×10^2
0.5	7000	0.6437×10^2	0.2720×10^2	0.3474×10^{-3}	0.3637×10^{-3}	0.1136×10^4	0.1535×10^4																
0.5	8000	0.7491×10^3	0.2759×10^2	0.3034×10^{-3}	0.2211×10^{-2}	0.1891×10^4	0.1576×10^4															0.5497×10^3	0.2681×10^2
0.5	9000	0.8933×10^3	0.2805×10^2	0.2679×10^{-3}	0.9161×10^{-2}	0.2621×10^4	0.1583×10^4																
0.5	10000	0.1137×10^3	0.2875×10^2	0.2364×10^{-3}	0.2895×10^{-1}	0.3386×10^4	0.1616×10^4																
0.5	11000	0.1587×10^3	0.2991×10^2	0.2057×10^{-3}	0.7492×10^{-1}	0.4208×10^4	0.1699×10^4															0.1136×10^4	0.2873×10^2
0.5	12000	0.2394×10^3	0.3182×10^2	0.1739×10^{-3}	0.1655	0.5085×10^4	0.1835×10^4																
0.5	13000	0.3699×10^3	0.3466×10^2	0.1421×10^{-3}	0.3168	0.5996×10^4	0.2028×10^4																
0.5	14000	0.5435×10^3	0.3817×10^2	0.1144×10^{-3}	0.5186	0.6886×10^4	0.2268×10^4															0.5421×10^3	0.3796×10^2
1.0	6000	0.5496×10^2	0.2612×10^2	0.8109×10^{-3}	0.2388×10^{-4}	0.2894×10^2	0.1441×10^4	0.5493×10^2	0.2611×10^2	0.2×10^{-4}	0.5493×10^2	0.2611×10^2	0.2463×10^{-4}	0.1443×10^4	0.5496×10^2	0.261×10^2	0.242×10^{-4}	0.1443×10^4	0.550×10^2	0.261×10^2	0.241×10^{-4}	0.5497×10^2	0.2612×10^2
1.0	7000	0.6429×10^2	0.2651×10^2	0.6949×10^{-4}	0.2572×10^{-3}	0.1050×10^4	0.1541×10^4																
1.0	8000	0.7443×10^2	0.2688×10^2	0.6072×10^{-3}	0.1564×10^{-2}	0.1878×10^4	0.1597×10^4																
1.0	9000	0.8731×10^2	0.2729×10^2	0.5371×10^{-3}	0.6478×10^{-2}	0.2673×10^4	0.1610×10^4																
1.0	10000	0.1072×10^3	0.2786×10^2	0.4768×10^{-3}	0.2048×10^{-1}	0.3493×10^4	0.1633×10^4	0.1072×10^3	0.2786×10^2	0.2×10^{-1}	0.1092×10^3	0.2792×10^2	0.2342×10^{-1}	0.1625×10^4	0.1077×10^3	0.279×10^2	0.207×10^{-1}	0.1628×10^4	0.1077×10^3	0.279×10^2	0.209×10^{-1}	0.1072×10^3	0.2786×10^2
1.0	11000	0.1418×10^3	0.2875×10^2	0.4200×10^{-3}	0.5305×10^{-1}	0.4369×10^4	0.1696×10^4																
1.0	12000	0.2021×10^3	0.3018×10^2	0.3627×10^{-3}	0.1179	0.5307×10^4	0.1806×10^4																
1.0	13000	0.3011×10^3	0.3234×10^2	0.3043×10^{-3}	0.2299	0.6293×10^4	0.1965×10^4																
1.0	14000	0.4440×10^3	0.3522×10^2	0.2493×10^{-3}	0.3942	0.7291×10^4	0.2174×10^4	0.4446×10^3	0.3525×10^2	0.3	0.4898×10^3	0.3625×10^2	0.459	0.2225×10^4	0.4592×10^3	0.356×10^2	0.396	0.2182×10^4	0.450×10^3	0.355×10^2	0.405	0.4428×10^3	0.3506×10^2
2.0	6000	0.5496×10^2	0.2542×10^2	0.1622	0.1689×10^{-4}	0.2233×10^3	0.1441×10^4															0.5496×10^2	0.2542×10^3
2.0	7000	0.6424×10^2	0.2581×10^2	0.1390	0.1819×10^{-3}	0.9142×10^3	0.1546×10^4																
2.0	8000	0.7408×10^2	0.2610×10^2	0.1215	0.1106×10^{-2}	0.1837×10^4	0.1613×10^4																
2.0	9000	0.8588×10^2	0.2655×10^2	0.1076	0.4581×10^{-2}	0.2708×10^4	0.1637×10^4																
2.0	10000	0.1026×10^3	0.2703×10^2	0.9592×10^{-1}	0.1448×10^{-1}	0.3595×10^4	0.1654×10^4																
2.0	11000	0.1298×10^3	0.2773×10^2	0.8526×10^{-1}	0.3754×10^{-1}	0.4534×10^4	0.1702×10^4															0.1026×10^4	0.2702×10^2
2.0	12000	0.1754×10^3	0.2881×10^2	0.7483×10^{-1}	0.8363×10^{-1}	0.5539×10^4	0.1790×10^4																
2.0	13000	0.2496×10^3	0.3043×10^2	0.6427×10^{-1}	0.1647	0.6603×10^4	0.1920×10^4																
2.0	14000	0.3608×10^3	0.3267×10^2	0.5387×10^{-1}	0.2902	0.7704×10^4	0.2095×10^4															0.3598×10^3	0.3255×10^2
3.0	6000	0.5496×10^2	0.2502×10^2	0.2433	0.1379×10^{-4}	0.1899×10^3	0.1442×10^4															0.5495×10^3	0.2502×10^2
3.0	7000	0.6421×10^2	0.2541×10^2	0.2085	0.1485×10^{-3}	0.8692×10^3	0.1548×10^4																
3.0	8000	0.7393×10^2	0.2576×10^2	0.1823	0.9028×10^{-3}	0.1797×10^4	0.1622×10^4																
3.0	9000	0.8524×10^2	0.2612×10^2	0.1616	0.3740×10^{-2}	0.2718×10^4	0.1652×10^4																
3.0	10000	0.1006×10^3	0.2656×10^2	0.1443	0.1182×10^{-1}	0.3649×10^4	0.1669×10^4															0.1006×10^4	0.2656×10^2
3.0	11000	0.1245×10^3	0.2718×10^2	0.1287	0.3066×10^{-1}	0.4630×10^4	0.1709×10^4																
3.0	12000	0.1634×10^3	0.2810×10^2	0.1139	0.6837×10^{-1}	0.5679×10^4	0.1786×10^4																
3.0	13000	0.2261×10^3	0.2947×10^2	0.9892×10^{-1}	0.1351	0.6792×10^4	0.1900×10^4																
3.0	14000	0.3209×10^3	0.3138×10^2	0.8406×10^{-1}	0.2404	0.7952×10^4	0.2058×10^4															0.3201×10^3	0.3128×10^2

Table 2. Conversion from metric to English units

Quantity	English units	Metric units	Conversion factor
In metric units	To obtain English units in	From metric units in	Multiply metric quantities by
Temperature	^{o}R	^{o}K	1.800
Density	lb_m/ft^3	kg/m^3	0.06243
Electrical conductivity	$(\text{ in.})^{-1}$	$(\text{ m})^{-1}$	0.02540
Sound Speed	ft/sec	m/sec	3.281
Mass flux	$lb_m/in.^2 sec$	kg/m^2 sec	1.422×10^{-3}
Velocity	ft/sec	m/sec	3.281
Reynolds number	$in.^{-1}$	cm^{-1}	2.540
Electron concentration	$number/in.^3$	$number/cm^3$	16.39